HAL
open science

Stochastic Galerkin finite element method in application to identification problems for failure models parameters in heterogeneous materials

Emir Karavelić

To cite this version:

Emir Karavelić. Stochastic Galerkin finite element method in application to identification problems for failure models parameters in heterogeneous materials. Mechanics [physics.med-ph]. Université de Technologie de Compiègne; Univerzitet u Sarajevu, 2019. English. NNT : 2019COMP2501 . tel-02514689

HAL Id: tel-02514689

https://theses.hal.science/tel-02514689v1

Submitted on 22 Mar 2020

HAL is a multi-disciplinary open access archive for the deposit and dissemination of scientific research documents, whether they are published or not. The documents may come from teaching and research institutions in France or abroad, or from public or private research centers.

L'archive ouverte pluridisciplinaire **HAL**, est destinée au dépôt et à la diffusion de documents scientifiques de niveau recherche, publiés ou non, émanant des établissements d'enseignement et de recherche français ou étrangers, des laboratoires publics ou privés.

Par **Emir KARAVELIĆ**

Stochastic Galerkin finite element method in application to identification problems for failure models parameters in heterogeneous materials

Thèse présentée en cotutelle pour l'obtention du grade de Docteur de l'UTC

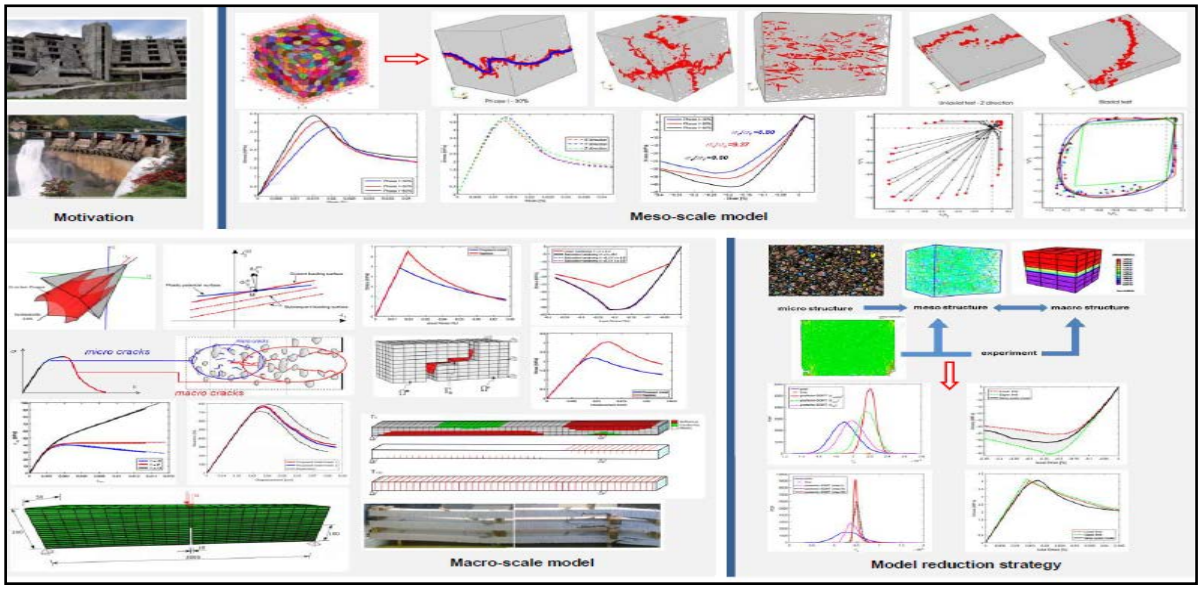

Soutenue le 17 septembre 2019

Spécialité : Mécanique Numérique : Unité de recherche en Mécanique - Laboratoire Roberval (FRE UTC - CNRS 2012)

D2501

University of Technology
of Compiègne

University of Sarajevo,
Faculty of Civil Engineering

Emir Karavelić

Stochastic Galerkin Finite Element Method in Application to Identification Problems for Failure Models Parameters in Heterogeneous Materials

DOCTORAL THESIS

Spécialité : Mécanique Numérique

Supervisors:

Prof. Adnan IBRAHIMBEGOVIĆ, PhD, University of Technology of Compiègne, France

Prof. Azra KURTOVIĆ, PhD, University of Sarajevo, Faculty of Civil Engineering, BiH

Sarajevo & Compiègne, 2019

University of Technology
of Compiègne

University of Sarajevo,
Faculty of Civil Engineering

This doctoral thesis is prepared in accordance with doctorate co-supervision agreement between Université de Technologie de Compiègne, France and University of Sarajevo, Faculty of Civil Engineering, Bosnia and Herzegovina.

The doctoral thesis is defended on September 17, 2019. at the University of Sarajevo, Faculty of Civil Engineering, before the following committee:

1. Prof. Adnan IBRAHIMBEGOVIĆ, PhD, University of Technology of Compiègne, France;
2. Prof. Azra KURTOVIĆ, PhD, University of Sarajevo, Faculty of Civil Engineering, BiH;
3. Prof. Samir DOLAREVIĆ, PhD, University of Sarajevo, Faculty of Civil Engineering, BiH;
4. Prof. Hermann MATTHIES, PhD, Institute of Scientific Computing Technische Universität Braunschweig, Germany;
5. Prof. Ivica KOŽAR, PhD, University of Rijeka, Faculty of Civil Engineering, Croatia;
6. Prof. Nikolaos LIMNIOS, PhD, University of Technology of Compiègne, France;
7. Prof. Željana NIKOLIĆ, PhD, University of Split, Faculty of Civil Engineering, Architecture and Geodesy, Croatia;
8. Prof. José Luis PÉREZ APARICIO, PhD, Universitat Politècnica de València, Spain.

To my family

Acknowledgements

Through my "doctoral journey" I faced many challenges that could not have been possible to overcome without the support and help of kind people around me. I gratefully acknowledge support of the Faculty of Civil Engineering in Sarajevo and the French Government for scholarship through the Campus France programme.

I would like to extend my profound gratitude to the following:

my supervisor prof. Adnan Ibrahimbegović, whose expertise, guidance and consistent advice helped me bring this study completed, and whose work demonstrated me that nothing is impossible. I would also like to thank to his wife Nita for delicious meatless dinners every time I come to France. I am thankful to my supervisor prof. Azra Kurtović for useful comments, suggestion and critiquing.

reviwers of this thesis prof. Ivica Kožar and prof. Hermann Matthies, for carefully reading my thesis, useful comments and remarks, and the members of the jury prof. Nikolaos Limnios, prof. Željana Nikolić and prof. Jose Luis Perez Aparicio for their participation and questions.

the former and the present dean of the Faculty of Civil Engineering in Sarajevo , prof. Mustafa Hrasnica and prof. Samir Dolarević, and prof. Esad Mešić, the head of materials and constructions department, for their advice and support during my study.

my colleagues from the Faculty of Civil Engineering in Sarajevo and University of Technology of Compiègne, who gave their particular contribution to the completion of this thesis, in particular to Mijo, Ismar, Adis, Emina-mala, Emina H., Tea, Pablo, Ivan, Sara, Andjelka, Adela, Jelena, Xuan Nam and Abir. My sincerest thanks also goes to Dr. Noémi Friedman, from Institute of Scientific Computing Technische Universität Braunschweig, for sharing her knowledge selflessly.

my family for their continuous and unconditional love, help and support. Mom, thank you for being you because you are the greatest person I have ever met.

Last but not the least, I wish to thank my loving and supportive wife, Ilma, for sleepless nights while she was raising our two beautiful little girls during my stay in France, for her understanding, sacrifice and unconditional love.

Abstract

This thesis deals with the localized failure for structures built of heterogeneous composite material, such as concrete, at two different scale. These two scale are latter connected through the stochastic upscaling, where any information obtained at meso-scale are used as prior knowledge at macro-scale.

At meso scale, lattice model is used to represent the multi-phase structure of concrete, namely cement and aggregates. The beam element represented by 3D Timoshenko beam embedded with strong discontinuities ensures complete mesh independency of crack propagation. Geometry of aggregate size is taken in agreement with EMPA and Fuller curve while Poisson distribution is used for spatial distribution. Material properties of each phase is obtained with Gaussian distribution which takes into account the Interface Transition Zone (ITZ) through the weakening of concrete.

At macro scale multisurface plasticity model is chosen that takes into account both the contribution of a strain hardening with non-associative flow rule as well as a strain softening model components for full set of different 3D failure modes. The plasticity model is represented with Drucker-Prager yield criterion, with similar plastic potential function governing hardening behavior while strain softening behavior is represented with St. Venant criterion.

The identification procedure for macro-scale model is perfomed in sequential way. Due to the fact that all ingredients of macro-scale model have physical interpretation we made calibration of material parameters relevant to particular stage. This approach is latter used for model reduction from meso-scale model to macro-scale model where all scales are considered as uncertain and probability computation is performed. When we are modeling homogeneous material each unknown parameter of reduced model is modeled as a random variable while for heterogeneous material, these material parameters are described as random fields. In order to make appropriate discretizations we choose p-method mesh refinement over probability domain and h-method over spatial domain. The forward model outputs are constructed by using Stochastic Galerkin method providing outputs more quickly the the full forward model. The probabilistic procedure of identification is performed with two different methods based on *Bayes's* theorem that allows incorporating new observation generated in a particular loading program. The first method Markov Chain Monte Carlo (MCMC) is identified as updating the measure, whereas the second method Polynomial Chaos Kalman Filter(PceKF) is updating the measurable function. The implementation aspects of presented models are given in full detail as well as their validation through the numerical examples against the experimental results or against the benchmarks available from literature.

Sažetak

Ova teza se bavi problemima lokalizovanog loma konstrukcija izgrađenih od heterogenih materijala, kao što je beton, na dva različita nivoa. Ova dva nivoa su povezane pomoću metoda stohastičkog uvećavanja, gdje je svaka informacija dobijena na mezo nivou iskorištena kao prethodno znanje na makro nivou.

Na mezo nivou korišten je rešetkasti model kako bi predstavili više komponentnu strukturu betona, odnosno cement i agregat. Gredni elementi modela su predstavljeni pomoću 3D Timošenkove grede sa dodatim jakim diskontinuitetom koji osigurava propagaciju pukotine neovisno od odabrane mreže. Veličina zrna agregata je uzeta u skladu sa EMPA i Fuller-ovom krivom, a prostorna raspodjela unutar domene je izvršena pomoću Poisson-ove distribucije. Materijalne karakteristike obje faze su odabrane pomoću Gauss-ove distribucije čime je kroz slabljenje betona uzeta u obzir i zona prelaza između ovih faza.

Na makro nivou je odabran višekriterijalni model plastičnosti koji uzima u obzir doprinos komponenti očršćavanja sa ne-asocijativnim zakonom tečenja kao i komponenti omekšavanja kako bi prikazali kompletan 3D način otkazivanja. Model plastičnosti je predstavljen pomoću Drucker-Prager-ovog kriterija tečenja, sa sličnom funkcijom plastičnog potencijala kojom je definisan način očršćavanja, dok je zakon omekšavanja predstavljen pomoću St. Venant-ovog kriterija.

Postupak identifikacije za makro model izvršen je postupno. Zbog činjenice da svi parametri makro modela imaju fizičko značenje, kalibracija parametara materijala je izvršena za svaku fazu relevantu za određeni parametar. Ovaj pristup je korišten i za redukciju makro modela, gdje su oba nivoa uzeta u obzir sa određenim izvorima nesigurnosti. U slučaju kada modeliramo homogeni materijal parametri modela su definisani kao slučajne promjenljive dok su u slučaju heterogenog materijala parametri definisani kao slučajna polja. Za diskretizaciju prostorne domene korišten je h-metoda progušćavanja mreže dok je za domenu vjerovatnoće korišten p-method. Korištenjem Stohastičke Galjerkinove metode formiran je zamjenski model koji nam daje mnogo brže rezultate proračuna nego puni proračunski model. Probabilistička procedura identifikacije parametara je izvršena sa dvije različite metode zasnovane na *Bayes*-ovoj teoremi koja nam omogućava da svaku novu informaciju dobijenu određenim ispitivanjima uključimo u proračun. Prva metoda, Markov Chain Monte Carlo (MCMC) metoda je zasnovana na ažuriranju mjere vjerovatnoće, dok je druga metoda Polynomial Chaos Kalman Filter (PceKF) predstavlja ažuriranje slučajne promjenljive. Implementacija predstavljenih modela je detaljno prikazana u radu kao i potvrđivanje modela poređenjem rezultata numeričkih simulacija sa eksperimentalnim rezultatima i rezultatima dostupnim u literaturi.

Contents

List of figures xv

List of tables xxiii

List of Publications xxv

1 Introduction 1
1.1 Motivation . . . 2
1.2 Multi-scale modeling of concrete . . . 2
1.2.1 Meso-scale modeling . . . 4
1.2.1.1 Particle models . . . 4
1.2.1.2 Rigid body spring models . . . 5
1.2.1.3 Lattice models . . . 6
1.2.1.4 Continuum models . . . 8
1.2.1.5 Generation of geometry for meso-scale . . . 8
1.2.1.6 Material Constitutive Models . . . 10
1.2.2 Macro-scale modeling . . . 11
1.2.2.1 Fracture principles: LEFM and NLFM . . . 11
1.2.2.2 Discrete crack approach . . . 12
1.2.2.3 Smeared crack approach . . . 13
1.2.2.4 Enhanced crack approach . . . 14
1.2.2.5 Weak/strong discontinuity approach . . . 14
1.3 Aims and scopes . . . 15
1.4 Organization of the thesis . . . 15

2 Concrete meso-scale model with full set of 3D failure modes 17
2.1 Introduction . . . 19
2.2 Meso-scale model for concrete failure . . . 22
2.3 Macroscopic response: numerical homogenization . . . 30
2.3.1 Construction of specimen . . . 30
2.3.2 Tension test . . . 31
2.3.2.1 Uniaxial tension test . . . 31
2.3.2.2 Hydrostatic tension test . . . 33
2.3.3 Compression test . . . 34
2.3.4 Failure surfaces for biaxial loading . . . 36
2.4 Final comments on the presented 3D concrete meso-scale model . . . 41

3 Multi-surface plasticity model for concrete with 3D failure modes 43
3.1 Introduction . . . 45
3.2 Continuum model formulation . . . 46
3.2.1 Thermodynamics framework . . . 47
3.2.2 Stress resultant hardening model . . . 52
3.2.3 Softening plasticity . . . 56
3.3 Space and time Discrete approximation . . . 61
3.3.1 Spatial discretization . . . 61
3.3.2 Integration of internal state variables for plasticity . . . 62
3.4 Numerical examples . . . 66
3.4.1 Uniaxial tension test . . . 66
3.4.2 Notched bar in tension . . . 67
3.4.3 Three point notched beam . . . 68
3.4.4 Shear test . . . 69
3.4.5 Compression test . . . 70
3.4.6 Bending test on a reinforced concrete beam . . . 72
3.5 Final comments on the presented 3D concrete macro-scale model . . . 75

4 Identification of macro-scale model parameters 79
4.1 Introduction . . . 81
4.2 A brief description of meso/macro-scale model . . . 82
4.3 Tension test . . . 85
4.3.1 Identification of elastic parameters . . . 85
4.4 Compression test . . . 87
4.4.1 Identification of elastic parameters . . . 87
4.4.2 Identification of hardening parameters . . . 89
4.5 Final comments on the presented identification procedure . . . 96

5 Reduced model of macro-scale stochastic plasticity 97
5.1 Introduction and motivation . . . 99
5.2 Plasticity at multiple scales . . . 101
5.3 Macro-scale reduced ED-FEM model . . . 109
5.4 Stochastic macro-scale plasticity model parameters identification . . . 115
5.4.1 MCMC Bayesian updating of the measure . . . 120
5.4.2 The Bayesian upadetes with linear Gauss-Markov-Kálmán filter . . . 123
5.5 Numerical simulations . . . 130
5.5.1 Identification of elastic parameters . . . 131
5.5.2 Identification of hardening parameters . . . 138
5.5.3 Identification of softening parameters . . . 141
5.5.4 Simultaneous identification of all macro-scale model parameters and use of standard experiments . . . 143
5.6 Final comments on the presented stochastic plasticity identification . 146

6 Conclusions and future perspectives 149

References **153**

Appendix A Tables **167**

List of figures

1.1 Structures built of heterogeneous materials: Hotel Igman (Sarajevo); Concrete bridge (Visoko); Hydropower Plant (Jablanica) 2
1.2 Representation of different levels of analysis: (a) macroscale; (b) concrete mesoscale; (c) micro scale 3
1.3 Meso-structure tessellation (left) and definition of nodal degrees of freedom and contact facets in two-dimension (right) [15] 5
1.4 Element formulation in RBSM [20] 6
1.5 Lattice-beam models: (a) regular triangular lattice; (b) regular square lattice, taken from [23] 7
1.6 (a) 2D irregular lattice with Voronoi cells (b) 3D irregular lattice with Voronoi cells 7
1.7 (a) 3D crack pattern in unaxial tension test for a structured mesh [39]; (b) 3D FE mesh of concrete with spherical aggregates [2] 8
1.8 Random particle drop method 10
1.9 Fictitious crack model 12
1.10 Comparison of Discrete crack model and Smeared crack model 13

2.1 (a) Structure of discrete lattice model with Voronoi cells as units of heterogeneous material and cohesive links between them (b) two neighbouring Voronoi cells 20
2.2 Grading curves 22
2.3 3D Timoshenko beam displacements 23
2.4 Three failure modes in concrete 23
2.5 Uniaxial tension test: macroscopic response for different aggregate volume fraction 31
2.6 Specimen contours at the end of uniaxial tension test. Beam elements in increasing softening are red colored 31
2.7 Uniaxial tension test: macroscopic responses for specimen (phase I-50%) in three loading directions 32
2.8 Specimen contours at the end of uniaxial tension test for phase I-50% specimen in all three loading directions. Beam elements in increasing softening are red colored 32
2.9 Macroscopic response - phase I-50%: (a) hydrostatic tension test; (b) hydrostatic-uniaxial tension test comparison for X direction 33
2.10 Specimen contour at the end of hydrostatic tension test for phase I-50% specimen. Beam elements in increasing softening are red colored 34

2.11 Macroscopic response for uniaxial compression test: (a) different aggregate volume fraction; (b) phase I-50% 35
2.12 Complete macroscopic response for different aggregate volume fraction 35
2.13 Specimen contour at the end of uniaxial compression test for phase I-50% specimen in three loading directions. Beam elements in increasing softening are red colored (upper row), displacements in the direction perpendicular to loading direction (lower row) 36
2.14 Specimen for biaxial test: boundary conditions and loading 37
2.15 Uniaxial macroscopic response for 6 realizations in plate specimen: (a) tension test; (b) compression test 38
2.16 Failure surfaces: (a) for realization 1; (b) for 6 realizations with the multisurface Drucker-Prager - Rankine surface (red line - eq. 36), coupled plasticity-damage model (black line - eq. 37), Saint-Venant (green line - eq. 38) and experimental (blue line) 38
2.17 Evolution of σ_1/σ_{ci} with respect to σ_3/σ_{ci} during loading until failure for realization 1 (red dots) 39
2.18 Biaxial-Uniaxial test comparison for realization 1 - phase I-50%: macroscopic response in X direction - tension test 39
2.19 Plate specimen contours at the end of uniaxial and biaxial tension test (upper row) and compression test (lower row). Beam elements in increasing softening are red colored 41

3.1 Multisurface criterion (a) in principal stress space (b) in meridian plane 47
3.2 The loading and plastic potential surfaces for the Drucker-Prager material with a non-associated flow rule 53
3.3 Elastic domain in principal stress space (a) 3D case (b) 2D case for $\sigma_3 = 0$ 56
3.4 Slip line Γ_s separating domain into Ω^+ and Ω^- 58
3.5 (a) Failure modes in both compression and tension (b) Influence of strain state on fracture energy 60
3.7 Vertical displacement at the end of uniaxial tension test for three different mesh versions: (a) 2 elements; (b) 3 elements; (c) 63 elements 66
3.6 Macroscopic response for uniaxial tension test 67
3.8 Notched specimen: geometry, boundary conditions and loading . . . 67
3.11 Macroscopic response for notched specimen in tension 68
3.12 Macroscopic response for double-notched specimen in tension 68
3.9 Displacement in loading direction at the end of numerical simulation:(a) Notched specimen ; (b) Double-notched specimen 69
3.10 Mesh without fractured elements with discontinuity surface Γ_s; (a) Notched specimen ; (b) Double-notched specimen 69
3.13 Three point notched beam: geometry, boundary conditions and loading 71
3.19 Bending test cross-section 72
3.14 Load-displacement diagram for three point notched beam and comparison with the experimental results 72
3.15 Three point notched beam: deformed mesh 73

3.16 Isochoric shear test: (a) Computed responses (solid line) and results taken from [120] (dash line); (b) boundary conditions and loading . . 74
3.17 Macroscopic response: (a) uniaxial compression test; (b) complete response 74
3.18 Bending test: loading and geometry 75
3.21 Bending test: state of specimen and crack propagation 75
3.20 Comparison of results: macroscopic stress-strain response 76
3.22 Bending test cross-section finite element mesh (red circles represent position of truss element) 76
3.23 (a) Load Q in terms of the deflection at the mid-point of the inner span; (b) Load T in terms of the resulting displacement for test $T2$. 76
3.24 Crack propagation: (a) experimental results for test T_0-lower beam,T_2-midlle beam, T_1-upper beam; (b) results taken from [123] 77

4.1 The graphical representation of uncertain one dimensinal material parameter(a) deterministic description $K(x) = const = 15$; (b) homogeneous material described by Gaussian radndom variable $K(x,\omega) = \mathcal{N}(15,1)$; (c) heterogeneous material described by random field $K(x,\omega) = \bar{K} + \gamma(x,\omega)$ where $\gamma(x,\omega)$ is Gaussian random field 82
4.2 (a) Displacements measured to evaluate the contraction $\Delta l = 0.25 \cdot (u_1 + u_2 + u_3 + u_4)$ of the specimen; (b) loading path 86
4.3 Objective function for unaixial tension test with loading in (a) X-direction; (b) Y-direction; (c) Z-direction 86
4.4 Numerical tests : (a) simple shear test; (b) hydrostatic pressure test; (c) loading path 87
4.5 Objective function for : (a) simple shear test - J_2; (b) hydrostatic pressure test -J_3 88
4.6 Objective function for single parameter: (a) simple shear test; (b) hydrostatic pressure test 88
4.7 (a) Displacements measured to evaluate the expansion $\Delta l = 0.25 \cdot (u_1 + u_2 + u_3 + u_4)$ of the specimen; (b) loading path 88
4.8 Objective function for: (a) uniaxial compression test; (b) simple shear test combined with hydrostatic pressure test 89
4.9 Internal variable q for σ_∞=10 MPa, σ_y=2 MPa : (a) β =1000; $K_{h,lin}$=0 (b) β =0; $K_{h,lin}$=200; (c) β =1000; $K_{h,lin}$=200 90
4.10 Macroscopic response for uniaxial compression test with lattice model - phase I-60% : (a) measurements on stress-strain curve; (b) measurements on volumetric strain-axial strain curve 91
4.11 Objective function J_6 91
4.12 Comparison of macroscopic response for uniaxial compression test with lattice model - phase I-60% and continuum model with linear hardening : (a) stress versus axial strain curve; (b) volumetric strain versus axial strain curve; (c) free energy-axial strain curve 91
4.13 (a) force measured on meso-scale model (red) and 3D solid model (black) with simplified model for identification of yield function; (b) loading path 92

4.14 Biaxial-Uniaxial compression test comparison with lattice model - phase I-50%: (a) stress versus axial strain curve; (b) volumetric strain versus axial strain curve; (c) free energy-axial strain curve 93
4.15 Objective function J_7 with measurements taken from: (a) uniaxial test; (b) biaxial test; (c) uniaxial and biaxial test combined 93
4.16 Measurements for objective function J_8 94
4.17 Measurements for objective function J_9 definition (a) stress-strain curve; (b) volumetric strain-axial strain 94
4.18 Objective function J_9 with measurements taken from uniaxial compression test (a) plastic dissipation (D^p); (b) plastic dissipation (D^p) + volumetric strain 95
4.19 Comparison of stress-strain diagram for uniaxial tension test with loading in: (a) X-direction; (b) Y-direction; (c) Z-direction 95
4.20 Comparison of results for uniaxial compression test: (a) X-direction; (b) stress-strain diagram; (c) volumetric-axial strain diagram 95

5.1 (a) Structure of discrete lattice model with Voronoi cells as units of heterogeneous material and cohesive links between them (b) two neighbouring Voronoi cells 101
5.2 i) Uniaxial tension test: macroscopic response for different aggregate volume fraction; ii) Specimen contours at the end of uniaxial tension test. Beam elements in increasing softening are red colored 102
5.3 i) Uniaxial tension test: macroscopic responses for specimen (phase I-50%) in three loading directions; ii) Specimen contours at the end of uniaxial tension test for phase I-50% specimen in all three loading directions. Beam elements in increasing softening are red colored . . . 102

5.4 Reduced-model in terms of generalized ED-FEM computed from meso-scale: (a) two-phase concrete model meso-scale representation [31, 24]: aggregate (white) vs. cement paste (violet); (b) cohesive links at meso-scale with structured mesh (keeping the same mesh for different realizations in probability computations) requiring both strain and displacement discontinuity implemented within ED-FEM with same number of parameters as X-FEM, but more clear role for each parameter resulting with higher computational efficiency [29]; (c) simple tension test force-displacement diagram (statistically isotropic=same in any direction) and failure mode in tension illustrated with displacement contours and cohesive link failure; d) replacement of tension failure mode at meso-scale (rough surface) with discontinuity (plane) at macro-scale with ED-FEM, not matching perfectly the crack but fracture energy material parameter G_f; (e) uniaxial compression force-displacement and failure mode with cohesive links failure; f) biaxial compression (confirming compressive strength increase from uniaxial case) and failure mode; (g) replacing failure criterion for different failure modes under biaxial stress (colors: showing increased resistance in compression for higher aggregate volume fraction, dots: providing computed value of fracture energy for corresponding failure mode) and comparison against classical Rankin, St. Venant or Drucker-Prager macro-scale plasticity criteria [73]. 104
5.5 Multisurface criterion (a) in principal stress space (b) in meridian plane 112
5.6 The algorithmic scheme of an inverse problem solved by (a) proxy MCMC filtering; (b) Square Root Polynomial Chaos based Linear Bayesian Update 130
5.7 Numerical tests : (a) simple shear test; (b) hydrostatic pressure test; (c) loading path 131
5.8 Comparison of prior and posterior pdf and the likelihood function for shear modulus - Simple shear test (upper row) and bulk modulus - hydrostatic compression test (lower row) with standard deviation for the prior σ_p=500 MPa (left) and σ_p=200 MPa (right) - energy measurements 132
5.9 Prior and posterior pdf for shear modulus - simple shear test and Bulk modulus - hydrostatic compression test, obtained by SQRT Kalman filter (left - force measurements) and comparison with MCMC (right - energy measurements) 133
5.10 Comparison of prior and posterior pdf and the likelihood function for bulk modulus-hydrostatic compression test for different initial point of MC 133
5.11 MCMC update of elastic material parameters $\{K, G\}$ using elastic step of load: (a) simple shear test; (b) hydrostatic compresion test . 134
5.12 The square root update of elastic material parameters $\{K, G\}$ using elastic step of load: (a) simple shear test; (b) hydrostatic compresion test 134

5.13 Comparison of prior and posterior pdf and the likelihood function for shear modulus-hydrostatic compression test and for bulk modulus-simple shear test . . . 135
5.14 Comparison of posterior PDF for different measurement points describing elastic material parameter: (a) shear modulus (G) - simple shear test; (b) bulk modulus (K) - hydrostatic compresion test . . . 135
5.15 Macroscopic response in elastic range with computed parameters . . . 135
5.16 (a) Displacements measured to evaluate the expansion $\Delta l = 0.25 \cdot (u_1 + u_2 + u_3 + u_4)$ of the specimen; (b) loading path . . . 136
5.17 Comparison of prior and posterior pdf function for: (a) shear modulus; (b) bulk modulus performed on uniaxial compression test obtained by MCMC (upper row) and by SQRT Kalman filter (lower row) . . . 136
5.18 Polynomial chaos approximation of the model response for uniaxial compression test: (a) bulk modulus; (b) shear modulus . . . 137
5.19 Comparison of prior and posterior pdf function obtained by SQRT Kalman filter for: (a) shear modulus; (b) bulk modulus performed on uniaxial tension test for three loading direction . . . 137
5.20 (a) force measured on meso-scale model (red) and 3D solid model (black) with simplified model for identification of yield function; (b) loading path . . . 138
5.21 Updates for plastic parameters $\{\sigma_y,\ tg_\Phi\}$ obtained by SQRT Kalman filter . . . 139
5.22 Objective function with measurements taken from: (a) uniaxial test; (b) biaxial test; (c) uniaxial and biaxial test combined . . . 139
5.23 Measurements for objective function for hardening parameters $(\beta, \tan(\psi))$ (a) stress-strain curve; (b) volumetric strain-axial strain . . . 140
5.24 Updates for plastic parameters $\{\beta,\ tg_\Psi\}$ obtained by SQRT Kalman filter with four measurement (plastic dissipation - D^p) shown in (a)-(b) and (plastic dissipation - D^p + volumetric strain) shown in (c)-(d), taken from uniaxial compression test . . . 140
5.25 Objective function J_9 with measurements taken from uniaxial compression test (a) plastic dissipation (D^p); (b) plastic dissipation (D^p) + volumetric strain . . . 141
5.26 Updates for softening parameters σ_u,and $G_{f,t}$ obtained by SQRT Kalman filter with three measurements taken from uniaxial tension test 142
5.27 Objective function for: (a) uniaxial tension test; (b) uniaxial compression test . . . 142
5.28 Updates for softening parameters σ_u,and $G_{f,t}$ obtained by SQRT Kalman filter with three measurements taken from uniaxial compression test . . . 142
5.29 Global response compute with 95% confidence interval of posterior distribution for: (a) uniaxial compression test; (b) uniaxial tension test 143
5.30 Updates for elastic and hardening parameters performed simultaneously on uniaxial compression test with measurements of force-displacement diagram . . . 144

5.31 Updates for elastic and plastic parameters performed simultaneously on uniaxial compression test 145
5.32 Updates for elastic and softening parameters performed simultaneously on uniaxial compression test 146
5.33 Updates for hardening and softening parameters performed simultaneously on uniaxial compression test 147

List of tables

2.1 Material parameters for meso-scale model 30
2.2 Fracture energy under particular couples of imposed displacements for realization 1 (red points) 40

3.1 Material parameters 67
3.2 Material parameters for uniaxial compression test 71
3.3 Material parameters for bending test 73

A.1 Uniaxial strength with 50% of aggregates 167
A.2 Ratios of ultimate strength with respect to σ_c along X and Z directions under different couples of imposed displacements for realization 1,2 and 3 168
A.3 Ratios of ultimate strength with respect to σ_c along X and Z directions under different couples of imposed displacements for realization 4,5 and 6 169

List of Publications

Journals

[1] Karavelic E., Nikolic M., Ibrahimbegovic A., Kurtovic A., 'Concrete meso-scale model with full set of 3D failure modes with random distribution of aggregate and cement phase. Part I: Formulation and numerical implementation', Comp. Methods Appl. Mech. Eng., 344, 1051-1072, (2019).

[2] Karavelic E., Ibrahimbegovic A., Dolarevic S.,'Multi-surface plasticity model for concrete with 3D hardening/softening failure modes for tension, compression and shear', Computers and Structures, 221, 74-90, (2019).

Chapters in Books

[1] Karavelic E. Nikolic M., Ibrahimbegovic A., 'Multiscale Model of Concrete Failure', in (ed. D. Brancherie, S. Bouvier, P. Feissel, A. Ibrahimbegovic), ISTE Wiley, 99-122, (2017)

Conferences and Workshops

[1] Karavelic E. Nikolic M., Ibrahimbegovic A., 'Lattice element model in simulation of Concrete failure', Eccomas Thematic Conference, 3nd International Conference on Computational Methods for Solids and Fluids, Ljubljana,Slovenia, September 20-22, 2017.

[2] Karavelic E., Ibrahimbegovic A., 'Multi-surface plasticity model with softening for solids with marked difference of failure', CILAMCE 2018 - XXIX Congres on Numerical Methods in Engineering, Paris/Compiegne, France, November 11-14, 2018

[3] Karavelic E., Ibrahimbegovic A., Kurtovic A., 'An embedded strong discontinuity multi-surface model for cracking of concrete', ECCOMAS MSF 2019 - Multiscale Comp. Methods for Solids and Fluids, Sarajevo, Bosnia-Herzegovina, 18-20 September 2019

1

Introduction

Contents

1.1 Motivation 2
1.2 Multi-scale modeling of concrete 2
1.2.1 Meso-scale modeling 4
1.2.1.1 Particle models 4
1.2.1.2 Rigid body spring models 5
1.2.1.3 Lattice models 6
1.2.1.4 Continuum models 8
1.2.1.5 Generation of geometry for meso-scale 8
1.2.1.6 Material Constitutive Models 10
1.2.2 Macro-scale modeling 11
1.2.2.1 Fracture principles: LEFM and NLFM 11
1.2.2.2 Discrete crack approach 12
1.2.2.3 Smeared crack approach 13
1.2.2.4 Enhanced crack approach 14
1.2.2.5 Weak/strong discontinuity approach 14
1.3 Aims and scopes 15
1.4 Organization of the thesis 15

1.1 Motivation

At many structures in Bosnia and Herzegovina there are visible scars of war after more than a two decades. As witnesses of a dark period, they are demolished, unstructured and horrific structures. Regardless of their condition, some of these structures are still being exploited (Figure 1.1). Thus, it is very important to determine the functionality of these structures and propose future action. Is it possible to repair these structures and retain their functionality, or it is necessary to demolish them completely depends on our knowledge about their durability (life-cycle integrity). Experimental testing for large structures is still lacking whether due to their size or due to different loading programs (natural or man-made) that cannot be fully reproduced in laboratory testing. Furthermore, the testing on small size structure are not sufficient to provide full validation because a well-known size-effect (for different size structures built of same heterogeneous material we can observed different failure modes). Moreover, many of these structures are built of probably the most used heterogeneous composite material, such as concrete which in traditional engineering studies have been considered as a homogeneous material. It is well-known by now that observation of concrete stands on three levels. Each of these levels have a life on their own and brings it to the next level.

All the specific features described above, which are characteristic for concrete-like materials, pushes us to construct a models for the structures built of heterogeneous composite materials capable to predict structure response probability distribution taking into account multi-scale analysis. In vast majority of recent works upscaling approach is based only on capturing the 'average' response on the larger scale or a pre-defined probability distribution is used. A large number of numerical models can be found in the literature dealing with mesostructure and macrostructure of heterogeneous materials and many shows some important limitations. Thus, in next section we provide an overview of numerical methods for simulation of concrete bahavior.

Figure 1.1: Structures built of heterogeneous materials: Hotel Igman (Sarajevo); Concrete bridge (Visoko); Hydropower Plant (Jablanica)

1.2 Multi-scale modeling of concrete

Concrete as a mixture of cement, water and aggregates of different sizes, can be modeled and understood considering it as a multiscale material which consist from

different scales: micro-scale (μm), meso-scale ($mm - cm$) and macro-scale (m) (Figure 1.2). At macro-scale concrete is considered as homogeneous material, and in most of the recent works proposed models at this scale are phenomenological. Disadvantage of macro-scale simulation is that we can not represent actual nonlinear behavior of concrete when constitutive materials are changed. Thus, combining phenomenological models with continuum-type constitutive models such as plasticity and/or damage theory along with some principles of fracture mechanics provides a satisfactory description of mechanical behavior of concrete. The price to pay is the complexity of models as well as additional parameters, in some cases physically-maeningless, required to describe such models.

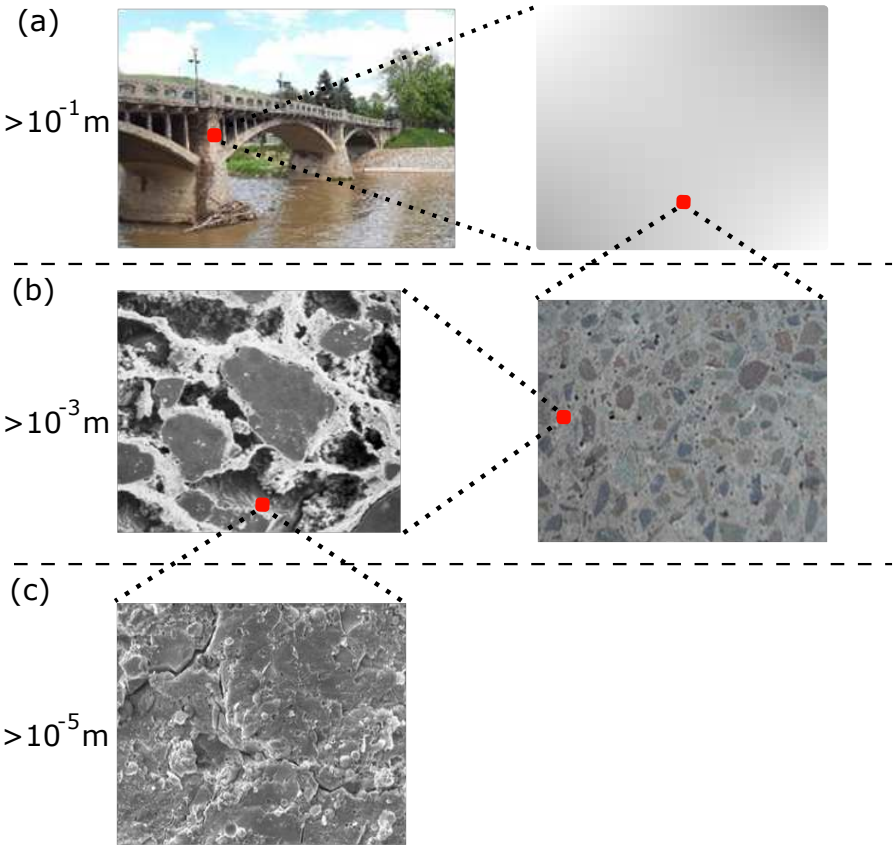

Figure 1.2: Representation of different levels of analysis: (a) macroscale; (b) concrete mesoscale; (c) micro scale

Numerical simulation of concrete at meso-scale starts to develop with the increase in computer power. At this scale concrete is modelled as a composite material consisting of three phases: the larger aggregates, the mortar, and the interfaces between these two (Figure 1.2b). ITZ properties vary substantially from the mortar matrix due to the gradient of porosity and the complementary gradient of anhydrous cement and hence, it is logical to model these phases separately in the mesoscale models [1]. This approach can be used effectively to study the effect of concrete mix on the macro properties of concrete and to investigate the nonlinear behaviour of concrete [2]. It is the most useful and practical way of modelling concrete when

the heterogeneous nature of concrete should be taken in to account in order to understand how the phases affect the macro behavior, fracture mechanics of concrete and how to improve the performance of concrete. By using mesoscale models to simulate the behavior of concrete, number of experimental tests and amount of time is spent can be reduced. Therefore, meso-scale modeling with accurate constitutive material behavior can be considered as cost-effective, and time effective alternative to predict mechanical behavior and optimum mix design method for concrete.

At the microscale level ITZ and internal structure of the hardened cement paste are taken into account. Chemical processes during hydration of cement, autogenous swelling and self-desiccation or aggressive agent impact can be studied at this scale. All these features can improve concrete resistance and durability. In recent decades a new experimental techniques are developed, such as nanoindentation which allows to determine the behavior of the calcium silicate hydrates (CSH). Also, there exist in the literature a developed program for modeling the microstructural development and performance properties of cement based materials [3] providing a influence of different process that happanes at this scale. Latter, it turns out to be very important to overall mechanical and time-dependent properties of concrete.

In multiscale analysis, the results from lower scale are transfered to the upper scale. For instance, in the case dealt with in this thesis, information obtained at meso-scale are used as a prior knowledge on macro-scale. This upscaling requires both meso-scale and macro-scale model which are latter coneccted through the deterministic or stochastic upscaling techniques.

1.2.1 Meso-scale modeling

Although concrete modeling at mesoscale has become popular in the last few decades, a large number of such models can be found in the literature. The pioneering continuum model [4], is followed by many others [5, 7, 6, 8–12] based on the lattice and continuous representation of heterogeneous media with a focus on the global response and the cracks propagation under the mechanical loads.

As already mention above, there is a large number of different mesoscale models and most of them may be included into the following broad groups: particle models, rigid body spring models, lattice models and continuum models. In following section we give a brief review and comparison of these meso-scale models.

1.2.1.1 Particle models

Lattice Discrete Particle Methods (LDPM) is a combination of the discrete element method (DEM), which was initially introduced to model granular systems, and the confinement shear lattice model [8, 13]. In LDPM, element size in the lattice is not a free parameter as in the traditional lattice methods. Element size is dependent on the aggregate arrangement of the concrete and the lattice nodes are coincident with the centroids of the aggregates. These lattice elements characterize the interaction between aggregates in concrete [14]. Lattice element structure connecting the concrete is obtained by 3D domain tessellation defining polyhedral set which includes one aggregate particle. Both normal and shear stresses characterize the interaction

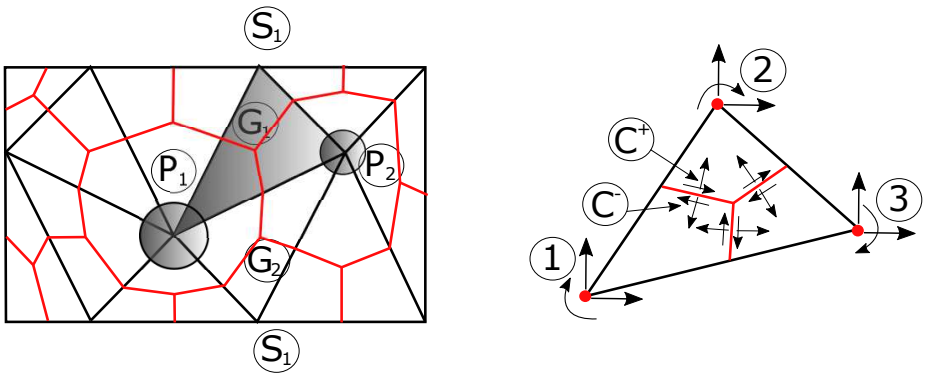

Figure 1.3: Meso-structure tessellation (left) and definition of nodal degrees of freedom and contact facets in two-dimension (right) [15]

between the aggregate particles. Four aggregates particles whose centers lie in the Delaunay tetrahedral participate to formulate the interactions among the particles. Stresses and strains are defined on the every face of the polyhedral which contain the aggregate particles [15].

Authors in [16] developed a mesoscale model using LDPM by assigning the average properties of two adjacent aggregates and the mortar matrix in between those two aggregates to the lattice element connecting the two aggregates. This model was satisfactory in simulating the meso structure of concrete with high aggregate density. LDPM has found to be realistically simulating most of the loading conditions including quasi static loading, predicting tensile and compressive strength, fracture modelling and size effect of concrete, damage in compression, confined loading conditions etc. [13].

Authors in [15] developed a lattice discrete particle meso model of concrete and validated with the experimental results and carried out simulations for unconfined compression, bi-axial behaviour, triaxial compression, torsional compressive behaviour, cyclic behaviour, tensile fracturing behaviour and tensile splitting test and found that all those loading conditions can be successfully simulated using LDPM.

The advantage of these models is that they are not computationally expensive, but they also have some drawbacks. The first is conceptual type: whenever we consider a lower scale of concrete, constitutive laws should be as simple as possible, which is not the case here. Another disadvantage of this models, in some previous works, relates to the unrealistic crack roughness at large scale.

1.2.1.2 Rigid body spring models

Rigid Body Spring Model (RBSM) was introduced in [17] where the structure is discretized in to rigid sections and these sections are connected using zero size springs distributed in the contact boundaries [18]. Voronoi diagrams are generally used to partition the continuum in to rigid bodies [19]. In this method, behavior of individual materials is represented using springs. Elastic behaviour of the representing material is obtained by assigning appropriate spring constants. This procedure requires a low computational capacity compared with the continuum finite element method [17].

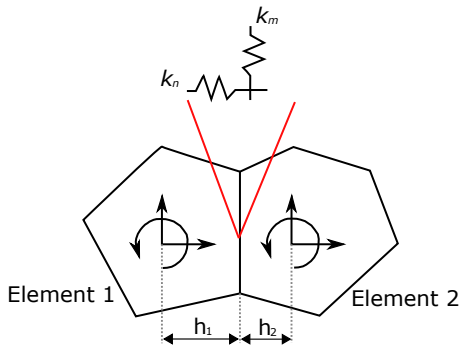

Figure 1.4: Element formulation in RBSM [20]

RBSM has the advantages of simplicity and freedom of mesh and layout generation [21].

In [20] authors carried out a mesoscale model analysis using a RBSM in 2D and in 3D. Each aggregate particle has two translational and one rotational degrees of freedom in 2D. Normal and shear springs are assigned to the boundary of these elements as shown in Figure 1.4. Normal springs can have both tensile and compressive stresses and the shear springs can have shear stresses. Fracture is known to happen if the normal spring reaches the tensile strength of the concrete or the shear springs reach the shear strength. It was found that using this model, compressive failure, tensile failure and crack propagation can be predicted.

Fracture analysis concrete can be effectively done using RBSM [21]. Fracture propagation can be modelled by removing the springs or degrading the stiffness values of the springs. In this method, fracture is propagated through interparticle boundaries and hence the fracture pattern might be affected by the arrangement of rigid particles [22]. This can be reduced by using a random mesh design.

1.2.1.3 Lattice models

In lattice models, a continuum is discretized using a set of points called 'sites' which forms a grid. These sites are connected by 1D elements such as beams, trusses and springs generating the meso structure of the material. Depending on the material represented by the bonds, a constitutive relationship is selected.

The lattice structures can have various geometrical arrangements such as triangular lattices, square lattices, random lattices as shown in Figure 1.5 [23]. It has been shown that fracture pattern is dependent on the element type used in the lattice as well as the orientation of the mesh in the model which can be solved by using a random lattice in the model [24].

The main idea in large number of lattice meso-scale models is that lattice elements progressively fail (leading to softening behaviour in failed elements) which eventually results in total macroscopic failure. However, there is still an ongoing problem of how to represent correctly the post peak softening behaviour, which is normally dependent on the mesh. This pertains to released fracture energy (i.e. area below the softening curve) which is not unique for different mesh size. Avoiding this fact can lead not only to wrong global fracture energy and wrong post peak response, but

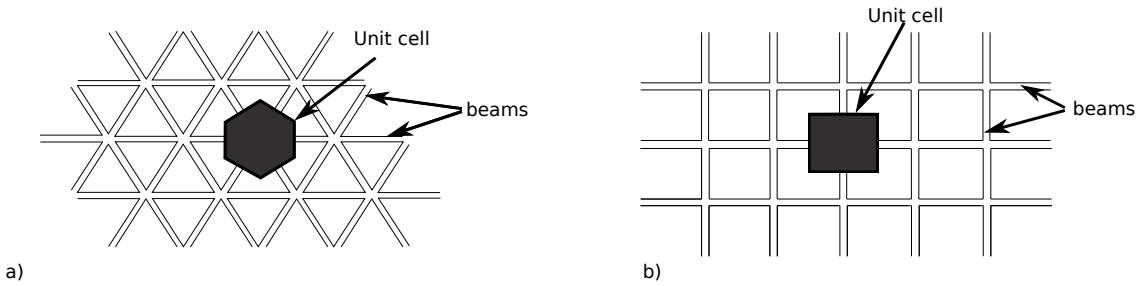

Figure 1.5: Lattice-beam models: (a) regular triangular lattice; (b) regular square lattice, taken from [23]

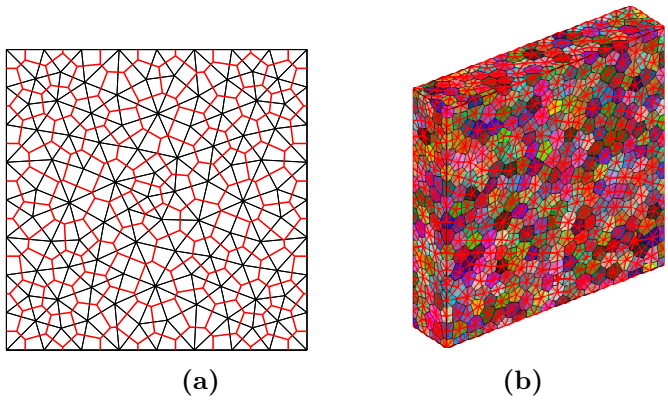

Figure 1.6: (a) 2D irregular lattice with Voronoi cells (b) 3D irregular lattice with Voronoi cells

it can also underestimate the global fracture limits. Many lattice element models use sequentially linear algorithms to avoid negative stiffness terms and deals with mesh-dependence by performing additional regularization procedures with scaling initial strength and ultimate strain on local element level to obtain correct fracture energy on a global level [25]. Some other models use incremental (sometimes also iterative) schemes in time, but the problem of fracture energy depending on mesh still remains, like in standard finite elements. One of the ways to provide mesh independent response is by using embedded strong discontinuity approach [26, 27], which is generalized to include the fracture process zone [28, 29].

There are basically two types of lattice models to analyze the meso structure of concrete. In the first type, single lattice elements are used to represent the interaction between aggregates [30]. In this model, midpoints of the concrete aggregates are used as the nodes for the finite element mesh. In the second type, heterogeneity of the concrete material is represented using a lattice element in which material properties are spatially varying [31, 32]. In some recent works authors proposed an element that has only two nodes and it is a two-phase or three-phase element [33, 31].

Advantages of lattice models compared with the finite element models. is that arrangement of the particle structure can be achieved without having to generate complicated shapes like polyhedrons and one-dimensional fracture criteria can be used instead of complex material models [34]. Another major advantage of the lattice

models is that heterogeneities can be represented by them conveniently. However, one drawback of the lattice element method compared with the continuum-based FE models is the difficulty in calculating the effective model parameters [35] because it is difficult to capture lattice parameters using conventional macro scale testing methods. This issue can be solved by using inverse procedure proposed in this work. In three-phase lattice models, ITZ has a thickness of one lattice element. However, this thickness values are overestimated because the thickness of ITZ in found to be 10-50 Îijm. To avoid this issue, either length of the ITZ elements should be reduced or the length of the all elements should be reduced. However, this will increase the number of elements and the computational time and memory as well [7].

1.2.1.4 Continuum models

Another family of meso-scale representations is the continuum-based models. During the last years a large number of continuum models have been developed either for meso-scale representation of concrete [2, 4, 11, 12, 36, 37] and mortar and cement paste with porosity taken into account [38]. The main advantages of these models is that composite materials are presented realistically (Figure 1.7), and they use a very simple constitutive law, consisting of the normal and shear cracking laws along the interface. However, one drawback of these models is that they are computational too expensive especially when they are used in large scale simulations.

Methods used to create the geometry, the cracking strategies, or meshing techniques used to generated particle arrangement are the main differences that exist between the above mentioned models. Many works are based on aligned meshing with no material discontinuities within the elements, while others use unaligned meshing with material interface within FE. Structured and non-structured mesh are used as well, although non-structured meshes yields a larger number of degrees of freedom increasing the computational cost.

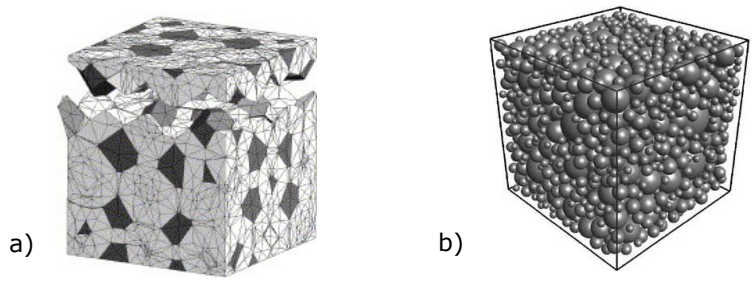

Figure 1.7: (a) 3D crack pattern in unaxial tension test for a structured mesh [39]; (b) 3D FE mesh of concrete with spherical aggregates [2]

1.2.1.5 Generation of geometry for meso-scale

One of the most important points in a mesoscale simulation becomes geometry generation since we want to capture the (desired) heterogeneous nature of the composite material, and at the same time to have FE mesh which is not too large for

latter computation. Generally, there are two methods to generate geometry of meso structure of the mesoscale models. First one is using the digital image based approach which uses image-processing techniques and the other method uses parameterization modelling approach for generating the meso structure [40].

Digital image based approach The mesoscale model is generated by processing the digital images of the concrete specimen. This approach can be used to create the concrete meso structure with a great extent of accuracy. There are two main approaches to generate the images of the concrete specimen. In the first method, concrete specimen is scraped and 2D images are taken using a scanner and these images are combined to get the full 3D geometry of the concrete specimen [20]. Second method uses scanning of an actual concrete cube using X-ray computed tomography (XCT) scanners and generate mesh using the digitally scanned elements [18]. This method is a nondestructive method of generating the mesoscale and this can identify the different components of a material. It can also be is used to visualize the materials because of the clear 3D visualizations and high resolution image generation [41]. In [34] is developed a mesoscale model using a medical CT scanner. By scanning the concrete specimen, a collection of 2D images were obtained and these 2D images were stacked on top of each other in a process called 'volume rendering' to obtain the 3D mesoscale model.

After generating the geometry of the meso-scale, it needs to be meshed before the analysis. A meshing preprocessor such as hypermesh [42], Gmsh [43], and TetGen [44] can be used to mesh the developed geometry. Analysis is carried out using a finite element software as same as in the meso-scale geometries developed using parameterization modelling. However, generating the meso structure is time consuming and costly. Also, there should be large number of samples for statistical analysis and this is not feasible with this method. Mesh generation of the scanned meso structure is complicated [40]. Another drawback is that when the volume rendering is done by stacking the obtained 2D images, resolution of the horizontal and vertical directions will be different because the spacing of the 2D images is larger compared with the image resolution. Thus, this method is much more suitable to simulate the performance of casted samples and can be used for validation of mesoscale modeling.

Parameterization modelling approach In the parameterization approach, the concrete meso structure is generated using algorithms. These algorithms to generate the meso structure can be direct or indirect. In the direct method, the aggregates, ITZ and mortar matrix are geometrically generated, and material properties are assigned, and finite element analysis is carried out. In the indirect method, consisting phases of the meso structure are not explicitly modelled. Equivalent material properties of the consisting phases are assigned to the representative elements such as lattice beams and trusses [40]. There are many direct algorithms to place the particles inside the area: *take and place method* [35, 2], *random particle drop method* [45] (Figure 1.8) , *divide and fill method* [37], *random extension method* [46], and the Voronoi/Delaunay tessellations [47, 48].

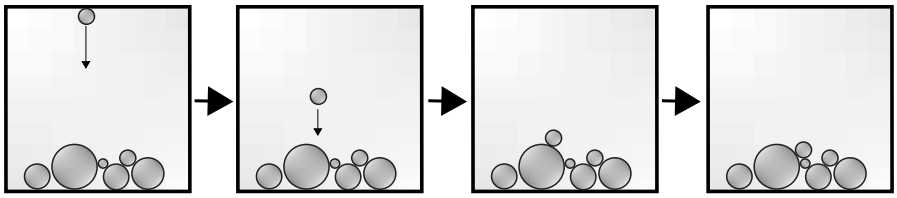

Figure 1.8: Random particle drop method

Different shapes such as spherical, ellipsoidal and polyhedral have been used to represent the aggregates. Spherical shape is the widely used aggregate shape due to the convenience in particle shape generation. Irregular shape of the particle is uniquely defined using a set of spherical harmonic coefficients. Using these irregular particle shapes, particles shapes similar to the actual aggregate shapes in concrete can be achieved. Shape of the aggregates plays a vital role in stress distribution in the concrete and the fracture. Also, this will affect the cracking behavior and damage of the concrete volume. Moreover, aggregate distribution is an important aspect in mesoscale modelling of concrete as this will affect the mechanical properties and behavior including the fracture. Most of the researchers have used Fuller curve [49] to obtain the Particle Size Distribution (PSD) curve for the mesoscale modelling of the concrete [2, 50, 36]. Fuller curve is widely accepted as the grading curve which gives the optimum compaction, density and strength in concrete and also a good workability and a good segregation resistance [2]. Two well-known grading curves, EMPA and Fuller, are defined with relations

$$\begin{aligned} p(d_{Fuller}) &= 100\sqrt{\frac{d}{d_{max}}} \\ p(d_{EMPA}) &= 50\left(\frac{d}{d_{max}} + \sqrt{\frac{d}{d_{max}}}\right) \end{aligned} \tag{1.1}$$

where $p(d_F)$ and $p(d_E)$ are the cumulative percent passing through a sieve with diameter d, with d_{max} as the diameter of the coarsest aggregate.

1.2.1.6 Material Constitutive Models

After meshing the developed geometry, finite element method can be used to analyze the mesoscale model with suitable material models and properties assigned to the consisting phases. To obtain an accurate response from the FE analysis, using suitable material parameters and material constitutive models for the consisting phases is vital.

Most of the researchers have used isotropic plasticity model combined with isotropic or anisotropic damage model in order to represent the mortar material behaviour [2, 46, 51, 52]. Also, a nonlinear isotropic damage model instead of a linear damage model is used [53]. Shear damage has also been considered in mesoscale models through Mohr-Coulomb criterion, Drucker-Prager material model or the Ottosen model [54]. Regarding the aggregate, most researchers have used a linear elastic material model in normal strength concrete under low rate of loadings which can be reasonable because the failure is going through the mortar and the ITZ while aggregate remain in elastic stage. However, for high strength concrete some

researchers stated that aggregate crushed and failure surface going through the aggregate rather going around the ITZ [55].

Material properties of the ITZ are generally assumed to be constant. In most of the instances, mechanical properties of ITZ is taken as a fraction of the properties of mortar matrix due to the lack of reliable material properties for ITZ. However, nano indentation and nano scratch methods can be used to determine the mechanical properties of ITZ [56]. Cohesive contacts and cohesive elements have been used to model the ITZ successfully [57]. Cohesive elements are founded on the basis of cohesive crack models. It is assumed that there is a Fracture Process Zone (FPZ) at the front of crack tip and tractions in normal and two shear direction exist. Traction separation graph is obtained using experiments and damage is incorporated by degrading the stiffness values in normal and shear directions when the separations increase assuming an irreversible progressive damage. However, the separation displacement is difficult to obtain from the experiments and hence, fracture energy is generally used as the fracture initiation criterion [24].

Material parameters which are needed for the simulation are generally taken using the past literature or conducting experiments. For the three phases in the mesoscale concrete , uniform constant material parameters such as elastic modulus, compressive strength are assigned in most of the meso-scale models. However, to capture the heterogeneity at the meso level, some researchers used Weibull probability distribution to vary the material properties of mortar paste while others used similar probability distribution to represent non-homogeneous properties in ITZ and aggregates.

1.2.2 Macro-scale modeling

To simulate the material failure at macroscopic level two frameworks are accepted: Fracture mechanics and Continuum mechanics. In Fracture mechanics after failure initiation the traction-separation relationship is invoked while in Continuum mechanics stress-strain relationship is assumed after strain localization which stands as a precursor for failure. Thus, in next section we present most important failure strategies.

1.2.2.1 Fracture principles: LEFM and NLFM

Fracture mechanics was first introduced by Inglis [58] on studies of the stress concetration in a large elastic plate with a eliptic hole. Later, these studies was used by Grifitth [59] to predict critical stress under which crack grows causing the material failure. Main assumptions for linear elastic fracture mechanics (LEFM) is that stress at the tip of the crack cannot be used as a failure criterion (stress becomes infinite in elastic continuum), and energy dissipation occurs only at the crack tip while the rest of the body remains linear elastic. This fracture energy can be define as amount of energy required to open a unit of crack area. For instance, when the work W_f neccesary to develop failure surface A_f is known then fracture energy can be expressed as $G_f = W_f/A_f$. When cracking happens in a zone which is small enough compared to the total structure, as in case of fracture in dams, then LEFM approach find to be usefull. In reality the size of developed nonlinear hardening zone

at the crack tip varies a lot. Thus, this zone is not negligible and it needs to be taken into account which is achived by NLFM where FPZ exist and material behaves inelastically. Another advantage of NLFM over LEFM is in its formulation which provides direct implementation into finite element analysis. Within the framework of NLFM the crack can be represented in two ways, either explicitly as a discontinuity in the continuum mesh as in a *discrete crack approach* [60, 61], or to propagate within the finite elements representing the continuum, *smeared crack approach* [62, 63].

1.2.2.2 Discrete crack approach

Discrete crack models are developed based on a Cohesive crack model, where stress can be transfered from one side to another (Figure 1.9), and they can be found in literature under different names: *cohesive zone models* developed for metals and composites [64], or *fictitious crack models* developed for concrete [61]. From Figure 1.9 we can note couples of two constitutive laws: first, in a non damaged zone given in terms of stress-strain relationship, and second as traction-separation (or stress-crack opening) relationship. In the latter, we can distinguish another two zone, true crack zone where is no more stress transfer and fracture process zone where stresses are still transferred.

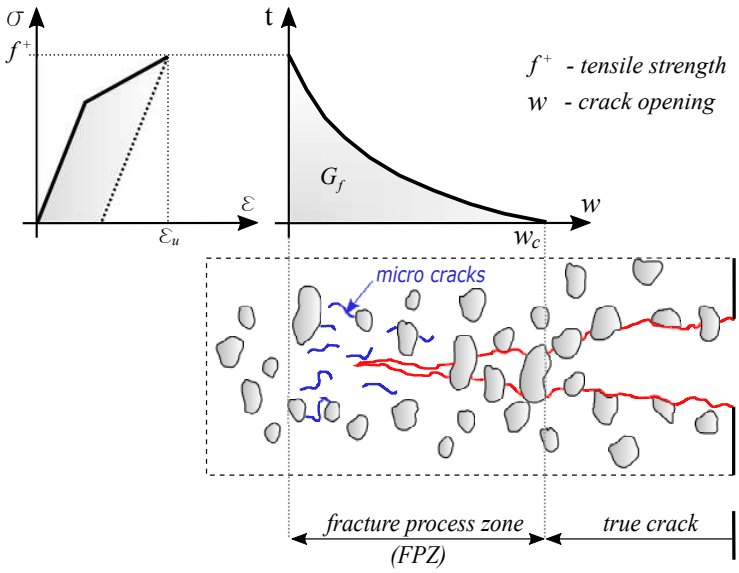

Figure 1.9: Fictitious crack model

Although at first glance these models are matching with the nature of physical crack [65], they still have some drawbacks. If we want to get the accurate results for the fixed FE mesh it is necessary to know the crack path apriori and elements should be oriented in the crack direction. This is implied by the fact that between adjacent elements special boundary conditions or interface elements are placed in order to simulate the crack propagation.

1.2.2.3 Smeared crack approach

In smeared crack approach both behaviors, fracture and continuum within same framework of continuum are considered. With this approach a infinitly many parralell cracks are imagined to be smeared (continuously distributed) over element [62]. This approach was also used in works carried out by [66, 67].

There are currently two types of models based on this approach: the fixed-crack model and rotating-crack model. In the first, the cracks forms perpendicular to the direction of principal tension stress and remain fixed throughout subsequent computation while in the second crack rotates with the direction of principal strains. In the latter a stress locking can be occurred. In order to overcome so-called localization instability in smeared crack models *Band Smeared crack models* are developed [63], also known as *Crack Band models* in case of tensile crack. This model is accepted from concept of Fictitious crack model and fracture energy is smeared over the width of the area of the crack domain, $G_f = g_f \cdot h^*$ (Figure 1.10).

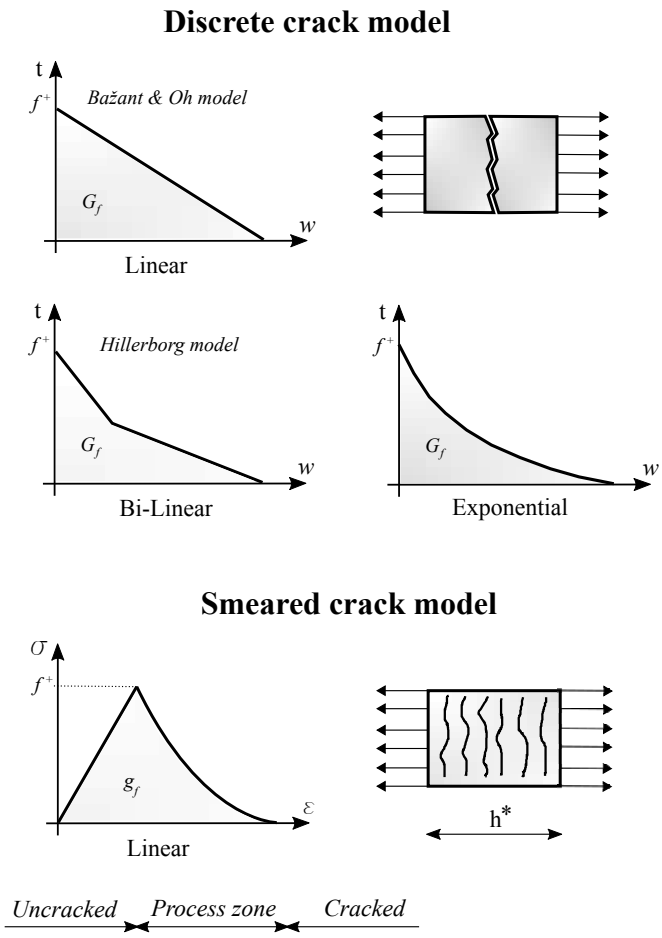

Figure 1.10: Comparison of Discrete crack model and Smeared crack model

The disadvantage of this approach is the inability to capture deformation jump, which results in the structure being able support more than it actually can. Furthermore, a very fine mesh is needed to capture a very high displacement gradient,

which can be computationally too expensive. Also, the orientation of cracks in such models depends on the mesh orientation, so-called mesh orientation bias.

1.2.2.4 Enhanced crack approach

When models with strain softening is used in framework of classical continuum, enhanced continua have been proposed in order to overcome boundary value ill-posed problem. This enhancement implied a minimal width of localized strain zone, and hence they are often called as *localization limiters*.

Cosserat continua In Cosserat continuum theory, developed by Cosserat brothers [68], additional independent rotation field are considered. Thus, in each point in continuum micromoments are added as the independent parameters in addition to the translation in classical continuum. Such enhanced kinematics implies a modification of stain measure, latter the choice is the Biot strain. With a such kind of enhacement characteristic length is required. Furthermore, models based on Cosserat continum theory (often called micro-polar continuum) can elimante FE mesh lack of objectivity but only when rotational degree of freedom is activated, with no use for separation failure.

Non-local methods In non-local methods enhancement no longer fits within the framework of classical continuum mechanics [69]. In this method stress value at a point depends on stress at this point but also on the average strains in the choosen neighborhood of that point, which is given by characteristic length. With a such approach inelastic dissipation remains independetnt of the choosen FE mesh, but its not easy to implement this method into standard FE procedure. Namely, the stress computation in any element will impose the communication with the elements in the neighborhood and in standard FE code we deal with only one element at the time.

Gradient enhanced models This model can be considered as an approximation of integral non-local damage models. They are typically characterized by explicit dependence of the yield function on Laplacian of the effective plastic strain. Displacement field and effective plastic strain are discretized by linear shape function.

1.2.2.5 Weak/strong discontinuity approach

Another family of methods, which will enhance the theoretical formulation is strong and weak discontinuity method. In discontinuity method a continuous displacement filed is considered [27] while in strong discontinuity method discontinuity in displacement field is considered [27, 26, 70, 71, 28, 24, 72] and this is the main difference between these two approach. In first method a strain filed is enhanced while in second displacement field is the one which is enhanced. The whole analysis can be perfomed in continuum mechanics framework. There are several advantages of this approach: the implementation in FE code is very easy, it is mesh independent approacg where re-meshing techniques are not neccesary and there is no need to introduce any material length scale (characteristic length).

1.3 Aims and scopes

The main scientific goal of this thesis is to provide approach for identification of failure models parameters in heterogenous materials by using Stochastic Galerkin finite element method. Analysis of any heterogenous materials is considered at three main level (micro-scale, meso-scale and macro-scale). Each of these levels pertains to concrete features which can not be captured on upper level. Thus, first goal of this thesis is to develop models for concrete-like materials at meso-scale and latter at macro-scale in order to describe all prominent feature for particular scale. For this purpose at meso-scale lattice model is taken to represent concrete failure, and at macro-scale non-associative Drucker-Prager with St. Veneant criterion is choosen for yield function and failure function, respectively.

Another goal of this thesis is to obtain material parameters, as deterministic value, for a macro-scale model with measurements taken with meso-scale model or from real experiment. Combining meso-scale model with macro-scale model and Bayesian inference can provide reduced macro-scale model, which can be stated as final goal of this thesis.

1.4 Organization of the thesis

This thesis is structured as follows. In Chapter 2 we present a formulation with several numerical simulation compered to experimental ones for novel concrete meso-scale model with full set of 3D failure modes with random distribution of aggregate and cement phase. Chapter 3 provides multi-surface plasticity model for concrete with 3D hardening/softening failure modes for tension, compression and shear, together with the numericaly obtained results that are compared to experimental ones. Considerations of inverese problem in deterministic setting is given in Chapter 4. The novel upscaling approach for reduced macro-scale model is presented in Chapter 5. In Chapter 6 conclusions and perspectives for future work are given.

2

Concrete meso-scale model with full set of 3D failure modes with random distribution of aggregate and cement phase: formulation and numerical implementation

Prediction of failure mechanisms in concrete is a fairly complex task due to heterogeneous concrete micro structure, localization process triggered by cracks, multiple crack interactions during their growth and coalescence, different dissipative mechanisms in fracture process zone prior to localized failure and in a localization zone during the failure. None of the currently used phenomenological models can represent the full set of 3D failure modes. This work presents an attempt to solve this with the 3D meso-scale model based on discrete lattice approach. In particular we show that we can capture such complexities at the meso-scale, which is able to represent microcracks in fracture process zone along with the localized failure represented in terms of embedded strong discontinuity and accompanied with softening constitutive law. The model can also successfully simulate salient features of concrete response, such as order of magnitude of reduction in strength in uniaxial tension versus compression, strength increase in biaxial loading or hydrostatic tension. Moreover, macro-scale representation of failure surfaces obtained with presented model for different loading programs confirms the need for failure concrete criterion of multi-surface kind. This chapter presents the proposed meso-scale based on extensive number of numerical simulations with multiple realizations of different concrete specimens, along as the optimal deterministic fit for several common concrete failure models. The ultimate interest of the this chapter is to provide detailed data set for different failure modes which can be used for identification of probability distribution of material parameters for different criterion. Such task is carried in Chapter 3. of this thesis.

Contents

2.1 Introduction 19
2.2 Meso-scale model for concrete failure 22
2.3 Macroscopic response: numerical homogenization 30
2.3.1 Construction of specimen 30
2.3.2 Tension test 31
2.3.2.1 Uniaxial tension test 31
2.3.2.2 Hydrostatic tension test 33
2.3.3 Compression test 34
2.3.4 Failure surfaces for biaxial loading 36
2.4 Final comments on the presented 3D concrete meso-scale model . . . 41

2.1 Introduction

The key assumption explored in this chapter pertains to the role of material heterogeneity in a study of the mechanical behavior and failure modes in concrete. When a concrete specimen under extreme loading condition enters in the stage where localized cracks and displacement discontinuities appear, the most appropriate model changes from continuous into discrete one. Crack propagation and final crack patterns in concrete are mostly based on accumulated microcracks of various kind of initial flaws, defects in aggregates structure,voids or pores inside concrete caused during fabrication. This processes of accumulation of microcracks leads to complete set of 3D failure mechanisms, usually governed by multiple crack interactions, growth and coalescence producing the brittle type failure characteristic for concrete. In order to provide a reliable predictive model for failure of such heterogeneous material, we build the model at meso-scale. The approach we focus upon in this chapter relies on spatial beam models, as a class of discrete lattice models [23]. For each random distribution realization of aggregate geometry is built using Delaunay triangulation. Such approach has an advantage of representing the multi-phase structure of concrete, namely cement paste and aggregates, and can provide the localized failure mechanisms with respect to heterogeneities. Here, the Delaunay edges in triangulation can be considered as lattice elements representing cohesive links between the Voronoi cells, each filled-in with a single phase of heterogeneous material (Figure 2.1a). Lattice elements are simulated with 3D Timoshenko beams which allows to represent the complete set of 3D failure modes. The Voronoi cells can guarantee the exact representation of linear elastic isotropic response, considering the concrete statistically as isotropic material. The geometrical properties of the beams can be extracted from common area between the two neighboring Voronoi cells (Figure 2.1b).

Another advantage of the chosen discrete model is ability to account all failure modes, I, II and III. The only remaining difficulty in failure analysis is to provide mesh-independent representation of the post-peak softening behavior [73]. The main idea in large number of lattice meso-scale models is that lattice elements progressively fail (leading to softening behaviour in failed elements) which eventually results in total macroscopic failure. However, there is still an ongoing problem of how to represent correctly the post peak softening behaviour, which is normally dependent on the mesh. This pertains to released fracture energy (i.e. area below the softening curve) which is not unique for different mesh size. Avoiding this fact can lead not only to wrong global fracture energy and wrong post peak response, but it can also underestimate the global fracture limits. Many lattice element models use sequentially linear algorithms to avoid negative stiffness terms and deals with mesh-dependence by performing additional regularization procedures with scaling initial strength and ultimate strain on local element level to obtain correct fracture energy on a global level [25]. Some other models use incremental (sometimes also iterative) schemes in time, but the problem of fracture energy depending on mesh still remains, like in standard finite elements. One of the ways to provide mesh independent response is by using embedded strong discontinuity approach [26, 27],

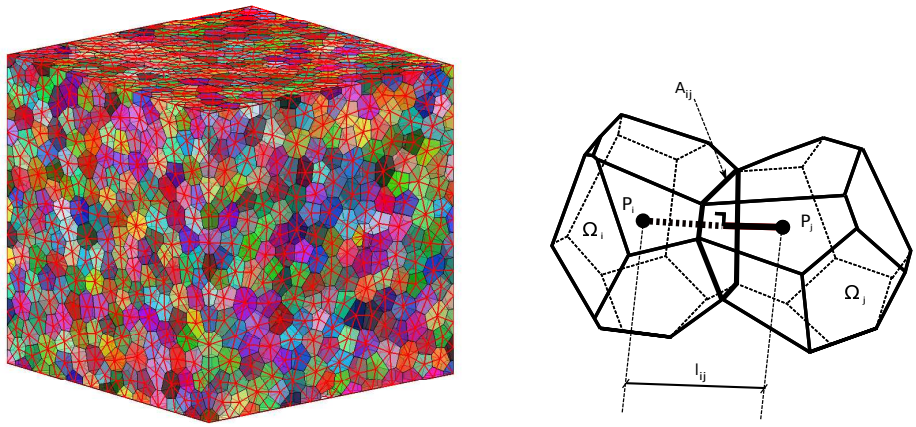

(a) **(b)**

Figure 2.1: (a) Structure of discrete lattice model with Voronoi cells as units of heterogeneous material and cohesive links between them (b) two neighbouring Voronoi cells

which is generalized to include the fracture process zone [28, 29]. The main reason for this mesh independence is that discontinuity, or displacement jump, always remains localized inside the element. This approach can be interpreted as a localization limiter that enhances the classical continuum mechanics theoretical formulation by admitting discontinuities in the displacement field. The numerical implementation of the discontinuity requires a modification of the standard finite element procedure, which is similar to the method of incompatible modes [74].

Embedded discontinuity formulation is developed here to enhance the 3D Timoshenko beam lattice elements to provide all three failure modes characteristic for concrete. The model is adopted from our previous works dealing with failure of rocks [76, 75, 72].

The adaptation concerns the microstructure representation being aggregate in agreement with the granulometric curve. In other words, we recognize that the concrete is highly heterogeneous composite material. One can distinguish between the two phases of the material at the observational meso-scale. The meso-scale can capture fundamental aspects of material heterogeneity without being computationally too expensive [15]. Various models of concrete failure can be found in literature [15, 5, 7, 6, 8–10, 77–79], none of them comparable to the present model that provides all failure modes I, II and III in terms of embedded discontinuities in Timoshenko lattice beam elements. By using only mode I at meso-scale we can successfully represent simple tension test, or even be able to deal with 3 point bending test when bending failure (not shear) remains dominant failure mode. However, the failure modes of concrete composites are more complex, in anything else from simple tension. The model for concrete failure restricted to truss bars and embedded discontinuities providing only mode I failure could get only 1:5 overall ratio between uniaxial tension and compression [31, 32]. The model concerning mode I at the meso-scale proposed by [80] is positioning the cohesive links in the direction of stress principal axes, which

automatically eliminates the contribution of shear. Lattice elements in this case are perfectly brittle upon reaching failure criterion, when they are physically removed from mesh. The algorithm for solution of equations fitting into this framework is based on sequentially linear analysis, which does not have the same stringent equilibrium enforcing properties, as the method proposed in this thesis, where lattice elements are not removed from mesh after reaching failure criterion, but they go into softening regime in agreement with defined fracture energy for modes I, II and III. Shear failure mechanisms contribute here mostly through presence of aggregate in concrete composite, which makes the crack deviate from shortest (orthogonal) path and introduces the contribution of modes II and III. Here, the failure criteria include modes II and III, together with Mohr-Coulomb law on local element level for shear failure under compression. Macroscopic mechanical response depends strongly on each phase properties, both for cement paste and aggregates, as well as on their spatial distribution. Spatial distribution of each phase is spread here with random process with Poisson distribution of the aggregates (phase I) subsequently filling the voids between them with cement paste (phase II). The distribution of aggregate size is taken in agreement with one of two well-known aggregates grading curves in concrete mixture [81]. The choice is made that all particles with size less than 2.0 mm be included in cement matrix volume, thus forming cement mortar. By using this way of distribution we are able to obtain realistic values of phase volume fraction. The Gaussian distribution of the material properties heterogeneity in each phase (aggregate and cement paste) is taken into account with standard deviation restricted to $\pm\ 2\sigma$. Such distribution of material properties takes into account the weakening of concrete through Interface Transition Zone (ITZ), whose properties are considered heterogeneous and represent weak spots in concrete decided by random process through the distribution of material properties for cement paste, from where the cracks are then triggered.

Various types of phenomenological constitutive models are widely used in structural scale computations for prediction of behavior in static or dynamic cases [82, 83]. In adopting to the case of a complex loading program, these models require choice of the elaborate and equally complex criterion. Because of their macroscopic point of view, these models encounter insurmountable difficulties in describing correctly the fine scale physical mechanisms, such as fracture or damage. The proposed meso-scale model can improve this and provide different failure mechanisms leading to macro-scale representation typically given in terms of multi-surface failure criterion for concrete. In order to identify the most appropriate failure criterion, we carry out large number of numerical tests at fine scale with different loading programs. In particular, we consider uniaxial tension and compression, biaxial tests with strength increase and hydrostatic tension. We thus obtain different values for compression and tension strength as a function of aggregate volume fraction.

The outline of the chapter is as follows: In Section 2 we describe the meso-scale model, with the cohesive links in terms of Timoshenko beam elements. In Section 3, we present the results of numerical simulations with the ultimate goal of computing corresponding macro-scale failure surface obtained with meso-scale model

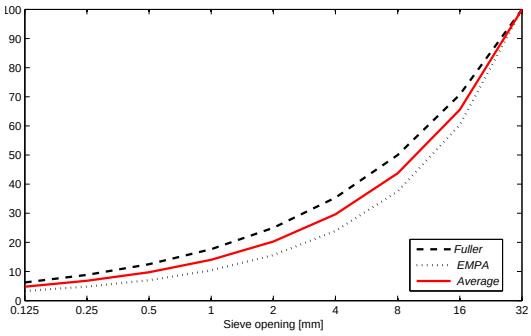

Figure 2.2: Grading curves

computations. Section 4 summarizes the conclusion regarding all the main findings and suggests the perspective studies.

2.2 Meso-scale model for concrete failure

In this section we give a description of the meso-scale model of concrete constitutive behavior as a two phase material. First, the 3D Delaunay triangulation [43] is performed in certain volume, representing the specimen. Second, the Voronoi diagram is extracted from Delaunay triangulation resulting with Voronoi cells that occupy smaller part of the volume. The size of the Voronoi cells should correspond to the representative size of heterogeneities, and thus form the grains in the material (Figures 2.1). Voronoi cells should be initially kept together, like grains, with cohesive forces which are represented by the beam lattice network extracted from Delaunay triangulation edges [84].

Phase I, chosen as the aggregate, is spatially spread across specimen by using the Poisson distribution seeking to achieve the corresponding grading curves for aggregate [81]. Two well-known grading curves, EMPA and Fuller (Figure 2.2), are defined with relations

$$\begin{aligned} p(d_{Fuller}) &= 100\sqrt{\frac{d}{d_{max}}} \\ p(d_{EMPA}) &= 50\left(\frac{d}{d_{max}} + \sqrt{\frac{d}{d_{max}}}\right) \end{aligned} \tag{2.1}$$

where $p(d_F)$ and $p(d_E)$ are the cumulative percent passing through a sieve with diameter d, white d_{max} as the diameter of the coarsest aggregate. We consider here the distribution of aggregate as an arithmetic mean of these two grading curves where all particles smaller than 2.00 mm are included in cement matrix volume forming cement mortar. The second, separate study of this phase is not necessary since formation of cement or mortar layer can be determined based on distribution of the aggregates. According to defined grading curve we use in further study, the aggregate with maximal diameter of 8 mm, 16 mm and 32 mm obtaining, respectively 30%, 50% and 60% volume fraction for phase I.

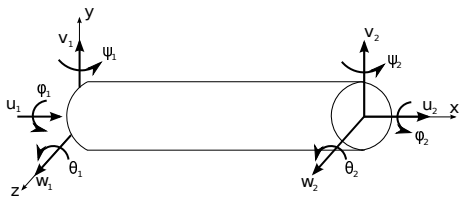

Figure 2.3: 3D Timoshenko beam displacements

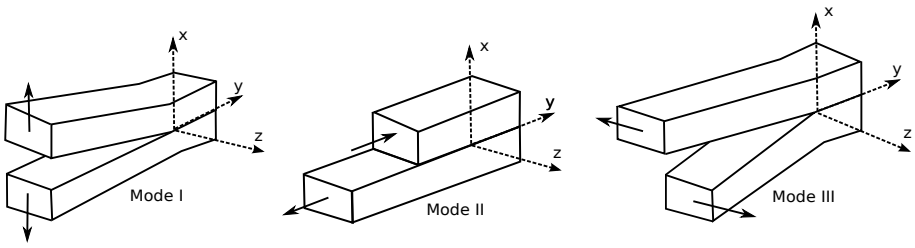

Figure 2.4: Three failure modes in concrete

Each phase material properties are assigned to corresponding beam elements which fall inside the particular phase. The geometric properties of beams are extracted from Voronoi diagram. Namely, the common area of the two neighboring Voronoi cells (Figure 2.1b) is approximated by circular cross section and used to compute the single beam diameter, from which the beam cross-section parameters are obtained [72]. This leads to the lattice of thick beams which can be represented by Timoshenko beam elements accounting for shear deformation. One can write the standard kinematics for 3D Timoshenko beam element with length l_e

$$\begin{aligned}
\epsilon(x) &= \frac{du(x)}{dx} \\
\gamma_y(x) &= \frac{dv(x)}{dx} - \theta(x) \\
\gamma_z(x) &= \frac{dw(x)}{dx} + \psi(x) \\
\kappa_x(x) &= \frac{d\varphi(x)}{dx} \\
\kappa_y(x) &= \frac{d\psi(x)}{dx} \\
\kappa_z(x) &= \frac{d\theta(x)}{dx}
\end{aligned} \tag{2.2}$$

By using the matrix notation, the Timoshenko beam strains are placed in a vector that can be written as $\boldsymbol{\epsilon} = \begin{bmatrix} \epsilon & \gamma_y & \gamma_z & \kappa_x & \kappa_y & \kappa_z \end{bmatrix}^T$. Vector $\mathbf{u} = \begin{bmatrix} u & v & w & \varphi & \psi & \theta \end{bmatrix}^T$ represents the beam axis displacements and cross-section notations as shown in Figure 2.3.

In order to represent the three failure modes in concrete, we consider discontinuities in the generalized displacement field of the 3D Timoshenko beam. Such enhancements of 3D Timoshenko beam can provide mode I as axial failure mode and modes II and III as shear failure modes between the Voronoi cells (Figure 2.4). To that end, the standard beam displacements are enhanced with Heaviside function

and decomposed into regular and singular parts in the following way

$$\mathbf{u}(x) = \overline{\mathbf{u}}(x) + \boldsymbol{\alpha} H_{x_c} = \begin{bmatrix} \overline{u}(x) \\ \overline{v}(x) \\ \overline{w}(x) \\ \overline{\varphi}(x) \\ \overline{\psi}(x) \\ \overline{\theta}(x) \end{bmatrix} + \begin{bmatrix} \alpha_u \\ \alpha_v \\ \alpha_w \\ 0 \\ 0 \\ 0 \end{bmatrix} H_{x_c} \tag{2.3}$$

Here, H_{x_c} is the Heaviside function defined by $H_{x_c}(x) = 0$ for $x \leq x_c$ and $H_{x_c}(x) = 1$ for $x > x_c$ and $\boldsymbol{\alpha} = [\alpha_u \;\; \alpha_v \;\; \alpha_w \;\; 0 \;\; 0 \;\; 0]^T$ represents the vector of displacement jumps at the point of discontinuity, which is positioned exactly in the middle of the beam. This is also the point where two neighboring Voronoi cells share the same side.

One can rewrite the equation 2.3 by adding and subtracting a regular differentiable function ϕ from Heaviside function, which will produce the following form of displacement field

$$\mathbf{u}(x) = \underbrace{\overline{\mathbf{u}}(x) + \boldsymbol{\alpha}\phi(x)}_{\text{regular part}} + \underbrace{\boldsymbol{\alpha}(H_{x_c} - \phi(x))}_{\text{localized part}} \tag{2.4}$$

In the context of finite elements, the regular part of displacement field is interpolated with standard shape functions. On the other side, localized part requires additional treatment which can be handled within the framework of incompatible modes [74], with element modification for localized discontinuity. The enhanced strain field is obtained through the Dirac delta δ_{x_c} resulting from the derivative of the Heaviside function multiplying a discontinuous displacement field from above

$$\boldsymbol{\epsilon}(x) = \tilde{\boldsymbol{\epsilon}}(x) + G\boldsymbol{\alpha} + \boldsymbol{\alpha}\delta_{x_c} \tag{2.5}$$

where $\tilde{\boldsymbol{\epsilon}}$ represents the regular part of the strain field obtained from the regular part of displacement field in equation 2.4. Operator G is defined as $L(-\phi(x))$, where L is the strain-displacement operator.

The finite element interpolation of the total displacement field from equation 2.3 can be written as

$$\mathbf{u}(x) = N_1(x)\overline{\mathbf{u}}_1 + N_2(x)\overline{\mathbf{u}}_2 + \boldsymbol{\alpha} H_{x_c} \tag{2.6}$$

where interpolation of the regular part of Timoshenko beam displacements can be performed with linear polynomials as shape functions, namely $N_1(x) = 1 - \frac{x}{l_e}$, $N_2(x) = \frac{x}{l_e}$. Vectors $\overline{\mathbf{u}}_1$ and $\overline{\mathbf{u}}_2$ are the nodal vectors of regular displacement part from (2.3) related to element nodes 1 and 2, respectively. Total displacements for nodes 1 and 2 can be written in terms of displacements of the regular part as

$$\begin{aligned} \mathbf{u}(x_1) &= \mathbf{u}_1 = \overline{\mathbf{u}}_1 \\ \mathbf{u}(x_2) &= \mathbf{u}_2 = \overline{\mathbf{u}}_2 + \boldsymbol{\alpha} \end{aligned} \tag{2.7}$$

and expression (2.6) can be rewritten with $\overline{\mathbf{u}}_2 = \mathbf{u}_2 - \boldsymbol{\alpha}$ in terms of total displacements as

$$\mathbf{u}(x) = N_1(x)\mathbf{u}_1 + N_2(x)\mathbf{u}_2 + \boldsymbol{\alpha}\underbrace{(H_{x_c} - N_2(x))}_{M(x)} \tag{2.8}$$

One can note that function $\phi(x)$ from (2.4) can be taken as $\phi(x) = N_2(x)$ for the chosen linear interpolation. Second part in (2.8), related to incompatible mode, can be denoted as interpolation function $M(x)$ for the discontinuity

$$M(x) = \begin{cases} -\frac{x}{l_e}; x \in [0, x_c\rangle \\ 1 - \frac{x}{l_e}; x \in \langle x_c, l_e] \end{cases} \tag{2.9}$$

The interpolation of total displacement field from (2.8) can thus be re-written in matrix form as

$$\mathbf{u} = \mathbf{N}\mathbf{u}_a + \mathbf{M}\boldsymbol{\alpha} \tag{2.10}$$

with $\mathbf{N}$ being $6x12$ element shape function matrix containing functions $N_1(x)$ and $N_2(x)$, $\mathbf{u}_a = \begin{bmatrix}\mathbf{u}_1 & \mathbf{u}_2\end{bmatrix}^T$ and $\mathbf{M}$ is $6x6$ matrix of discontinuity interpolation functions M positioned at the diagonal first three entries related to translational degrees of freedom.

In order to obtain interpolated enhanced strain field, one needs to consider derivatives of shape functions $B_1(x) = -\frac{1}{l_e}$, $B_2(x) = \frac{1}{l_e}$ and the derivative of discontinuity interpolation function, leading to

$$G(x) = \overline{G}(x) + \delta_{x_c}, \;\; \overline{G}(x) = -\frac{1}{l_e} \tag{2.11}$$

The function G is split into regular part $\overline{G}$ and singular part in terms of δ_{x_c}. With preferred choice of ϕ, the expression above reduces to $\overline{G}(x) = -B_2(x)$. The interpolated enhanced strain field can finally be obtained with

$$\boldsymbol{\epsilon} = \mathbf{B}\mathbf{u}_a + \overline{\mathbf{G}}\boldsymbol{\alpha} + \boldsymbol{\alpha}\delta_{x_c} \tag{2.12}$$

where $\mathbf{B}$ is $6x12$ beam strain-displacement matrix corresponding to equation (2.2) and $\overline{\mathbf{G}}$ is the $6x6$ matrix of derivatives of discontinuity interpolation function $\overline{G}$ at the entries related to translational degrees of freedom.

The same kind of interpolations for virtual strain field is used to construct the weak form of equilibrium equations

$$\delta\boldsymbol{\epsilon} = \mathbf{B}\delta\mathbf{u}_a + \overline{\mathbf{G}}_v\delta\boldsymbol{\alpha} + \delta\boldsymbol{\alpha}\delta_{x_c} \tag{2.13}$$

where $\delta\mathbf{u}_a$ and $\delta\boldsymbol{\alpha}$ denote the total virtual displacement field and virtual displacement jump, respectively. Enforcement of orthogonality between the enhanced strain and constant stress is needed within the element by fulfilling the patch test condition [74]

$$\mathbf{G}_v = \mathbf{G} - \frac{1}{l_e}\int_0^{l_e} \mathbf{G}dx \tag{2.14}$$

For this element, where reduced one Gauss point integration is used, it hold that $\mathbf{G}_v = \mathbf{G}$.

The virtual work equation can be written at element level

$$G^{int,(e)} - G^{ext,(e)} = 0 \tag{2.15}$$

where $G^{int,(e)} = \int_0^{l_e} (\delta\boldsymbol{\epsilon})^T \boldsymbol{\sigma} dx$. By replacing the virtual strain field from (2.13) into virtual work equation, we end up with a set of two equations

$$\begin{aligned} &\int_0^{l_e} (\delta\mathbf{u}_a)\mathbf{B}^T\boldsymbol{\sigma} dx = G^{ext} \\ &\int_0^{l_e} (\delta\boldsymbol{\alpha})(\overline{\mathbf{G}} + \boldsymbol{\delta}_{x_c})^T\boldsymbol{\sigma} dx = 0 \end{aligned} \tag{2.16}$$

The standard internal force vector $\mathbf{f}^{int,(e)}$ is obtained from the standard part of internal virtual work, while the enhanced part produces the element residual $\mathbf{h}^{(e)}$ at discontinuity. By using the standard finite element assembly procedure, we get

$$\begin{aligned} &A_{e=1}^{n_{el}} \left(\mathbf{f}^{int,(e)} - \mathbf{f}^{ext}\right) = 0 \\ &\mathbf{h}^{(e)} = \int_0^{l_e} \overline{\mathbf{G}}^T \boldsymbol{\sigma} dx + \mathbf{t}, \ \ \forall e \in [1, n_{el}] \end{aligned} \tag{2.17}$$

where $f^{int,(e)} = \int_0^{l_e} \mathbf{B}^T\boldsymbol{\sigma} dx$. The condition $\mathbf{h}^{(e)} = 0$ needs to be enforced for each element where discontinuity is activated, which leads to definition of the traction vector at discontinuity

$$\mathbf{t} = -\int_0^{l_e} \overline{\mathbf{G}}\boldsymbol{\sigma} dx \tag{2.18}$$

Note that assembly operator in the first equation in (2.17) considers all elements, while the second equation remains limited to a particular element due to character of interpolation function for discontinuity which takes zero values at the element boundary.

In order to solve the nonlinear problem in (2.17), the consistent linearization of both equations has to be performed. The standard Newton incremental-iterative procedure is used to provide new iterative values of nodal displacements

$$\begin{aligned} &A_{e=1}^{n_{el}} \left[\mathbf{K}_{n+1}^{e,(i)} \Delta\mathbf{u}_{n+1}^{(i)} + \mathbf{F}_{n+1}^{e,(i)} \Delta\boldsymbol{\alpha}_{n+1}^{(i)}\right] = A_{e=1}^{n_{el}} \left[\mathbf{f}_{n+1}^{ext,e} - \mathbf{f}_{n+1}^{int,e,(i)}\right] \\ &\mathbf{h}_{n+1}^{e,(i)} + \left(\mathbf{F}_{v,n+1}^{e,(i)} + \mathbf{K}_{d,n+1}^{(i)}\right) \Delta\mathbf{u}_{n+1}^{(i)} + \left(\mathbf{H}_{n+1}^{e,(i)} + \mathbf{K}_{\alpha,n+1}^{(i)}\right) \Delta\boldsymbol{\alpha}_{n+1}^{(i)} = 0 \end{aligned} \tag{2.19}$$

where the explicit form of matrices are

$$\begin{aligned} &\mathbf{K}_{n+1}^{e,(i)} = \int_0^{l_e} \mathbf{B}^T \mathbf{C}_{n+1}^{(i)} \mathbf{B} dx, \ \ \mathbf{F}_{n+1}^{e,(i)} = \int_0^{l_e} \mathbf{B}^T \mathbf{C}_{n+1}^{(i)} \overline{\mathbf{G}} dx \\ &\mathbf{F}_{v,n+1}^{e,(i)} = \int_0^{l_e} \overline{\mathbf{G}}^T \mathbf{C}_{n+1}^{(i)} \mathbf{B} dx, \ \ \mathbf{H}_{n+1}^{e,(i)} = \int_0^{l_e} \overline{\mathbf{G}}^T \mathbf{C}_{n+1}^{(i)} \overline{\mathbf{G}} dx \end{aligned} \tag{2.20}$$

and $\mathbf{C}_{n+1}^{(i)} = diag(EA, GA, GA, GI_p, EI_{11}, EI_{22})$ is the tangent stiffness for 3D Timoshenko beam.

Similary, $\mathbf{K}^{(i)}_{d,n+1}$ and $\mathbf{K}^{(i)}_{\alpha,n+1}$ are the consistent tangent stiffness for discontinuity

$$\Delta\mathbf{t}^{(i)}_{n+1} = \mathbf{K}^{(i)}_{d,n+1}\Delta\mathbf{u}^{(i)}_{n+1} + \mathbf{K}^{(i)}_{\alpha,n+1}\Delta\boldsymbol{\alpha}^{(i)}_{n+1} \tag{2.21}$$

By enforcing the local equation in (2.17), to be equal to zero, allows to use the static condensation (e.g. [73]) of the system providing elimination of the incompatible mode parameters $\boldsymbol{\alpha}$ from global equations. This leads to the reduced size of stiffness matrix, which is calculated as follows:

$$\widehat{\mathbf{K}}^{e,(i)}_{n+1} = \mathbf{K}^{e,(i)}_{n+1} - \mathbf{F}^{e,(i),T}_{n+1}(\mathbf{H}^{e,(i)}_{n+1} + K^{(i)}_{\alpha,n+1})^{-1}(\mathbf{F}^{e,(i)}_{v,n+1} + K^{(i)}_{d,n+1}) \tag{2.22}$$

Such a reduced stiffness matrix can be sent to the standard finite element assembly procedure to provide global set of linearized equilibrium equations. Computed incremental displacements $\Delta\mathbf{u}^{(i)}_{n+1}$ are used to perform corresponding displacement vector update

$$\begin{aligned} &A^{n_{el}}_{e=1}\widehat{\mathbf{K}}^{e}_{n+1}\Delta\mathbf{u}^{(i)}_{n+1} = A^{n_{el}}_{e=1}\left[\mathbf{f}^{ext,e}_{n+1} - \mathbf{f}^{int,e,(i)}_{n+1}\right] \\ &\implies \mathbf{u}^{(i+1)}_{n+1} = \mathbf{u}^{(i)}_{n+1} + \Delta\mathbf{u}^{(i)}_{n+1} \end{aligned} \tag{2.23}$$

Solution of equation (2.23) requires the computation of internal force vector, $\boldsymbol{\sigma} = \begin{bmatrix} N & V & W & M_x & M_y & M_z \end{bmatrix}^T$, with the particular values of stress resultants vector. Rotations of 3D Timoshenko beams as lattice elements are kept linear elastic like in [72], while axial and two shear stress resultants undergo softening plasticity regime upon reaching failure threshold which corresponds to failure in modes I, II or III. Although the plasticity model is used in present study, one can note that damage model could be used as well. However, as long as we do not go to true cyclic loading applications, either of them can be successfully applied to obtain the limit load in quasi-static applications. Softening plasticity constitutive law is enforced by producing plastic deformation in the localized part of the element at the position of discontinuity. This is guided by singular part of deformation field presented with the Dirac delta function. The computation of vector $\boldsymbol{\sigma}$ can be split into scalar equations, where each translational component with potential discontinuity appears separately. In order to simplify the following presentation, we will give the evolution of softening plasticity with a scalar variable, knowing that each step is the same for all three directional components corresponding to three failure modes. Namely, the evolution equations for discontinuity can be written similarly to standard plasticity with the main difference that in softening the plastic deformation remains localized at the position of Dirac function

$$\begin{aligned} \dot{\alpha} &= \dot{\lambda}\frac{\partial\Phi}{\partial\sigma} = \dot{\lambda}sign(\sigma) \\ \dot{\xi} &= \dot{\lambda}\frac{\partial\Phi}{\partial q} = \dot{\lambda} \end{aligned} \tag{2.24}$$

where λ is the plastic multiplier associated with the softening behavior and α (also corresponding to incompatible mode parameter) is equivalent to the accumulated

plastic strain at the discontinuity. The failure function involves the stress value at the point of discontinuity δ_{x_c} where the plastic strain localizes

$$\Phi(t,q) = t - (\sigma_u - q) \leq 0 \tag{2.25}$$

Here, t is a traction computed from (2.18) acting at the discontinuity, σ_u is a failure threshold and q is the internal plasticity variable for evolution of softening. When the softening constitutive law is chosen to be exponential, internal variable for plasticity can be written as

$$q = \sigma_u \left(1 - exp\left(-\xi \frac{\sigma_u}{G_f}\right)\right) \tag{2.26}$$

with G_f as the corresponding value of fracture energy.

In order to compute the internal variables related to discontinuity and perform the corresponding stress updates, element-wise algorithm should be performed for each directional component. Such algorithm is similar to return mapping algorithm of standard plasticity, except for the trial state computation. Computing the internal variables locally, the global solution procedure with Newton incremental/iterative procedure can be performed to give the best iterative value of displacements $u_{n+1}^{(i)}$, for which we can obtain the trial value of the traction force

$$t_{n+1}^{trial} = -\int_0^{l_e} \overline{G} \left[EA \left(\sum_{a=1}^{2} B_a u_{a,n+1}^{(i)} + \overline{G}\alpha_n \right) \right] dx \tag{2.27}$$

where α_n represents the accumulated plastic deformation at previous time step for softening plasticity. Note that we computed the trial value of traction force with regular part of strain field from (2.12) and that singular part (Dirac function) vanished. This holds because when keeping the stress rate bounded, one needs to ensure that the plastic multiplier λ be proportional to Dirac function. This results with localized plastic deformation at the discontinuity and the softening law reinterpreted in distributional sense [73, 26]. Computation of trial values for shear forces in the beam requires the independent internal variables α for shear directions, shear stiffness GA and strains for shear $\sum_{a=1}^{2} B_a v_{a,n+1}^{(i)} - N_a \theta_{a,n+1}^{(i)}$ and $\sum_{a=1}^{2} B_a w_{a,n+1}^{(i)} + N_a \psi_{a,n+1}^{(i)}$. The trial value of failure functions is calculated as

$$\Phi_{n+1}^{trial} = \left| t_{n+1}^{trial} \right| - (\sigma_u - q_n) \tag{2.28}$$

with q_n defined in (2.26). If the trial values of the failure functions are negative or zero, the elastic trial step is accepted for final, with no need to modify the plastic strain from the previous time step

$$\alpha_{n+1} = \alpha_n; \;\; \xi_{n+1} = \xi_n \tag{2.29}$$

The plastic softening parameters remain intact, while the traction force is changed due to displacement increment. This step represents the unloading of the discontinuity which is crucial for the case when many cracks star to appear but some of them become

dominant and continue to grow, while the others unload from the discontinuity. The consistent tangent stiffness for discontinuity is $\mathbf{K}^{(i)}_{d,n+1} = -\mathbf{F}^{e,(i)}_{v,n+1}$ and $\mathbf{K}^{(i)}_{\alpha,n+1} = 0$ in this case.

On the other hand, if the trial values of failure functions are positive, the current step is in the softening plasticity and internal variables should be modified to re-establish the plastic admissibility at discontinuity. The internal softening plasticity variables are updated by using evolution equations

$$\alpha_{n+1} = \alpha_n + \lambda_{n+1} sign\left(t^{trial}_{n+1}\right) \tag{2.30}$$

and

$$\xi_{n+1} = \xi_n + \lambda_{n+1} \tag{2.31}$$

where λ_{n+1} is softening plastic multiplier. The value of the plastic multiplier is determined from the condition $\Phi_{n+1} \leq tol$

$$\Phi_{n+1} = \Phi^{trial}_{n+1} + (q_{n+1} - q_n) + EA\overline{G}\lambda_{n+1} \leq tol \tag{2.32}$$

The solution of local nonlinear equation providing the value of plastic multiplier can be obtained iteratively by using the Newton method. Finally, one can update the stress values by updated internal variables. Traction forces are produced by a change of discontinuity parameters with discontinuity tangent stiffness $\mathbf{K}^{(i)}_{\alpha,n+1} = \overline{\overline{K}}^{(i)}_{\alpha,n+1}$ and $\mathbf{K}^{(i)}_{d,n+1} = 0$. Here, $\overline{\overline{K}}^{(i)}_{\alpha,n+1}$ is obtained as the derivative of exponential softening law (26) with respect to internal variable ξ.

In order to represent the failure behavior of concrete-like materials, it is necessary to study crack growth under mixed modes I, II and III in the presence of heterogeneities. Heterogeneous concrete samples are prepared with random process with Gaussian distribution to define limit stress for each phase with restriction to $\pm\, 2\sigma$, setting mean value and standard deviation for each limit stress. The heterogeneities also play a crucial role in making the computational iterative procedure more robust by eliminating the academic case of localized failure of homogeneous material under homogeneous stress field. The computational model of this kind thus leads to more robust iterative procedure.

The three trial failure surfaces regarding three directions of local frame are defined in order to detect softening behavior in the tension case

$$\begin{aligned} \Phi^{trial}_{u,n+1} &= t^{trial}_{u,n+1} - (\sigma_{u,t} - q_{u,n}) \\ \Phi^{trial}_{v,n+1} &= \left|t^{trial}_{v,n+1}\right| - (\tau_{u,v} - q_{v,n}) \\ \Phi^{trial}_{w,n+1} &= \left|t^{trial}_{w,n+1}\right| - (\tau_{u,w} - q_{w,n}) \end{aligned} \tag{2.33}$$

where $\sigma_{u,t}$, $\tau_{u,v}$ and $\tau_{u,w}$ are limit stress values randomly assigned for each element using Gaussian distribution with mean value and standard deviation. Moreover, when the softening is detected with only one of these failure surfaces, the limit stress values of other two failure surfaces are reduced to current stress computational values leading to simultaneous softening in all three failure modes.

Cement matrix			**Aggregate**
E=15 GPa			E=70 GPa
ν=0.25			ν=0.25
fracture limits:			
	mean value	st. dev	-
$\sigma_{u,t}$	4 MPa	0.15	-
$\sigma_{u,c}$	40 MPa	0.5	-
$\tau_{u,v}$	1 MPa	0.1	-
$\tau_{u,w}$	1 MPa	0.1	-
fracture energies:			
G_{fu}	6 N/m		-
G_{fv}	100 N/m		-
G_{fw}	100 N/m		-
Φ=20°			-

Table 2.1: Material parameters for meso-scale model

Failure in compression case is detected by

$$\begin{aligned} \Phi^{trial}_{u,n+1} &= \left|t^{trial}_{u,n+1}\right| - (\sigma_{u,c} - q_{u,n}) \\ \Phi^{trial}_{v,n+1} &= \left|t^{trial}_{v,n+1}\right| - \left(\tau_{f,v} - q_{v,n}\right) \\ \Phi^{trial}_{w,n+1} &= \left|t^{trial}_{w,n+1}\right| - \left(\tau_{f,w} - q_{w,n}\right) \end{aligned} \tag{2.34}$$

where failure in each mode is handled independently of other two failure surfaces. Moreover, the compression force influences the failure threshold for shear sliding with the Mohr-Coulomb friction law

$$\tau_{f,v} = \tau_{u,v} + \sigma tan(\Phi); \;\; \tau_{f,w} = \tau_{u,w} + \sigma tan(\Phi) \tag{2.35}$$

and it magnifies the shear strength by internal angle of friction Φ.

2.3 Macroscopic response: numerical homogenization

In this section we present the numerical simulations and computed macroscopic responses for a number of different concrete specimens and various loading conditions. The computations are performed by a research version of computer program FEAP, developed by R.L. Taylor at UC Berkeley [85].

2.3.1 Construction of specimen

As already elaborated in previous section, the presented approach relies on meso-scale model with cohesive links in terms of spatial beams. Such beams are generated by computing the 3D Delaunay triangulation which is performed by using Gmsh

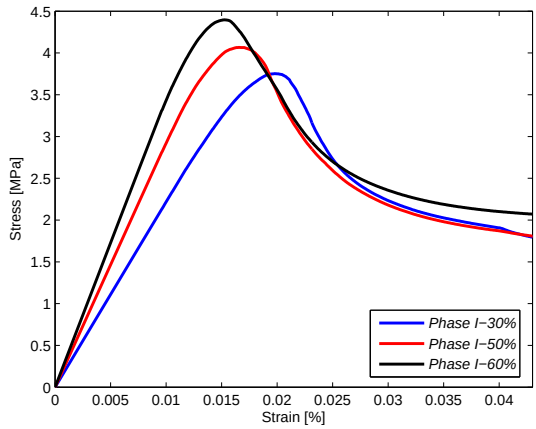

Figure 2.5: Uniaxial tension test: macroscopic response for different aggregate volume fraction

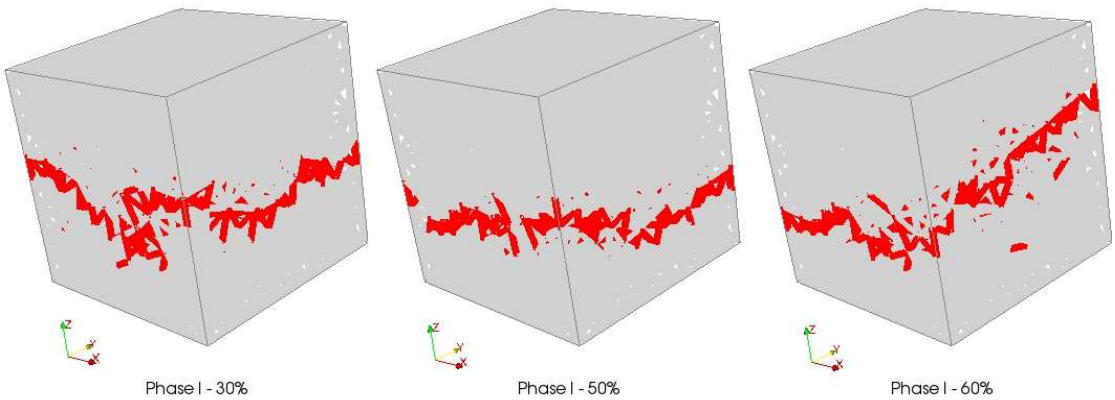

Figure 2.6: Specimen contours at the end of uniaxial tension test. Beam elements in increasing softening are red colored

[43] over the spatial domain of interest. The edges of the resulting tetrahedral elements are converted into the beams whose cross sections are computed from the corresponding Voronoi tessellation. Such task is computed using a code written in Matlab.

2.3.2 Tension test

2.3.2.1 Uniaxial tension test

We consider here the specimen given as a cube with 15 cm side length with different volume fraction of aggregates (phase I), namely 30%, 50% and 60%. Table 2.1 summarizes the chosen mechanical properties for each phase. The values for shear strength (cohesion) of Portland cement are determined in agreement with empirical

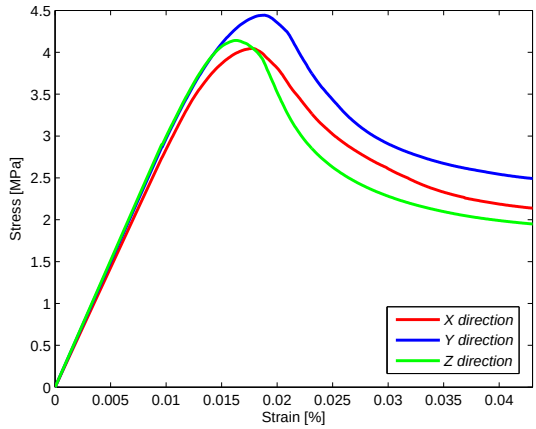

Figure 2.7: Uniaxial tension test: macroscopic responses for specimen (phase I-50%) in three loading directions

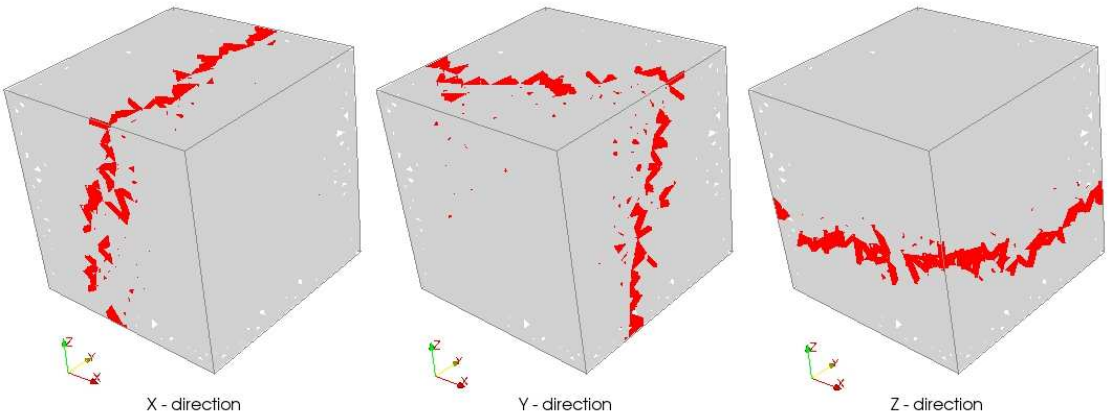

Figure 2.8: Specimen contours at the end of uniaxial tension test for phase I-50% specimen in all three loading directions. Beam elements in increasing softening are red colored

relations [86, 87]. However, meso scale parameters can be obtained from inverse identification of parameters, which will be given in Part II. One can note that aggregate is much stiffer than the cement matrix and is kept linear elastic. These computations (and the subsequent ones) are all made under the displacement control with unrestrained lateral displacements for tension test.

Figure 2.5 shows macroscopic stress (sum of all reactions in Z direction per cross-sectional area of the concrete cube) with respect to strain. The macroscopic Young's modulus and limit stress which triggers the global softening change due to volume fraction of phase I for 30%, 50% and 60%. With an increase of phase I volume fraction, the global modulus of elasticity increases, as well as elastic limit stress point. It can also be seen that when volume fraction ratio of phase II increases, the failure of specimen becomes more ductile with larger fracture process zone (before reaching elastic limit point) and more brittle in softening response. The main physical

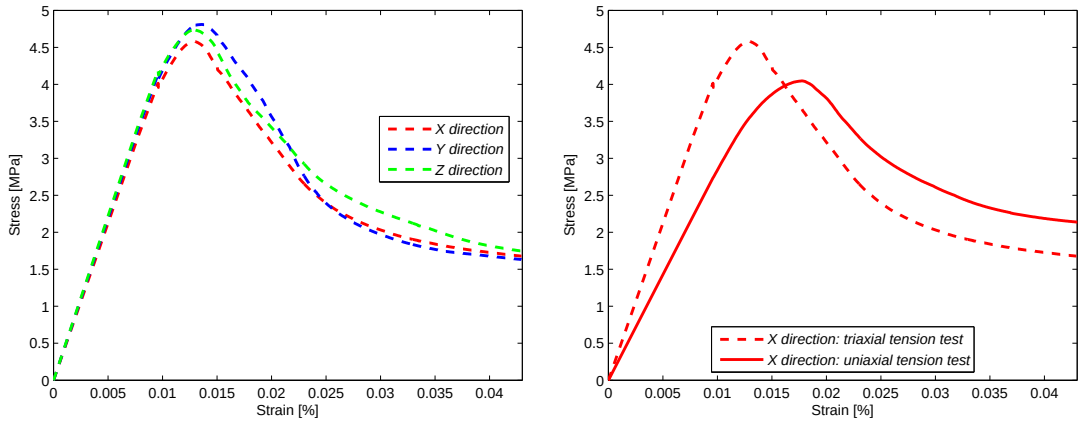

(a) (b)

Figure 2.9: Macroscopic response - phase I-50%: (a) hydrostatic tension test; (b) hydrostatic-uniaxial tension test comparison for X direction

explanation of this influence lies in total volume of voids in concrete. The structure of cement paste is complex and there exist several sources of flaws and defects even before the application of external load, up to 50% of the volume of cement paste may consist of pores (gel pores, capillary pores and accidental or entrapped air). If we ignore all voids in aggregate (for normal aggregates these are minimal) with increasing aggregate-cement ratio, the cement paste will represent smaller proportion of specimen volume. Thus the total porosity is lower, and hence the limit stress point is higher [81].

Figure 2.6 presents beam elements in subsequent stages of increasing softening at the end of tension test computation for three different heterogeneous specimen. Here, macro-crack lies in direction perpendicular to the imposed displacement. One dominant macro-crack is present in any specimen inducing the final failure mechanism formed differently depending on the distribution of weaker phase, which decides the final crack position. Failure due to mode I is more pronounced in tension test.

Figure 2.7 shows macroscopic stress (sum of all reactions in X, Y and Z direction per cross-sectional area of concrete cube) with respect to strain curve for 50% volume fraction of phase I. The macroscopic limit stress which triggers the global softening changes mainly due to the beam spatial position of phase II with respect to loading direction while the macroscopic Young's modulus remains unchanged. Figure 2.8 presents beam elements in increasing softening at the end of tension test computations with 50% of phase I for each loading direction. Here again, we can note that one dominant macro-crack is present in each direction inducing the final failure mechanism.

2.3.2.2 Hydrostatic tension test

For simulation of hydrostatic tension test the chosen material and geometry properties remain the same as for uniaxial case (see Table 2.1). This computation is made under simultaneously imposed displacements along X, Y and Z axes. Figure 2.9a shows macroscopic stress (sum of all reactions in X, Y and Z direction per cross-sectional

area) with respect to strain curve for 50% volume fraction of phase I. In Figure 2.9b, the comparison in X direction between macroscopic stresses for 50% volume fraction of phase I obtained in uniaxial tension test and in hydrostatic case is given. It can be noted that hydrostatic response is stiffer and less ductile comparing to uniaxial response. Figure 2.10 presents beam elements in increasing softening at the end of hydrostatic tension test computations. We can observe several macro-cracks contrary to a simple tension test where only one macro-crack is observed.

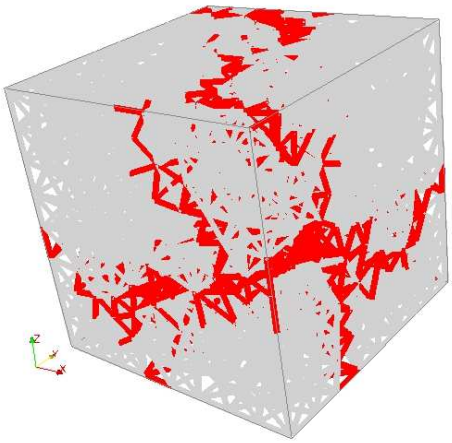

Figure 2.10: Specimen contour at the end of hydrostatic tension test for phase I-50% specimen. Beam elements in increasing softening are red colored

2.3.3 Compression test

The results of numerical simulations and corresponding macroscopic responses for specimens under uniaxial (unconfined) compression loading program are given here. Simulations in compression test are conducted with displacement control, while lateral displacements are restrained which corresponds to the case with higher friction between the load platen and the specimen. Geometric, material parameters and distribution of aggregate and cement paste are the same as for the previously used specimens (see Table 2.1). Macroscopic responses (Figure 2.11a) reveal the change in modulus of elasticity and elastic limit stress point due to different volume fraction of aggregate. With an increase of phase I, the global modulus of elasticity and elastic limit point increase similar to tension test case. The difference with respect to uniaxial tension test mechanism concerns the ductile phase of the response during creation of the fracture process zone, which is more pronounced in compression test than in tension test. Thus, not only the ductile part with fracture process zone is larger, but also its contribution to total dissipation compression failure. The main reason for this is that more elements are subjected to shear and compression simultaneously, where crack propagates because of the shear, which leads to mode II or mode III failure. If the crack propagates in mode II or III, it is still possible to transfer the compression force through the specimen, assuming that two separated blocks formed during cracking in mode II or III, lean on each other. Compression

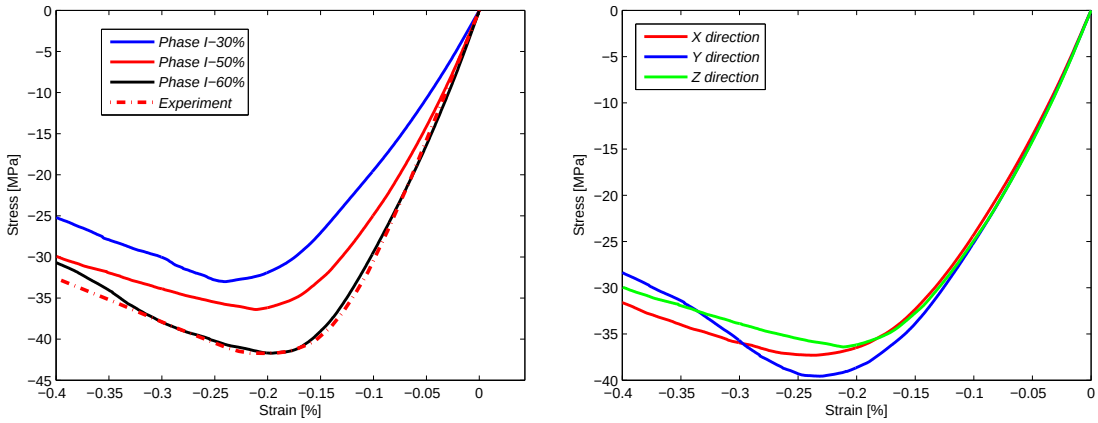

(a) (b)

Figure 2.11: Macroscopic response for uniaxial compression test: (a) different aggregate volume fraction; (b) phase I-50%

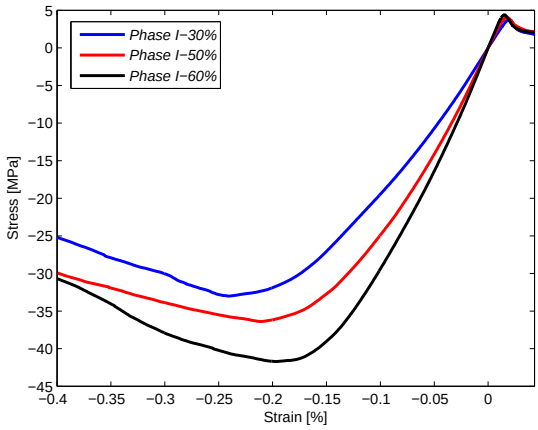

Figure 2.12: Complete macroscopic response for different aggregate volume fraction

force in this situation increases until the point where significant damage on the specimen is made, and until cracking is extensive enough that loading capacity starts to decrease. One can note that macroscopic response for numerical specimen with 60% of aggregate fits very well with experimental result conducted on the concrete cube with similar properties taken from [88].

Figure 2.11b shows macroscopic stress (sum of all reactions in X, Y and Z direction per cross-sectional area) versus strain curve for 50% volume fraction of phase I. The macroscopic limit stress which triggers the softening changes mainly due to the beam spatial position of phase II with respect to loading direction while the macroscopic Young's modulus remain unchanged as in tension case.

In order to compare the macroscopic responses corresponding to uniaxial tension and compression, Figure 2.12 presents macroscopic curves and reveals that the overall compression-tension ratio is equal to 8.8, 9.37 and 9.50 for respectively 30%, 50% and 60% of phase I.

Figure 2.13 (upper row) presents beam elements in increasing softening at the end of compression test computations for phase I - 50% specimen in three loading

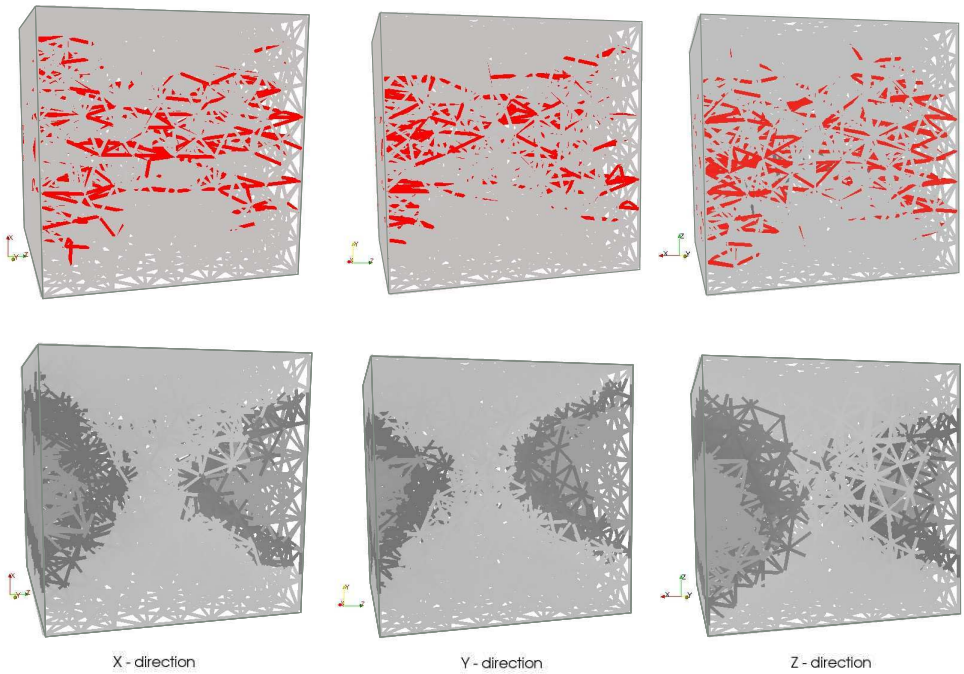

Figure 2.13: Specimen contour at the end of uniaxial compression test for phase I-50% specimen in three loading directions. Beam elements in increasing softening are red colored (upper row), displacements in the direction perpendicular to loading direction (lower row)

directions. Contrary to tension test crack patterns, in compression test much more macro-cracks are needed to drive the specimens to failure and these are influenced more by mode II and mode III mechanisms, which form the final crack patterns together with mode I. Figure 2.13 (lower row) reveals the displacements in beam elements at the end of compression test computations which correspond to the upper row figures. Here, we can see clearly that the diagonal orientation failure mode is dominant.

2.3.4 Failure surfaces for biaxial loading

In this section we show how to obtain macroscopic multi-surface criterion for concrete-like materials by taking into account heterogeneities and different process of cracking using meso-scale model proposed in previous section. The most appropriate combination of multi-surface models for concrete can be considered combining Drucker-Prager for compression stress and Rankine for tensile stress with plasticity model describing the failure of structure. It can be written in terms of the principal stress values according to:

$$\begin{aligned} \Phi^{DP} &= \sqrt{J_2} + \mu I_1/\sqrt{6} - (f_c - \hat{q}^c(\xi^c)) \leq 0 \\ \Phi_i^R &= \sigma_i - (f_t - \hat{q}^t(\xi^t)) \leq 0 \end{aligned} \tag{2.36}$$

where Φ^{DP} and Φ_i^R are, respectively, the Drucker-Prager and Rankine yield surfaces, σ_i, J_2 and I_1 are principal values, the second and the first invariant of stress tensor, f_c

and f_t are compressive and tensile yield stress values, q^c and q^t are the corresponding internal variables that control the plasticity threshold evolution resulting with desired amount of fracture energy for any particular mode of localized failure [32].

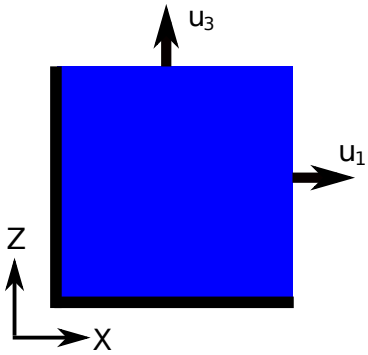

Figure 2.14: Specimen for biaxial test: boundary conditions and loading

In addition to this criterion we can find coupled plasticity-damage model [89] and Saint-Venant multisurface criterion [90]. The coupled plasticity-damage model components are selected in order to provide the representation of concrete in compaction where the plastic component is given in terms of the Drucker-Prager criterion and damage criterion in terms of the spherical part of stress tensor:

$$\begin{aligned} \Phi^p(\boldsymbol{\sigma}) &= \sqrt{J_2} + tan(\alpha)\tfrac{1}{3}tr(\boldsymbol{\sigma}) - \sqrt{2/3}\sigma_f^p \\ \Phi^d(\boldsymbol{\sigma}, q^d) &= tr(\boldsymbol{\sigma}) - (\sigma_f^d - q^d) \end{aligned} \tag{2.37}$$

where $tan(\alpha)$ is material parameter which can characterize the internal friction, σ_f^d is the elasticity limit point for damage and q^d is hardening damage variable.

Furthermore, we can express the Saint-Venant multisurface plasticity criterion directly in stress space, in terms of principal values of stress tensor:

$$\begin{aligned} \Phi_1(\boldsymbol{\sigma}) &= \tfrac{\bar{\lambda}+2\mu}{2\mu}\sigma_1 - \tfrac{\bar{\lambda}}{2\mu}\sigma_2 - \sigma_y \leq 0 \\ \Phi_2(\boldsymbol{\sigma}) &= -\tfrac{\bar{\lambda}}{2\mu}\sigma_1 + \tfrac{\bar{\lambda}+2\mu}{2\mu}\sigma_2 - \sigma_y \leq 0 \end{aligned} \tag{2.38}$$

where the value of elasticity limit point is obtained from biaxial tension test.

In order to test biaxial failure behavior, we choose the plate specimen with the dimensions of 150 mm x 30 m x 150 mm. The plate is subjected to biaxial imposed displacements, producing the following stress combinations: tension-tension, compression-compression, compression-tension and tension-compression (Figure 2.14). Uniaxial compressive strength value is taken from uniaxial compressive test performed on plate concrete specimen for 6 different distribution of each phase with 50% of aggregates volume (Table A.1).

Figure 2.15 shows macroscopic tension and compression stress (sum of all reactions in X direction per cross-sectional area) versus strain curve for 6 realizations with 50% volume fraction of phase I. Macroscopic responses reveal the changes in elastic limit point mainly due to different spatial beam position of phase II with respect to loading direction.

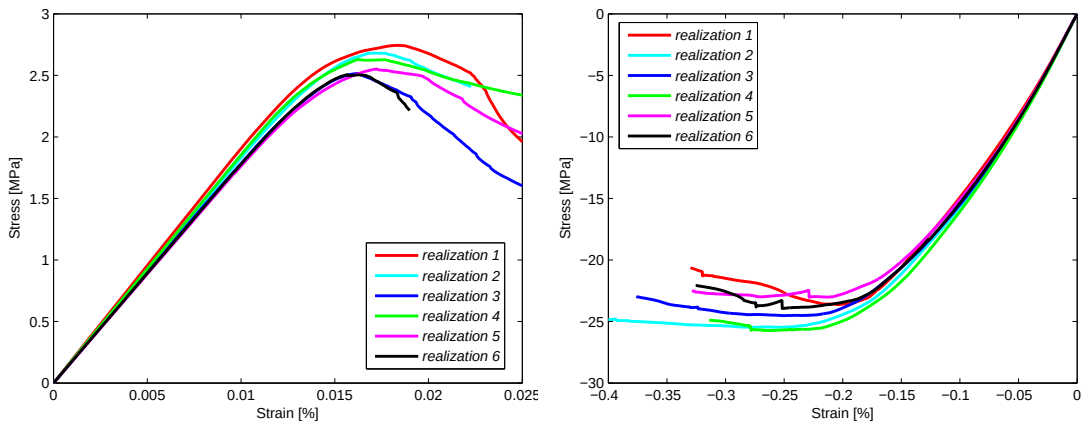

(a) (b)

Figure 2.15: Uniaxial macroscopic response for 6 realizations in plate specimen: (a) tension test; (b) compression test

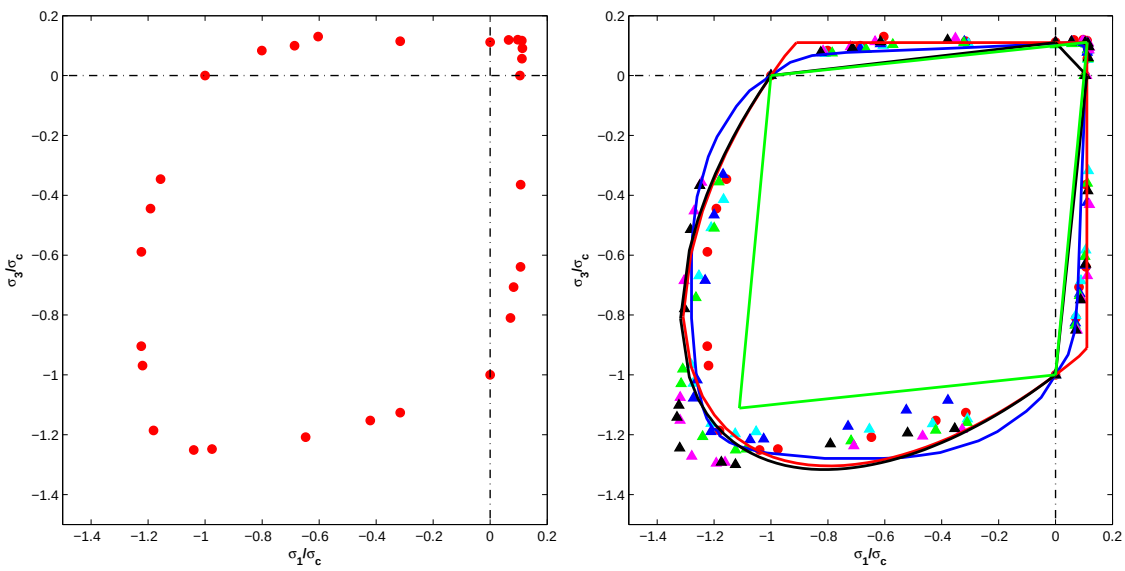

(a) (b)

Figure 2.16: Failure surfaces: (a) for realization 1; (b) for 6 realizations with the multisurface Drucker-Prager - Rankine surface (red line - eq. 36), coupled plasticity-damage model (black line - eq. 37), Saint-Venant (green line - eq. 38) and experimental (blue line)

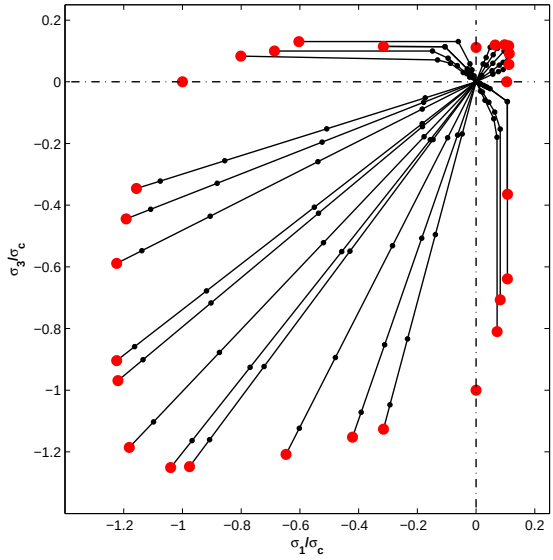

Figure 2.17: Evolution of σ_1/σ_{ci} with respect to σ_3/σ_{ci} during loading until failure for realization 1 (red dots)

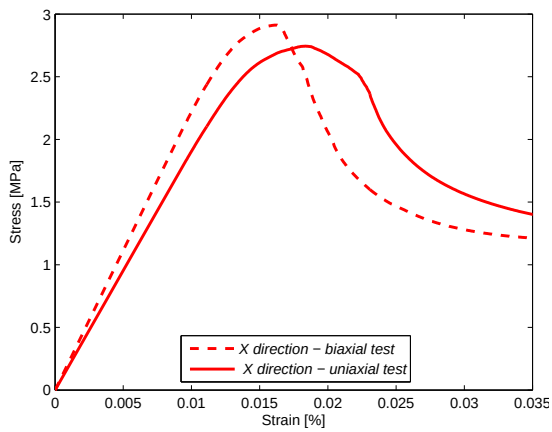

Figure 2.18: Biaxial-Uniaxial test comparison for realization 1 - phase I-50%: macroscopic response in X direction - tension test

In order to obtain four loading combinations (compression - compression, tension - tension, compression - tension and tension - compression), we perform a circular loading program based upon the trigonometrical circle $cos(\alpha)^2 + sin(\alpha)^2 = 1$. Thus, couples of imposed displacements ($u_1 = cos(\alpha)$, $u_3 = sin(\alpha)$) are parametrized in terms of angle α. Faces X = 150 mm and Z = 150 mm are respectively subjected to imposed displacements u_1 and u_3, while faces X = 0 mm and Z = 0 mm are blocked in X and Z directions (Figure 2.14). Compressive and tensile are chosen with negative and positive values, respectively. Stress in the principal direction 1 (X direction) is labelled as $\overline{\sigma}_1$ and stress in principal direction 3 (Z direction) as $\overline{\sigma}_3$. The ultimate strength in the principal direction 1 is written σ_1 and the one in the direction 3, σ_3. Tables A.2 and A.2 (See Appendix) contain all computed data on

ratio of ultimate strengths σ_1 and σ_3 with respect to σ_{ci} under different values of imposed displacements.

Graphical representations of Tables A.2 and A.3 are presented in Figure 2.16a (1 realization) and Figure 2.16b (6 realizations), while Figure 2.17 shows evolution of σ_1/σ_{ci} with respect to σ_3/σ_{ci} during loading until failure for realization 1. Figure 2.16b also provides some plots of failure criteria the Drucker-Prager and the Rankine from equation (36), coupled plasticity-damage from equation (37) and the Saint-Venant multisurface from equation (38). Results computed with the proposed model best fits with the multisurface Drucker-Prager Rankine criterion and experimental results on biaxial specimens taken from [88]. Table 2 contains the computed macroscopic fracture energies under particular couples of imposed displacements for realization 1 (red dots). Macroscopic differences between uniaxial and biaxial test on a plate specimen for tension case can be observed (Figure 2.18). It can be noted that in biaxial response strength increase is observed compared to the uniaxial one. Moreover, specimen is also less ductile in biaxial loading condition than in uniaxial response either. The same is observed for biaxial compression case. The contours of the plate specimens can be observed in Figure 2.19 with red colored beam elements in increasing softening regime at the end of both tension (upper row) and compression test (lower row) computations.

Combined regions	u_1(mm),u_3(mm)	G_f (N/m)
Tension-tension	0.0200,0.0200	6.525
Compres-compres	-0.2000,-0.2000	357.351
Tension-compres	0.0224,-0.0380	73.157
Compres-Tension	-0.0380,0.0224	72.241

Table 2.2: Fracture energy under particular couples of imposed displacements for realization 1 (red points)

Symmetrical failure behavior of concrete in relation with the 45° line under biaxial loading is observed in Figures 16.a and 16.b, as well as in experimental approaches [91]. As already shown, the ultimate compression strength of concrete is higher under biaxial compression test than in uniaxial compression. Most likely, this happens due to concrete compaction effect leading to decrease in porosity during biaxial compression test. Increase of ultimate biaxial compression strength in relation to the corresponding uniaxial compression strength is observed for each couples of imposed displacement in compression-compression region. Maximum value of ultimate compression strength is obtained for imposed displacements u_1=-0.1800 mm, u_3=-0.0872 mm and u_1=-0.0872 mm, u_3=-0.1800 mm for σ_1 and σ_3, respectively, in each realization. In tension-tension region the value of the concrete ultimate strength for each couples of imposed displacement is very close to the corresponding uniaxial tensile strength. Finally, in tension-compression and compression-tension region, concrete compression ultimate strength increases while the tension decreases.

Figure 17 shows that in the region compression-compression, behavior of concrete is linear between σ_1/σ_{ci} and σ_3/σ_{ci} due to prevented cracks opening. Moreover, biaxial compression loading in X and Z direction tends to prevent crack opening

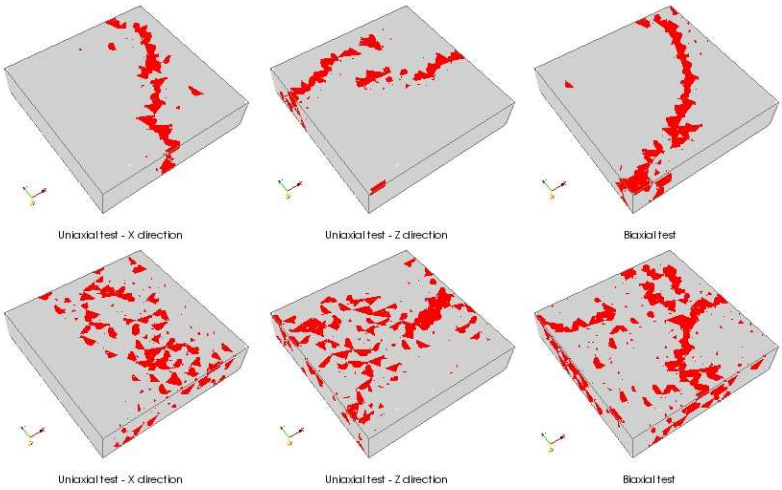

Figure 2.19: Plate specimen contours at the end of uniaxial and biaxial tension test (upper row) and compression test (lower row). Beam elements in increasing softening are red colored

respectively in Z and X direction and dominant failure mechanism occurs in Y direction (out of plane). For other regions (tension-tension, tension-compression, compression-tension) linear relation between σ_1/σ_{ci} and σ_3/σ_{ci} is firstly observed until cracking is not present, and non-linear relation between these two ratios, where cracking is more pronounced. In regions tension-compression and compression-tension one can note that the ultimate tension strength is sooner reached rather then for compression due to higher ratio of imposed displacements.

2.4 Final comments on the presented 3D concrete meso-scale model

In this chapter we proposed meso-scale constitutive model for concrete employing a three-dimensional beam lattice model. We confirmed the model capability to represent the salient features of failure phenomena for concrete-like materials. The model is able to provide the corresponding variability of material parameters for macro-scale failure criterion, combining the Drucker-Prager for compression stress and the Rankine for tensile stress. The numerical tests carried out with a meso-scale model consider different volume fraction of cohesive links or spatial beam elements representing cement paste and aggregates in agreement with the chosen granulometric curve. The beam element is represented by 3D Timoshenko beam, embedded with strong discontinuities in local coordinate system directions, which provides the capability to simulate the localized failure in modes I, II and III. Failure can occur individually in any mode or in mixed mode. The failure criteria is different under tension or compression force. In tension case, softening is activated simultaneously for all modes as soon as one failure surface becomes active, whereas in compression the failure modes are handled separately. The compression force influences the shear strength threshold in the Mohr-Coulomb manner. Another feature of the

model is that each material phase parameters are introduced through the Gaussian distribution representing heterogeneities of each phase. We illustrated here that the model of this kind can be used successfully to present quite complex macroscopic responses. Three concrete specimens with 30%, 50% and 60% volume fractions of aggregate were subjected to uniaxial tension and compression tests. We confirm that the resistance to tension is much lower than the one in compression. We can observe one dominant macro-crack that lead to specimen failure in tension case, whereas for compression case many more macro-cracks are needed to drive the specimens to failure, with a significant contribution of mode II and mode III mechanisms. We also find that ultimate strength increases with increase of volume fraction of aggregates, and also influences the crack path. Overall compression-tension ratio σ_c/σ_t is equal to 8.8, 9.37 and 9.50 for 30%, 50% and 60% of phase I, respectively. All these points fit well with typical observations made for concrete-like materials [92, 93].

Finally, one of the most significant findings is that this approach can provide the definition of the parameters, such as the fracture energy, ultimate strength taking into account the heterogeneity and different process of cracking governing the final failure mechanism. This approach can also be used for parameters identification of multi-surface models (e.g. coupled plasticity-damage model [89], Saint-Venant plasticity model [90] or combination of the Rankine and the Drucker-Prager criteria [94]) providing more predictive results from classical phenomenological models in structural analysis. Such task is carried in next chapter of this thesis.

The proposed meso-scale model provides many enhanced features, but also requires a more refined procedure to obtain the model parameters, and their distribution typical of material heterogeneities. The subsequent work, presented in next chapter of this thesis, describes the solution to inverse identification problem by using coupled nonlinear mechanics-probability approach to provide not only the parameters, but also their probability distribution. This pertains not only to elastic model parameters, but also to all different parameters governing the complete failure process. The latter requires very careful description of the experimental procedure and the ability to provide the corresponding computational result to any given measurement, as well as the most extensive set of experimental results.

3

Multi-surface plasticity model for concrete with 3D hardening/softening failure modes for tension, compression and shear

In this chapter multi-surface plasticity model is developed which can reproduce the inelastic behavior and failure modes of concrete in tension, compression and shear. The main novelty of the proposed concrete model can also capture all different phases of localized failure for massive structures, where the elastic behavior is followed by the creation of the fracture process zone with a large number of micro-cracks and subsequent final failure mode with micro-cracks coalescence into the macro-crack. The fracture process zone is represented by homogenized plasticity criterion with hardening (in particular the non-associated Drucker-Prager) since the number of micro-cracks is considered sufficiently large and their orientation random. The macro-crack is represented with a surface of displacement discontinuity, which is typical of all localized dissipative mechanisms due to the apparition and development of localization zones. The main novelty of proposed model is to provide the full set of 3D localization modes for tension, for compression and for shear, with each mode using corresponding fracture energy.

Contents

3.1 Introduction 45
3.2 Continuum model formulation 46
3.2.1 Thermodynamics framework 47
3.2.2 Stress resultant hardening model 52
3.2.3 Softening plasticity 56
3.3 Space and time Discrete approximation 61
3.3.1 Spatial discretization 61
3.3.2 Integration of internal state variables for plasticity 62
3.4 Numerical examples 66
3.4.1 Uniaxial tension test 66
3.4.2 Notched bar in tension 67
3.4.3 Three point notched beam 68
3.4.4 Shear test 69
3.4.5 Compression test 70
3.4.6 Bending test on a reinforced concrete beam 72
3.5 Final comments on the presented 3D concrete macro-scale model . . . 75

3.1 Introduction

The intensive investigations made over recent years have led to a much better understanding of the constitutive behavior of concrete under complex loading conditions. A variety of constitutive models have been proposed, and many of them are phenomenological. In order to achieve a more reliable prediction of the limit load and structural design, it is required to provide model which describe not only pre-failure hardening regime but also post-peak softening response. The evolution in the behavior of quasi-brittle materials, especially concrete, submitted to quasi-static external mechanical loads, compression or tension, is initially characterized by a quasi-elastic phase, in which the material can recover its initial state upon unloading. Then, as the load increases, microcracks (the size of which depend on the material components) appear in a regular way and will coalesce to form a macrocrack. This macrocrack will grow and spread until the final material fractures. The appearance and development of these cracks play an essential role in the failure or collapse of concrete structures. Several proposed approaches, enable us to describe this behavior, range from discrete crack concepts [95, 96], either with or without remeshing, to various types of smeared crack concepts, either with fixed or with rotating fracture planes [97, 98]. Separation in discrete crack models can occur only at element interface which is why these models are dependent on mesh alignment. Due to this special re-meshing techniques appears to be necessary [99]. When the classical continuum is applied for softening materials as for smeared crack models it results with dependency on element alignment and element size. Thus, with such method infromation over crack orientation is not provided. The application of gradient [100] and non-local [101, 69, 102] continuum theories has proved successful in overcoming the deficiency of the classical continuum when analyzing softening materials. All the modifications of this kind requires a fine mesh within the localisation zone in order to capture the high strain gradients or in other words a priori knowledge of where failure will occur. Thus, the potential of such methods for structural scale problems, especially in three-dimensions is limited. For that reason, they are often replaced by a particular modification of the classical continuum that allows for either displacement [73, 28, 26, 103, 104, 71, 105, 106, 70, 107, 108] or strain discontinuities in the formulation [27, 110, 111]. The main advantage of the modified continuum models of this kind is to provide the adequate measure of the total inelastic dissipation of the strain softening component regardless of the chosen finite element mesh. However, the vast majority of previous works are mainly developed by combining elastic response with strain softening and thus completely ignore the possible inelastic deformation in fracture process zone that proceeds the strain-softening. In some previous work based on smeared crack concept the inelastic deformation during hardening is taken into account [112]. Moreover, it is well known by now that the nonlinear volume change during hardening is prominent feature of concrete-like materials. This sort of behavior generally violates the associated flow rule. Therefore a separate plastic potential rather than loading function is needed to define flow rule.

In this chapter, we develop model capable of taking into account both types of dissipative mechanisms which can better reproduce the behavior of massive structures:

a bulk dissipation characterized by the development of micro-cracks and a surface dissipation in localization zones in terms of the macro-cracks. Here plasticity model with Drucker-Prager yield criterion is considered, with similar plastic potential function governing hardening behavior and corresponding shear line representing the strain softening behavior. Although the plasticity model is used in present study, one can note that damage model could be used as well. However, as long as we do not go to true cyclic loading applications, either of them can be successfully applied to obtain the adequate value of limit load in quasi-static applications. Another advantage of proposed model is ability to represent nonlinear volume change during hardening obtained by using plastic potential function similar to yield function in order to define flow rule.

The condition which allows to connect pre- and post-localization state, pertains to imposing the equivalence of the corresponding dissipations, which can be cast as the stress orthogonality with respect to localization induced enhanced strain field. The standard finite element implementation ought to be modified in order to account for this orthogonality condition and addition of corresponding displacement modes representing displacement discontinuity along yield line, which can be carried out in a very similar manner as for the method of incompatible modes [28, 74].

Other multi-surface model ingredients pertains of St. Venant criterion that can handle failure in tension and in compression. Figure 3.1a shows a graphic illustration of the proposed criterion in principal axes of stress tensor. One can note that in tension region elastic stage is followed by softening, while in compression not only the ductile part with fracture process zone is larger, but also its contribution to total dissipation for compression failure. Figure 3.1b clearly reveals that the only special load case which is not limited, is a three-axial compression that can be produced by hydrostatic pressure.

The outline of the chapter is as follows. Next section briefly present the theoretical framework capable of accommodating both strain-hardening and strain-softening effects. We first start with hardening for non-associative flow rule written in six-dimensional and in principal stress space followed by softening plasticity model. Considerations of the discrete approximation, based on the finite element method, are given in Section 3. The results for several numerical examples are presented in Section 4. In Section 5 we state some closing remarks.

3.2 Continuum model formulation

In this section, we present the concrete model built in the view of failure models for massive structures, where the elastic behavior is followed by the creation of the fracture process zone with a large number of micro-cracks and subsequent final failure mode in terms of the macro-cracks. The fracture process zone is represented by the non-associated Drucker-Prager continuum plasticity model since the number of micro-cracks is considered sufficiently large and their orientation random. The macro-crack is represented with a surface of displacement discontinuity, where all localized dissipative mechanisms will led to development of localization zones.

3.2.1 Thermodynamics framework

To simplify our discussion we consider the Euclidean setting and corresponding tensor [73]. We consider the displacement vector, $\mathbf{u}$, as a function of both space position $\mathbf{x}$ and pseudo-time t

$$\mathbf{u}(\mathbf{x},t) = u_i(\mathbf{x},t)\mathbf{e}_i; \qquad \mathbf{x} = x_i\mathbf{e}_i \tag{3.1}$$

Standard kinematic considerations define the tensor of total strains, ϵ, as the symmetric part of the displacement gradient tensor

$$\boldsymbol{\epsilon} = \nabla^s\mathbf{u}; \qquad \epsilon_{ij}\mathbf{e}_i \otimes \mathbf{e}_j = \frac{1}{2}\left(\frac{\partial u_i}{\partial x_j} + \frac{\partial u_j}{\partial x_i}\right)\mathbf{e}_i \otimes \mathbf{e}_j \tag{3.2}$$

The hypothesis of small displacement gradient allows us to express the equilibrium equations in terms of Cauchy (or true) stress, $\boldsymbol{\sigma} = \sigma_{ij}\mathbf{e}_i \otimes \mathbf{e}_j$ directly in the initial configuration

$$div[\boldsymbol{\sigma}] + \mathbf{b} = \mathbf{0} \Longleftrightarrow \frac{\partial \sigma_{ij}}{\partial x_j} + b_i = 0 \tag{3.3}$$

where $\mathbf{b}$ is the body force. In elasticity the constitutive model is governed by Hooke's law which only requires to specify the material parameters that allows to construct corresponding elasticity tensor $\boldsymbol{C}$

$$\boldsymbol{\sigma} = \boldsymbol{C}\boldsymbol{\epsilon}; \qquad \sigma_{ijkl} = C_{ijkl}\epsilon_{kl} \tag{3.4}$$

The elasticity tensor of the simplest case of isotropic material (we refer to [24] where fine scale model confirms that concrete is statistically close to isotropic) can be constructed with two parameters only; by choosing Lame's parameters, λ and μ, we can write such an elasticity tensor as:

$$\boldsymbol{C} = \lambda\mathbf{1} \otimes \mathbf{1} + 2\mu\mathbf{I} \tag{3.5}$$

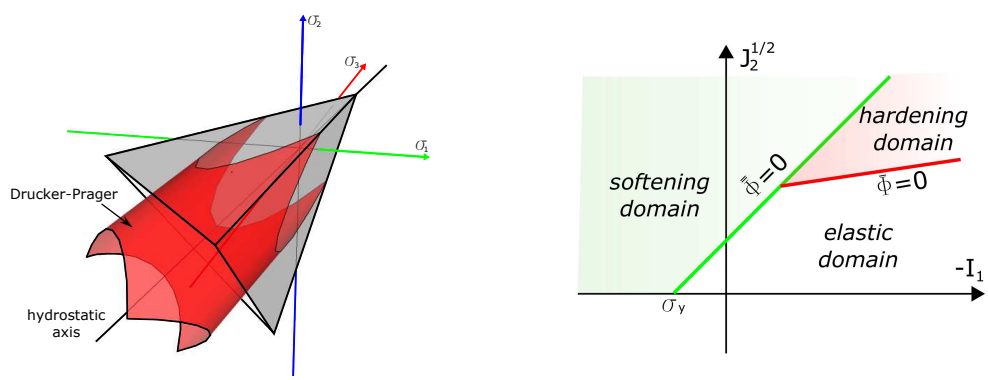

(a) (b)

Figure 3.1: Multisurface criterion (a) in principal stress space (b) in meridian plane

with $\mathbf{I}$ and $\mathbf{1}$ being, respectively, fourth and second order unit tensors. Alternatively, the elasticity tensor can be expressed in terms of bulk (K) and shear modulus (G)

$$\boldsymbol{C} = K\mathbf{1}\otimes\mathbf{1} + 2G\left(\mathbf{I} - \tfrac{1}{3}\mathbf{1}\otimes\mathbf{1}\right) \tag{3.6}$$

In the presence of plastic deformation, the constitutive relation in (3.4) is no longer featuring the total but the elastic deformation. Namely, by assuming the independence of the elastic response on plastic flow, the total deformation can be split additively into elastic $\boldsymbol{\epsilon}^e$ and plastic part $\boldsymbol{\epsilon}^p$,

$$\boldsymbol{\epsilon} = \boldsymbol{\epsilon}^e + \boldsymbol{\epsilon}^p \tag{3.7}$$

By further assuming that the elastic response remains linear, reducing to Hooke's law in (3.4) in the absence of plastic deformation, we can construct the free energy potential as a quadratic form in terms of deformations

$$\psi(\boldsymbol{\epsilon},\boldsymbol{\epsilon}^p,\boldsymbol{\zeta}) := \tfrac{1}{2}(\boldsymbol{\epsilon} - \boldsymbol{\epsilon}^p)\cdot\boldsymbol{C}(\boldsymbol{\epsilon} - \boldsymbol{\epsilon}^p)) + \tfrac{1}{2}\zeta K\zeta \tag{3.8}$$

Besides the stress tensor $\boldsymbol{\sigma}$ we define the stress-like internal variable q, which is dual to the strain-like internal state variable ζ. We assume that this dual variable is used to define the yield criterion which corresponds to the classical Drucker-Prager model:

$$\phi_y(\boldsymbol{\sigma}, q) := \| \, dev[\boldsymbol{\sigma}] \, \| + \frac{1}{3} tan(\varphi) tr[\boldsymbol{\sigma}] - \sqrt{\frac{2}{3}}(\sigma_y - q) \tag{3.9}$$

where

$$dev[\boldsymbol{\sigma}] = \boldsymbol{\sigma} - \tfrac{1}{3}(tr[\boldsymbol{\sigma}])\mathbf{1} \tag{3.10}$$

is the deviatoric part of the stress tensor, $tan(\varphi)$ is material parameter that can characterize the internal friction and σ_y is uni-axial yield stress identified from a tension test. In (3.10) the Frobenius norm is used with $\| \, \sigma \, \| := \sqrt{\sigma : \sigma}$. Instead to the yield function, plastic flow develops along the normal to the plastic potential function resulting with non-associated Drucker-Prager model. Here, we will use plastic potential function that is different then yield function

$$\phi_p(\boldsymbol{\sigma}, q) := \| \, dev[\boldsymbol{\sigma}] \, \| + \tfrac{1}{3} tan(\psi) tr[\boldsymbol{\sigma}] \tag{3.11}$$

where $tan(\psi)$ is material parameter describing the angle of dilatancy.

Specifying three fundamental equations in (3.7), (3.8) and (3.9) along with (3.11), are sufficient to completely define the stress tensor computation as well as the internal variables evolution corresponding to the plasticity model. Namely, we simply use the second principle of thermodynamics and the principle of maximum plastic dissipation.

For the isothermal case of dissipation inequality, we have:

$$\begin{aligned} 0 \leq D &:= \boldsymbol{\sigma} \cdot \dot{\boldsymbol{\epsilon}} - \frac{\partial}{\partial t}\psi \\ &= \boldsymbol{\sigma} \cdot \dot{\boldsymbol{\epsilon}} - \frac{\partial \psi}{\partial \boldsymbol{\epsilon}} \cdot \dot{\boldsymbol{\epsilon}} - \frac{\partial \psi}{\partial \boldsymbol{\epsilon}^p} \cdot \dot{\boldsymbol{\epsilon}}^p - \frac{\partial \psi}{\partial \zeta} \cdot \dot{\zeta} \\ &= (\boldsymbol{\sigma} - \frac{\partial \psi}{\partial \boldsymbol{\epsilon}}) \cdot \dot{\boldsymbol{\epsilon}} - \frac{\partial \psi}{\partial \boldsymbol{\epsilon}^p} \cdot \dot{\boldsymbol{\epsilon}}^p - \frac{\partial \psi}{\partial \zeta} \cdot \dot{\zeta} \end{aligned} \tag{3.12}$$

In the elastic case, where plastic dissipation remains equal to zero with no change of internal variables, $\dot{\boldsymbol{\epsilon}}^p = \mathbf{0}$ and $\dot{\zeta} = 0$, the last result confirms that the stress can be computed as:

$$D = 0; \quad \dot{\boldsymbol{\epsilon}}^p = \mathbf{0}; \quad \dot{\zeta} = 0; \quad \boldsymbol{\sigma} := \frac{\partial \psi}{\partial \boldsymbol{\epsilon}} = \boldsymbol{C}(\boldsymbol{\epsilon} - \boldsymbol{\epsilon}^p) \tag{3.13}$$

By assuming that such a stress computation remains valid in the plastic case, and by introducing the thermodynamic fluxes conjugate to internal variables,

$$\boldsymbol{\sigma} := -\frac{\partial \psi}{\partial \boldsymbol{\epsilon}^p} \quad q := -\frac{\partial \psi}{\partial \zeta} \tag{3.14}$$

we can obtain the final expression for the plastic dissipation according to:

$$0 \leq D^p := \boldsymbol{\sigma} \cdot \dot{\boldsymbol{\epsilon}}^p + q \cdot \dot{\zeta} \tag{3.15}$$

The principle of maximum plastic dissipation is then invoked stating that among all the admissible stress states (for which $\phi_y(\boldsymbol{\sigma}, q) \lneq 0$) , we ought to choose those which maximize the plastic dissipation:

$$D^p(\boldsymbol{\sigma}, q) = max_{\phi_y(\boldsymbol{\sigma}^*, q^*) \leq 0} \left[D^p(\boldsymbol{\sigma}^*, q^*) \right]; \tag{3.16}$$

By the Lagrange multiplier method, this problem of computing the maximum under the corresponding constraint can be transformed into an unconstrained minimization problem:

$$\begin{aligned} L^p(\boldsymbol{\sigma}, q, \dot{\gamma}) &= \max_{\dot{\gamma} \geq 0} \min_{\forall \boldsymbol{\sigma}^*, q^*} \left[L^p(\boldsymbol{\sigma}^*, q^*, \dot{\gamma}^*) \right] \\ L^p(\boldsymbol{\sigma}, q, \dot{\gamma}) &:= -D^p(\boldsymbol{\sigma}, q) + \dot{\gamma} \phi_y(\boldsymbol{\sigma}, q) \end{aligned} \tag{3.17}$$

The associated Kuhn-Tucker optimality conditions will provide the corresponding evolution equation for internal variables:

$$\begin{aligned} 0 &= \frac{\partial L^p(\boldsymbol{\sigma}, q, \dot{\gamma})}{\partial \boldsymbol{\sigma}} = -\dot{\boldsymbol{\epsilon}}^p + \dot{\gamma} \frac{\partial \phi_y(\boldsymbol{\sigma}, q)}{\partial \boldsymbol{\sigma}}; \\ 0 &= \frac{\partial L^p(\boldsymbol{\sigma}, q, \dot{\gamma})}{\partial q} = -\dot{\zeta} + \dot{\gamma} \frac{\partial \phi_y(\boldsymbol{\sigma}, q)}{\partial q}; \\ \dot{\gamma} &\geq 0; \quad \phi_y(\boldsymbol{\sigma}, q) \leq 0; \quad \dot{\gamma} \phi_y(\boldsymbol{\sigma}, q) = 0 \end{aligned} \tag{3.18}$$

The corresponding value of each Lagrange multiplier $\dot{\gamma}$ for associative plasticity model is obtained from the consistency condition, which assures that in a plastic loading process, subsequent stress and deformation states remains on subsequent yield surface:

$$\begin{aligned} 0 = \dot{\phi}_y &= \frac{\partial \phi_y}{\partial \boldsymbol{\sigma}} \cdot \dot{\boldsymbol{\sigma}} + \frac{\partial \phi_y}{\partial q} \cdot \dot{q} \\ &= \frac{\partial \phi_y}{\partial \boldsymbol{\sigma}} \cdot \boldsymbol{C}\dot{\boldsymbol{\epsilon}} - G_y \dot{\gamma}; \end{aligned} \tag{3.19}$$

where

$$G_y = \frac{\partial \phi_y}{\partial \boldsymbol{\sigma}} \cdot \boldsymbol{C} \frac{\partial \phi_y}{\partial \boldsymbol{\sigma}} + \frac{\partial \phi_y}{\partial q} \cdot K \frac{\partial \phi_y}{\partial q} \tag{3.20}$$

Since $\dot{\gamma}$ is non-zero only when yield surface is active it follows that

$$0 = \dot{\phi}_y \Rightarrow \dot{\gamma} = G_y^{-1} \left(\frac{\partial \phi_y}{\partial \boldsymbol{\sigma}} \cdot \boldsymbol{C}\dot{\boldsymbol{\epsilon}} \right) \tag{3.21}$$

where G_{ij}^{-1} is the inverse of matrix G_{ij}. By using the last result we obtain the rate form of the stress-strain relations in (3.4)

$$\dot{\boldsymbol{\sigma}} = \boldsymbol{C}^{ep} \dot{\boldsymbol{\epsilon}} \tag{3.22}$$

where $\boldsymbol{C}^{ep}$ are elastoplastic tangent moduli given by the expression

$$\boldsymbol{C}^{ep} = \begin{cases} \boldsymbol{C}; & \forall \dot{\gamma}_i = 0; \quad i = 1, 2, ..., m \\ \boldsymbol{C} - G_y^{-1} \boldsymbol{C} \frac{\partial \phi_y}{\partial \boldsymbol{\sigma}} \otimes \boldsymbol{C} \frac{\partial \phi_y}{\partial \boldsymbol{\sigma}} \end{cases} \tag{3.23}$$

The consequences of the principle of maximum plastic dissipation characterizing such associative plasticity model is the convexity of the yield surface in stress space and normality of plastic flow with respect to the yield surface. Drucker's stability postulate is also in agreement with this principle. By changing the proposed flow rule with separate potential in (3.11) we can conclude that proposed model results with Drucker-Prager non-associative plasticity that is not stable in the sense of Drucker. However, stability postulate is sufficient but not a necessary criterion. Since the uniqueness of stress and strain trajectories for a given loading exists, the material can be regarded as locally stable, thus the condition of uniqueness rather than the stability postulate may be regarded as a basic for establishing stress-strain relationship. The non-associative flow rule for the plastic strain rate tensor, using (3.11) and strain-like hardening variable , is given by

$$\begin{aligned} 0 &= -\dot{\boldsymbol{\epsilon}}^p + \dot{\gamma} \frac{\partial \phi_p(\boldsymbol{\sigma}, q)}{\partial \boldsymbol{\sigma}} \\ 0 &= -\dot{\zeta} + \dot{\gamma} \frac{\partial \phi_y(\boldsymbol{\sigma}, q)}{\partial q} \end{aligned} \tag{3.24}$$

The loading/unloading conditions can be expressed in the Kuhn-Tucker form as

$$\dot{\gamma} \geq 0; \quad \phi_y(\boldsymbol{\sigma}, q) \leq 0; \quad \dot{\gamma}\phi_y = 0 \tag{3.25}$$

The plastic multiplier $\dot{\gamma}$ using the plastic consistency condition $\dot{\phi}_y = 0$ can be expressed in the form

$$\begin{aligned} 0 = \dot{\phi}_y &= \frac{\partial \phi_y}{\partial \boldsymbol{\sigma}} \cdot \dot{\boldsymbol{\sigma}} + \frac{\partial \phi_y}{\partial q} \cdot \dot{q} \\ &= \frac{\partial \phi_y}{\partial \boldsymbol{\sigma}} \cdot \boldsymbol{C}\dot{\boldsymbol{\epsilon}} - \dot{\gamma}\left(\frac{\partial \phi_y}{\partial \boldsymbol{\sigma}} \cdot \boldsymbol{C}\frac{\partial \phi_p}{\partial \boldsymbol{\sigma}} + \frac{\partial \phi_y}{\partial q} \cdot K\frac{\partial \phi_y}{\partial q}\right) \\ \Rightarrow \dot{\gamma} &= h^{-1}\frac{\partial \phi_y}{\partial \boldsymbol{\sigma}} \cdot \boldsymbol{C}\dot{\boldsymbol{\epsilon}} \end{aligned} \tag{3.26}$$

where we used relation

$$h^{-1} = \frac{\partial \phi_y}{\partial \boldsymbol{\sigma}} \cdot \boldsymbol{C}\frac{\partial \phi_p}{\partial \boldsymbol{\sigma}} + \frac{\partial \phi_y}{\partial q} \cdot K\frac{\partial \phi_y}{\partial q} \tag{3.27}$$

We can simplify corresponding results in (3.26) for proposed model to obtain:

$$\dot{\gamma} = \frac{2G\boldsymbol{\nu} : \dot{\boldsymbol{\epsilon}} + 3K\alpha_1 tr(\dot{\boldsymbol{\epsilon}})}{2G + 9K\alpha_1\alpha_2 + \frac{2}{3}K_h} \tag{3.28}$$

where

$$\begin{aligned} &\boldsymbol{\nu} = \frac{dev[\boldsymbol{\sigma}]}{\parallel dev[\boldsymbol{\sigma}] \parallel}; \quad \alpha_1 = \frac{1}{3}tan\varphi; \quad \alpha_2 = \frac{1}{3}tan\psi; \\ &K_h = \frac{dq(\zeta)}{d\zeta}; \\ &q(\zeta) = -(\sigma_\infty - \sigma_y)\left[1 - exp(-\beta\zeta)\right] + K_{h,lin}\zeta; \end{aligned} \tag{3.29}$$

In (3.29) above, σ_y is initial uniaxial yield stress, β is the hardening parameter that governs the rate with which the saturation is achieved, σ_∞ is limit until the stress increase,$K_{h,lin}$ is hardening modulus.

Once the scalar function $\dot{\gamma}$ is determined the plastic strain increment from flow rule can be expressed as

$$\dot{\boldsymbol{\epsilon}}^p = \dot{\gamma}\frac{\partial \phi_p}{\partial \boldsymbol{\sigma}} = h^{-1}\underbrace{\frac{\partial \phi_y}{\partial \boldsymbol{\sigma}} \cdot \boldsymbol{C}}_{\boldsymbol{H}}\frac{\partial \phi_p}{\partial \boldsymbol{\sigma}}\dot{\boldsymbol{\epsilon}} \tag{3.30}$$

and corresponding stress increment can be determined from (3.4) and (3.7) combining with last expression

$$\begin{aligned} \dot{\boldsymbol{\sigma}} &= \boldsymbol{C}\left(\dot{\boldsymbol{\epsilon}} - \dot{\gamma}\frac{\partial \phi_p}{\partial \boldsymbol{\sigma}}\right) \\ &= \left(\boldsymbol{C} - h^{-1}\boldsymbol{C}\frac{\partial \phi_y}{\partial \boldsymbol{\sigma}} \otimes \boldsymbol{C}\frac{\partial \phi_p}{\partial \boldsymbol{\sigma}}\right)\dot{\boldsymbol{\epsilon}} \\ &= \boldsymbol{C}^{ep}\dot{\boldsymbol{\epsilon}} \end{aligned} \tag{3.31}$$

Thus the tangent elastoplastic tensor can be written in an additive format

$$\boldsymbol{C}^{ep} = \boldsymbol{C} + \boldsymbol{C}^{p} \tag{3.32}$$

with

$$\boldsymbol{C}^{p} = -h^{-1}\boldsymbol{C}\frac{\partial \phi_y}{\partial \boldsymbol{\sigma}} \otimes \boldsymbol{C}\frac{\partial \phi_p}{\partial \boldsymbol{\sigma}} = -h^{-1}\boldsymbol{H} \otimes \boldsymbol{H}^{*} \tag{3.33}$$

where $\boldsymbol{C}^{p}$ is plastic tangent stiffness tensor and represents the degradation of the stiffness of material due to plastic flow. It can be noted from (3.33) that tensor $\boldsymbol{C}^{p}$ lacks symmetry. The same holds for $\boldsymbol{C}^{ep}$ with a non-associative flow rule is used as stated for chosen Drucker-Prager model:

$$\boldsymbol{C}^{ep} = \boldsymbol{C} - \frac{(2G\boldsymbol{\nu}_{n+1} + 3K\alpha_1\mathbf{1}) \otimes (2G\boldsymbol{\nu}_{n+1} + 3K\alpha_2\mathbf{1})}{2G + 9K\alpha_1\alpha_2 + \frac{2}{3}K_{h,iso}} \tag{3.34}$$

3.2.2 Stress resultant hardening model

The stress update and formation of the elastoplastic tangent modulus requires the derivative of the yield function and the plastic potential function. Even for linear criteria, this is a cumbersome task when carried out in the general six-dimensional stress space. It will be shown in the following that computation in principal stress space simplifies procedure, presented in Section 3.2.1.. First, the dimension of the problem reduces from six to three, and second, in the three-dimensional stress space the stress states can be easily visualized graphically, making it possible to successfully apply geometric arguments. The approach is applicable to general isotropic yield criteria (e.g [113–115]), but in the following only Drucker-Prager criteria will be considered. As only isotropic material models are considered, the manipulations can be carried out with respect to any set of coordinates. Therefore the predictor stress is transformed into principal stress space, to compute the return to the yield surface. Considering the fact that the stress return preserves the principal directions, the updated stress can then be transformed back into the original Cartesian coordinates. The constitutive matrices are also first formed in principal stress space and then subsequently transformed to standard coordinates.

The Drucker-Prager model in principal stress space is right-circular cone with its axis equally inclined with respect to each of the coordinate axes, and with its apex in the tension octant. It can be shown that plastic deformation must be accompanied by an increase in volume if $\varphi \neq 0$. This property known as dilatancy is consequences of the dependency of yield surface for associative or plastic potential surface for non-associative flow rule, on hydrostatic pressure. Figure 3.2 shows Drucker-Prager yield surface open in direction of the negative hydrostatic axis along with plastic potential function. From flow rule the plastic strain increment $d\epsilon_{ij}^{p}$ is perpendicular to plastic potential surface at the actual yield point M. The vector $d\epsilon_{ij}^{p}$ can be decomposed into vertical and horizontal component where horizontal components $d\epsilon_{ij}^{pv}$ represents the plastic volume change, which is always positive for $\psi > 0$ so

and for associative plasticity. When using a negative dilatancy angle, we find that stress-strain curve gradually approaches a line with a negative slope. In other words, hardening is followed by softening leading to unstable behavior where the material resistance vanishes.

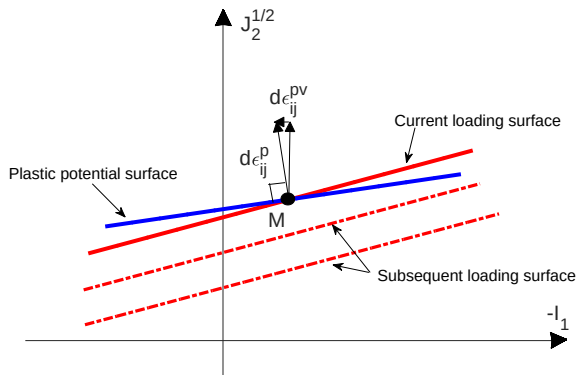

Figure 3.2: The loading and plastic potential surfaces for the Drucker-Prager material with a non-associated flow rule

Defining three main ingredients sufficient for the constitutive model of plasticity we can provide the stress tensor computation as well as internal variables evolution:

- additive decomposition of total strain into elastic and plastic component
  $\overline{\varepsilon} = \overline{\varepsilon}^e + \overline{\varepsilon}^p$

- the free energy function constructed in terms of deformations
  $\psi(\overline{\boldsymbol{\epsilon}}, \overline{\boldsymbol{\epsilon}}^p, \overline{\boldsymbol{\zeta}}) := \frac{1}{2}(\overline{\boldsymbol{\epsilon}} - \overline{\boldsymbol{\epsilon}}^p) \cdot \hat{\boldsymbol{C}}(\overline{\boldsymbol{\epsilon}} - \overline{\boldsymbol{\epsilon}}^p) + \frac{1}{2}\overline{\zeta} K \overline{\zeta}$

- the yield criterion takes a very simple form in the principal axis representation
  $\phi_{y,s}(\overline{\boldsymbol{\sigma}}, q) := \sqrt{J_2} + \frac{1}{3} tan(\varphi) I_1 - \sqrt{\frac{2}{3}}(\sigma_y - q)$

  while plastic potential function is defined as
  $\phi_{p,s}(\overline{\boldsymbol{\sigma}}, q) := \sqrt{J_2} + \frac{1}{3} tan(\psi) I_1$

  where
  $J_2 = 1/6 \left[(\overline{\boldsymbol{\sigma}}_1 - \overline{\boldsymbol{\sigma}}_2)^2 + (\overline{\boldsymbol{\sigma}}_2 - \overline{\boldsymbol{\sigma}}_3)^2 + (\overline{\boldsymbol{\sigma}}_3 - \overline{\boldsymbol{\sigma}}_1)^2 \right]$
  $I_1 = \overline{\boldsymbol{\sigma}}_1 + \overline{\boldsymbol{\sigma}}_2 + \overline{\boldsymbol{\sigma}}_3$
  is the second invariant of the deviatoric part of the Cauchy stress and the first invariant of the Cauchy stress, respectively.

The principal stresses and deformations as well as their directions are found by solving the eigenvalue problem

$$\begin{aligned} (\boldsymbol{\sigma} - \overline{\sigma}_i \mathbf{I}) \mathbf{n}_i = 0 \\ (\boldsymbol{\varepsilon} - \overline{\varepsilon}_i \mathbf{I}) \mathbf{m}_i = 0 \end{aligned} \tag{3.35}$$

where $\boldsymbol{\sigma}$,$\boldsymbol{\varepsilon}$ are stress and deformation tensor, $\overline{\boldsymbol{\sigma}}_i$,$\overline{\boldsymbol{\varepsilon}}_i$ are the eigenvalues, $\mathbf{I}$ is identity matrix and $\mathbf{n}_i, \mathbf{m}_i$ are eigenvectors. The three eigenvectors of deformation tensor form a coordinate transformation tensor $Q_{i,j}$

$$\begin{aligned} Q_{i,j} &= \begin{bmatrix} n_{j,1} & n_{j,2} & n_{j,3} \end{bmatrix} = \\ &= \begin{bmatrix} cos(x,\overline{x}) & cos(y,\overline{x}) & cos(z,\overline{x}) \\ cos(x,\overline{y}) & cos(y,\overline{x}) & cos(z,\overline{x}) \\ cos(x,\overline{z}) & cos(y,\overline{x}) & cos(z,\overline{x}) \end{bmatrix} = \begin{bmatrix} c_{x\overline{x}} & c_{y\overline{x}} & c_{z\overline{x}} \\ c_{x\overline{y}} & c_{y\overline{y}} & c_{z\overline{y}} \\ c_{x\overline{z}} & c_{y\overline{z}} & c_{z\overline{z}} \end{bmatrix} \end{aligned} \tag{3.36}$$

where the components are direction cosines between the two sets of axes. With the elements of $Q_{i,j}$ the transformation matrix can be written as:

$$T = \begin{bmatrix} c^2_{x\overline{x}} & c^2_{y\overline{x}} & c^2_{z\overline{x}} \\ c^2_{x\overline{y}} & c^2_{y\overline{y}} & c^2_{z\overline{y}} \\ c^2_{x\overline{z}} & c^2_{y\overline{z}} & c^2_{z\overline{z}} \\ c_{x\overline{x}}c_{x\overline{y}} & c_{x\overline{y}}c_{x\overline{z}} & c_{x\overline{x}}c_{x\overline{z}} \\ c_{y\overline{x}}c_{y\overline{y}} & c_{y\overline{y}}c_{y\overline{z}} & c_{y\overline{x}}c_{y\overline{z}} \\ c_{z\overline{x}}c_{z\overline{y}} & c_{z\overline{y}}c_{z\overline{z}} & c_{z\overline{x}}c_{z\overline{z}} \end{bmatrix} \tag{3.37}$$

All the remaining ingredients of the plasticity model can be obtained from the standard thermodynamics considerations. Namely, the plastic strain rate tensor and strain-like hardening variable in principal direction, is given in same way as given in (3.24).

Using plastic consistency condition we can obtain plastic multiplier in same way as for computation in local coordinates and then update stress in the principal stress space. Stress tensor in local coordinates can be obtain by using transformation matrix either using spectral decomposition of the principal stresses

$$\boldsymbol{\sigma} = \sum_{i=1}^{3} \overline{\sigma}_i \mathbf{n}_i \otimes \mathbf{n}_i \rightarrow \boldsymbol{\sigma} = \mathbf{T}\overline{\boldsymbol{\sigma}} \tag{3.38}$$

After this computation, we also have to obtain the elastoplastic tangent modulus which consists of a material and of a geometric part

$$\begin{aligned} \boldsymbol{C} &= \frac{\partial \boldsymbol{\sigma}}{\partial \boldsymbol{\epsilon}} \\ &= \underbrace{\sum_{i=1}^{3} \frac{\partial \overline{\sigma}_i}{\partial \boldsymbol{\epsilon}} \mathbf{n}_i \otimes \mathbf{n}_i}_{Cmat} + \underbrace{\sum_{i=1}^{3} \overline{\sigma}_i \frac{\partial}{\partial \boldsymbol{\epsilon}} (\mathbf{n}_i \otimes \mathbf{n}_i)}_{Cgeo} \end{aligned} \tag{3.39}$$

By applying the Gâteaux derivative formalism to the eigenvalue problem in (3.35) we obtain

$$\frac{\partial \overline{\varepsilon}_i}{\partial \boldsymbol{\epsilon}} = \mathbf{n}_i \otimes \mathbf{n}_i \tag{3.40}$$

By exploiting this results we can provide the closed form expression for the material part of elastoplastic tangent modulus in terms of its reduced form in

principal axes D_{ij}^{ep}:

$$\begin{aligned}\boldsymbol{C}_{mat}^{ep} &= \sum_{i=1}^{3} \frac{\partial \overline{\sigma}_i}{\partial \boldsymbol{\epsilon}} \mathbf{n}_i \otimes \mathbf{n}_i \\ &= \sum_{i=1}^{3}\sum_{j=1}^{3} \frac{\partial \overline{\sigma}_i}{\partial \overline{\varepsilon}_j}\frac{\partial \overline{\varepsilon}_j}{\partial \boldsymbol{\epsilon}} \mathbf{n}_i \otimes \mathbf{n}_i \\ &= \sum_{i=1}^{3}\sum_{j=1}^{3} \boldsymbol{D}_{ij}^{ep} [\mathbf{n}_i \otimes \mathbf{n}_i] \otimes [\mathbf{n}_j \otimes \mathbf{n}_j]\end{aligned} \tag{3.41}$$

In particular, for an elastic step the elastoplastic tangent modulus in principal direction is the same as the elasticity tensor D_{ij}, while for a plastic step it is computed as the corresponding modification of elasticity tensor taking into account the final value of stress tensor for plastic step defined in (3.38):

$$\boldsymbol{D}^{ep} = \boldsymbol{D} - \frac{\boldsymbol{D}\frac{\partial \phi_{y,s}}{\partial \boldsymbol{\sigma}} \otimes \boldsymbol{D}\frac{\partial \phi_{p,s}}{\partial \boldsymbol{\sigma}}}{\frac{\partial \phi_{y,s}}{\partial \boldsymbol{\sigma}} \cdot \boldsymbol{D}\frac{\partial \phi_{p,s}}{\partial \boldsymbol{\sigma}} + \frac{\partial \phi_{y,s}}{\partial q} \cdot K\frac{\partial \phi_{y,s}}{\partial q}} \tag{3.42}$$

In order to obtain geometric part of the tangent tensor we use fact that $\mathbf{n}_i \otimes \mathbf{n}_i$ can be obtained in closed form in terms of $\boldsymbol{\epsilon}$ which follows from Serrin's representation theorem. If all ε_i are distinct, then

$$\mathbf{n}_i \otimes \mathbf{n}_i = \frac{\varepsilon_i}{d_i}\left[\boldsymbol{\epsilon} - (i_1 - \varepsilon_i)\mathbf{I} + i_3 \varepsilon_i^{-1} \boldsymbol{\epsilon}^{-1}\right] \tag{3.43}$$

if and only if $d_i \neq 0$ where $i_i; i$=1,2,3 are the principal invariants of deformation tensor and

$$d_i = (\varepsilon_i - \varepsilon_j)(\varepsilon_i - \varepsilon_k) \tag{3.44}$$

With this result in hand and using chain rule we can write the geometric part of tangent modulus as:

$$\begin{aligned}\boldsymbol{C}_{geo} = \ & \frac{\sigma_i}{d_i}\Big[\mathbf{I} - \mathbf{1} \otimes \mathbf{1} - i_3 \varepsilon_i^{-1}(\mathbf{I}_{\boldsymbol{\epsilon}^{-1}} - \boldsymbol{\epsilon}^{-1} \otimes \boldsymbol{\epsilon}^{-1}) + \mathbf{1} \otimes \mathbf{n}_i \\ & + \mathbf{n}_i \otimes \mathbf{1} - i_3 \varepsilon_i^{-2} \times ((\mathbf{n}_i \otimes \mathbf{n}_i) \otimes \boldsymbol{\epsilon}^{-1} + \boldsymbol{\epsilon}^{-1} \otimes (\mathbf{n}_i \otimes \mathbf{n}_i) \\ & + 2(i_3 \varepsilon_i^{-3} - 1)(\mathbf{n}_i \otimes \mathbf{n}_i) \otimes (\mathbf{n}_i \otimes \mathbf{n}_i)\Big]\end{aligned} \tag{3.45}$$

where

$$\mathbf{I}_{\boldsymbol{\epsilon}^{-1}}^{ABCD} = \frac{1}{2}(\boldsymbol{\epsilon}^{-1AC}\boldsymbol{\epsilon}^{-1BD} + \boldsymbol{\epsilon}^{-1AD}\boldsymbol{\epsilon}^{-1BC}) \tag{3.46}$$

In the case two or even all three principal deformation are the same, we can obtain similar expression (3.43) by using numerical perturbation of the identical values.

Finally, we can write the tangent tensor in matrix form using transformation matrix

$$\underbrace{\boldsymbol{C}^{ep}}_{6x6} = \underbrace{T}_{6x3} \underbrace{C^{ep}_{mat}}_{3x3} \underbrace{T^T}_{3x6} + \underbrace{C_{geo}}_{6x6} \tag{3.47}$$

3.2.3 Softening plasticity

In this section, we present the theoretical formulation of the strong discontinuity approach for modeling the cracking of concrete. While in compression it can be observed three different deformation stages, linear elastic, nonlinear inelastic and localized stage in tension, elastic stage is followed by unstable softening stage. In order to take into account these two types of dissipative mechanisms we build multi-surface model in order to better reproduce the behavior of massive structures: a bulk dissipation characterized by the development of micro-cracks, which is taken into account by the introduction of Drucker-Prager model and a surface dissipation taking place at the level of the localization zones in terms of the macro-cracks triggered with St. Venant plasticity criterion in strain space defined by three surfaces.

$$\begin{aligned} \phi_1(\boldsymbol{\epsilon}^e) &= \epsilon_1^e - (\epsilon_y - q) \leq 0 \\ \phi_2(\boldsymbol{\epsilon}^e) &= \epsilon_2^e - (\epsilon_y - q) \leq 0 \\ \phi_3(\boldsymbol{\epsilon}^e) &= \epsilon_3^e - (\epsilon_y - q) \leq 0 \end{aligned} \tag{3.48}$$

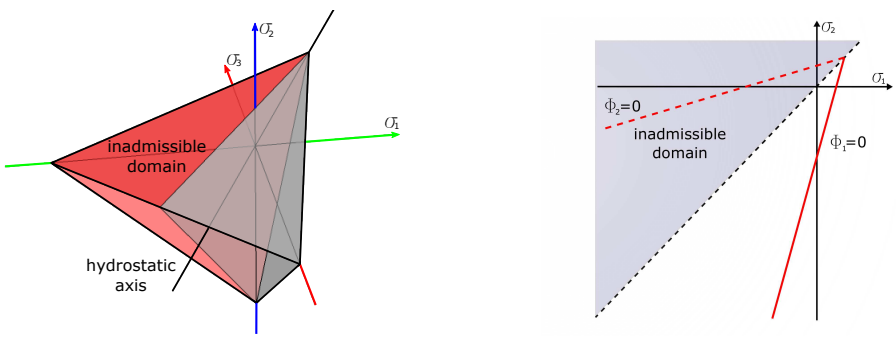

(a) **(b)**

Figure 3.3: Elastic domain in principal stress space (a) 3D case (b) 2D case for $\sigma_3 = 0$

One can also recover the standard format of the limit criterion in the stress space, which is more efficient in numerical implementation,according to:

$$\begin{aligned}
\phi_1(\boldsymbol{\sigma}) &= \frac{3K+G}{9KG}\sigma_1 - \frac{3K-2G}{18KG}(\sigma_2+\sigma_3) - (\sigma_y - q) \leq 0 \\
\phi_2(\boldsymbol{\sigma}) &= \frac{3K+G}{9KG}\sigma_2 - \frac{3K-2G}{18KG}(\sigma_1+\sigma_3) - (\sigma_y - q) \leq 0 \\
\phi_3(\boldsymbol{\sigma}) &= \frac{3K+G}{9KG}\sigma_3 - \frac{3K-2G}{18KG}(\sigma_1+\sigma_2) - (\sigma_y - q) \leq 0
\end{aligned} \tag{3.49}$$

where we have chosen the reference value of the elasticity limit obtained from hydrostatic tension test.

Figure 3.3 present the principal axis representation of this three dimensional criterion. The three surfaces are therefore simply represented by planes in 3D or straight lines in 2D case. We should note that $\Phi_1 \geq \Phi_2 \geq \Phi_3$, so that the second and third surface can never be the only one active, for 2D case the second surface is the one which can never be the only one active (see Figure 3.3b). In pure tension mode, the limit of the elastic domain is,

$$\phi_1(\boldsymbol{\sigma}_2) = \frac{3K+G}{9KG}\sigma_1 - \sigma_y \leq 0 \tag{3.50}$$

and, in pure compression:

$$\phi_1(\boldsymbol{\sigma}_1) = \frac{3K-2G}{18KG}\sigma_2 - \sigma_y \leq 0 \tag{3.51}$$

where we have chosen the reference value of the elasticity limit obtained from hydrostatic tension test.

In order to provide reliable predictive model for concrete taking into account two types of dissipative mechanisms, we combine this multi-surface model in order to represent localized failure. The fracture process zone is still represented with non-associative Drucker-Prager model. Figure 3.1a shows a graphic illustration of the proposed criterion in principal axes of stress tensor. One can note that in tension region elastic stage is followed by softening, while in compression not only the ductile part with fracture process zone is larger, but also its contribution to total dissipation for compression failure. Figure 3.1b clearly reveals that the only special load case which is not limited, is a three-axial compression that can be produced by hydrostatic pressure.

In order to provide the appropriate interpretation of the localized plastic deformation, we consider a domain Ω split into two sub-domains Ω^+ and Ω^- by a surface of discontinuity, denoted as Γ_s, see Figure 3.4 The total displacement field $\mathbf{u}$ is written as the sum of a smooth regular part $\bar{\mathbf{u}}$ and the displacement discontinuity $\bar{\bar{\mathbf{u}}}$, centered at the Γ_s. The surface of discontinuity Γ_s is characterized at each point by a unit vector of exterior normal denoted as $\mathbf{n}$, a tangential vector denoted as $\mathbf{m}$

and binormal vector $\mathbf{b}$. The discontinuous displacement field can then be written as

$$\begin{aligned} \mathbf{u}(\mathbf{x},t) &= \bar{\mathbf{u}}(\mathbf{x},t) + \bar{\bar{\mathbf{u}}}(\mathbf{x},t) M_{\Gamma_s}(\mathbf{x}) \\ M_{\Gamma_s}(\mathbf{x}) &= H_{\Gamma_s}(\mathbf{x}) - N_{\tilde{\Omega}}(\mathbf{x}) \end{aligned} \tag{3.52}$$

where $H_{\Gamma_s}(\mathbf{x})$ is the Heaviside function being equal to 1 in Ω^+ and to 0 in Ω^-, whereas $N_{\tilde{\Omega}}(\mathbf{x})$ is continuous function which can be sketched arbitrary except for satisfying following two conditions:

$$N_{\tilde{\Omega}}(\mathbf{x}) = \begin{cases} 1; & \mathbf{x} \in \Omega^+ \\ 0; & \mathbf{x} \in \Omega^- \end{cases}$$

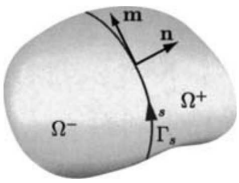

Figure 3.4: Slip line Γ_s separating domain into Ω^+ and Ω^-

By combining the Newton third law which imposes the continuity of traction across displacement discontinuity line Γ_s and the Cauchy principle, we can write:

$$\mathbf{0} = \dot{\mathbf{t}} = \dot{\boldsymbol{\sigma}}\mathbf{n} + \boldsymbol{\sigma} \underbrace{\dot{\mathbf{n}}}_{=0} \tag{3.53}$$

where the second term drops out because it is assumed that the direction of the discontinuity remains fixed in time.

Furthermore, by using last results with assumption that the bifurcation phenomena in an elasto-plastic response can be interpolated as the difference between two smooth stress fields, defining the corresponding jump in the stress rate, we obtain:

$$\begin{aligned} 0 &= \mathbf{C}^{ep}(\mathbf{m} \otimes \mathbf{n}\dot{\alpha})\mathbf{n} \\ &= \mathbf{A}^{ep}\mathbf{m}\dot{\alpha}; \quad \mathbf{A}^{ep} = \mathbf{n}\mathbf{C}^{ep}\mathbf{n} \end{aligned} \tag{3.54}$$

where $\mathbf{A}^{ep}$ is the acoustic tensor. Herein, we assume that the critical mode $\mathbf{m}$ is parallel to a normal vector $\mathbf{n}$ providing mode I as a opening mode in tension.

The corresponding deformation field that is produced by such a displacement field can be written as

$$\begin{aligned} \boldsymbol{\epsilon}(\mathbf{x},t) &= \underbrace{\nabla^s \bar{\mathbf{u}}(\mathbf{x},t) + \bar{G}(\mathbf{x})\bar{\bar{\mathbf{u}}}(t)}_{\bar{\boldsymbol{\epsilon}}} + (\bar{\bar{\mathbf{u}}}(t) \otimes \mathbf{n})^s \delta_\Gamma(\mathbf{x}) \\ \bar{G}(\mathbf{x}) &= -\nabla^s N_{\tilde{\Omega}}(\mathbf{x}) \end{aligned} \tag{3.55}$$

The strain field appears then to be decomposed into a regular part and a singular part, the latter accompanying the Dirac-delta function $\delta_\Gamma(\mathbf{x})$. The strain energy in

this case can be written:

$$\psi(\boldsymbol{\epsilon},\bar{\zeta},\bar{\bar{\zeta}}) := \underbrace{\psi^e(\boldsymbol{\epsilon}^e)+\bar{\Xi}(\bar{\zeta})}_{regular}+\bar{\bar{\Xi}}(\bar{\bar{\zeta}})\delta_{\Gamma_s} \tag{3.56}$$

where the first term is the elastic energy, whereas the second and the third terms are the contributions of hardening and softening mechanisms, respectively.The total plastic dissipation can be expressed as the sum of the dissipation from fracture process zone in $\tilde{\Omega}$ and from the discontinuity on Γ_s, which can be written:

$$\begin{aligned} 0 \leq D^p_{\tilde{\Omega}} &= \int_{\tilde{\Omega}} \left[\boldsymbol{\sigma}\cdot\dot{\boldsymbol{\epsilon}} - \dot{\psi}(\boldsymbol{\epsilon},\bar{\zeta},\bar{\bar{\zeta}})\right] dV \\ &= \int_{\tilde{\Omega}} \left[\boldsymbol{\sigma}\cdot\dot{\bar{\boldsymbol{\epsilon}}} - (\dot{\psi}^e(\boldsymbol{\epsilon}^e)+\dot{\bar{\Xi}}(\bar{\zeta}))\right] dV \\ &+ \int_{\Gamma_s} [\mathbf{t}\cdot\mathbf{m}]\,\dot{\alpha} dA - \int_{\Gamma_s} \dot{\bar{\bar{\Xi}}}(\bar{\bar{\zeta}}) dA \end{aligned} \tag{3.57}$$

From results above we can then obtain the additive decomposition of the total plastic dissipation into a regular and a singular part:

$$D^p_{\tilde{\Omega}} = \int_{\tilde{\Omega}} \left(\boldsymbol{\sigma}\cdot\dot{\bar{\boldsymbol{\epsilon}}}^p + \bar{q}\dot{\bar{\zeta}}\right) dV + \int_{\Gamma_s} \bar{\bar{q}}\dot{\bar{\bar{\zeta}}} dA \tag{3.58}$$

For the last result to be valid we assume that the following stress orthogonality condition must be satisfied:

$$\int_{\tilde{\Omega}} \boldsymbol{\sigma}\cdot\tilde{\mathbf{G}}\mathbf{m}\dot{\alpha} dV + \int_{\Gamma_s} (\mathbf{t}\cdot\mathbf{m})\,\dot{\alpha} dA = 0 \tag{3.59}$$

The yield condition controlling inelastic deformation at discontinuity is set directly in terms of the traction vector component $t_m = \mathbf{t}\cdot\mathbf{m} \quad (\Leftarrow \mathbf{m}=\mathbf{n})$:

$$\bar{\bar{\Phi}}(t_m,\bar{\bar{q}}) = |\underbrace{\mathbf{t}\cdot\mathbf{m}}_{t_m}| - (\sigma_y - \bar{\bar{q}}) \tag{3.60}$$

Here, σ_y is a failure threshold and $\bar{\bar{q}}$ is the internal plasticity variable for evolution of softening. When the softening constitutive law is chosen to be exponential, the internal variable for plasticity can be written as:

$$\bar{\bar{q}} = \sigma_y\left(1 - exp\left(-\bar{\bar{\zeta}}\frac{\sigma_y}{G_f}\right)\right) \tag{3.61}$$

where G_f is the corresponding value of fracture energy. Since the compressive and the tension failure mechanisms are reproduced according to the same fracture mode driven by the principal tensile strains, the corresponding amount of fracture energy can be quite different because of the number of cracks created in those two cases. This is illustrated in Figure 3.5a representing the crack pattern in simple tension and the one in simple compression test, leading to quite different dissipated energy. Here, we indicate that the fracture energy is supposed to change continuously from

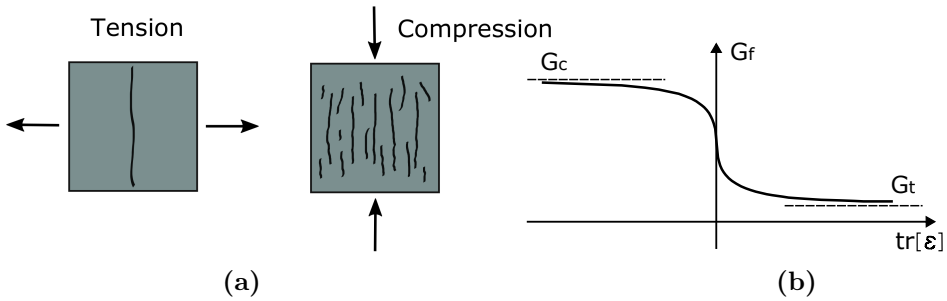

Figure 3.5: (a) Failure modes in both compression and tension (b) Influence of strain state on fracture energy

a specified value in tension G_t to compression G_c (Figure 3.5b) according to:

$$G_f = \frac{G_c + G_t}{2} - \frac{G_c - G_t}{2}\tanh(\beta \mathrm{tr}[\epsilon]) \tag{3.62}$$

where β is a parameter to be chosen to set a more or less rapid transition.

Assuming further that the plastic multiplier takes the form $\dot{\gamma} = \dot{\bar{\gamma}} + \dot{\bar{\bar{\gamma}}}\delta_{\Gamma_s}$, we can make use of the principle of maximum plastic dissipation with

$$\begin{aligned} \bar{\bar{L}}^p(\boldsymbol{\sigma}, \bar{q}, \dot{\bar{\bar{\gamma}}}) &= \max_{\dot{\bar{\bar{\gamma}}} \geq 0} \min_{\forall (t^*, \bar{\bar{q}}^*)} \left[\bar{\bar{L}}^p(\boldsymbol{\sigma}^*, \bar{q}^*, \dot{\bar{\bar{\gamma}}}^*) \right] \\ &= -D^{loc}_{\Omega}(\cdot) + \int_{\Omega} \dot{\bar{\gamma}} \bar{\Phi} dV + \int_{\Gamma_s} \dot{\bar{\bar{\gamma}}} \bar{\bar{\Phi}} dA \end{aligned} \tag{3.63}$$

The Kuhn-Tucker optimality condition will provide the corresponding evolution equation for internal variables:

$$\begin{aligned} 0 &= \int_{\Omega} \left(-\dot{\bar{\boldsymbol{\epsilon}}}^p + \dot{\bar{\gamma}} \frac{\partial \bar{\phi}}{\partial \boldsymbol{\sigma}} \right) dV; \\ 0 &= \int_{\Omega} \left(-\dot{\bar{\zeta}}^p + \dot{\bar{\gamma}} \frac{\partial \bar{\phi}}{\partial \bar{q}} \right) dV; \end{aligned} \tag{3.64}$$

accompanied with

$$0 = \int_{\Gamma_s} \left(-\dot{\bar{\bar{\zeta}}} + \dot{\bar{\bar{\gamma}}} \frac{\partial \bar{\bar{\phi}}}{\partial \bar{\bar{q}}} \right) dA \quad \Rightarrow \int_{\Gamma_s} \dot{\bar{\bar{\zeta}}} dA = \int_{\Gamma_s} \dot{\bar{\bar{\gamma}}} dA \tag{3.65}$$

The plastic multiplier can be computed from plastic consistency condition enforcing that $\bar{\bar{\Phi}} = 0$, which results with:

$$\dot{\bar{\bar{\gamma}}} = \frac{1}{\bar{\bar{K}}} \int_{\Omega} \dot{\boldsymbol{\sigma}} \bar{\mathbf{G}} dV \tag{3.66}$$

3.3 Space and time Discrete approximation

In this section we will present the main steps in applying the implicit backward Euler scheme to 3D plasticity model for concrete materials.

3.3.1 Spatial discretization

We first elaborate upon the solution of the initial boundary value problem, posed by the weak form of the equilibrium equations (3.3) and the evolution equations (3.24). We use standard semi-discretization procedure to construct the finite-element-based displacement approximation over a single element Ω^e

$$\mathbf{u}(\mathbf{x},t)\,|_{\Omega^e} = \sum_{a=1}^{n_{en}} \mathbf{N}_a^e(\mathbf{x})\mathbf{u}_a(t) \tag{3.67}$$

where 'n_{en}' is the total number of element nodes, $\mathbf{N}_a^e(\mathbf{x})$ are the finite element shape functions and $\mathbf{u}_a(t)$ are the nodal displacements. Upon replacing this approximation into the weak form of the equilibrium equations in (3.3) we can integrate with respect to the space variables $\mathbf{x}$, thus reducing the current problem to tracing the pseudo-time history of the state variables. In other words, the weak form of equilibrium equations can be written as

$$\begin{aligned} G = \mathop{A}_{e=1}^{n_{el}} \{ &\textstyle\int_{\Omega^e} \mathbf{B}_a^{eT}(\mathbf{x})\boldsymbol{\sigma}(\boldsymbol{\epsilon}(\mathbf{x},t),\boldsymbol{\epsilon}^p(\mathbf{x},t),\zeta(\boldsymbol{\xi},t))\,dV \\ &- \textstyle\int_{\Omega^e} \mathbf{N}_a^e(\mathbf{x})\cdot\mathbf{b}(\mathbf{x},t)\,dV - \int_{\Gamma_\sigma} \mathbf{N}_a^e(\mathbf{x})\cdot\mathbf{t}(\mathbf{x},t)\,dA\} = \mathbf{0} \end{aligned} \tag{3.68}$$

where $\mathop{A}_{e=1}^{n_{el}}$ denotes the standard finite element assembly procedure over the total number of elements n_{el}.

By choosing the Gauss quadrature rule with n_{in} points, with abscissas $\boldsymbol{\xi}_l$ and integration points w_l we can rewrite equilibrium equations as

$$\begin{aligned} G = \mathop{A}_{e=1}^{n_{el}} \{ &\textstyle\sum_{l=1}^{n_{in}} (w_l \mathbf{B}_a^{eT}(\boldsymbol{\xi}_l)\boldsymbol{\sigma}(\boldsymbol{\epsilon}(\boldsymbol{\xi}_l,t),\boldsymbol{\epsilon}^p(\boldsymbol{\xi}_l,t),\zeta(\boldsymbol{\xi}_l,t))\,j(\boldsymbol{\xi}_l) \\ &- w_l \mathbf{N}_a^e(\boldsymbol{\xi}_l)\cdot\mathbf{b}(\boldsymbol{\xi}_l,t)\,j(\boldsymbol{\xi}_l) - \textstyle\sum_{l=1}^{n_{in}} w_l \mathbf{N}_a^e(\boldsymbol{\xi}_l)\cdot\mathbf{t}(\boldsymbol{\xi}_l,t)\,\} = \mathbf{0} \end{aligned} \tag{3.69}$$

The numerical integration introduces a crucial simplification concerning the internal state variable computation, in that their values need to be obtained only at the integration points. The computed values of internal variables, obtained for a particular value of pseudo-time, are then stored at each integration point for subsequent use. The corresponding values of the total strains at a numerical integration point $\boldsymbol{\xi}_l$ can be simply recovered from the chosen displacement approximation as

$$\boldsymbol{\epsilon}(\boldsymbol{\xi}_l,t) = \mathbf{B}_a^e(\boldsymbol{\xi}_l)\mathbf{u}^e(t) \tag{3.70}$$

3.3.2 Integration of internal state variables for plasticity

As the result of using the semi-discretization procedure, the evolution equations (3.18) become the ordinary differential equations in time. Integrating those equations in the time interval of interest, $[0; T]$, we can trace the evolution of the internal state variables. This integration is carried out numerically by using the unconditionally stable backward Euler time integration scheme. The solution is thus obtained for the chosen values of pseudo-time in the incremental sequence: $0 < t_1 < t_2 < ... < t_n < t_n + 1 < ... < T$. Considering that the backward Euler is one-step integration scheme, it only remains to elaborate upon the solution procedure over a typical time increment. To that end, let

$$\boldsymbol{\epsilon}_n = \boldsymbol{\epsilon}(t_n); \quad \boldsymbol{\epsilon}^p_n = \boldsymbol{\epsilon}^p(t_n); \quad \zeta_n = \zeta(t_n); \tag{3.71}$$

be given data at time t_n, and $\Delta t = t_{n+1} - t_n$ the given time increment. The problem is to obtain the corresponding values of the state variables at time t_{n+1},

$$\boldsymbol{\epsilon}_{n+1}; \quad \boldsymbol{\epsilon}^p_{n+1}; \quad \zeta_{n+1}; \tag{3.72}$$

which are admissible in the sense that the yield criterion is satisfied.

Tackling this problem in the spirit of the operator split method, we assume to be given the total strain increment $\Delta\boldsymbol{\epsilon}^{(k)}_{n+1}$ which corresponds to the best iterative guess of the displacement value $\mathbf{u}^{(k)}$, with k being the iteration counter. The first part of the computation reduces to a simple additive update of the total deformation field

$$\boldsymbol{\epsilon}^{(k)}_{n+1} = \boldsymbol{\epsilon}_n + \Delta\boldsymbol{\epsilon}^{(k)}_{n+1} \tag{3.73}$$

The computation of the remaining state variables is carried out by applying the backward Euler method to the evolution equations (3.24) leading to following system:

$$\begin{aligned}
\boldsymbol{\epsilon}^p_{n+1} &= \boldsymbol{\epsilon}^p_n + \gamma_{n+1}(\boldsymbol{\nu}_{n+1} + \alpha_2 \mathbf{1}) \\
\zeta_{n+1} &= \zeta_n + \gamma_{n+1}\sqrt{\frac{2}{3}} \\
\boldsymbol{\sigma}_{n+1} &= \boldsymbol{C}\left(\boldsymbol{\epsilon}_{n+1} - \boldsymbol{\epsilon}^p_{n+1}\right) \\
q_{n+1} &= -K\zeta_{n+1}
\end{aligned} \tag{3.74}$$

In addition, the discrete counterpart of Kuhn-Tucker conditions becomes:

$$\begin{aligned}
\phi_y\left(\boldsymbol{\sigma}_{n+1}, q_{n+1}\right) &\leq 0 \\
\gamma_{i,n+1} &\geq 0 \\
\gamma_{n+1}\phi_y\left(\boldsymbol{\sigma}_{n+1}, q_{n+1}\right) &= 0
\end{aligned} \tag{3.75}$$

However, since the correct value of plastic multiplier $\dot{\gamma}_{n+1} \geq 0$ is not known a priori, we proceed with the elastic trial test. Namely, we start by assuming that the step remains elastic and setting $\dot{\gamma}^{trial}_{n+1} = 0$, which results with the corresponding trial

values of the internal variables

$$\boldsymbol{\epsilon}_{n+1}^{p,trial} = \boldsymbol{\epsilon}_n^p; \quad \zeta_{n+1}^{trial} = \zeta_n; \tag{3.76}$$

We can thus readily compute the trial values of stress

$$\begin{aligned} \boldsymbol{\sigma}_{n+1}^{trial} &= \boldsymbol{C}(\boldsymbol{\epsilon}_{n+1} - \boldsymbol{\epsilon}_n^p); \\ \bar{q}_{n+1}^{trial} &= \bar{q}_n = -K\zeta_n; \\ \phi_{y,n+1}^{trial} &= \phi_y\left(\boldsymbol{\sigma}_{n+1}^{trial}, q_{n+1}^{trial}\right) \end{aligned} \tag{3.77}$$

If the trial value of yield functions is indeed not positive, the trial state is accepted for final, and the internal variables will not change their values with respect to the previous step.

$$\begin{aligned} 0 \geq \phi_{y,n+1}^{trial}(\boldsymbol{\sigma}_{n+1}^{trial}, q_{n+1}^{trial}) &:= \| \, dev[\boldsymbol{\sigma}_{n+1}^{trial}] \, \| \\ &+ \frac{1}{3} tan(\alpha) tr[\boldsymbol{\sigma}_{n+1}^{trial}] - \sqrt{\frac{2}{3}}(\sigma_y - q_{n+1}^{trial}) \\ \boldsymbol{\epsilon}_{n+1}^p = \boldsymbol{\epsilon}_n^p; &\quad \zeta_{n+1} = \zeta_n \end{aligned} \tag{3.78}$$

In the opposite case producing a positive trial value of yield function $\phi_{n+1}^{trial} > 0$, we know that the step is plastic in fact. Thus we have to find the true (positive) value of plastic multiplier $\gamma_{n+1} > 0$, which will reestablish the plastic admissibility of stress with $\phi_{n+1} = 0$. The corresponding value of the plastic multiplier is obtained from the consistency condition taking into account non-associative flow rule to obtain:

$$\gamma_{n+1} = \frac{\phi_{y,n+1}^{trial}}{2G + 9K\alpha_1\alpha_2 + \frac{2}{3}K_{h,lin}} \tag{3.79}$$

This value of plastic multiplier will also provide the corresponding new values of plastic deformation, hardening variable and the corresponding stress:

$$\boldsymbol{\sigma}_{n+1} = \boldsymbol{\sigma}_{n+1}^{trial} - \gamma_{n+1}\boldsymbol{C}(\boldsymbol{\nu}_{n+1} + \alpha_2\mathbf{1}) \tag{3.80}$$

After the convergence of this computation, we also have to obtain the consistent elastoplastic tangent modulus, which can be written:

$$\begin{aligned} \boldsymbol{C}^{ep} = \boldsymbol{C} &- \frac{(2G\boldsymbol{\nu}_{n+1} + 3K\alpha_1\mathbf{1}) \otimes (2G\boldsymbol{\nu}_{n+1} + 3K\alpha_2\mathbf{1})}{2G + 9K\alpha_1\alpha_2 + \frac{2}{3}K_{h,iso}} \\ &- \frac{4G^2}{\| \, dev[\boldsymbol{\sigma}_{n+1}^{trial}] \, \|}\left[\mathcal{I} - \boldsymbol{\nu}_{n+1} \otimes \boldsymbol{\nu}_{n+1} - \frac{1}{3}\mathbf{I} \otimes \mathbf{I}\right] \end{aligned} \tag{3.81}$$

We note in passing that the consistent elastoplastic tangent modulus given above is different from the corresponding one valid for the continuum problem in (3.34). The difference between the consistent and continuum tangent moduli concerns the third term in (3.81) above, which is due to the change of normal to the yield surface

over a time step. Equivalent computations are carried out in strain softening phase, which is started once the localization condition in (3.54) happens to be verified for one of the quadrature points. One can thus obtain that:

$$\begin{aligned} &\bar{\bar{\Phi}}(\bar{\bar{\gamma}}_{n+1}) = 0; \quad t_{m,n+1} = t_y - \bar{\bar{q}}(\bar{\bar{\zeta}}_{n+1}) \\ &\bar{\bar{K}} = -\frac{d\bar{\bar{q}}}{d\bar{\bar{\zeta}}_{n+1}} \end{aligned} \tag{3.82}$$

The finite element interpolation is chosen to take into account a displacement discontinuity, by considering the incompatible mode methods. More precisely, we choose the finite element interpolation according to:

$$\mathbf{u}^h(\mathbf{x},t) = \mathbf{N}(\mathbf{x})\mathbf{u}_a + \boldsymbol{\alpha}(t)\mathbf{M}(\mathbf{x}) \tag{3.83}$$

where $\mathbf{N}(\mathbf{x})$ is the classical shape function associated to the considered brick element, $\mathbf{u}_a$ denotes the nodal displacement and $\mathbf{M}(\mathbf{x})$ is a discontinuous interpolation function. The discontinuity can be introduced by splitting the 8-node brick in such a way that a pair of nodes is placed at each side of the discontinuity. If Ω^+ denotes the part of the element on one side of the opening surface, we can thus write:

$$\mathbf{M}(\mathbf{x}) = H_{\Gamma_s}(\mathbf{x}) - \sum_{b\in\Omega^+} \mathbf{N}_b(\mathbf{x}) \tag{3.84}$$

With such an approximation, the finite element interpolation of the strain field can be written as:

$$\boldsymbol{\epsilon}^h(\mathbf{x},t) = \mathbf{B}(\mathbf{x})\mathbf{u}_a + \boldsymbol{\alpha}(t)\mathbf{G}_r(\mathbf{x}) \tag{3.85}$$

where $\mathbf{G}_r(\mathbf{x}) = \mathbf{L}\mathbf{M}(\mathbf{x})$ with $\mathbf{L}$ the matrix associated to the operator ∇^s. The finite element interpolation of the virtual strain field can be constructed with the same scheme as

$$\delta\boldsymbol{\epsilon}^h(\mathbf{x},t) = \mathbf{B}(\mathbf{x})\delta\mathbf{u}_a + \delta\boldsymbol{\alpha}(t)\mathbf{G}_v(\mathbf{x}) \tag{3.86}$$

where $\delta\mathbf{u}_a$ and $\delta\boldsymbol{\alpha}(t)$ denote, respectively, the virtual displacement field and virtual displacement jump field. $\mathbf{G}_v(\mathbf{x})$ is a modified incompatible mode function constructed from the function $\mathbf{G}_r(\mathbf{x})$ so as to guarantee the satisfaction of the patch-test. We note that in general $\mathbf{G}_v(\mathbf{x})$ is different from the function $\mathbf{G}_r(\mathbf{x})$. It has to be noted that, as $\mathbf{M}(\mathbf{x})$ is a discontinuous function, the functions $\mathbf{G}_r(\mathbf{x})$ and $\mathbf{G}_v(\mathbf{x})$ can be decomposed into a regular and a singular part as

$$\begin{aligned} \mathbf{G}_r(\mathbf{x}) &= \bar{\mathbf{G}}_r(\mathbf{x}) + \bar{\bar{\mathbf{G}}}_r(\mathbf{x})\delta_{\Gamma_s} \\ \mathbf{G}_v(\mathbf{x}) &= \bar{\mathbf{G}}_v(\mathbf{x}) + \bar{\bar{\mathbf{G}}}_v(\mathbf{x})\delta_{\Gamma_s} \end{aligned} \tag{3.87}$$

With those interpolations for real and virtual strain fields using the incompatible mode, the discretized problem can be written as

$$\begin{aligned} &A_{e=1}^{n_{el}}\left(\mathbf{f}^{int,(e)}-\mathbf{f}^{ext}\right)=0; \quad \mathbf{f}^{int,(e)}=\int_{\Omega^e}\mathbf{B}^T\cdot\boldsymbol{\sigma}_{n+1}dV \\ &\mathbf{h}_{n+1}^{(e)}=\int_{\Omega^e}\bar{\mathbf{G}}_v^T(\mathbf{x})\cdot\boldsymbol{\sigma}_{n+1}dV+\int_{\Gamma_s}t_{m,n+1}dA; \ \ \forall e\in[1,n_{el}] \end{aligned} \tag{3.88}$$

The weak form of equilibrium is written as a system of two equations. The first one is the set of global equilibrium equations, which is classically written in the finite element method. The second one is a local equilibrium equation written in each localized element. Independently this equation can be interpreted as the weak form of the traction continuity condition along the surface of discontinuity. The consistent linearization of system (3.88) leads to the set of equilibrium equations, which can be written for time step $n+1$ and iteration (i):

$$\begin{aligned} &A_{e=1}^{n_{el}}\left[\mathbf{K}_{n+1}^{e,(i)}\Delta\mathbf{u}_{n+1}^{(i)}+\mathbf{F}_{n+1}^{e,(i)}\Delta\boldsymbol{\alpha}_{n+1}^{(i)}\right]=A_{e=1}^{n_{el}}\left[\mathbf{f}_{n+1}^{ext,e}-\mathbf{f}_{n+1}^{int,e,(i)}\right] \\ &\mathbf{h}_{n+1}^{e,(i)}+\left(\mathbf{F}_{v,n+1}^{e,(i)}+\mathbf{K}_{d,n+1}^{(i)}\right)\Delta\mathbf{u}_{n+1}^{(i)}+ \\ &\qquad\left(\mathbf{H}_{n+1}^{e,(i)}+\mathbf{K}_{\alpha,n+1}^{(i)}\right)\Delta\boldsymbol{\alpha}_{n+1}^{(i)}=0 \end{aligned} \tag{3.89}$$

where:

$$\begin{aligned} &\mathbf{K}_{n+1}^{e,(i)}=\textstyle\int_{\Omega^e}\mathbf{B}^T\mathbf{C}_{n+1}^{ep,(i)}\mathbf{B}dV, \ \ \mathbf{F}_{n+1}^{e,(i)}=\int_{\Omega^e}\mathbf{B}^T\mathbf{C}_{n+1}^{ep,(i)}\bar{\mathbf{G}}\mathbf{m}dV \\ &\mathbf{F}_{v,n+1}^{e,(i)}=\textstyle\int_{\Omega^e}\mathbf{m}^T\bar{\mathbf{G}}^T\mathbf{C}_{n+1}^{ep,(i)}\mathbf{B}dV, \\ &\mathbf{H}_{n+1}^{e,(i)}=\textstyle\int_{\Omega^e}\mathbf{m}^T\bar{\mathbf{G}}^T\mathbf{C}_{n+1}^{ep,(i)}\bar{\mathbf{G}}\mathbf{m}^TdV \\ &\mathbf{K}_{d,n+1}^{e,(i)}=A_{\Gamma_s^e}\tfrac{\partial t_m}{\partial u}|_{n+1}^{(i)}, \ \ \mathbf{K}_{\alpha,n+1}^{e,(i)}=A_{\Gamma_s^e}\tfrac{\partial t_m}{\partial \alpha}|_{n+1}^{(i)} \end{aligned} \tag{3.90}$$

At that stage there are a couple of possibilities to solve the above set of equilibrium equations. The first possibility consists in solving simultaneously at global level the two equations. The second possibility, which is chosen herein, consists in taking advantage of the fact that the second equation is written locally in each localized element. Then, this second equation is solved at the element level for a given value of the displacement field increment $\Delta\mathbf{u}_{n+1}^{(i)}$. This allows determining the value of the displacement jump increment $\Delta\boldsymbol{\alpha}_{n+1}^{(i)}$. Then by static condensation at the element level, the system of equations in (90) is reduced to a single equation which takes the classical form in the finite element method as:

$$\begin{aligned} &A_{e=1}^{n_{el}}\widehat{\mathbf{K}}_{n+1}^{e}\Delta\mathbf{u}_{n+1}^{(i)}=A_{e=1}^{n_{el}}\left[\mathbf{f}_{n+1}^{ext,e}-\mathbf{f}_{n+1}^{int,e,(i)}\right] \quad \text{with} \\ &\widehat{\mathbf{K}}_{n+1}^{e,(i)}=\mathbf{K}_{n+1}^{e,(i)}-\mathbf{F}_{n+1}^{e,(i),T}(\mathbf{H}_{n+1}^{e,(i)}+K_{\alpha,n+1}^{(i)})^{-1}(\mathbf{F}_{v,n+1}^{e,(i)}+K_{d,n+1}^{(i)}) \end{aligned} \tag{3.91}$$

3.4 Numerical examples

In this section we present the numerical simulations and computed macroscopic responses for a number of different concrete specimens and various loading conditions illustrating the ability of the proposed procedure to describe the behavior till complete failure. The computations are performed by a research version of computer program FEAP, developed by R.L. Taylor at UC Berkeley [85]

3.4.1 Uniaxial tension test

We consider here the specimen given as a cube with 15 cm side length. The material parameters adopted are shown in Table 3.1. These computations (and subsequent ones) are made under the displacement control with unrestrained lateral displacements for tension test.

In order to avoid the ambiguity of the failure pattern under homogeneous stress field in the solid elements, the slight imperfection is introduced into only one element. This allows to avoid the academic case when the uniform load is applied to a series of homogeneous solid elements resulting in localized failure in different elements at the same time, or only decided by numerical round-off errors [24].

Figure 3.6a shows macroscopic stress (sum of all reactions in vertical direction divided by cross-section area of the concrete cube) with respect to strain. Limit stress which triggers the global softening obtained with proposed model is lower then the limit stress obtained with Rankine criterion with the same parameters. Namely, the limit stress for proposed model is chosen to correspond to elasticity limit in hydrostatic tension test. Thus, for uniaxial and biaxial loading we can note from (3.49) that this limit is lower compared to the limit stress obtained with Rankine type of failure (Figure 3.2). We can note from Figure 3.6b that the model gives the mesh independent results when the imperfection is added to one of the solid finite elements and the exponential softening drives the solid to complete failure.

Moreover, we can see from Figure 3.7 that all displacements plotted at the end of computation are localized in zone where we placed element with slight imperfection and where final failure surface is formed.

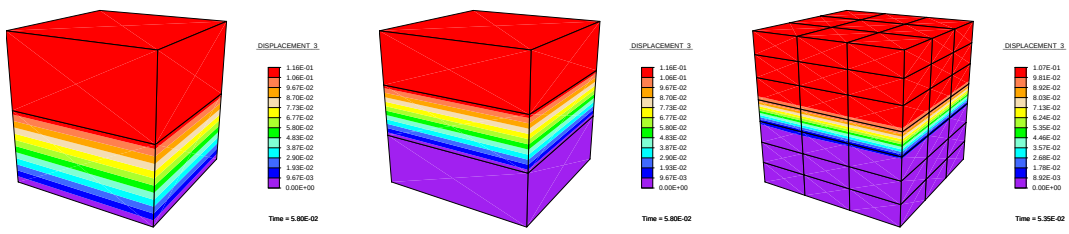

(a) **(b)** **(c)**

Figure 3.7: Vertical displacement at the end of uniaxial tension test for three different mesh versions: (a) 2 elements; (b) 3 elements; (c) 63 elements

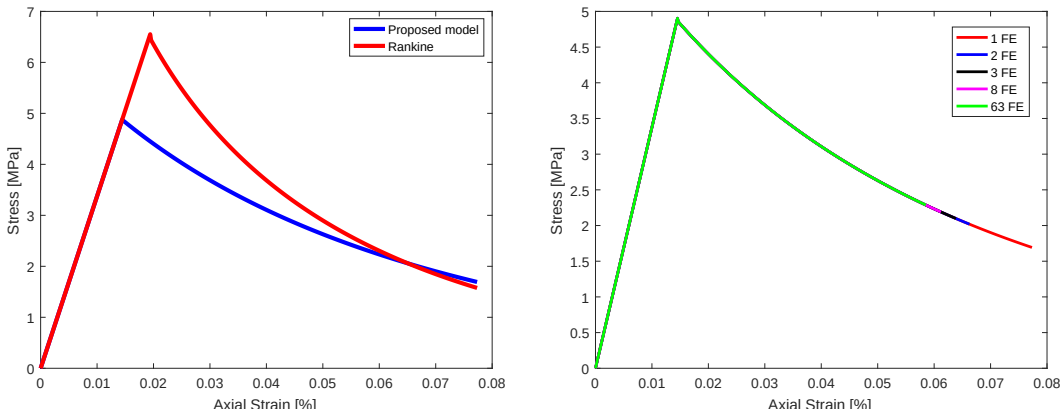

(a) (b)

Figure 3.6: Macroscopic response for uniaxial tension test

K	15 GPa
G	15 GPa
σ_u	6.5 MPa
$G_{f,t}$	0.5 N/mm

Table 3.1: Material parameters

3.4.2 Notched bar in tension

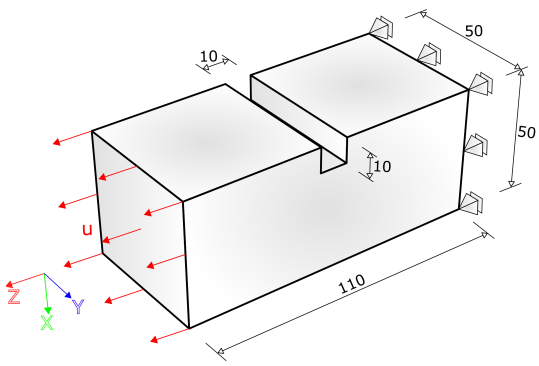

Figure 3.8: Notched specimen: geometry, boundary conditions and loading

In this example we construct specimen with a notch as presented in Figure 3.8. The specimen dimensions are given in millimeters. The proposed values of material properties are: K=17.0 GPa, G=15.0 GPa, σ_u=6.5 MPa and $G_{f,t}$=0.14 N/mm.

A double-notched specimen is constructed by placing notch on two side of specimen, at the one-third and at two-thirds of the specimen length.

Figure 3.9 shows localization of displacement in loading direction. It can be noted that for single notched specimen all displacement at the end of computation are localized where we placed notch, while for double-notched specimen this zone connect two notches.

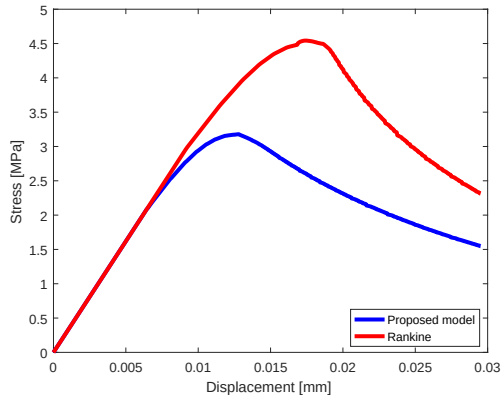

Figure 3.11: Macroscopic response for notched specimen in tension

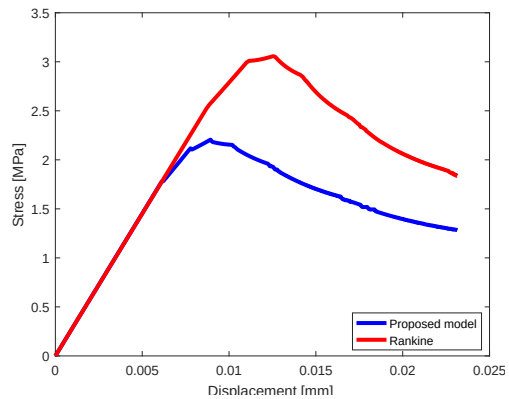

Figure 3.12: Macroscopic response for double-notched specimen in tension

Figure 3.10 reveals that at the and of computation single notch specimen is split in two parts with flat failure surface while for double-notched specimen failure surfaces split specimen in two L-shaped parts.

Macroscopic response (stress vs. imposed displacement) is presented in Figure 3.11 and 3.12 for both specimen and compared to response obtained with Rankine type of failure. Again, due to definition of elasticity limit stress in proposed model we can observe different limit stress for these two kinds of computed response.

3.4.3 Three point notched beam

We consider a simply supported concrete beam (Figure 3.13) of length l = 2000 mm, height h = 200 mm and thickness t = 50 mm. At its half-length it has a notch of dimensions a = 10 mm and b = 100 1m. The beam is loaded at the middle of the span, on the upper edge, with imposed vertical displacement. The material properties are chosen as in [116]: elastic modulus E = 30 GPa, Poisson ratio ν = 0.2, ultimate strength σ_u = 4.5 MPa and fracture energy $G_{f,t}$=0.120 N/mm. Figure 3.13 shows the used finite element mesh with geometry, boundary conditions and loading. Computation is performed under displacement control.

In Figure 3.14 is presented dependence of the reaction force on the imposed displacement for coarse and fine mesh, with 20 (mesh 1) and 40 (mesh 2) finite

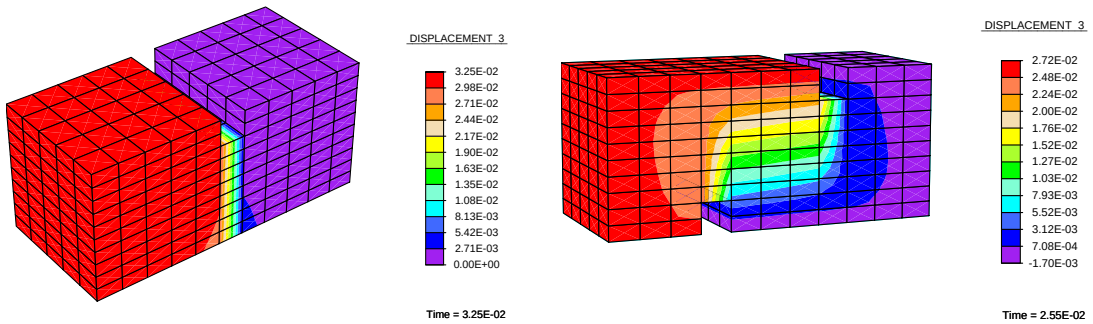

(a) **(b)**

Figure 3.9: Displacement in loading direction at the end of numerical simulation:(a) Notched specimen ; (b) Double-notched specimen

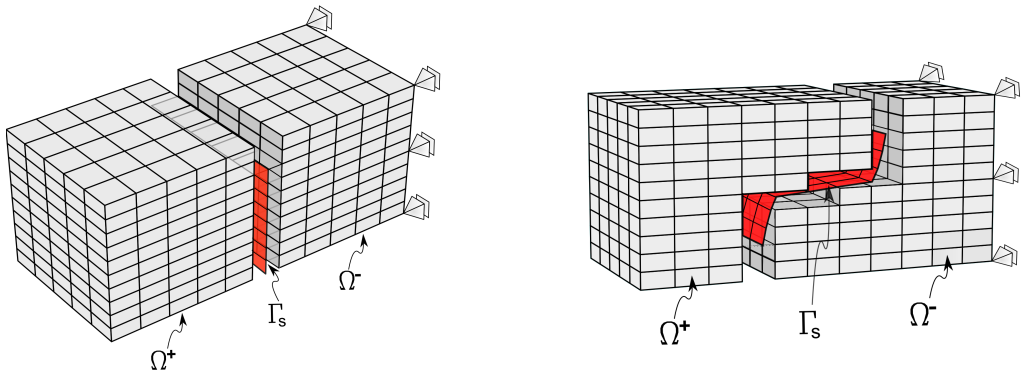

(a) **(b)**

Figure 3.10: Mesh without fractured elements with discontinuity surface Γ_s; (a) Notched specimen ; (b) Double-notched specimen

element along the height of the beam. We can note that for small number of element in the region where the crack is expected to occur and propagate force-displacement curves exhibit jumps. At jump, the crack propagated through the element much faster for coarse mesh than to the response with refined mesh. Moreover, we can note nice matching of the computed results with the range of experimental data presented in [117]. Upper and lower curve from experiment corresponds to $G_{f,t}$=0.137 N/mm and $G_{f,t}$=0.115 N/mm , respectively. The crack propagates along the mesh only in mode I (crack opening mode). This is also evident from Figure 3.15 where final deformed configuration of the mesh is presented.

3.4.4 Shear test

The shear-box test is widely used test to determine the shear strength of soils, rock and similar materials. This test has fallen from favor as an instrument of fundamental research because it tends to give non-uniform stresses in the rupture zone [118]. In order to obtain uniform stresses, a so-called simple-shear apparatus was developed

[119] in such way (Figure 3.16b) that all normal strains can be kept equal to zero, so that we have a so-called isochoric test (with no volume changes). These tests are used for soils and also in some previous research projects for concrete [118]. Thus, we consider such test for sand in order to verify proposed model, but it can be also used for concrete-like materials. The material properties are: E= 45 MPa, ν=0.2, Φ=43° and σ_y=$K_{h,lin}$=β=0, . For the initial stress state in the specimen, we assume σ_{yy} = - 100 kPa, σ_{xx}= σ_{zz} = - 25 kPa and σ_{xy} = 0. During the test all strain rates vanish, with the exception of the shear-strain rate $\dot{\gamma}_{xy}$. Test is performed on cube specimen with 15 cm side length under displacement control.

In Figure 3.16a is presented dependency of shear stress on shear strain which fits well with results given in [120]. The upper curve is obtained for a dilatancy angle of 15°. Despite the use of a non-hardening model, this curve shows hardening. Indeed, the slope of the curve gradually decreases to reach a constant, but positive value. So elastic-perfectly plastic models do not necessarily involve limit loads. When using a negative dilatancy angle, we find the lower curve presented in Figure 3.16a. This stress-strain curve gradually approaches a line with a negative slope. In other words, hardening is followed by softening and during this unstable behavior the shear resistance vanishes completely. Thus, even if the model is based on perfect plasticity we find softening behavior which is due to non-associated plasticity.

In order to arrive at a better understanding of this phenomenon, it is helpful to consider the stress path for the isochoric shear test in principal stress space. The stress path begins at the point A with coordinates A$_{\sigma_1}$ = - 100 kPa and A$_{\sigma_2}$= A$_{\sigma_3}$ = - 25 kPa. Then the stresses are more or less controlled by the elastic volume change. In the beginning of the test the strains are entirely elastic, so that the condition of zero volume strain implies that sum of stress rate is also equal to zero. This give a elastic path until we reach the yield surface. From this point on plastic strains develop, including plastic volume change when Ψ is non-zero. Then an elastic volume change is needed to compensate for the plastic volume change. For a negative dilatancy angle, plastic contraction must be balanced by elastic expansion, or $\dot{\epsilon}_v^e$=-$\dot{\epsilon}_v^p$. The elastic expansion gives rise to tensile stress increments, so that the existing compressive stresses will vanish. Then we can note that the plastic strain-rate vector forms an obtuse angle with the stress rate vector. As a consequence the inner product is negative ($\dot{\boldsymbol{\sigma}}^T\dot{\boldsymbol{\epsilon}}^p < 0$), which is the Drucker definition of unstable material behavior. The negativeness of the above inner product is a necessary but not a sufficient condition for softening behavior. For softening we need to consider the inner product of the stress rate and the total strain rate rather than the plastic strain rate. The total strain rate is always parallel to the line of elastic path, making an obtuse angle to the stress-rate vector. Finally it is noted that softening is not only possible for $\Psi < 0$ but more generally for $\Psi < \Phi$.

3.4.5 Compression test

The results of numerical simulations and corresponding macroscopic response for specimen under uniaxial (unconfined) compression loading program are given here. Simulations in compression test are conducted with displacement control, while

K	15 GPa
G	15 GPa
σ_y	10.0 MPa
β	7500.0
σ_∞	36.7 MPa
$K_{h,lin}$	10.0 MPa
σ_u	6.5 MPa
$G_{f,c}$	20.0 N/mm
$tan(\Phi)$	0.3
$tan(\Psi)$	0.3

Table 3.2: Material parameters for uniaxial compression test

lateral displacements are unrestrained which corresponds to the case with no friction between the load platen and the specimen. Geometry of specimen is the same as for specimen used for uniaxial tension test. Table 3.2 summarizes the chosen mechanical properties of specimen where σ_y is yield stress defined for a simple tension test, β is the hardening parameter that governs the rate with which the saturation is achieved, σ_∞ is limit stress until the stress increase,$K_{h,lin}$ is hardening modulus, σ_u is ultimate stress which triggers the softening, $G_{f,c}$ is fracture energy in compression, while $tan(\Phi)$ and $tan(\Psi)$ are internal friction angle and dilatancy angle defined in meridian plane.

Figure 3.17a shows macroscopic stress (sum of all reactions in vertical direction divided by cross-section area of concrete cube) versus strain curves for saturation type of hardening (black line) and linear isotropic hardening (red line). The macroscopic limit stress which triggers the softening changes due to the type of hardening while limit strains remains the same. This is in accordance with the concrete material model, which is defined in terms of limit strains. Also, we can find that for non-associative hardening limit stress is not changed but only the total dissipation energy in small amount.

The difference with respect to uniaxial tension test mechanism concerns the ductile phase of the response during creation of the fracture process zone, which

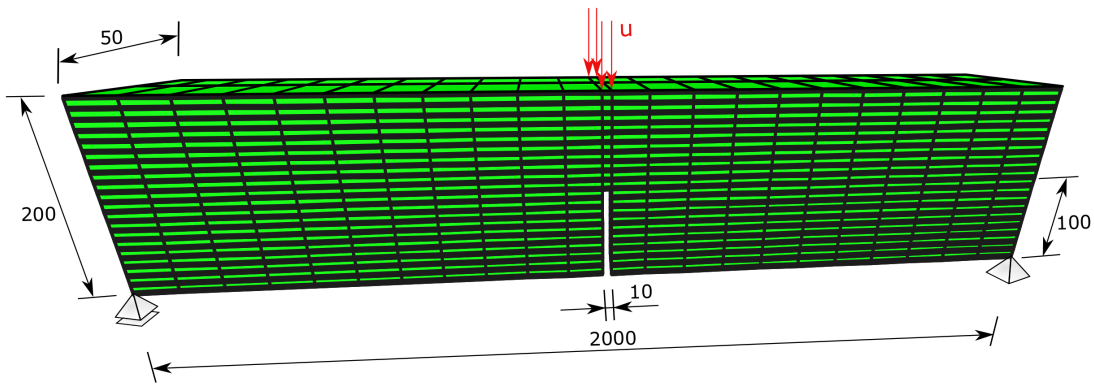

Figure 3.13: Three point notched beam: geometry, boundary conditions and loading

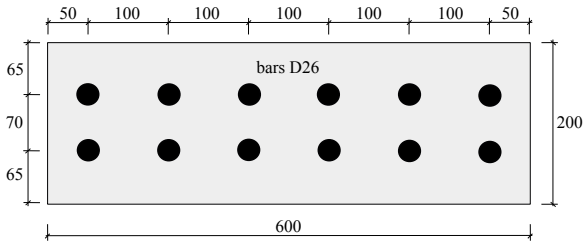

Figure 3.19: Bending test cross-section

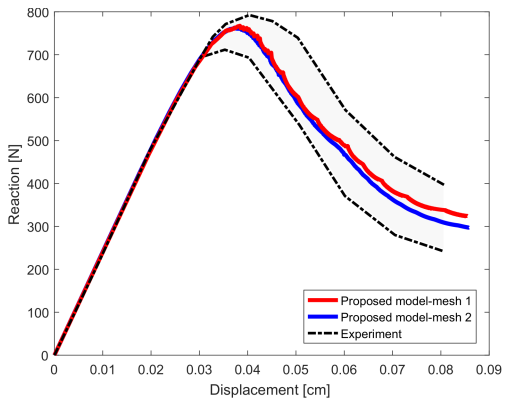

Figure 3.14: Load-displacement diagram for three point notched beam and comparison with the experimental results

is more pronounced in compression test than in tension test. Thus, not only the ductile part with fracture process zone is larger, but also its contribution to the total dissipation in compression failure.

In order to compare the macroscopic responses corresponding to uniaxial tension and compression, Figure 3.17b presents macroscopic curves and reveals that the overall compression-tension ratio is equal to 8.5 which fits well to typical observation made for a concrete [92, 121].

3.4.6 Bending test on a reinforced concrete beam

We consider here a beam of length L = 8.89 m, with a rectangular cross-section: width 60 cm and height 20 cm. Six reinforcement longitudinal bars of diameter 26 mm are placed at the top side, and six with the same diameter at the bottom side of the cross-section (see Figures 3.18 and 3.19 for details on the geometry). This test was proposed as a benchmark for different failure modes of reinforced concrete by ETH Institute for Concrete Structures [122], who also provided a detailed description of the chosen test specimens.

Three loading condition are considered. In each case, the beam is subjected to three loads Q applied vertically in the span between the two supports and a load P applied at the free end. The first test, marked as T_0, is performed without axial load T, while in test T_1 and T_2 axial load T is limited to 1911 kN and 956 kN, respectively. All tests follow the same procedure: First, the axial load T is increased linearly up

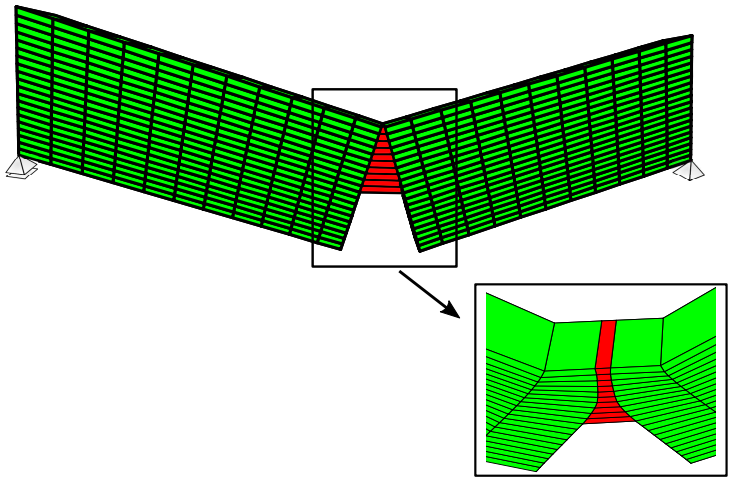

Figure 3.15: Three point notched beam: deformed mesh

K	15.482 GPa
G	12.998 GPa
σ_y	10.0 MPa
β	7000.0
σ_∞	36.7 MPa
σ_u	6.1 MPa
$G_{f,c}$	21.5 N/mm
$G_{f,t}$	0.5 N/mm
$tan(\Phi)$	0.32
$tan(\Psi)$	0.21

Table 3.3: Material parameters for bending test

to the chosen value and held constant. Second, the transverse loads Q and P are increased linearly with $P = 8.58$ kN $+1.44Q$ for test T_0, $P = 15.84$ kN $+1.90Q$ for test T_1, $P = 12.21$ kN $+1.68Q$ for test T_2.

The material properties of concrete, as summarized in Table 3.3,, are determined by inverse procedure in order to obtain matching of stress-strain diagram for compression test (Figure 3.20) with average experimental results performed on a cube and cylinder specimen [122]. For the steel bar we use truss element with Von Mises plasticity model.

Material properties for bars are: Young's modulus of elasticity, E_s= 215 GPa, Yield strength, f_{sy}= 498 MPa, Hardening modulus K_{sh} = 20 GPa. Interface between concrete and steel is represented with perfect bond providing that the dilatations in adjacent steel and concrete remain the same in each step of computation. The computation is carried out using the arc-length method (e.g. [73]). The mesh grading in the horizontal direction is chosen to comply with solid/truss elements of length 0.2 m. In the vertical direction, the finite element mesh along cross-section is built up in order to ensure position of longitudinal steel bars. This results with the mesh with 112 and 224 FE along cross-section (Figure 3.22).

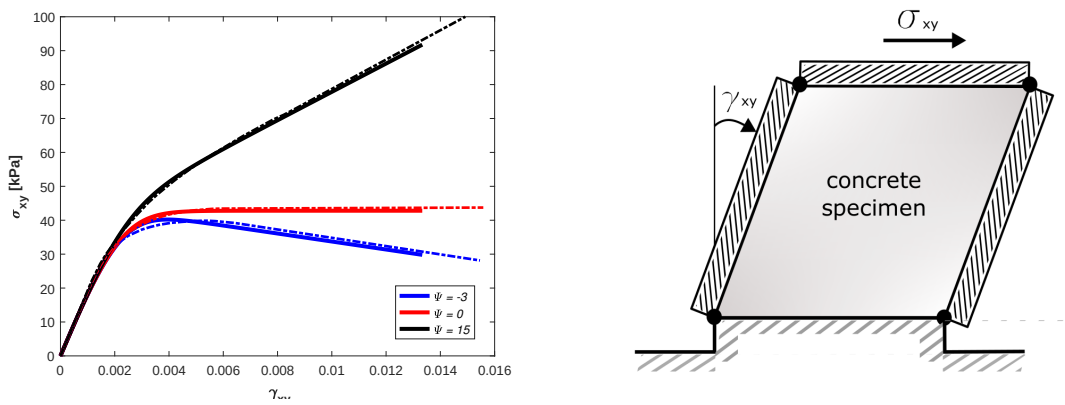

(a) (b)

Figure 3.16: Isochoric shear test: (a) Computed responses (solid line) and results taken from [120] (dash line); (b) boundary conditions and loading

Figure 3.21 (upper part) shows the state of specimen at the end of computation, where white color represents elements that remain in elastic phase, green color represents hardening in compression and red color represents element in softening phase. A major part of the concrete cross-section starts softening in tension (the bottom part between the supports and the top part above the right support). Concrete gets into the hardening phase of compression in the top layers at the middle of the span and the bottom ones above the right support. A few steps before the end of the analysis, the compressed layers of concrete above the right support also start softening. Also, the top reinforcement layer above right support starts to yield just before the end of analysis.

Figure 3.21 (middle) shows that crack propagates mostly due to tension stress, while crack above right support propagates due to compression stress.

The results for test T_0, for two adopted FE mesh, in terms of load/deflection are given in Figure 3.23a (Q in terms of deflection at the mid-point of the inner span). We can note that after major part of beam starts softening global resistance decrease.

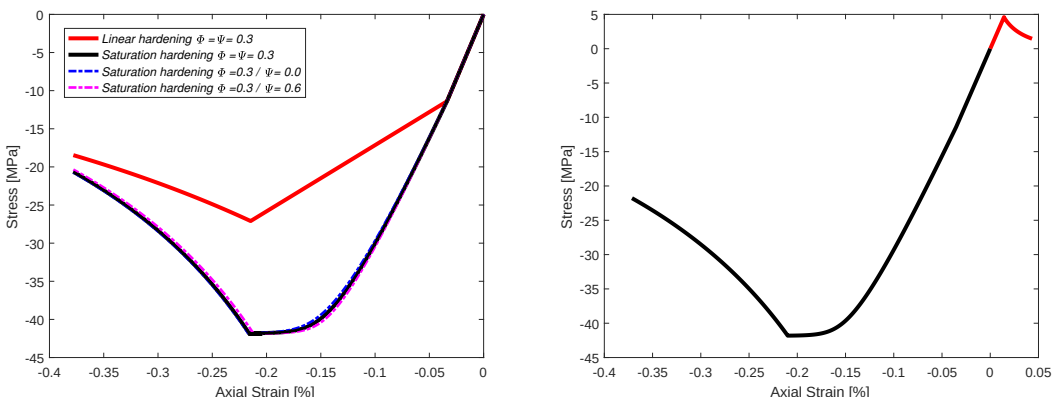

(a) (b)

Figure 3.17: Macroscopic response: (a) uniaxial compression test; (b) complete response

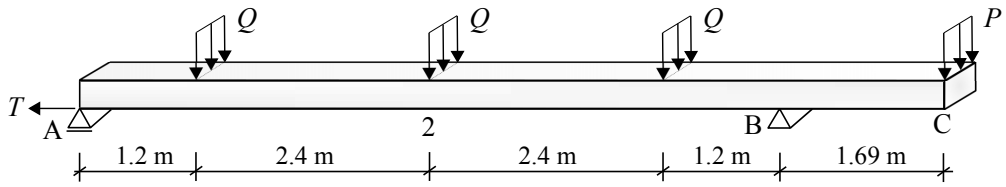

Figure 3.18: Bending test: loading and geometry

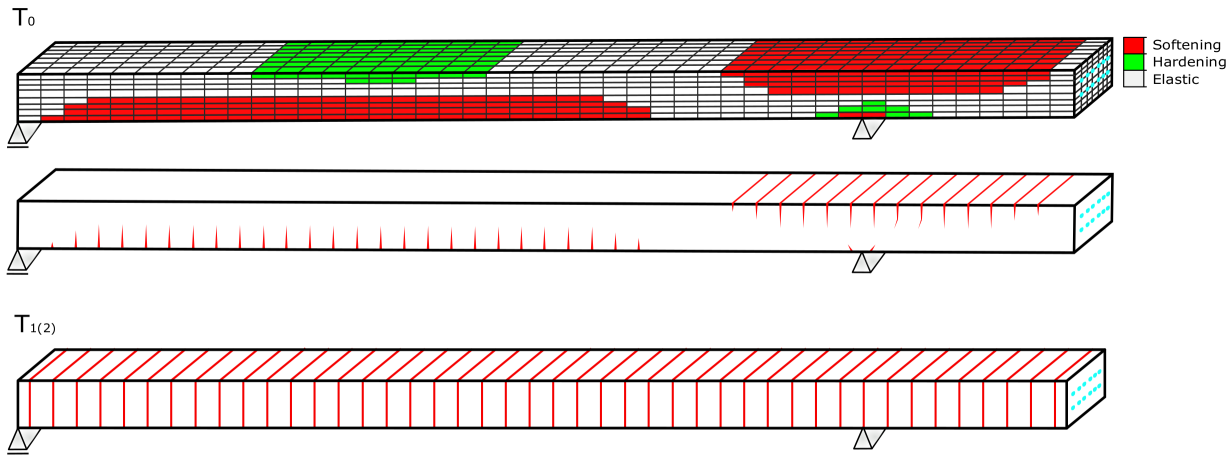

Figure 3.21: Bending test: state of specimen and crack propagation

This computation is limited to predefined load because further load increase can not drive the beam to total failure due to elastoplastic model of steel bar.

For test marked as T_1 and T_2 at the end of first phase, when beam is subjected to axial load, all element reaches elastic limit stress point in tension, thus forming cracks along the beam which are perpendicular to the subjected load (Figure 3.21-lower). Figure 3.23b reveals that during first phase, the global stiffness of the beam is decreased and latter transverse loads is transferred only through the steel bars until they starts yielding.

To validate the prediction of our model, we compared the obtained results with the stress-resultant reinforced-concrete model for Timoshenko beam that can capture the localized failure in shear, see [123]. We have also compared our results against the experimental results (Figure 3.24). The prediction result we obtain in terms of crack pattern for concrete fits well with these experimental results.

3.5 Final comments on the presented 3D concrete macro-scale model

In this chapter we proposed multisurface plasticity model for concrete that takes into account both the contribution of a strain hardening with non-associative flow rule as well as a strain softening model components for full set of different 3D failure modes. The proposed model is capable of representing the localized failure of massive structures, where final failure mechanism is preceded by significant development of

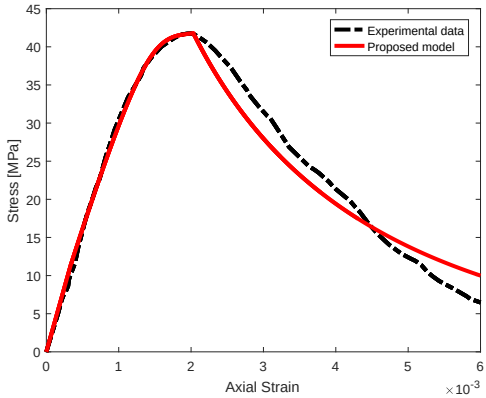

Figure 3.20: Comparison of results: macroscopic stress-strain response

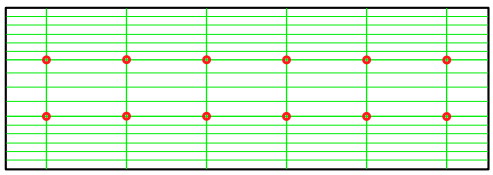

Figure 3.22: Bending test cross-section finite element mesh (red circles represent position of truss element)

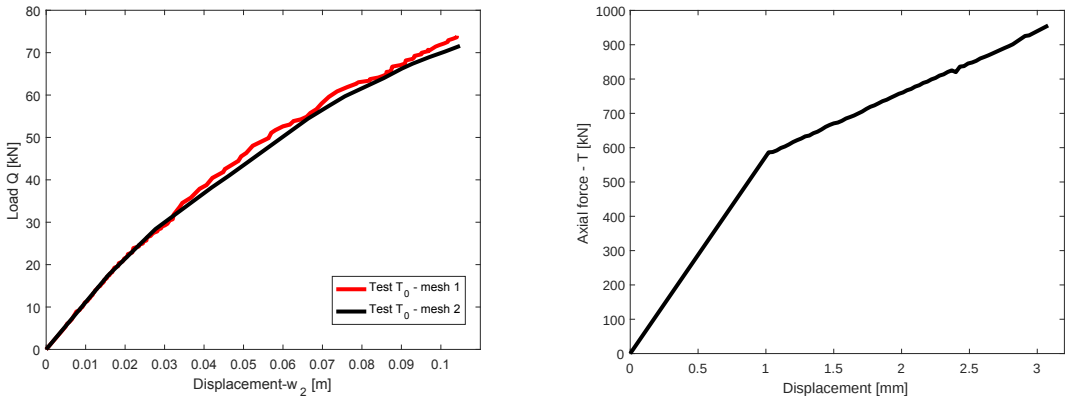

(a) **(b)**

Figure 3.23: (a) Load Q in terms of the deflection at the mid-point of the inner span; (b) Load T in terms of the resulting displacement for test $T2$

plastic deformations in so-called fracture process zone, which provides an important contribution to total plastic dissipation as the final failure mechanism. The plasticity model is represented with Drucker-Prager yield criterion, with similar plastic potential function governing hardening behavior while strain softening behavior is represented with St. Venant criterion.

We illustrated here that the model of this kind ensures complete mesh independency of the discrete approximation constructed by the finite element methods. In particular, for representing the failure, a displacement jump is embedded in the element to describe the post-peak behavior. Another feature of the model is ability

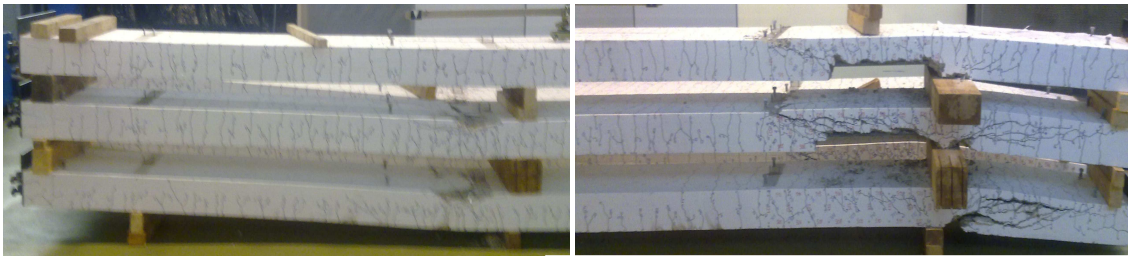

(a)

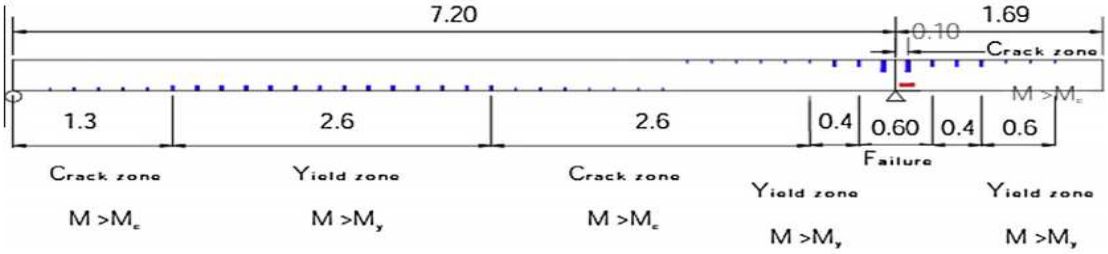

(b)

Figure 3.24: Crack propagation: (a) experimental results for test T_0-lower beam,T_2-midlle beam, T_1-upper beam; (b) results taken from [123]

to represent nonlinear volume change during hardening, which is obtained by using plastic potential function defining the plastic flow rule, which is similar to (but not the same as) the yield function.

The model is validated by presenting several numerical examples where we confirm that the resistance of concrete to tension is much lower than the one in compression. The computed results fits quite well with the corresponding experimental results, pertinent not only to global but also to local results, such as the resulting crack pattern for the bending test on a reinforced concrete beam.

Although the chosen model problem considers plasticity model, the proposed concept of combining the inelastic hardening and inelastic softening to fully explain the failure of a massive structure can easily be adapted to other models of inelastic response, such as damage or combined damage plasticity.

4

Identification of macro-scale model parameters

In chapter 2 and chapter 3 meso-scale and macro scale model capable to represent failure of concrete-like materials are presented. In this chapter the identification of the model parameters from different kind of numerical experiments is presented. While meso-scale model is used for numerical simulation of experimental results, macro-scale model, capable to take into account different type of dissipation, is used as a model on which the identification procedure is based. The sequential identification approach employed in this chapter is accomplished due the fact that all macro-scale parameters have a clear physical interpretation. Moreover, substantial computational time savings can be achieved by using only the part of test simulation for each of three stages.

Contents

4.1 Introduction 81
4.2 A brief description of meso/macro-scale model 82
4.3 Tension test 85
4.3.1 Identification of elastic parameters 85
4.4 Compression test 87
4.4.1 Identification of elastic parameters 87
4.4.2 Identification of hardening parameters 89
4.5 Final comments on the presented identification procedure 96

4.1 Introduction

In chapter 2 and chapter 3 both scale model (meso-scale and macro-scale model) are presented. It has been shown that meso-scale model is capable to represent the salient features of failure phenomena for concrete-like materials for different loading regime [24]. Moreover, this meso-scale model can be used to provide the definition of the parameters, such as the fracture energy or ultimate strength taking into account the heterogeneity and different process of cracking governing the final mechanisms. On the other hand, macro-scale model can reproduce the inelastic behavior and failure modes of concrete taking into account both dissipative mechanisms. The model contains all the ingredients for taking into account both phases of localized failure, where the elastic phase is followed by the creation of the fracture process zone with large number of micro-cracks as well as final failure mode with micro-cracks coalescence into the macro-crack. Plasticity model with Drucker-Prager criterion is considered for yield function with similar plastic potential function governing hardening behavior and the strain softening bahavior is represented with St. Venant criterion. This kind of model ingredients definition allows to straightforward visualize the model parameters in terms of stress-strain diagram. Later, it can be shown that this knowledge can be used to greatly simplify the optimization procedure.

The proposed identification procedure presented in this chapter relies on measurements obtained with numerical simulation for different loading condition. Without limiting only to numerical measurements, which can be much easier to obtain as well as much appropriate (e.g. free energy and dissipation) due to fact that both models are prepared in accordance with FE method definition, the proposed approach can be successfully used with experimental measurements. It will be shown latter that all modification concerns about appropriate change of measurements made on meso-scale model with experimental measurements.

Complexity of identification procedure depends on numerical or experimental setup. Thus, the simplest test to execute, in identification point of view, is simple tension test. This type of test is commonly used for determination of material parameters such as metals and rarly for concrete-like materials due to specimen grapping condition. By using numerical simulation instead of laboratory experiment this test could be reproduce providing us a additional information about material behavior. In experimental practice simple tension test could be replaced by uniaxial compression test or by three point bending test. Both kind of test are simple to perform and their results are well-reproducible, especially for the uniaxial compression test. In this chapter, we present which type of numerical/experimental test can provide more information about parameters which we are try to identify and the how chooses of numerical simulation affects the final results. This material calibration procedure can be defined as one special case of *Bayesian updating procedure* presented in chapter 5 (Figure 4.1). In this case, our prior knowledge is very poor and it can be presented with a large deviation, while information/measurement provided by meso-scale model is almost deterministic with very narrow probability region. Moreover, material parameters in identification approach presented in this chapter

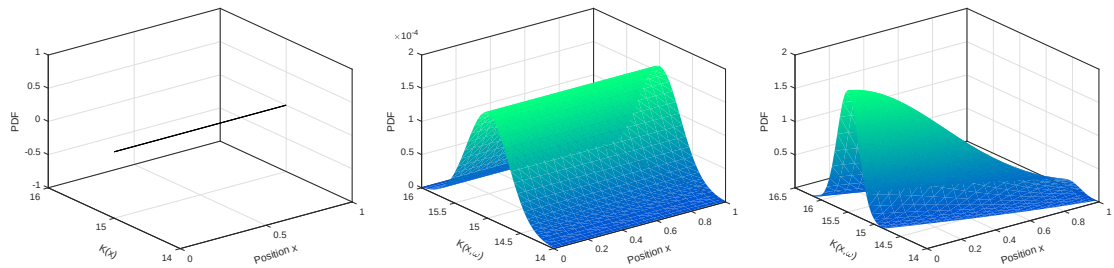

(a) (b) (c)

Figure 4.1: The graphical representation of uncertain one dimensinal material parameter(a) deterministic description $K(x) = const = 15$; (b) homogeneous material described by Gaussian radndom variable $K(x,\omega) = \mathcal{N}(15,1)$; (c) heterogeneous material described by random field $K(x,\omega) = \bar{K} + \gamma(x,\omega)$ where $\gamma(x,\omega)$ is Gaussian random field

are deterministic on both scale and modeled without any measurements or model error.

In order to take advantage of the model structure the identification procedure is divided into three completly separete stages. Such aprroach allows us to perform identification only for part of simulation depending on particular material parameters providing a much more efficient computation then for a full-scale problem. Thus, the material calibration can be understood as a sequential optimization problem.

Optimization algorithm used to find minimum of objective function adopted in this work is *downhill simplex* or *Nelder-Mead method* [124]. Note, that variety of techniques is available for optimization problem e.g gradient-based methods [125–128], stochastic evolutionary algorithms [129–132] or adaptive smoothing of the objective function by artificial neural networks [133–135].

The outline of this chapter is as follows. In next section we briefly describe meso-scale and maco-scale model. Material calibration obtain from tension test is presented in section 3 followed by results from compression test in section 4. Closing remarks can be found in section 5.

4.2 A brief description of meso/macro-scale model

In the following section, we give a brief description of the meso-scale model on which the measurements are performed and macro-scale model on which the identification procedure is based. Complete description for both scale model is given in chapter 2 and chapter 3. Here, we give a main ingredients for each of the two models.

As already mention above, in chapter 2 of this work we present a fine scale constitutive model of concrete capable to take into acccount the complete set of 3D failure mechanisms. Microstructure at meso-scale is able to distinguish between the two phases of the material (aggregate and cement), where aggregate is in agreement with the granulometric curve. Multi-surface criteria set in local frame are defined in

order to detect softening behavior in the tension case

$$\begin{aligned}\phi_{u,n+1} &:= t_{u,n+1} - (\sigma_{u,t} - q_{u,n}) \leq 0\\ \phi_{v,n+1} &:= |t_{v,n+1}| - (\tau_{u,v} - q_{v,n}) \leq 0\\ \phi_{w,n+1} &:= |t_{w,n+1}| - (\tau_{u,w} - q_{w,n}) \leq 0\end{aligned} \tag{4.1}$$

where $\sigma_{u,t}$, $\tau_{u,v}$ and $\tau_{u,w}$ are fracture stress values in mode I, mode II and mode III, respectively. The variability of these fracture values can be quantified in terms of independent Gaussian random variables. Moreover, once the condition in (4.3) at least in one direction is detected simultaneous softening in all three failure modes occurs. Failure in compression is defined with similary multi-surface criteria

$$\begin{aligned}\phi_{u,n+1} &:= |t_{u,n+1}| - (\sigma_{u,c} - q_{u,n}) \leq 0\\ \phi_{v,n+1} &:= |t_{v,n+1}| - \left(\tau_{f,v} - q_{v,n}\right) \leq 0\\ \phi_{w,n+1} &:= |t_{w,n+1}| - \left(\tau_{f,w} - q_{w,n}\right) \leq 0\end{aligned} \tag{4.2}$$

where failure in each mode occurs independently. Note that shear strength is magnified by friction angle ϕ in agreement with the Mohr-Coulomb law

$$\tau_{f,v} = \tau_{u,v} + \sigma tan(\Phi); \quad \tau_{f,w} = \tau_{u,w} + \sigma tan(\Phi) \tag{4.3}$$

Computation of the failure require the solution to the following set of equation

$$\begin{aligned}r &:= A_{e=1}^{n_{el}} \left(\mathbf{f}^{int,(e)} - \mathbf{f}^{ext}\right) = 0\\ \mathbf{h}^{(e)} &:= \int_0^{l_e} \overline{\mathbf{G}}^T \boldsymbol{\sigma} dx + \mathbf{t} = 0, \quad \forall e \in [1, n_{el}^e]\end{aligned} \tag{4.4}$$

where $\mathbf{f}^{int,(e)} = \int_0^{l_e} \mathbf{B}^T \boldsymbol{\sigma} dx$ the standard internal force vector obtained from the internal stress resultans $\sigma = (N, V, M)$, while the enhanced part $\mathbf{h}^{(e)}$ is added for every beam with active failure mode for which the yield condition in (5.1) applies. Thus, for any such beam $\forall e \in [1, n_{el}^e]$ with a active micro-crack, we first have to compute the current crack opening $\alpha_{n+1}^{(i,j)}$ in agreement with current displacement value $u_{n+1}^{(i)}$ and obtain corresponding traction value.

In order to solve nonlinear problem in (4.4) we carry out new iterative sweep on to provide new iterative values of nodal displacements

$$\begin{aligned}&A_{e=1}^{n_{el}} \widehat{\mathbf{K}}_{n+1}^{e} \Delta \mathbf{u}_{n+1}^{(i)} = A_{e=1}^{n_{el}} \left[\mathbf{f}_{n+1}^{ext,e} - \mathbf{f}_{n+1}^{int,e,(i)}\right]\\ &\Longrightarrow \mathbf{u}_{n+1}^{(i+1)} = \mathbf{u}_{n+1}^{(i)} + \Delta \mathbf{u}_{n+1}^{(i)}\end{aligned} \tag{4.5}$$

$$\widehat{\mathbf{K}}_{n+1}^{e,(i)} = \mathbf{K}_{n+1}^{e,(i)} - \mathbf{F}_{n+1}^{e,(i),T} (\mathbf{H}_{n+1}^{e,(i)} + K_{\alpha,n+1}^{(i)})^{-1} (\mathbf{F}_{v,n+1}^{e,(i)} + K_{d,n+1}^{(i)}) \tag{4.6}$$

$$\begin{aligned}&\mathbf{K}_{n+1}^{e,(i)} = \int_0^{l_e} \mathbf{B}^T \mathbf{C}_{n+1}^{(i)} \mathbf{B} dx, \quad \mathbf{F}_{n+1}^{e,(i)} = \int_0^{l_e} \mathbf{B}^T \mathbf{C}_{n+1}^{(i)} \overline{\mathbf{G}} dx\\ &\mathbf{F}_{v,n+1}^{e,(i)} = \int_0^{l_e} \overline{\mathbf{G}}^T \mathbf{C}_{n+1}^{(i)} \mathbf{B} dx, \quad \mathbf{H}_{n+1}^{e,(i)} = \int_0^{l_e} \overline{\mathbf{G}}^T \mathbf{C}_{n+1}^{(i)} \overline{\mathbf{G}} dx\end{aligned} \tag{4.7}$$

and $\mathbf{C}_{n+1}^{(i)} = diag(EA, GA, GA, GI_p, EI_{11}, EI_{22})$ is the tangent stiffness for 3D Timoshenko beam.

In order to describe macro-scale model in following we define three main ingredients for constitutive model of plasticity sufficient for the stress tensor computation as well as internal variables evolution

- additive decomposition of total strain into elastic and plastic component $\boldsymbol{\epsilon} = \boldsymbol{\epsilon}^e + \boldsymbol{\epsilon}^p$
- the free energy function constructed in terms of deformations $\psi(\boldsymbol{\epsilon}, \boldsymbol{\epsilon}^p, \zeta) := \frac{1}{2}(\boldsymbol{\epsilon} - \boldsymbol{\epsilon}^p) \cdot \boldsymbol{C}(\boldsymbol{\epsilon} - \boldsymbol{\epsilon}^p)) + \frac{1}{2}\zeta K \zeta$
- the yield criterion which corresponds to the classical Drucker-Prager model $\phi_y(\boldsymbol{\sigma}, q) := \| \, dev[\boldsymbol{\sigma}] \, \| + \frac{1}{3} tan(\varphi) tr[\boldsymbol{\sigma}] - \sqrt{\frac{2}{3}}(\sigma_y - q) = 0; \quad dev[\boldsymbol{\sigma}] = \boldsymbol{\sigma} - \frac{1}{3}(tr[\boldsymbol{\sigma}])\mathbf{1}$

  while plastic potential function is defined as $\phi_p(\boldsymbol{\sigma}, q) := \| \, dev[\boldsymbol{\sigma}] \, \| + \frac{1}{3} tan(\psi) tr[\boldsymbol{\sigma}]$

where $\| \, \sigma \, \| := \sqrt{\sigma : \sigma}$ is the Frobenius norm, $dev[\boldsymbol{\sigma}]$ is the deviatoric part of the stress tensor, $tan(\varphi)$ is material parameter that can characterize the internal friction, $tan(\psi)$ is material parameter describing the angle of dilatancy and σ_y is uni-axial yield stress identified from a tension test.

We can note that for plastic potential function different than yield function material instability phenomena occurs even in hardening. Another material instability taken into account on macro-scale model, refered to typical case, is associated with the softening. Adopting the strong discontinuity formulation we can represent the cracking of concrete both in tension and compression. While in tension we can observe elastic stage followed by unstable softening stage, in compression we can observe three different deformation stages, linear elastic, hardening and localized softening. With the macro-scale model able to take into account all these types of dissipative mechanisms we can represent behavior of massive structure: bulk dissipation characterized by the development of micro-cracks (Drucker-Prager model) and a surface dissipation in localization zones in terms of the macro-cracks (St. Venant plasticity criterion). The latter is defined in strain space defined by three surfaces, but it can be written in standard format in stress space

$$\begin{aligned}
\phi_1(\boldsymbol{\sigma}) &= \frac{3K+G}{9KG}\sigma_1 - \frac{3K-2G}{18KG}(\sigma_2+\sigma_3) - (\sigma_y - q) \leq 0 \\
\phi_2(\boldsymbol{\sigma}) &= \frac{3K+G}{9KG}\sigma_2 - \frac{3K-2G}{18KG}(\sigma_1+\sigma_3) - (\sigma_y - q) \leq 0 \\
\phi_3(\boldsymbol{\sigma}) &= \frac{3K+G}{9KG}\sigma_3 - \frac{3K-2G}{18KG}(\sigma_1+\sigma_2) - (\sigma_y - q) \leq 0
\end{aligned} \tag{4.8}$$

where we have chosen the reference value of the elasticity limit obtained from hydrostatic tension test.

The weak form of equilibrium can be written as a system of global and local equilibrium equations. The first set of equations is classically written in the finite element method while the letter is written in each localized element.

$$\begin{aligned} &A_{e=1}^{n_{el}}\left[\mathbf{K}_{n+1}^{e,(i)}\Delta\mathbf{u}_{n+1}^{(i)}+\mathbf{F}_{n+1}^{e,(i)}\Delta\boldsymbol{\alpha}_{n+1}^{(i)}\right]=A_{e=1}^{n_{el}}\left[\mathbf{f}_{n+1}^{ext,e}-\mathbf{f}_{n+1}^{int,e,(i)}\right]\\ &\mathbf{h}_{n+1}^{e,(i)}+\left(\mathbf{F}_{v,n+1}^{e,(i)}+\mathbf{K}_{d,n+1}^{(i)}\right)\Delta\mathbf{u}_{n+1}^{(i)}+\left(\mathbf{H}_{n+1}^{e,(i)}+\mathbf{K}_{\alpha,n+1}^{(i)}\right)\Delta\boldsymbol{\alpha}_{n+1}^{(i)}=0 \end{aligned} \tag{4.9}$$

where:

$$\begin{aligned} &\mathbf{K}_{n+1}^{e,(i)}=\textstyle\int_{\Omega^e}\mathbf{B}^T\mathbf{C}_{n+1}^{ep,(i)}\mathbf{B}dV,\ \ \mathbf{F}_{n+1}^{e,(i)}=\int_{\Omega^e}\mathbf{B}^T\mathbf{C}_{n+1}^{ep,(i)}\bar{\mathbf{G}}\mathbf{m}dV\\ &\mathbf{F}_{v,n+1}^{e,(i)}=\textstyle\int_{\Omega^e}\mathbf{m}^T\bar{\mathbf{G}}^T\mathbf{C}_{n+1}^{ep,(i)}\mathbf{B}dV,\\ &\mathbf{H}_{n+1}^{e,(i)}=\textstyle\int_{\Omega^e}\mathbf{m}^T\bar{\mathbf{G}}^T\mathbf{C}_{n+1}^{ep,(i)}\bar{\mathbf{G}}\mathbf{m}^TdV\\ &\mathbf{K}_{d,n+1}^{e,(i)}=A_{\Gamma_s^e}\tfrac{\partial t_m}{\partial u}|_{n+1}^{(i)},\ \ \mathbf{K}_{\alpha,n+1}^{e,(i)}=A_{\Gamma_s^e}\tfrac{\partial t_m}{\partial \alpha}|_{n+1}^{(i)} \end{aligned} \tag{4.10}$$

To take advantage of the fact that the second equation is written locally in each localized element, it can be solved at the element level which further allows determining the value of the displacement jump increment $\Delta\alpha(i)$. Latter, by static condensation the system of equations in (4.9) can be reduced to a single equation which takes the classical form in the finite element.

4.3 Tension test

In the case of uniaxial tension test, the strain and stress fields remain homogeneous during the whole computation until the final localized failure phase. Thus, this kind of test is the simplest one to use in order to identify material parameters. We can note that bahavior on structural level is very close to the response of material point. Moreover, fracture process zone (FPZ) is less pronounced in tension test than in compression test. Thus, the global stress-strain diagram on meso-scale can be divided into two parts which is in agreement with macro-scale respone in tension: the first one which corresponds to the elastic response and the second one describing softening regime. Following the same pattern we can perform calibration of model parameters: first, from elastic part Bulk modulus K and Shear modulus G are determined, followed by elasticity limit stress σ_y and fracture energy in tension $G_{f,t}$ estimated from softening part.

4.3.1 Identification of elastic parameters

In order to perform identification procedure for Bulk modulus K and Shear modulus G force or energy measurement needs to be supplemented with an additional one. In particular, we include the lateral contraction Δl defined as the average horizontal displacements of central point on each free side of the specimen (as indicated by arrows in the Figure 4.2a).

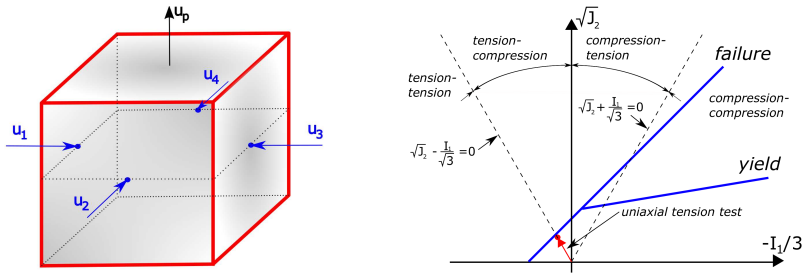

(a) (b)

Figure 4.2: (a) Displacements measured to evaluate the contraction $\Delta l = 0.25 \cdot (u_1 + u_2 + u_3 + u_4)$ of the specimen; (b) loading path

The objective function J_1 applicable for the determination of elastic parameters using only uniaxial tension test can be defined as follows:

$$\begin{aligned} J_1 &= \Big(F_{ref,t}(u_p) - F_{r,t}(u_p)\Big)^2 \cdot w_1 + \Big(\Delta l_{ref,t}(u_p) - \Delta l_{r,t}(u_p)\Big)^2 \cdot w_2; \\ u_p &= 0.00005 \text{ mm} \end{aligned} \tag{4.11}$$

where $F_{ref}(u)$ is reaction force obtained with lattice model and $F_r(u)$ is reaction force obtained with 3D solid model. The corresponding value of weights w_1 and w_2 were chosen in order to get similar norm of each of summation terms. Taking into account that in beginning of loading regime only elastic parameters are important simulation can be sttoped after reaching prescribed value of imposed displacement u_p. This makes first optimization stage computationally very efficient. Additional savings in computation can be achieved by using proxy or surrogate model on macro-scale as it presented in chapter 4. In this case we need to take into consideration model error in computation of objective function. For the sake of illustration, the shape of objective function J_1 is shown in the Figure 4.3 for loading in 3 different direction.

We can note from Figure 4.3 that in each loading direction elastic parameters varies only a little indicating that concrete is statistically isotropic material. Also, Figure 4.3 shows that objective function remains convex in the neighborhood of the optimal value.

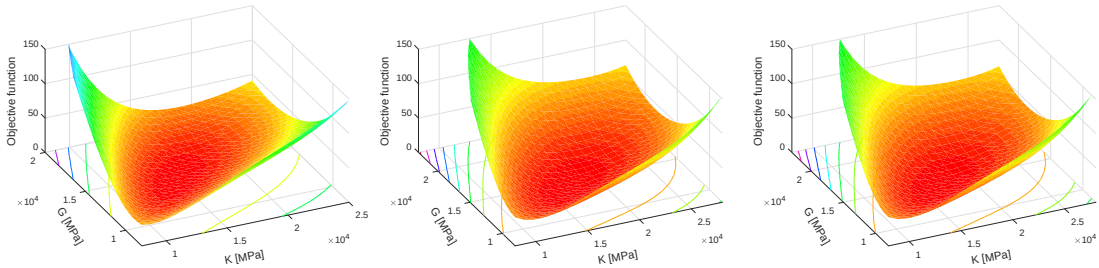

(a) (b) (c)

Figure 4.3: Objective function for unaixial tension test with loading in (a) X-direction; (b) Y-direction; (c) Z-direction

4.4 Compression test

Similary to the uniaxial tension test, the solution of the optimization process for compression test is divided into three subsequent stages: elastic, hardening and softening. Another simplification of optimization process concern hardening part. In the following of this chapter we present each of this parts.

4.4.1 Identification of elastic parameters

In elastic range, Bulk modulus (K) and Shear modulus (G) can be determined using a short simulations describing only the elastic response of a specimen under applied loading. In order to identify only Shear modulus, which controls the resistance to the change of shape, we can use simple shear test (Figure 4.4a), whereas for identification of Bulk modulus, which controls the material resistance to the volume change, we can use hydrostatic compression test (Figure 4.4b), instead uniaxial compression test. For both procedure force or energy is only which is compered to the measurement obtained with meso-scale model.

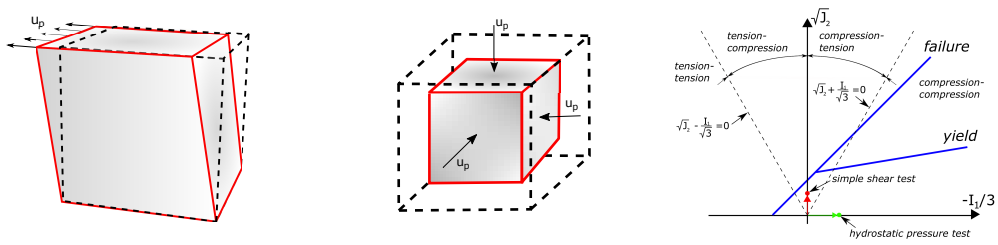

(a) (b) (c)

Figure 4.4: Numerical tests : (a) simple shear test; (b) hydrostatic pressure test; (c) loading path

The objective function J_2 and J_3 applicable for the determination of elastic parameters using simple shear and hydrostatic test can be defined as follows:

$$\begin{aligned} J_2 &= \Big(F_{ref,sh}(u_p) - F_{r,sh}(u_p)\Big)^2; \qquad & u_p = 0.001 \text{ mm} \\ J_3 &= \Big(F_{ref,hp}(u_p) - F_{r,hp}(u_p)\Big)^2; \qquad & u_p = 0.00025 \text{ mm} \end{aligned} \tag{4.12}$$

where u_p is the prescribed imposed displacement for praticular test.

The shape of objective functions J_2 and J_3 are shown in the Figure 4.5 and 4.5. As shown in this figures, the objective function for simple shear test remains linear in direction which corresponds to the Bulk modulus whereas for hydrostatic pressure test it is linear in direction which corresponds to the Shear modulus. With such simplification, there is only one independent material parameters to be identified in both tests (Figure 4.6). Identified Bulk and Shear modulus are the same as the one obtained with meso-scale model *(G=14,918 GPa; K=17,232 GPa)*.

Although this kind of calibration procedure is robust and accurate, the experiment dealing with a simple shear test and especially hydrostatic pressure test are rather

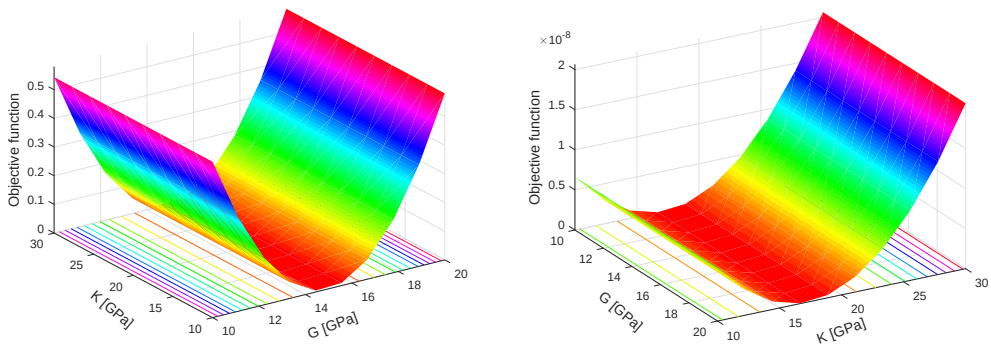

(a) (b)

Figure 4.5: Objective function for : (a) simple shear test - J_2; (b) hydrostatic pressure test -J_3

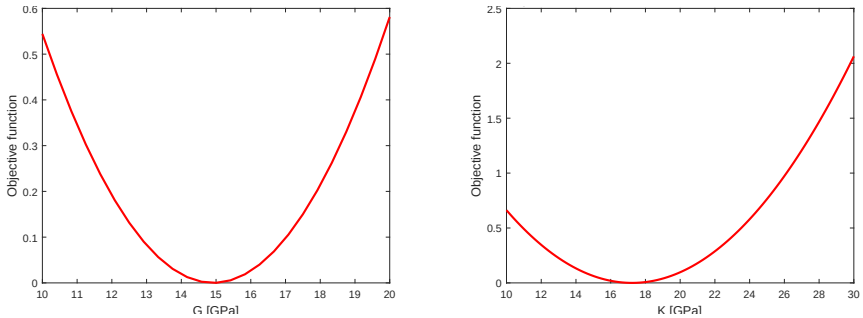

(a) (b)

Figure 4.6: Objective function for single parameter: (a) simple shear test; (b) hydrostatic pressure test

difficult to perform in a well-reproducible way. For that reason, we turn to study the possibility of parameter estimates by using only uniaxial compression test. To identify both elastic parameters information about force needs to be supplemented with an additional measurement. In particular, we propose to include the specimen expansion Δl defined as the average horizontal displacements of central point on each free side of the specimen (as indicated by arrows in the Figure 4.7).

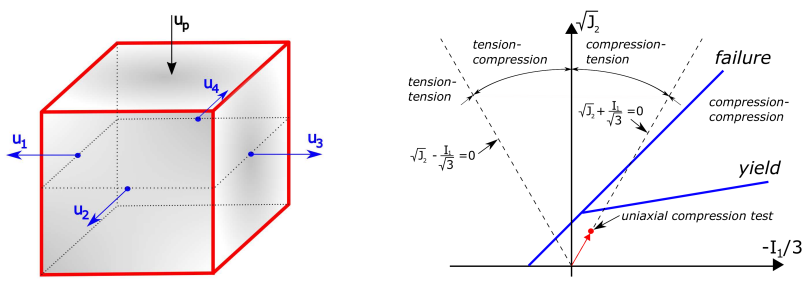

(a) (b)

Figure 4.7: (a) Displacements measured to evaluate the expansion $\Delta l = 0.25 \cdot (u_1 + u_2 + u_3 + u_4)$ of the specimen; (b) loading path

The objective function J_4 applicable for the determination of elastic parameters using only uniaxial compression test can be defined as:

$$\begin{aligned} J_4 &= \left(F_{ref,c}(u_p) - F_{r,c}(u_p)\right)^2 \cdot w_3 + \left(\Delta l_{ref,c}(u_p) - \Delta l_{r,c}(u_p)\right)^2 \cdot w_4; \\ u_p &= 0.0005mm \end{aligned} \tag{4.13}$$

where again $F_{ref}(u)$ is reaction force obtained with lattice model and $F_r(u)$ is reaction force obtained with 3D solid model. As shown in this Figure 4.8a, the objective function remains rather wiggly in the neighborhood of the optimal value.

Combining results from simple shear and hydrostatic pressure tests we can define new objective function (Figure 4.8b) in order to provide better optimization. Note that in all propsed objective functions instead of force we can include information about free potential energy computed on meso-scale (lattice model) and macro scale (3D solid model). The shape of objective function will remain the same.

$$J_5 = \left(F_{ref,sh}(u_p) - F_{r,sh}(u_p)\right)^2 \cdot w_5 + \left(F_{ref,hp}(u_p) - F_{r,hp}(u_p)\right)^2 \cdot w_6; \tag{4.14}$$

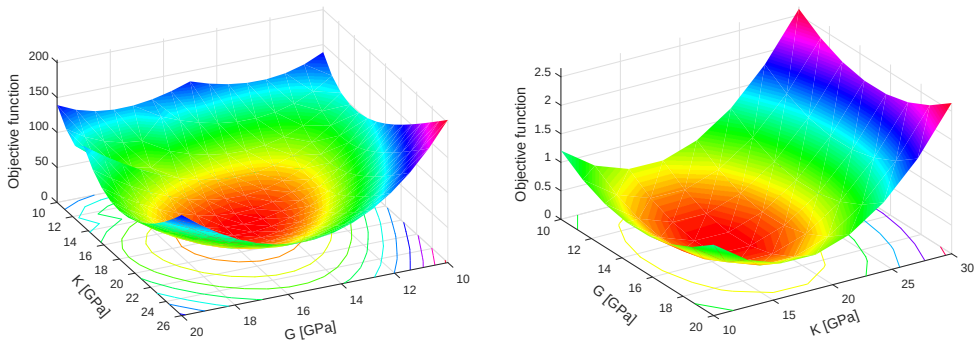

(a) **(b)**

Figure 4.8: Objective function for: (a) uniaxial compression test; (b) simple shear test combined with hydrostatic pressure test

4.4.2 Identification of hardening parameters

Once we have successfully determined Bulk and Shear modulus, we can continue towards the estimate of the parameters of Drucker-Prager yield surface defined as:

$$\phi_y(\boldsymbol{\sigma}, q) := \| \, dev[\boldsymbol{\sigma}] \, \| + \frac{1}{3} tan(\varphi) tr[\boldsymbol{\sigma}]) - \sqrt{\frac{2}{3}}(\sigma_y - q) \tag{4.15}$$

where

$$q = -(\sigma_\infty - \sigma_y)[1 - exp(-\beta\zeta)] - K_{h,lin} \cdot \zeta \tag{4.16}$$

In (4.16) above, β is the hardening parameter that governs the rate with which the saturation is achieved, σ_∞ is limit stress until the stress increase and $K_{h,lin}$ is hardening modulus. Defining hardening in such way we are able to obtain nonlinear isotropic hardening taking simply $K_{h,lin}$ to be equal to zero, while in the opposite taking β to be equal to zero we obtain isotropic linear hardening.

In order to define yield criterion we need to determine $tan(\varphi)$, which can characterize the internal friction, σ_y as uniaxial yield stress and $K_{h,lin}$ for linear hardening while for nonlinear hardening additionally we need to identify σ_∞ and β. Regardless of the type of hardening for plastic potential function we need to identify $tan(\psi)$. Note that nonlinear hardening is represented with six parameters while for linear hardening we need four parameters. In order to simplify optimization procedure we assume that for nonlinear hardening $K_{h,lin}$=0 which leads to $\sigma_\infty = \sigma_{max,ref} + \sigma_y$ (Figure 4.9).

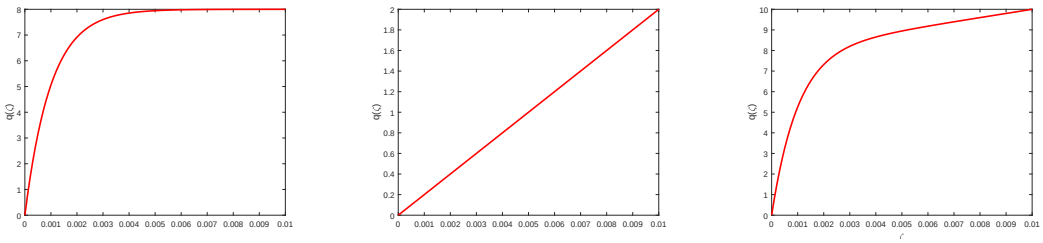

(a) **(b)** **(c)**

Figure 4.9: Internal variable q for σ_∞=10 MPa, σ_y=2 MPa : (a) β =1000; $K_{h,lin}$=0 (b) β =0; $K_{h,lin}$=200; (c) β =1000; $K_{h,lin}$=200

With such simplification, there are four material parameters to be identified:

- for linear isotropic hardening: $\sigma_y, tan(\varphi), tan(\psi), K_{h,lin}$
- for nonlinear isotropic hardening: $\sigma_y, tan(\varphi), tan(\psi), \beta$

By using only uniaxial compression test these parameters can be idenfied where objective function include information about force (energy or dissipation) and corresponding volumetric strain for four measurements (Figure 4.10). Thus, objective function is defined as:

$$\begin{aligned} J_6 = & \left[\left(F_{ref,c}(u_1) - F_{r,c}(u_1)\right)^2 + \left(F_{ref,c}(u_2) - F_{r,c}(u_2)\right)^2\right] \cdot w_7 + \\ & \left[\left(F_{ref,c}(u_3) - F_{r,c}(u_3)\right)^2 + \left(F_{ref,c}(u_4) - F_{r,c}(u_4)\right)^2\right] \cdot w_7 + \\ & \left[\left(V_{ref,c}(u_1) - V_{r,c}(u_1)\right)^2 + \left(V_{ref,c}(u_2) - V_{r,c}(u_2)\right)^2\right] \cdot w_8 + \\ & \left[\left(V_{ref,c}(u_3) - V_{r,c}(u_3)\right)^2 + \left(V_{ref,c}(u_4) - V_{r,c}(u_4)\right)^2\right] \cdot w_8; \end{aligned} \tag{4.17}$$

where $V_{ref}(u_i)$ and $V_r(u_i)$ represents volumetric strain obtain with meso-scale model and 3D solid model, respectively.

Figure 4.11a shows objective function J_6 where axis represent three parameters that we are recovering (σ_y, K_h and $tan(\varphi)$) while the size of circle represent the

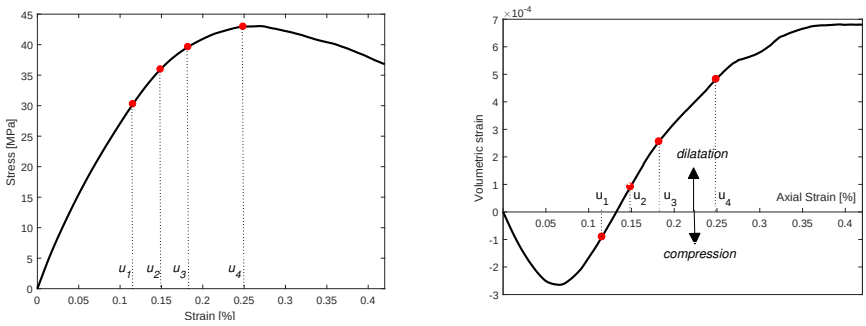

(a) **(b)**

Figure 4.10: Macroscopic response for uniaxial compression test with lattice model - phase I-60% : (a) measurements on stress-strain curve; (b) measurements on volumetric strain-axial strain curve

fourth parameter $tan(\psi)$. Values of objective function are presented with colormap. For the better representation Figure 4.11b and 4.11c shows objective function drawn for pair of identified parameters.

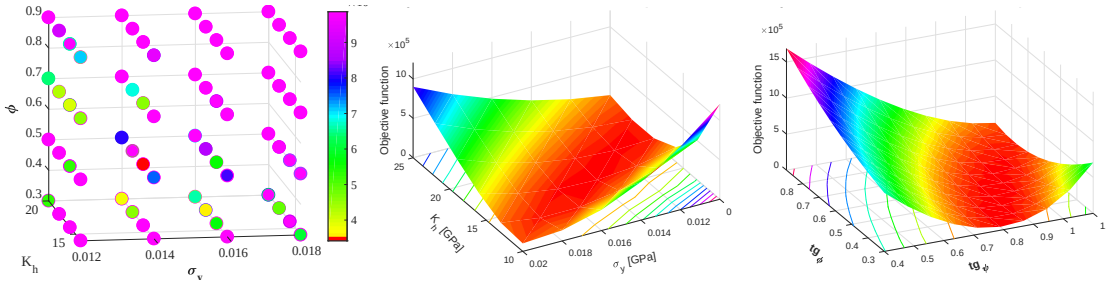

(a) **(b)** **(c)**

Figure 4.11: Objective function J_6

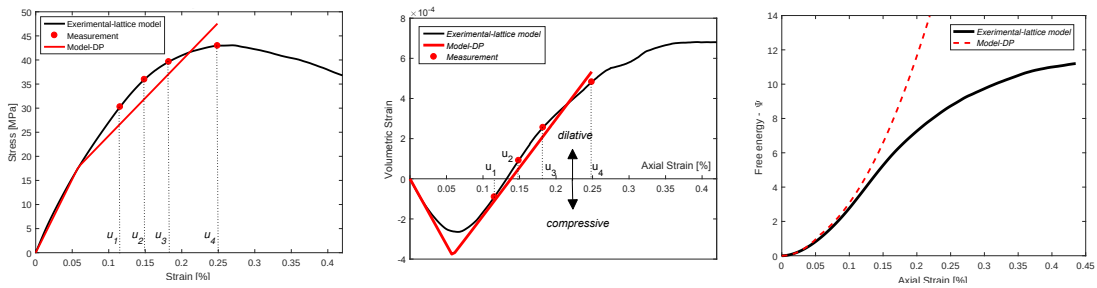

(a) **(b)** **(c)**

Figure 4.12: Comparison of macroscopic response for uniaxial compression test with lattice model - phase I-60% and continuum model with linear hardening : (a) stress versus axial strain curve; (b) volumetric strain versus axial strain curve; (c) free energy-axial strain curve

With such objective function optimization process is not only computationally too expensive but also significant difference can be noted on stress-strain curve and

also in the free energy potential obtained with lattice model compared to results obtained with 3D solid model using identified parameters (Figure 4.12). In order to avoid this problem we propose to split identification process of hardening parameters in two step.

From (4.15) it can be noted that σ_y and $tan(\varphi)$ are sufficient to define Drucker-Prage yield point while the hardening parameter β and $tan(\psi)$ can be identified during hardening process. Thus, first step is identification of yield stress and internal friction. The objective function applicable for the determination of these two parameters can be defined as follows:

$$J_7 = \left(F_{ref,max,c}(D^p = 0) - F_{r,max,c}\right)^2 \cdot w_9 + \left(F_{ref,max,bc}(D^p = 0) - F_{r,max,bc}\right)^2 \cdot w_{10}; \tag{4.18}$$

where $F_{ref,max}(D^p = 0)$ is maximum reaction force obtained with lattice model where plastic dissipation remains equal to zero and $F_{r,max}$ is maximum reaction force obtained with 3D solid model setting parameters to correspond to perfect plasticity. The quantities with index $_c$ and $_{bc}$ correspond to the values taken from the uniaxial and biaxial compression test,respectively. Measurements are obtained with lattice model, thus we can determine point where plasticity start (Figure 4.13a). To keep this optimization step efficient, the simulations should again be restricted to a limited loading range, where the limit imposed displacement correspond to axial strain ϵ_{axial}=0.2%.

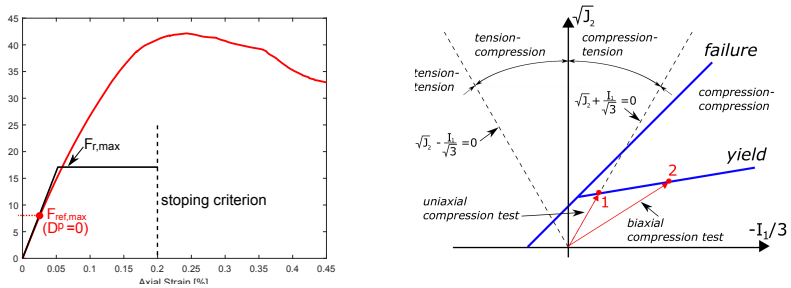

(a) **(b)**

Figure 4.13: (a) force measured on meso-scale model (red) and 3D solid model (black) with simplified model for identification of yield function; (b) loading path

Note that objective function J_7 contains measurement taken from the uniaxial and biaxial compression test performed on a plate specimen with the dimensions of 150 mm x 30 m x 150 mm with 50% volume fraction of aggregate (Figure 4.13b). Figure 4.14 reveals differences in macroscopic response for uniaxial test compared to biaxial compression test performed on a plate specimen.

Figure 5.22a and 5.22b shows that we can draw a infinitely many line through point 1 or point 2 (Figure 4.13b) if objective function depends on the measurement of a single test, uniaxial either biaxial test. The shape of objective function J_7 is shown in the Figure 5.22c. As shown in this figure, the objective function remains rather wiggly in the neighborhood of the optimal value and hence more easy to optimize

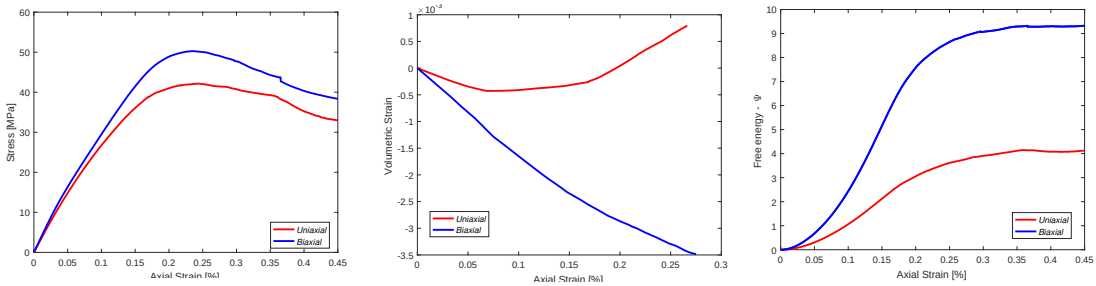

(a) **(b)** **(c)**

Figure 4.14: Biaxial-Uniaxial compression test comparison with lattice model - phase I-50%: (a) stress versus axial strain curve; (b) volumetric strain versus axial strain curve; (c) free energy-axial strain curve

compered to objective function J_6. Identified parameters, yield stress and internal friction, in such way can be used for linear either nonlinear hardening.

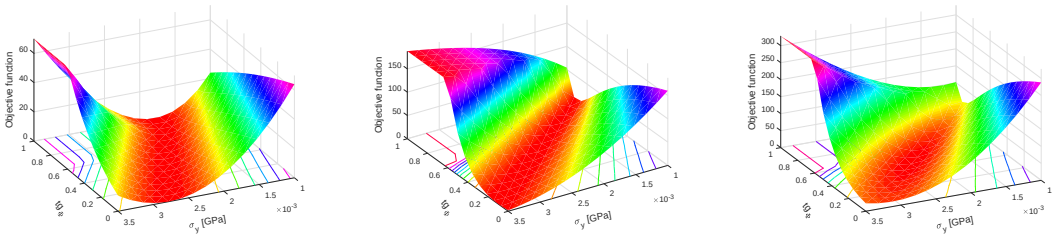

(a) **(b)** **(c)**

Figure 4.15: Objective function J_7 with measurements taken from: (a) uniaxial test; (b) biaxial test; (c) uniaxial and biaxial test combined

Although this kind of calibration procedure is robust and accurate, dissipation and free energy potential can not be computed in laboratory experiment. For that reason we propose objective function in form:

$$J_8 = \Big(F_{ref,c}(\epsilon_y) - F_{r,c}(\epsilon_y)\Big)^2 \cdot w_{11} + \Big(F_{ref,bc}(\epsilon_y) - F_{r,bc}(\epsilon_y)\Big)^2 \cdot w_{12}; \tag{4.19}$$

where $F_{ref,c}(\epsilon_y)$ is reaction which is related to the limit strain ϵ_y at the end of the linear part of the stress-strain diagram (Figure 4.16) while $F_r(\epsilon_y)$ is reaction obtained with 3D solid model. As before, the quantities with index $_c$ and $_{bc}$ correspond to the values taken from the uniaxial and biaxial compression test,respectively. The shape of objective function J_8 is same as objective function J_7.

The second stage of identification of hardening parameters involves the angle of dilatancy $tan(\psi)$ and the hardening parameter β for nonlinear or K_h for linear hardening. There are two requirements for the choice of measurements. First, measurements should be choosen between ϵ_y and strain which corresponds to the limit stress and second, the number of measurements should ensure convex objective function. If the first requirement is fulfilled the corresponding objective function depends only on values of the hardening parameter or hardening modulus, according

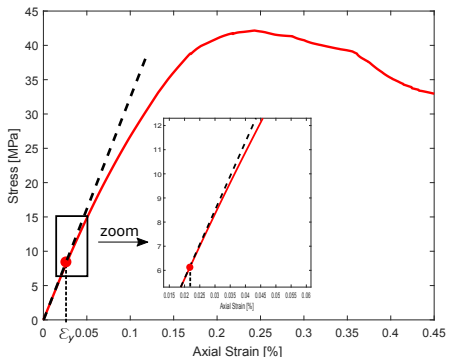

Figure 4.16: Measurements for objective function J_8

to the choice of hardening, and the dilatancy angle, because Bulk and Shear modulus as well as yield stress and internal friction are fixed on the optimal values determined during the previous optimization stage. To identify these two parameters we propose to include four measurements not only of force or dissipation but also of volumetric strain (Figure 4.17). Then, objective function can be defined as follows:

$$\begin{aligned} J_9 = &\left[\left(D^p_{ref,c}(u_1) - D^p_{r,c}(u_1)\right)^2 + \left(D^p_{ref,c}(u_2) - D^p_{r,c}(u_2)\right)^2\right] \cdot w_{13} + \\ &\left[\left(D^p_{ref,c}(u_3) - D^p_{r,c}(u_3)\right)^2 + \left(D^p_{ref,c}(u_4) - D^p_{r,c}(u_4)\right)^2\right] \cdot w_{13} + \\ &\left[\left(V_{ref,c}(u_1) - V_{r,c}(u_1)\right)^2 + \left(V_{ref,c}(u_2) - V_{r,c}(u_2)\right)^2\right] \cdot w_{14} + \\ &\left[\left(V_{ref,c}(u_3) - V_{r,c}(u_3)\right)^2 + \left(V_{ref,c}(u_4) - V_{r,c}(u_4)\right)^2\right] \cdot w_{14}; \end{aligned} \tag{4.20}$$

where $D^p_{ref}(u_i)$ and $D^p_r(u_i)$ represents plastic dissipation energy obtained with meso-scale model and 3D solid model,respectively. Objective function J_9 can be wrriten in terms of force instead of the plastic dissipation energy regardless of hardening type.

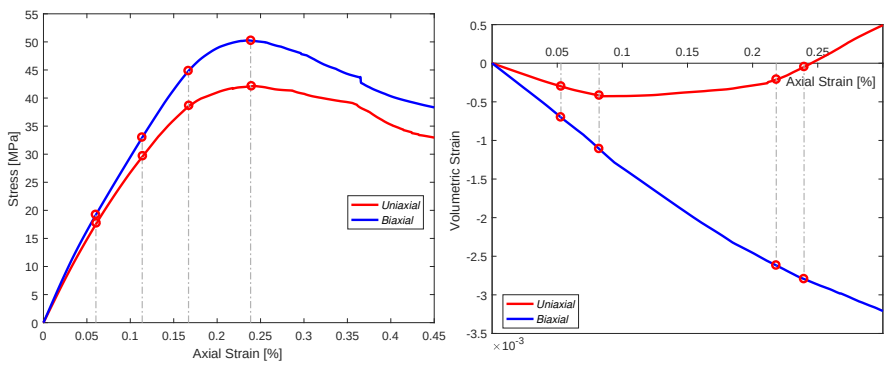

(a) **(b)**

Figure 4.17: Measurements for objective function J_9 definition (a) stress-strain curve; (b) volumetric strain-axial strain

Figure 4.18a shows the shape of objective function J_9 where only plastic disipation energy is taken into account. We can note that measuring only plastic dissipation

D^p objective function is unchagned for wide range of parameters (β, tan_Φ). Taking into account volumetric strain, objective function is improved with addditional measurements which can capture any change of tg_Φ resulting with optimal value as it presented in Figure 4.18b.

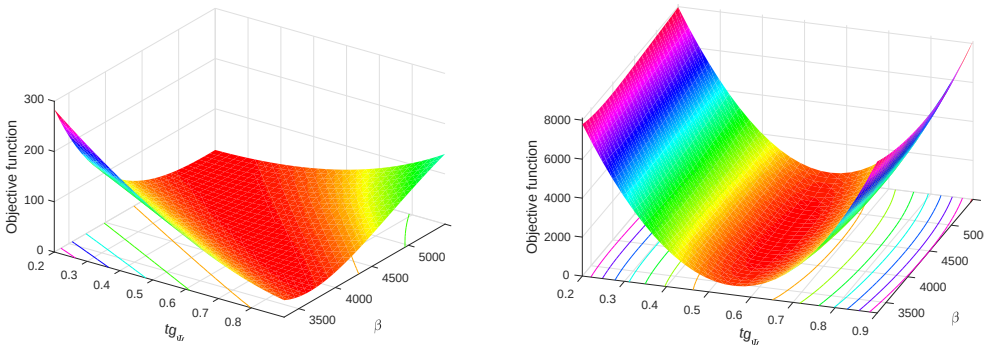

(a) **(b)**

Figure 4.18: Objective function J_9 with measurements taken from uniaxial compression test (a) plastic dissipation (D^p); (b) plastic dissipation (D^p) + volumetric strain

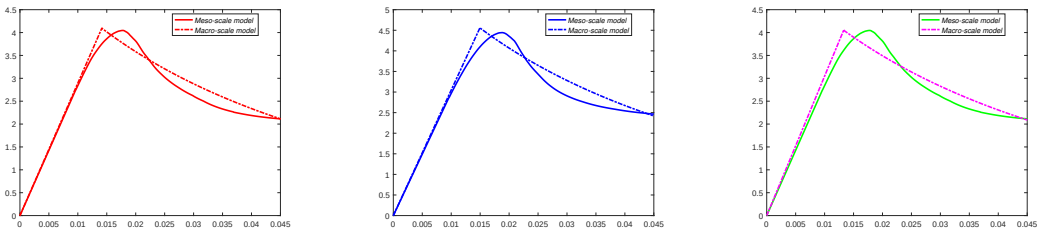

(a) **(b)** **(c)**

Figure 4.19: Comparison of stress-strain diagram for uniaxial tension test with loading in: (a) X-direction; (b) Y-direction; (c) Z-direction

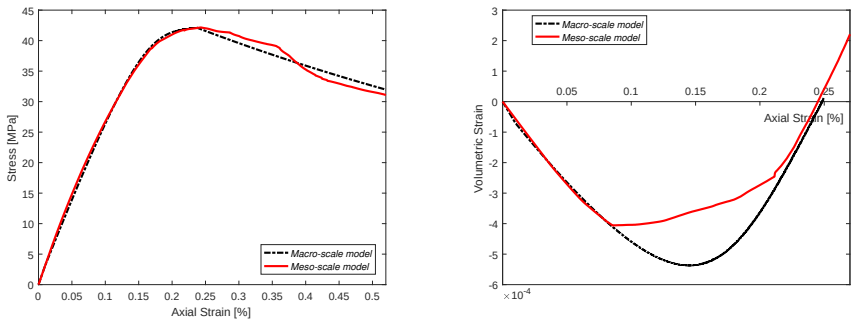

(a) **(b)**

Figure 4.20: Comparison of results for uniaxial compression test: (a) X-direction; (b) stress-strain diagram; (c) volumetric-axial strain diagram

Results of identification procedure for tension test and for compression test are presented in Figure 4.19 and 4.20. This figure reaveals nice matching with results obtained by meso-scale model for macroscopic stress-strain response and computed total energy as well as for volume changes. Note, that matching with meso-scale model,here simulates experimental results, is performed in agreement with total energy. Thus, stress-strain diagram fits well in elastic part while in softening part fracture energy on macro-scale model corresponds to meso-scale model results.

4.5 Final comments on the presented identification procedure of macro-scale model parameters

In this chapter we proposed identification procedure for material paremeters of macro-scale model used for representation of failure of massive structure. Approach presented here is based on sequential identification procedure employed for uniaxial tension test and for uniaxial compression test. The proposed algorithm can be directly used for other type of tests. Each stage in identification is stopped when prescribed imposed displacement value is reached which significantly reduce computation time. Moreover, we propose to split optimization procedure not only on elastic, hardening and softening stage, but also hardening part in compression is divided into two part. First part, which deals with the yield function and latter which deals with the plastic potential function.

Due to the fact that all ingredients of macro-scale model have physical interpretation we can construct simple objective function sensitive to the relevant material parameters. We aslo show that elastic parameters can be identified from simple shear test and hydrostatic pressure test. Measurements used for optimization can be expressed in terms of force or displacement in case of labaratory experiments, but also in terms of free energy or plastic dissipation.

As the result of a sequential identification approach we present macroscopic response and we find nice matching with meso-scale results. The major difficulty of the proposed procedure is properly recognition of the three stages of structural behavior, especially for experimental results. In order to fully accept the propose procedure the experimental validation of the method is necessary.

5

Reduced model of macro-scale stochastic plasticity identification by Bayesian inference

In this chapter we deal with constructing probability-based scale bridging when passing the detailed information of the meso-scale plasticity model for localized failure of concrete towards the chosen reduced model at macro-scale. This is accomplished by using Bayesian inference providing the probability distribution of macro-scale model parameters expressed as random variables or fields in order to compensate for model reduction. The original aspect of this approach is in resulting macro-scale stochastic plasticity model, which can best quantify uncertainty due to data loss in terms of corresponding probability distribution. The proposed procedure is illustrated in detail for concrete meso-scale model presented in chapter 2 of this work (see [24]), both for simple elastic response and plastic response with hardening in fracture process zone, as well as for softening response in localized failure phase. The latter implies that the classical homogenization procedure no longer applies, and should be replaced by macro-scale reduced model defined with respect to the quantity of interest, not necessarily the same for each particular response phase. The complete set of results for parameters identification are combined together at the level of a solid finite element with embedded discontinuity, granting it very powerful predictive properties.

Contents

5.1 Introduction and motivation 99
5.2 Plasticity at multiple scales 101
5.3 Macro-scale reduced ED-FEM model 109
5.4 Stochastic macro-scale plasticity model parameters identification . . . 115
5.4.1 MCMC Bayesian updating of the measure 120
5.4.2 The Bayesian upadetes with linear Gauss-Markov-Kálmán filter 123
5.5 Numerical simulations 130
5.5.1 Identification of elastic parameters 131
5.5.2 Identification of hardening parameters 138
5.5.3 Identification of softening parameters 141
5.5.4 Simultaneous identification of all macro-scale model parameters and use of standard experiments 143
5.6 Final comments on the presented stochastic plasticity identification . 146

5.1 Introduction and motivation

Of special interest for this work are stochastic model that can capture localized failure sensitivity for structures built of heterogeneous composite material, such as concrete. The biggest benefits are for industrial applications of the probably the most used material in construction and the potential high gain for this composite materials is in improved durability. From standpoint of constructing predictive stochastic plasticity fracture models, this kind of composite material has rather favorable features with: two-phase meso-structure (aggregate vs. cement), non-local dimension brought by typical fracture modes of massive structures with significant contribution of fracture process zone (FPZ), and fabrication that is comparable to large-scale additive-manufacturing, where the complete structure is cast with the same material rather than an assembly of various components. The latter is the crucial hypothesis that can render the proposed macro-scale stochastic plasticity model feasible in terms of predicting probability-distribution-based estimates of structure properties.

The main novelty is seen in the fact that all scales are to be treated probabilistically, and not only capturing the average response on the larger scale. This is particularly important for testing of heterogeneous cement-based composites, where the scales in test specimen are in general not well separated. Such is the case when testing reduced-size specimen with respect to microstructure heterogeneities, where significant variability occurs in the test results due to small-scale uncertainty. [136]. More important for these quasi-brittle composite materials is fracture sensitivity to small-scale defects that trigger crack coalescence and accelerates structure failures. This is especially visible when more than one failure mode is active, where only fine-scale models representing material heterogeneities can provide sufficiently predictive results, whereas those based upon homogenization (with average properties) fail. Therefore, despite ample literature (e.g. see [137] or [138] for summary), the fully predictive macro-scale model for localized failure of concrete remains somewhat elusive goal, due to a number of uncertainties that influence the nonlinear response.

In this work we focus in particular upon uncertainty propagation that allows connecting the inelasticity at multiple scales, starting from the fine scale (here meso-scale for concrete) where the heterogeneous composite failure mechanisms and the variability of model parameters can be captured much better by corresponding representation of different phases (here aggregate versus cement paste). The main goal is to provide the corresponding macro-scale reduced model, which can significantly increase the computational efficiency and render the analysis of complex structures feasible. The proposed approach can be considered as a part of a scale-coarsening strategy, but much different from ad-hoc choices ([139]). Namely, once the crack pattern at meso-scale has stabilized, we will use an efficient Bayesian updating, replacing subsequently meso-scale by macro-scale generalized ED-FEM element with parameters/arrays as random fields. The probability distribution of such random field will be computed separately between loading program variability and microstructure variability. With such an approach we can recover a reduced model that defines probability distribution of fracture parameters describing localized failure with both

volume and surface dissipation ([73], [28]). Such a 'mechanics-based' model reduction is fundamentally different from vast majority of recent works ([140], [141], [109], [142], [143], [144]) using statistical modes with either POD-proper orthogonal decomposition or PGD-proper generalized decomposition. Moreover, we can recover any probability distribution of structure failure modes for advanced safety evaluation, contrary to pre-defined distributions currently used: log-normal distribution to construct fragility curves ([146]), uniform to construct bounds ([147]), Weibull to account for weakest link failure ([148]), or ad-hoc combination of power law and Gaussian as two asymptotic values ([149]). We note that stochastic upscaling is an original approach providing coarse-scaling of uncertainty in inelasticity at multiple scales. This is an off-line probability computation using efficient Bayesian updates with many realizations to assimilate information on microstructure evolution, obtained by simulations or measurements, to provide probability distribution of coarse-scale fracture parameters expressed as random field. Higher computational efficiency is obtained by not seeking detailed representation of microstructure initial defects, but their effects on quantity-of-interest (e.g. dissipation), new PCE Kalman filter that simplifies the Bayesian updates. Similar off-line probability computations are also used for an original scale-coarsening strategy, using variability in loading program, to provide mechanics-based model reduction; one such reduced model can replace stabilized meso-scale crack pattern by generalized ED-FEM model with parameters/arrays expressed as random fields.

Model reduction from meso-scale to macro-scale defining generalized ED-FEM in probability framework that we seek to develop is one of the crucial ingredients of the proposed approach, which allows for stochastic coarse graining. This is illustrated in switching from meso-scale to macro-scale, in order to provide a replacement with a generalized ED-FEM once the crack pattern inside the element is stabilized. Namely, the goal is to then replace the meso-scale computation with the corresponding probability distribution of the macro-scale model parameters of such ED-FEM. We will illustrate this idea on a plasticity model, where such parameters q would also include yield and ultimate stress.

Two different methods for Bayesian inference have been tested and compared in the proposed approach, both based upon the Bayes theorem that allows incorporating new information generated in a particular loading program. Each unknown parameter of reduced model is modeled as a random variable (which can also be high-dimensional). Such description has two constituents, the measurable function and the measure. One method (MCMC) is identified as updating the measure, whereas the other method (PceKF) changes the measurable function. We formulate both methods as functional approximation of stochastic problems, and introduce especially in combination with the second method a new procedure which does not need any sampling, hence works completely deterministically. It also seems to be the fastest and more reliable when compared with other methods. We show by example that it also works for highly nonlinear non-smooth problems with non-Gaussian measures.

The outline of the chapter is as follows: In Section 2 we describe the meso-scale and macro-scale plasticity model for concrete, and the corresponding manner to identify its reduced model in terms of stochastic plasticity. Considerations of the

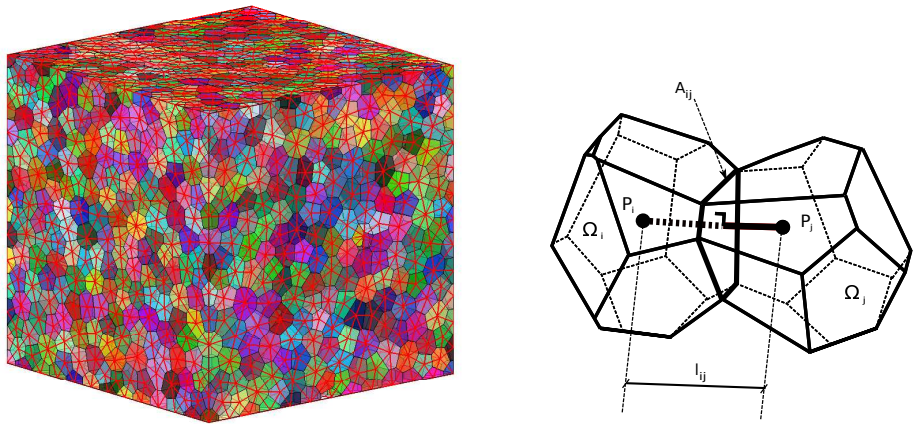

(a) **(b)**

Figure 5.1: (a) Structure of discrete lattice model with Voronoi cells as units of heterogeneous material and cohesive links between them (b) two neighbouring Voronoi cells

Bayesian inference replacing inverse problem by direct coupled mechanics-probability problem, are given in Section 3. The results for several numerical examples are presented in Section 4. In Section 5 we state some closing remarks.

5.2 Plasticity at multiple scales: meso-scale model for failure analysis of concrete with parameters as random fields

In chapter 2 of this work [24] we developed a fine scale constitutive model of concrete that can distinguish the complete set of 3D failure mechanisms. The price to pay is to start with the microstructure at meso-scale that is able to distinguish between aggregate and cement paste (see Figure 5.1) and which allows to explicitly handle the failure at their interface.

The typical failure modes at interface in tension are described by multi-surface criteria set in local frame:

$$\begin{aligned} \phi_{u,n+1} &:= t_{u,n+1} - (\sigma_{u,t} - q_{u,n}) \leq 0 \\ \phi_{v,n+1} &:= |t_{v,n+1}| - (\tau_{u,v} - q_{v,n}) \leq 0 \\ \phi_{w,n+1} &:= |t_{w,n+1}| - (\tau_{u,w} - q_{w,n}) \leq 0 \end{aligned} \tag{5.1}$$

where $\sigma_{u,t}$, $\tau_{u,v}$ and $\tau_{u,w}$ are fracture stress values in mode I, mode II and mode III, respectively. The variability of interface fracture values can be quantified in terms of independent Gaussian random variables in agreement with random field distribution as explained next. First, we note that [24] fracture stress in tension does not vary a lot with respect to variation of aggregate, for we need only one failure surface for complete fracture of the representative volume element (see Figure 5.2).

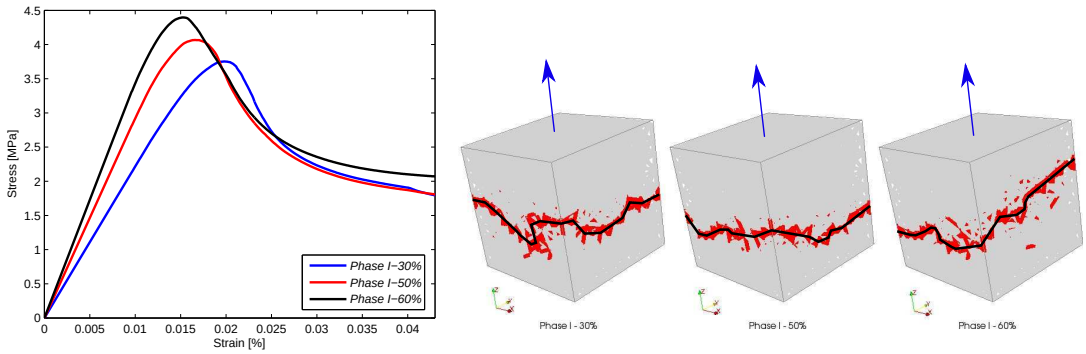

Figure 5.2: i) Uniaxial tension test: macroscopic response for different aggregate volume fraction; ii) Specimen contours at the end of uniaxial tension test. Beam elements in increasing softening are red colored

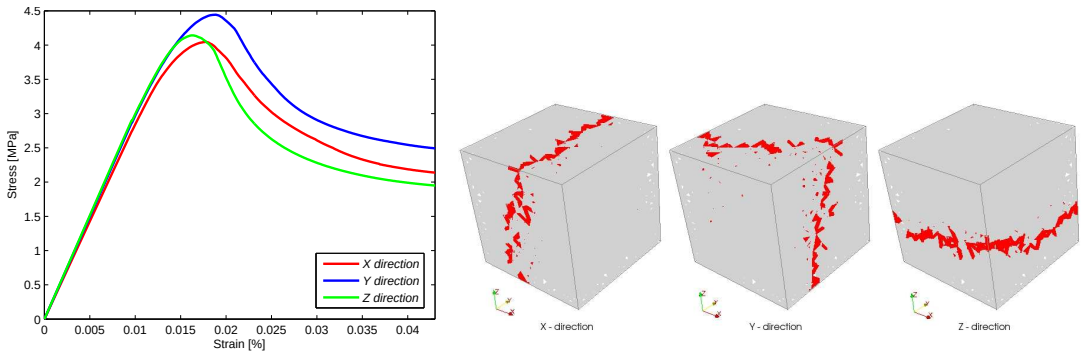

Figure 5.3: i) Uniaxial tension test: macroscopic responses for specimen (phase I-50%) in three loading directions; ii) Specimen contours at the end of uniaxial tension test for phase I-50% specimen in all three loading directions. Beam elements in increasing softening are red colored

Moreover, even for high volume fraction of aggregate, the fracture stress in tension varies only a little for tests in 3 different directions (see Figure 5.3) indicating that concrete is statistically isotropic material. Thus, given distribution of the fracture stress , it remains to clarify two subsequent steps: how to carry on computation for a single realization of properties variations and how to obatin uncertainty propagation in computed response. The failure is discussed in detail in Chapter 2 of this work [24] as the deterministic computation requiring the solution to the following set of equation:

$$\begin{aligned} \mathbf{r} &:= A_{e=1}^{n_{el}} \left(\mathbf{f}^{int,(e)} - \mathbf{f}^{ext} \right) = 0 \\ \mathbf{h}^{(e)} &:= \int_0^{l_e} \overline{\mathbf{G}}^T \boldsymbol{\sigma} dx + \mathbf{t} = 0, \quad \forall e \in [1, n_{el}^e] \end{aligned} \tag{5.2}$$

where $\mathbf{f}^{int,(e)} = \int_0^{l_e} \mathbf{B}^T \boldsymbol{\sigma} dx$ the standard internal force vector obtained from the internal stress resultans $\sigma = (N, V, M)$, while the enhanced part $\mathbf{h}^{(e)}$ is added for every beam with active failure mode for which the yield condition in (5.1) applies.

Thus, for any such beam $\forall e \in [1, n_{el}^e]$ with a active micro-crack, we first have to compute the current crack opening $\alpha_{n+1}^{(i,j)}$ in agreement with current displacement value $u_{n+1}^{(i)}$ and obtain corresponding traction value.

$$\begin{aligned} \phi^{trial}(t_{n+1}^{(i)}, \alpha_{n+1}^{(j)}) > 0 \Rightarrow \Delta \mathbf{t}_{n+1}^{(j,i)} &= \mathbf{K}_{d,n+1}^{(j,i)} \Delta \mathbf{u}_{n+1}^{(i)} + \mathbf{K}_{\alpha,n+1}^{(j,i)} \Delta \boldsymbol{\alpha}_{n+1}^{(j,i)} \qquad j = 1, 2, \ldots \\ \boldsymbol{\alpha}_{n+1}^{(j+1,i)} &= \boldsymbol{\alpha}_{n+1}^{(j,i)} + \Delta \boldsymbol{\alpha}_{n+1}^{(j,i)} \\ \phi(t_{n+1}^{(j+1,i)}, \alpha_{n+1}^{(i+1)}) \leq 0 \qquad & (i) \leftarrow (j+1) \end{aligned} \tag{5.3}$$

where $\mathbf{K}_{d,n+1}^{(j,i)}$ and $\mathbf{K}_{\alpha,n+1}^{(j,i)}$ are the consistent tangent stiffness for discontinuity (see [24]).

In order to solve nonlinear problem in (5.2) we carry out new iterative sweep on to provide new iterative values of nodal displacements

$$\begin{aligned} A_{e=1}^{n_{el}} \widehat{\mathbf{K}}_{n+1}^{e} \Delta \mathbf{u}_{n+1}^{(i)} &= A_{e=1}^{n_{el}} \left[\mathbf{f}_{n+1}^{ext,e} - \mathbf{f}_{n+1}^{int,e,(i)} \right] \\ \Longrightarrow \mathbf{u}_{n+1}^{(i+1)} &= \mathbf{u}_{n+1}^{(i)} + \Delta \mathbf{u}_{n+1}^{(i)} \end{aligned} \tag{5.4}$$

$$\widehat{\mathbf{K}}_{n+1}^{e,(i)} = \mathbf{K}_{n+1}^{e,(i)} - \mathbf{F}_{n+1}^{e,(i),T} (\mathbf{H}_{n+1}^{e,(i)} + K_{\alpha,n+1}^{(i)})^{-1} (\mathbf{F}_{v,n+1}^{e,(i)} + K_{d,n+1}^{(i)}) \tag{5.5}$$

$$\begin{aligned} \mathbf{K}_{n+1}^{e,(i)} &= \textstyle\int_0^{l_e} \mathbf{B}^T \mathbf{C}_{n+1}^{(i)} \mathbf{B} dx, \;\; \mathbf{F}_{n+1}^{e,(i)} = \int_0^{l_e} \mathbf{B}^T \mathbf{C}_{n+1}^{(i)} \overline{\mathbf{G}} dx \\ \mathbf{F}_{v,n+1}^{e,(i)} &= \textstyle\int_0^{l_e} \overline{\mathbf{G}}^T \mathbf{C}_{n+1}^{(i)} \mathbf{B} dx, \;\; \mathbf{H}_{n+1}^{e,(i)} = \int_0^{l_e} \overline{\mathbf{G}}^T \mathbf{C}_{n+1}^{(i)} \overline{\mathbf{G}} dx \end{aligned} \tag{5.6}$$

and $\mathbf{C}_{n+1}^{(i)} = diag(EA, GA, GA, GI_p, EI_{11}, EI_{22})$ is the tangent stiffness for 3D Timoshenko beam.

In Chapter 2 of this work [24], the material parameters are considered as random variables. Here, we will generalize this development for the case where these fracture parameters of the meso-scale plasticity model can be considered as random fields, i.e. with properties that might be changing from point-to-point.

This point-of-view is also in agreement with the role of probability, which is needed to retain the unresolved physics of the smaller scale as the probabilistic noise at bigger scale. This is done through stochastic upscaling (opposite of methods like relative entropy,([150]). Namely, due to composite material heterogeneities one cannot predict exact microstructure evolution with initial defects, unless assuming prior distribution of meso-scale fracture parameters (at phase-interface). We can thus find solution to a multiphysics problem with chemistry of cement hydration (e.g. NIST model [3]) combined with cement-drying next to aggregates resulting with self-desiccation induced micro-cracks. Such results are then used to improve posterior probability distribution of meso-scale fracture parameters through Bayesian inference. This is can be done in off-line probability computation performed as a pre-processing step were we can to use many different microstructure simulations (or measurements) to construct predictive posterior distribution of meso-scale fracture parameters expressed as random fields. Subsequently, we will use an on-line probability computation to

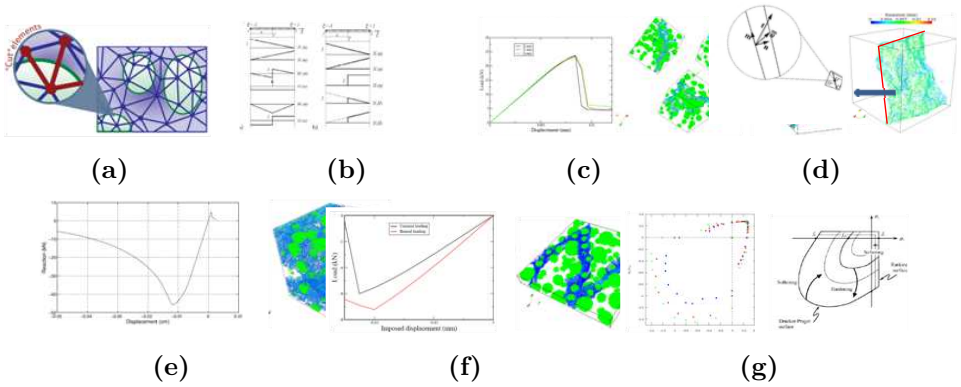

Figure 5.4: Reduced-model in terms of generalized ED-FEM computed from meso-scale: (a) two-phase concrete model meso-scale representation [31, 24]: aggregate (white) vs. cement paste (violet); (b) cohesive links at meso-scale with structured mesh (keeping the same mesh for different realizations in probability computations) requiring both strain and displacement discontinuity implemented within ED-FEM with same number of parameters as X-FEM, but more clear role for each parameter resulting with higher computational efficiency [29]; (c) simple tension test force-displacement diagram (statistically isotropic=same in any direction) and failure mode in tension illustrated with displacement contours and cohesive link failure; d) replacement of tension failure mode at meso-scale (rough surface) with discontinuity (plane) at macro-scale with ED-FEM, not matching perfectly the crack but fracture energy material parameter G_f; (e) uniaxial compression force-displacement and failure mode with cohesive links failure; f) biaxial compression (confirming compressive strength increase from uniaxial case) and failure mode; (g) replacing failure criterion for different failure modes under biaxial stress (colors: showing increased resistance in compression for higher aggregate volume fraction, dots: providing computed value of fracture energy for corresponding failure mode) and comparison against classical Rankin, St. Venant or Drucker-Prager macro-scale plasticity criteria [73].

provide the variability of structure response (here, a macro-scale solid element with ED-FEM discrete approximation) with uncertainty propagation starting from such meso-scale parameters probability distribution, where stochastic upscaling will be used again for scale-coarsening producing mechanics-based reduced model at macro-scale to grant computational efficiency (see Figure 5.4).

The first step in building such coupled-probability model concerns representing the source of uncertainty , here the fracture stress parameters $p = (\sigma_n, \tau_v, \tau_w)$, When we are not quite sure about their value, we model them as random variables $p(\omega)$ that can take different values according to the given probability distribution. When we are modeling heterogeneous material, these material parameters are described as random fields. It means that the uncertainty in the particular material parameter p is modeled by defining $p(x,\omega)$ for each point in the region $x \in \boldsymbol{V} \in \mathbb{R}^d$ as a random variable on a suitable probability space $(\Omega, \mathfrak{U}, \mathbb{P})$ where Ω is set off all random events, $\mathfrak{U}$ is a class of subsets or σ- algebra to which a real number in interval $[0,1]$ can be assigned reffered as a measure $\mathbb{P}$ in region $x \in \boldsymbol{V} \in \mathbb{R}^d$. For $p(x,\omega) : G \times \boldsymbol{V} \to \mathbb{R}$ as a random field one may identify Ω with the set of all possible values of parameters, or so-called realization in the space of all real-valued functions $p_{\bar{\omega}}(x)$ on $\boldsymbol{V}$. Alternatively, $p(x,\omega)$

can be seen as a collection of real-valued random variables $p_{\bar{x}}(\omega)$ indexed by $x \in \boldsymbol{V}$. Assuming the random field $p(x,\omega)$ to be Gaussian, its distribution can be defined by its mean

$$\mu_p(x) = \mathbb{E}\left[p(x,\omega)\right] = \int_\Omega p(x,\omega)\mathbb{P}(d\omega) \tag{5.7}$$

and its covariance

$$\begin{aligned} C_p(x,x') &= \mathbb{E}\left[(p(x,\omega)-\mu_p(x))(p(x',\omega)-\mu_p(x'))\right] \\ &= \int_\Omega (p(x,\omega)-\mu_p(x))(p(x',\omega)-\mu_p(x'))\mathbb{P}(d\omega) \end{aligned} \tag{5.8}$$

We note that non-Gaussian fields (e.g. log-normal) may be expressed directly as functions of Gaussian fields (see e.g. [152]) or [153]), that is $p(x,\omega) = \Xi(x,\theta(\omega))$, where Ξ is a pointwise transformation, and $\theta(\omega)$ is a standard normal random variable. Thus we further use these variables with zero mean unit variance variable $\theta(\omega) \sim \mathcal{N}(0,1)$ which allows for a uncoupled integration over probability domain Ω much like Cartesian coordinates over physical domain ([153]).

In a computational setting with the finite physical domain $\boldsymbol{V}$, this field must be discretized. If a parameter field $p(x)$ can be adequately represented on a finite collection of points $x_i \in \mathbb{R}(i = 1,2,\ldots,n)$, then we can write both the prior and posterior densities in terms of $p = (p(\mathbf{x}_1),\ldots,p(\mathbf{x}_n))^T$, where $p_i = p(\mathbf{x}_i)$ are random variables usually correlated among each other. The spatial coefficient functions are given by simple projection $q^\alpha(x) = \mathbb{E}(q(x,\cdot)H_\alpha(\boldsymbol{\theta}(\cdot))$. The computational cost usually goes high with this approach where the PCE is completely general and is defined without any reference to the random field $q(x,\omega)$. This means that an excessive number of RVs $\theta_1(\omega),...,\theta_k(\omega),...$ may be needed to give an accurate enough approximation when the above PCE is truncated to some $\alpha \in \mathcal{J} \subset \mathcal{N}$. We can replace them with variables through the Karhunen-Loève expansion.

Karhunen-Loève expansion (KLE) is also a useful tool for more concise representation of the stochastic processes ([155]).

$$p(x,\omega) = \mu_p(x) + \sum_{i=0}^{\infty} \sqrt{\lambda_i}\xi_i(\omega)\varphi_i(x) \tag{5.9}$$

where $\xi_i(\omega)$ is a set of uncorrelated Gaussian random variables of zero mean and unit variance whereas λ_i are eigenvalues and $\varphi_i(x)$ are the eigenfunctions obtained by solving the Fredholm integral equation with the covariance function as the integral kernel

$$\int_{\mathcal{V}} C_p(x,x')\varphi_i(x)dx' = \lambda_i\varphi_i(x) \tag{5.10}$$

This results allows to provide the spectral decomposition of the covariance

$$C_p(x,x') = \sum_{i=0}^{\infty} \lambda_i\varphi_i(x)\varphi_i(x') \tag{5.11}$$

$$\xi_j(\omega) = \frac{1}{\sqrt{\lambda_j}} \int_{\mathcal{V}} \left(p(x,\omega) - \bar{\mu}_p(x)\right)\varphi_j(x)dx \tag{5.12}$$

where λ_i are positive eigenvalues ordered in a descending order.

For more complex physical domain computing the eigenfunctions analytically is usually not feasible, but we have to discretize the covariance spatially according to chosen grid points (in finite element mesh). The resulting covariance C_p is again symmetric and positive definite matrix, and Fredholm equation in Eq. (5.10) becomes a symmetric matrix eigenvalue problem, where the eigenfunctions $\varphi_i(x)$ are replaced by eigenvectors $\boldsymbol{\varphi}_i$.The eigenvalue problem of this kind can be solved by a Krylov subspace method with a sparse matrix approximation ([156], [157]).

With descending sequence of eigenvalues, a sufficient accuracy can be obtain even with the series in Eq. (5.9) and Eq. (5.11) truncated after N_ξ terms, leading to the approximations

$$\hat{\boldsymbol{p}}(\omega) = \mu_p + \sigma_c \sum_{i=0}^{N_\xi} \sqrt{\lambda_i} \xi_i(\omega) \varphi_i(x) \tag{5.13}$$

which has the same mean $\bar{p}(x)$ as the original field and covariance $c_p(x_1, x_2) = \sigma_c \sum_{j \leq M} \lambda_j q_j(x_1) q_j(x_2)$. If the correction factor σ_c is chosen as $\sigma_c = \sqrt{\sigma_t^2/(\sigma_t^2 - \sigma_r^2)}$, the approximate field will also have the correct total variance-only distributed on the modes $\varphi_j(x)$ with $j \leq M$. Thus, such spatial semi-discretization is optimal in the sense that the mean square error resulting from a truncation after the N_ξ-th term is minimized.

In summary, the vector of model parameters $\boldsymbol{p}(\omega)$ represents now the discretized spatial field $p(x,\omega)$ which is described by a limited number N_ξ of uncorrelated random variables $\xi(\omega) = (\xi_1(\omega), \ldots, \xi_{N_\xi}(\omega))^T$. Hence, all the other response for the discretized system has also the random nature and can be expressed in terms of the same random variables $\xi(\omega)$. Having chosen $\xi(\omega)$ as standard Gaussian random variables any surrogate model (or discrete approximation in probability space) can be constructed with the Wiener polynomial chaos expansion. For example, displacement $u(.,\omega) = (\ldots u_i(.,\omega) \ldots)^T \in \mathbb{V}\ (p(\omega))$ can be written as

$$\tilde{\boldsymbol{u}}(\xi) = \sum_\alpha \beta_\alpha \boldsymbol{H}_\alpha(\xi(\omega)) \tag{5.14}$$

where $\boldsymbol{\beta}_i = (\ldots \beta_{\alpha,i} \ldots)^T$ is a vector of PCE coefficients $\beta_{\alpha,i}$ corresponding to a particular component of system response $u_i(\omega) \ldots)$ whereas $\boldsymbol{H}_\alpha(\xi(\omega))$ are multivariate Hermite polynomials constructed as product of $h_\alpha(\xi(\omega))$ the univariate Hermite polynomials.

$$\boldsymbol{H}_\alpha(\xi(\omega)) = \prod_{j=1}^{\infty} h_{\alpha_j}(\xi_j(\omega)) \tag{5.15}$$

Univariate Hermite polynomials can be obtained as

$$h_k(t) := (-1)^k e^{t^2/2} \left(\frac{d}{dt}\right)^k e^{-t^2/2}; \quad \forall t \in \mathbb{R}, k \in \mathbb{N}_0 \tag{5.16}$$

where the coefficient of the highest power of t-which is t^k for h_k- is equal to unity. For example the first five polynomials can be written as

$$\begin{aligned} &h_0(t) = 1, \qquad h_1(t) = t, \qquad h_2(t) = t^2 - 1, \\ &h_3(t) = t^3 - 3t, \qquad h_4(t) = t^4 - 6t^2 + 3 \end{aligned} \tag{5.17}$$

and each subsequent follows from the recursion relation for these polynomials given as

$$h_{k+1}(t) = th_k(t) - kh_{k-1}(t); k \in \mathbb{N} \tag{5.18}$$

The optimality in such choice in PCE follows from the orthogonality of Hermite polynomials with respect to standard Gaussian probability measure $\Gamma(dt) = (2\pi)^{-1/2}e^{-t^2/2}dt$. Hence, the set $\{h_k(t)\sqrt{k!}|k \in \mathbb{N}_0\}$ forms complete orthonormal system in $L_2(\mathbb{R}, \Gamma)$ with the Hermite polynomials that satisfy

$$\int_{-\infty}^{\infty} h_m(t)h_n(t)\Gamma(dt) = n!\delta_{nm} \tag{5.19}$$

One way of interpretation of their choice for surrogate model construction is in terms of discrete approximation, where the probability set Ω is treated as an approximation domain over which we choose p-method mesh refinement (e.g.[158]). Theoretically, the whole domain Ω can be N-dimensional $\boldsymbol{t} = (t_1, t_2, \ldots, t_n) \in \mathbb{R}^{\mathbb{N}}$ and multi-variate Hermite polynomials can be defined for infinite number of terms.

$$\boldsymbol{H}_\alpha(t) = \prod_{j=1}^{\infty} h_{\alpha_j}(t_j); \quad \forall t \in \mathbb{R}^{\mathbb{N}}, \alpha \in \mathcal{J} \tag{5.20}$$

where $\alpha = (\alpha_1, \alpha_2, \ldots, \alpha_j, \ldots) \in \mathcal{J}$ is multi-index introduced for short-hand notation ([153]).

The expansion Eq. (5.14) is truncated to the limited number of terms N, which is related to the dimension N_ξ of vector $\xi(\omega)$ and to the maximal degree of polynomials N_p according to the relation

$$N = \frac{(N_p + N_\xi)!}{N_p! N_\xi!} \tag{5.21}$$

Thus, the complete discrete approximation of displacement field combining finite element (h-method) and PCE (p-method) can be written as

$$\boldsymbol{u}^h(x, \omega) = \boldsymbol{N}(x)\tilde{\boldsymbol{u}}(\xi); \qquad \tilde{\boldsymbol{u}}(\xi) = (\boldsymbol{I} \otimes \boldsymbol{H}^*(\xi)) \cdot \beta \tag{5.22}$$

where $\boldsymbol{N}(x)$ are standard FE shape function $\boldsymbol{I} \in \mathbb{R}^{M,M}$ is the unity matrix , $\boldsymbol{H}(\xi)$ is an N-dimensional vector of Hermite polynomials, and $\boldsymbol{H}^*(\xi))$ is its dual, $\beta_i = (\ldots \beta_{\alpha_i} \ldots)^T \in \mathbb{R}^{M,N}$ is a vector of PC coefficients, M is the number of chosen grid points (e.g. nodes in FE mesh) discretizing the spatial domain $\boldsymbol{V}$, and $\otimes$ is a tensor product.

With chosen appropriate discretization over spatial and probability domains, the response further obtained by Stochastic Galerkin method ([153]) resulting with a

system of equations. Considering elastic case, for simplicity, we can write

$$\boldsymbol{K}\left(p(u)\right)\tilde{\boldsymbol{u}} = \boldsymbol{f} \tag{5.23}$$

By approximating the model response $\tilde{\boldsymbol{u}}$ by its PC approximation $\tilde{\boldsymbol{u}}$ given in (5.22) and applying Galerkin weighting residual procedure we can compute PCE coefficients corresponding to displacement field:

$$\int_{\Omega} \boldsymbol{H}(\xi) \otimes \boldsymbol{K}\left(p(\xi)\right) \otimes \boldsymbol{H}^{*}(\xi)) d\mathbb{P}(\omega) \cdot \beta - \int_{\Omega} \boldsymbol{H}(\xi) d\mathbb{P}(\omega) \otimes \boldsymbol{f} \tag{5.24}$$

Moreover, if the operator $\boldsymbol{K}(p)$ is linear also with respect to model parameters $\boldsymbol{p}(\omega)$, it can directly be expanded according to (Eq. (5.13)) as

$$\hat{\boldsymbol{K}}(\hat{p}(\xi)) \approx \bar{\boldsymbol{K}} + \sum_{i=0}^{N_\xi} \sqrt{\lambda_i} \xi_i \boldsymbol{K}_i \tag{5.25}$$

and then substituted in Eq. (5.24), which results with final product of Stochastic Galerkin method as N_ξ 'copies' of deterministic computation

$$\begin{aligned} \left[\bar{\boldsymbol{K}} \otimes \int_{\Omega} \boldsymbol{H}(\xi) \otimes \boldsymbol{H}^{*}(\xi) d\mathbb{P} + \sum_{i=0}^{N_\xi} \sqrt{\lambda_i} \boldsymbol{K}_i \otimes \int_{\Omega} \xi_i \cdot \boldsymbol{H}(\xi) \otimes \boldsymbol{H}^{*}(\xi) d\mathbb{P} \right] \cdot \beta \\ - \int_{\Omega} \boldsymbol{H}(\xi) d\mathbb{P}(\omega) \otimes \boldsymbol{f} = 0 \end{aligned} \tag{5.26}$$

The integrals in Eq. (5.26) can be solved numerically or analytically for less complex case resulting with a system of $M \times N$ equations for PCE coefficients β. These computation can be somewhat simplified by normalizing the Hermite polynomials, with $\int_{\Omega} \boldsymbol{H}(\xi) \otimes \boldsymbol{H}^{*} d\mathbb{P}(\xi)$ as the identity matrix and $\int_{\Omega} \boldsymbol{H}(\xi) d\mathbb{P}(\xi)$ as the first unit vector.

It is clear that the number of terms of PCE expansion increases quite fast with the increasing degree of polynomials N_p and/or dimensions N_ξ of $\xi(\omega)$ according to Eq. (5.21). The number of random variables is already reduced by transformation from vector of correlated random variables for model parameters $p(\omega)$ into uncorrelated variables $\xi(\omega)$. These variables are related to eigenvalues of different magnitude expressing the importance of particular eigenmodes. One possibility to decrease N is to neglect terms in PC expansion, where less important variables ξ_i are in higher orders ([153]). The maximal degree of polynomials p can be also reduced e.g. by a division of modeled domain $\boldsymbol{V}$ as presented e.g. by [155]. Other computational savings can be achieved by formulating Eq. (5.13) in tensorial notation instead of matrix one ([153]). These methods effectively create a 'surrogate' containing PCE representations of the forward model outputs. This model approximation may be evaluated in orders of magnitude more quickly than the 'direct' evaluation containing the full forward problem.

5.3 Plasticity at multiple scales: macro-scale reduced ED-FEM model for localized failure analysis of concrete

We also indicated in Chapter 2 that none of the classical plasticity criteria for concrete, which go under names of St. Venant or Rankine (e.g. see [73]), even when combined together [154], can not fully match the results obtained by our meso-scale model (see also Figure 5.4). Yet there is the need for concrete macro-scale model that can make structure scale computations accessible. Hence, the first goal of this paper is to provide the computational plasticity multi-surface criteria for concrete that can do better job than any classical criteria only in representing the full set of failure modes. The second goal is to enhance such model by making it stochastic plasticity in the sense that the parameters of such plasticity models are replaced by random fields or random variables. More importantly, we also seek to present the procedure of Bayesian inference providing probability distributions for such random variable that can serve as indication of quality of the particular model; for example with a smaller or larger value of standard deviation for such random variable, if it is Gaussian (although the proposed approach is not limited to Gaussian distribution, but can recover much more complex one). This development is carried out on a typical realization of the microstructure, and can thus be considered as the approach to provide the reduced model quantifying the lack of knowledge with respect to a given quantity of interest. If the latter is the internal energy, we recover the standard homogenization result on linear elastic response for any loading program (e.g. [159] or [160]), provided we have separation of scales with sufficient number of typical microstructure details.

To simplify our discussion we first consider deterministic case in the Euclidean setting and corresponding tensor notation [73], with displacement vector, $\mathbf{u}$, as a function of both space position $\mathbf{x}$ and pseudo-time t

$$\mathbf{u}(\mathbf{x},t) = u_i(\mathbf{x},t)\mathbf{e}_i; \qquad \mathbf{x} = x_i\mathbf{e}_i \tag{5.27}$$

Linearized kinematics is used to define the total strain tensor, ϵ, as the symmetric part of the displacement gradient

$$\boldsymbol{\epsilon} = \nabla^s\mathbf{u}; \qquad \epsilon_{ij}\mathbf{e}_i\otimes\mathbf{e}_j = \frac{1}{2}\left(\frac{\partial u_i}{\partial x_j} + \frac{\partial u_j}{\partial x_i}\right)\mathbf{e}_i\otimes\mathbf{e}_j \tag{5.28}$$

The same hypothesis on small displacement gradient allows us to express the equilibrium equations directly in the initial configuration in terms of Cauchy or true stress, $\boldsymbol{\sigma} = \sigma_{ij}\mathbf{e}_i\otimes\mathbf{e}_j$

In the presence of plastic deformation, the stress is computed not from the total but the elastic deformation. Namely, by assuming the independence of the elastic response on plastic flow, the total deformation can be split additively into elastic $\boldsymbol{\epsilon}^e$ and plastic part $\boldsymbol{\epsilon}^p$,

$$\boldsymbol{\epsilon} = \boldsymbol{\epsilon}^e + \boldsymbol{\epsilon}^p \tag{5.29}$$

By further assuming that the elastic response remains linear, reducing to Hooke's law in the absence of plastic deformation, we can construct the free energy potential as a quadratic form in terms of deformation tensor

$$\psi(\boldsymbol{\epsilon},\boldsymbol{\epsilon}^p,\zeta) := \tfrac{1}{2}(\boldsymbol{\epsilon}-\boldsymbol{\epsilon}^p)\cdot \boldsymbol{C}(\boldsymbol{\epsilon}-\boldsymbol{\epsilon}^p)) + \tfrac{1}{2}\zeta K\zeta \tag{5.30}$$

With concrete as statistically isotropic material we can fully characterize the elasticity tensor from two parameters only, such as bulk modulus K and shear modulus G. For simplicity, we also assume isotropic hardening case where qi is the stress-like internal variable dual to the strain-like internal state variable ζ. When limited to hardening regime in the fracture process zone the last ingredient of macro-plasticity model to define is the yield criterion. For example we take the classical Drucker-Prager model assuming shear failure:

$$\phi_y(\boldsymbol{\sigma},q) := \| \, dev[\boldsymbol{\sigma}] \, \| + \frac{1}{3}tan(\varphi)tr[\boldsymbol{\sigma}] - \sqrt{\frac{2}{3}}(\sigma_y - q) = 0; \quad dev[\boldsymbol{\sigma}] = \boldsymbol{\sigma} - \frac{1}{3}(tr[\boldsymbol{\sigma}])\mathbf{1} \tag{5.31}$$

where $\| \, \sigma \, \| := \sqrt{\sigma : \sigma}$ is the norm of the deviatoric part of the stress tensor $dev[\boldsymbol{\sigma}]$, $tan(\varphi)$ is material parameter that can characterize the internal friction and σ_y is uni-axial yield stress identified from a tension test.

By specifying three fundamental ingredients in (5.29), (5.30) and (5.31), we can completely define the stress tensor computation as well as the internal variables evolution for particular plasticity model. To that end we simply use the second principle of thermodynamics specifying the plastic dissipation:

$$0 \leq D^p := (\boldsymbol{\sigma} - \frac{\partial \psi}{\partial \boldsymbol{\epsilon}}) \cdot \dot{\boldsymbol{\epsilon}} - \frac{\partial \psi}{\partial \boldsymbol{\epsilon}^p} \cdot \dot{\boldsymbol{\epsilon}}^p - \frac{\partial \psi}{\partial \zeta} \cdot \dot{\zeta} \tag{5.32}$$

In the elastic case for $\phi < 0$, the plastic dissipation remains equal to zero, which allows to define the constitutive equation $D^p = 0$.

$$\boldsymbol{\sigma} := -\frac{\partial \psi}{\partial \boldsymbol{\epsilon}^p} \quad q := -\frac{\partial \psi}{\partial \zeta} \tag{5.33}$$

By assuming these equation remain valid for plastic case for $\phi < 0$ we can obtain the final expression for the plastic dissipation in inelastic case:

$$\phi = 0 \Rightarrow 0 < D^p := \boldsymbol{\sigma} \cdot \dot{\boldsymbol{\epsilon}}^p + q \cdot \dot{\zeta} \tag{5.34}$$

The principle of maximum plastic dissipation can be invoked stating that among all the admissible stress states (for which $\phi_y(\boldsymbol{\sigma},q) = 0$) , we ought to choose the one which maximizes the plastic dissipation. This problem of computing the maximum under the plastic admissibility constraint can be transformed into the corresponding

unconstrained minimization problem (see [73])

$$L^p(\boldsymbol{\sigma}, q, \dot{\gamma}) = \max_{\dot{\gamma}=0} \min_{\forall(\boldsymbol{\sigma}^*, q^*)} \left[L^p(\boldsymbol{\sigma}^*, q^*, \dot{\gamma}^*) \right]; \quad L^p(\boldsymbol{\sigma}, q, \dot{\gamma}) := -D^p(\boldsymbol{\sigma}, q) + \dot{\gamma}\phi_y(\boldsymbol{\sigma}, q) \tag{5.35}$$

The associated Kuhn-Tucker optimality conditions lead to evolution equations for internal variables:

$$\begin{aligned} 0 &= \frac{\partial L^p(\boldsymbol{\sigma}, q, \dot{\gamma})}{\partial \boldsymbol{\sigma}} = -\dot{\boldsymbol{\epsilon}}^p + \dot{\gamma}\frac{\partial \phi_y(\boldsymbol{\sigma}, q)}{\partial \boldsymbol{\sigma}}; \\ 0 &= \frac{\partial L^p(\boldsymbol{\sigma}, q, \dot{\gamma})}{\partial q} = -\dot{\zeta} + \dot{\gamma}\frac{\partial \phi_y(\boldsymbol{\sigma}, q)}{\partial q}; \\ \dot{\gamma} &\geq 0; \quad \phi_y(\boldsymbol{\sigma}, q) \leq 0; \quad \dot{\gamma}\phi_y(\boldsymbol{\sigma}, q) = 0 \end{aligned} \tag{5.36}$$

For a concrete-like material the dilatancy of plastic flow develops, which requires that the plastic potential function be different than the yield function

$$\phi_p(\boldsymbol{\sigma}, q) := \| \, dev[\boldsymbol{\sigma}] \, \| + \tfrac{1}{3} tan(\psi) tr[\boldsymbol{\sigma}] \tag{5.37}$$

where $tan(\psi)$ is material parameter describing the angle of dilatancy. It is important that such a choice can further lead to material instability phenomena even in hardening [73]. More typical case of material instability for either tension or compression failure which dealt with is associated with softening where stress decreases for increasing strain. Namely, we further present the strong discontinuity approach that can represent the cracking of concrete both in tension and compression. In compression, the model can represent three different deformation stages: linear elastic, hardening and localized softening. In tension, we only take elastic stage followed by unstable softening stage. In order to take into account all these dissipative mechanisms, we build multi-surface model which can reproduce the behavior of massive structures: a bulk dissipation characterized by the development of micro-cracks with Drucker-Prager citerion and a surface dissipation in localization zones in terms of the macro-cracks with St. Venant plasticity criterion. The latter is normally defined as three surface criterion ([73]) in strain space, but it can also be recast in standard format in stress space leading to:

$$\begin{aligned} \phi_1(\boldsymbol{\sigma}) &= \frac{3K+G}{9KG}\sigma_1 - \frac{3K-2G}{18KG}(\sigma_2+\sigma_3) - (\sigma_y - q) \leq 0 \\ \phi_2(\boldsymbol{\sigma}) &= \frac{3K+G}{9KG}\sigma_2 - \frac{3K-2G}{18KG}(\sigma_1+\sigma_3) - (\sigma_y - q) \leq 0 \\ \phi_3(\boldsymbol{\sigma}) &= \frac{3K+G}{9KG}\sigma_3 - \frac{3K-2G}{18KG}(\sigma_1+\sigma_2) - (\sigma_y - q) \leq 0 \end{aligned} \tag{5.38}$$

where we have chosen the reference value of the elasticity limit obtained from hydrostatic tension test. Figure 5.5.a shows a graphic illustration of the proposed multy-surface plasticity criterion in space of principal axes of stress tensor. We note that elastic region in tension is directly followed by softening. In compression, not only the ductile part with fracture process zone is larger, but also its contribution

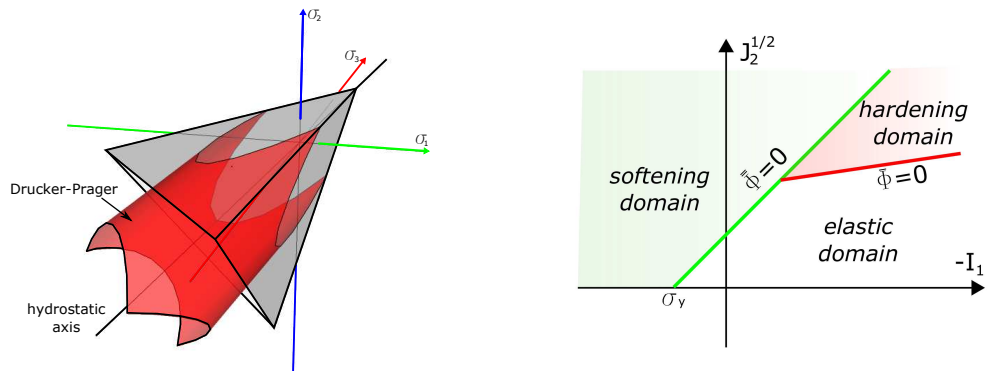

(a) (b)

Figure 5.5: Multisurface criterion (a) in principal stress space (b) in meridian plane

to total dissipation for compression failure. Figure 5.5.b reveals that the only load case which is not covered by this plasticity criterion, is a special case of failure under hydrostatic pressure.

It is now well understood that the softening phenomena require special interpolation referred as embedded discontinuity [162, 163] which can provide sharp representation of the crack. What is less well understood, is the kind of modification that such embedded discontinuity approach provides to representing the total plastic dissipation smeared in fracture process zone and sharp over macro crack [164]. More precisely, in order to provide the appropriate interpretation of the localized plastic deformation, we consider a domain $\mathcal{V}$ split into two sub-domains $\mathcal{V}^+$ and $\mathcal{V}^-$ by a crack as a surface of discontinuity. The total displacement field $\mathbf{u}$ is written as the sum of a smooth regular part $\bar{\mathbf{u}}$ and the displacement discontinuity $\bar{\bar{\mathbf{u}}}$, centered at the Γ_s. For the surface of discontinuity, we can define at each point a unit vector of exterior normal $\mathbf{n}$, a tangential vector $\mathbf{m}$ and binormal vector $\mathbf{b}$. The discontinuous displacement field can then be written as

$$\mathbf{u}(\mathbf{x},t) = \bar{\mathbf{u}}(\mathbf{x},t) + \bar{\bar{\mathbf{u}}}(\mathbf{x},t) M_{\Gamma_s}(\mathbf{x}); \qquad M_{\Gamma_s}(\mathbf{x}) = H_{\Gamma_s}(\mathbf{x}) - N_{\tilde{\mathcal{V}}}(\mathbf{x}) \tag{5.39}$$

where $H_{\Gamma_s}(\mathbf{x})$ is the Heaviside function being equal to 1 in $\mathcal{V}^+$ and to 0 in $\mathcal{V}^-$, whereas $N_{\tilde{\mathcal{V}}}(\mathbf{x})$ is chosen function which leaves only regular part of displacement fiels at nodes (typically judicious combination of shape functions)

The corresponding deformation field produced by such a displacement can be decomposed into a regular part and a singular part as

$$\boldsymbol{\epsilon}(\mathbf{x},t) = \underbrace{\nabla^s \bar{\mathbf{u}}(\mathbf{x},t) + \bar{G}(\mathbf{x})\bar{\bar{\mathbf{u}}}(t)}_{\bar{\boldsymbol{\epsilon}}=\bar{\boldsymbol{\epsilon}}^e+\bar{\boldsymbol{\epsilon}}^p} + \underbrace{(\bar{\bar{\mathbf{u}}}(t)\otimes\mathbf{n})^s}_{\bar{\bar{\boldsymbol{\epsilon}}}^p=\alpha\boldsymbol{m}\otimes\boldsymbol{n}} \delta_\Gamma(\mathbf{x}); \qquad \bar{G}(\mathbf{x}) = -\nabla^s N_{\tilde{\mathcal{V}}}(\mathbf{x}) \tag{5.40}$$

The strain field appears then to be decomposed into a regular part and a singular part. The latter is used to express localized plastic deformation by means of the

Dirac-delta function $\delta_\Gamma(\mathbf{x})$. The strain energy in this case can be written:

$$\psi(\boldsymbol{\epsilon},\bar{\zeta},\bar{\bar{\zeta}}) := \underbrace{\bar{\psi}^e(\boldsymbol{\epsilon}^e,\bar{\zeta})}_{regular} + \bar{\bar{\Xi}}(\bar{\bar{\zeta}})\delta_{\Gamma_s} \tag{5.41}$$

where the first term is the elastic energy and hardening, whereas the second term is the contributions of softening mechanisms. The total plastic dissipation can be expressed as the sum of the dissipation in the fracture process zone in $\tilde{\mathcal{V}}$ and from the crack induced discontinuity on Γ_s, which can be written:

$$0 \leq D^p_{\tilde{\mathcal{V}}} = \int_{\tilde{\mathcal{V}}} \left[\boldsymbol{\sigma}\cdot\dot{\bar{\boldsymbol{\epsilon}}} - (\dot{\psi}^e(\boldsymbol{\epsilon}^e) + \dot{\bar{\bar{\Xi}}}(\bar{\zeta}))\right] dV + \int_{\Gamma_s} [\mathbf{t}\cdot\mathbf{m}]\,\dot{\alpha} dA - \int_{\Gamma_s} \dot{\bar{\bar{\Xi}}}(\bar{\bar{\zeta}}) dA \tag{5.42}$$

Provided we enforce the weak form of the Cauchy principle connecting stress in the fracture process zone with traction at discontinuity

$$\int_{\tilde{\mathcal{V}}} \boldsymbol{\sigma}\cdot\tilde{\mathbf{G}}\mathbf{m}\dot{\alpha} dV + \int_{\Gamma_s} (\mathbf{t}\cdot\mathbf{m})\,\dot{\alpha} dA = 0 \tag{5.43}$$

we can further obtain the additive decomposition of the total plastic dissipation into a regular part in fracture process zone and a singular part at crack of surface of discontinuity:

$$D^p_{\tilde{\mathcal{V}}} = \int_{\tilde{\mathcal{V}}} \left(\boldsymbol{\sigma}\cdot\dot{\bar{\boldsymbol{\epsilon}}}^p + \bar{q}\dot{\bar{\zeta}}\right) dV + \int_{\Gamma_s} \bar{\bar{q}}\dot{\bar{\bar{\zeta}}} dA \tag{5.44}$$

The yield condition controlling evolution of the inelastic deformation at discontinuity is set directly in terms of the traction vector:

$$\bar{\bar{\phi}}(t_m,\bar{\bar{q}}) = |\underbrace{\mathbf{t}\cdot\mathbf{m}}_{t_m}| - (\sigma_y - \bar{\bar{q}}) \tag{5.45}$$

where σ_y is a localized failure threshold and $\bar{\bar{q}}$ is the internal variable for softening. When choosing exponential constitutive law for softening, we define stress like internal variable for softening plasticity as:

$$\bar{\bar{q}} = \sigma_y\left(1 - exp\left(-\bar{\bar{\zeta}}\frac{\sigma_y}{G_f}\right)\right) \tag{5.46}$$

where G_f is the corresponding value of fracture energy. At the level of meso-scale model the compressive and the tension failure mechanisms are reproduced according to the same fracture mode driven by the principal tensile strains. However, at present macro-scale, the corresponding amount of fracture energy can be quite different because of the number of cracks created in those two cases. This can be handled by modifying in (5.46) how to compute fracture energy change from a value in tension G_t to compression in agreement with dominant elastic strain:

$$G_f = \frac{G_c + G_t}{2} - \frac{G_c - G_t}{2}\tanh(\beta \mathrm{tr}[\epsilon]) \tag{5.47}$$

where β is a parameter to be chosen to set a more or less rapid transition.

In the case where both fracture process zone and macro crack are active, we assume most general condition of plastic deformation with the plastic multiplier that takes the form $\dot{\gamma} = \dot{\bar{\gamma}} + \dot{\bar{\bar{\gamma}}}\delta_{\Gamma_s}$. The principle of maximum plastic dissipation can be stated for the complete macro-scale domain including the crack (or for a particular finite element with embedded discontinuity)

$$\bar{\bar{L}}^p_{\mathcal{V}}(\boldsymbol{\sigma}, \bar{q}, \bar{\bar{q}}, \dot{\bar{\bar{\gamma}}}) = \max_{\dot{\bar{\bar{\gamma}}} \geq 0} \min_{\forall (t^*, \bar{\bar{q}}^*)} \left[\bar{\bar{L}}^p_{\mathcal{V}}(\boldsymbol{\sigma}^*, \bar{q}^*, \bar{\bar{q}}^*, \dot{\bar{\bar{\gamma}}}^*) \right] = -D^{loc}_{\mathcal{V}}(\cdot) + \int_{\mathcal{V}} \dot{\bar{\gamma}} \bar{\Phi} dV + \int_{\Gamma_s} \dot{\bar{\bar{\gamma}}} \bar{\bar{\Phi}} dA \tag{5.48}$$

The Kuhn-Tucker optimality condition will provide the global form of corresponding evolution on (5.36)equation for internal variables:

$$\begin{aligned} 0 &= \int_{\mathcal{V}} \left(-\dot{\bar{\boldsymbol{\epsilon}}}^p + \dot{\bar{\gamma}} \frac{\partial \bar{\phi}}{\partial \boldsymbol{\sigma}} \right) dV; \\ 0 &= \int_{\mathcal{V}} \left(-\dot{\bar{\zeta}}^p + \dot{\bar{\gamma}} \frac{\partial \bar{\phi}}{\partial \bar{q}} \right) dV; \end{aligned} \tag{5.49}$$

along with evolution equation for softening internal variable

$$0 = \int_{\Gamma_s} \left(-\dot{\bar{\bar{\zeta}}} + \dot{\bar{\bar{\gamma}}} \frac{\partial \bar{\bar{\phi}}}{\partial \bar{\bar{q}}} \right) dA \quad \Rightarrow \int_{\Gamma_s} \dot{\bar{\bar{\zeta}}} dA = \int_{\Gamma_s} \dot{\bar{\bar{\gamma}}} dA \tag{5.50}$$

The plastic multiplier can be computed from enforcing plastic consistency condition which by means of (5.45) results with:

$$\int_{\mathcal{V}} \dot{\bar{\bar{\gamma}}} \Gamma_s \dot{\bar{\bar{\phi}}} \Rightarrow \dot{\bar{\bar{\gamma}}} = \frac{1}{\bar{\bar{K}}} \int_{\mathcal{V}} \bar{\mathbf{G}} \dot{\boldsymbol{\sigma}} dV \tag{5.51}$$

The finite element implementation of macro-scale model in deterministic setting is based upon standard semi-discretization procedure [73] to construct the finite-element-based displacement approximation over a single element $\mathcal{V}^e$

$$\mathbf{u}(\mathbf{x}, t)\,|_{\mathcal{V}^e} = \sum_{a=1}^{n_{en}} \mathbf{N}^e_a(\mathbf{x}) \mathbf{u}_a(t) \tag{5.52}$$

where 'n_{en}' is the total number of element nodes, $\mathbf{N}^e_a(\mathbf{x})$ are the finite element shape functions and $\mathbf{u}_a(t)$ are the nodal displacements. By replacing this discrete approximation into the weak form of the equilibrium equations and integrating with respect to the space variables $\mathbf{x}$, we reduce the problem to tracing the pseudo-time history of the state variables. In other words, the strong form of evolution equations in (5.49) will accompany the weak form of equilibrium equations that can be written as

$$\begin{aligned} G := \mathop{A}_{e=1}^{n_{el}} \{ &\textstyle\int_{\mathcal{V}^e} \mathbf{B}^{eT}_a(\mathbf{x}) \boldsymbol{\sigma}(\boldsymbol{\epsilon}(\mathbf{x}, t), \boldsymbol{\epsilon}^p(\mathbf{x}, t), \zeta(\boldsymbol{\xi}, t))\, dV \\ &- \textstyle\int_{\mathcal{V}^e} \mathbf{N}^e_a(\mathbf{x}) \cdot \mathbf{b}(\mathbf{x}, t) dV - \int_{\Gamma_\sigma} \mathbf{N}^e_a(\mathbf{x}) \cdot \mathbf{t}(\mathbf{x}, t)\, dA \} = \mathbf{0} \end{aligned} \tag{5.53}$$

where $\overset{n_{el}}{\underset{e=1}{A}}$ denotes the standard finite element assembly procedure over the total number of elements n_{el}.

By choosing the Gauss quadrature rule with n_{in} points, with abscissas $\boldsymbol{\xi}_l$ and integration weights w_l we can significantly reduce the computation for evolution of internal variables to a finite number of numerical integration points:

$$\begin{aligned} G = \overset{n_{el}}{\underset{e=1}{A}} \{ \sum_{l=1}^{n_{in}} (w_l \mathbf{B}_a^{eT}(\boldsymbol{\xi}_l) \boldsymbol{\sigma}(\boldsymbol{\epsilon}(\boldsymbol{\xi}_l,t), \boldsymbol{\epsilon}^p(\boldsymbol{\xi}_l,t), \zeta(\boldsymbol{\xi}_l,t)) j(\boldsymbol{\xi}_l) \\ - w_l \mathbf{N}_a^e(\boldsymbol{\xi}_l) \cdot \mathbf{b}(\boldsymbol{\xi}_l,t) j(\boldsymbol{\xi}_l) - \sum_{l=1}^{n_{in}} w_l \mathbf{N}_a^e(\boldsymbol{\xi}_l) \cdot \mathbf{t}(\boldsymbol{\xi}_l,t) \} = \mathbf{0} \end{aligned} \tag{5.54}$$

In the softening phase the finite element interpolation is chosen to take into account a displacement discontinuity, by considering the incompatible mode methods [74], we choose :

$$\mathbf{u}^h(\mathbf{x},t)|_{\mathcal{V}^e} = \mathbf{N}(\mathbf{x})\mathbf{u}_a(t) + \mathbf{M}(\mathbf{x})\boldsymbol{\alpha}(t) \tag{5.55}$$

where $\boldsymbol{\alpha}(t)$ is incompatible mode parameters and $\mathbf{M}(\mathbf{x})$ are discontinuous interpolation functions. The discontinuity can be introduced by splitting the 8-node brick element such that a pair of nodes is placed at each side of the discontinuity, if $\mathcal{V}^+$ denotes the part of the element on one side of the opening surface, we can thus write:

$$\mathbf{M}(\mathbf{x})|_{\mathcal{V}^e} = H_{\Gamma_s}(\mathbf{x}) - \sum_{b \in \mathcal{V}^+} \mathbf{N}_b(\mathbf{x}) \tag{5.56}$$

With such a discrete approximation, the finite element interpolation of the strain field can be written as:

$$\boldsymbol{\epsilon}^h(\mathbf{x},t)|_{\mathcal{V}^e} = \mathbf{B}(\mathbf{x})\mathbf{u}_a + \mathbf{G}_r(\mathbf{x})\boldsymbol{\alpha}(t) \tag{5.57}$$

where $\mathbf{G}_r(\mathbf{x})$ is strain-incompatible-modes matrix. The finite element interpolation of the virtual strain field can be constructed with the same scheme but with the modified strain-incompatible-modes matrix so that the patch test condition of its orthogonality as constant stress field is meet [73].

$$\delta\boldsymbol{\epsilon}^h(\mathbf{x})|_{\mathcal{V}^e} = \mathbf{B}(\mathbf{x})\delta\mathbf{u}_a + \delta\boldsymbol{\alpha}\mathbf{G}_v(\mathbf{x}); \qquad \int_{\mathcal{V}^e} \mathbf{G}_v(\alpha) dV = 0 \tag{5.58}$$

where $\delta\mathbf{u}_a$ and $\delta\boldsymbol{\alpha}(t)$ denote, respectively, the virtual displacement field and incompatible modes variations.

5.4 Stochastic macro-scale plasticity model parameters identification by Bayesian inference

It is the first goal of this work to consider inelastic response, both in plastic hardening and localized failure regime, and define the corresponding choice of model parameters

described as random variables and provide their probability distributions. Here, this will be accomplished in terms of Bayesian inference adapted to here proposed framework, where the data generated by both experiments and computations with the concrete meso-scale model obtained for a particular realization of the microstructure and for a particular loading program will be considered as information produced by dynamic process. The main benefits of the proposed approach and this point-of-view is in providing the way of selecting the most appropriate model ingredients in handling different phases of inelastic response, as well as the most adequate loading programs that favors the sharp estimates of the probability distributions of each macro-scale model parameter.

The proposed approach is targeting the stochastic scale transition, which need not discard the excessive information from fine scales when providing the coarse scale model parameters, such as done in homogenization. Thus, it can also be thought as the part of the multi-scale modeling strategy. However, the same approach should be used in combination with experiments, where possible measurements (force, displacement) are completed by the fine scale results that replace the real measurements on the specimen for a particular loading program. For this particular case, the quality of identification results is improved by fine scale simulations with the response of real heterogeneous materials. Hence, the choice of the quantity of interest, which here corresponds to the cost function for particular inverse problem, need not be significantly reduced to using only the quantities that can be directly measured.

Two modifications are needed for stochastic plasticity described in this section. First, we replace the Galerkin procedure domain $\mathcal{V}$ by combined spatial $\mathcal{V}$ and probability domain Ω. Second, we need to obtain the probability distribution on stochastic plasticity model parameters (or stochastic discretization) in order to be able to solve this coupled mechanics-probability problem. In summary, the deterministic model of macro-scale plasticity is defined by a set of model parameters $p = (K, G, \sigma_y, \beta, tan(\phi), tan(\psi), \sigma_u, G_{f,t}, G_{f,c})$ denoting respectively bulk modulus, shear modulus, yield stress, angle of internal friction, angle of internal dilatancy, ultimate stress and fracture energy in tension and in compression. This prediction depends on how the parameters are chosen. They have to be chosen so that the difference between the prediction of the mathematical model and the observed system response (micro-scale prediction or experiment) will be as small as possible. Different possibilities for this task have been explored.

One possibility is to look at the difference between predicted and observed behavior and to try to minimise this difference. This is an optimisation approach which leads to regularization procedures, see e.g. [165, 166, 133]. This is a purely deterministic procedure, where no previous knowledge on the possible parameter values enters the picture, and where the functional of the difference alluded to above is usually chosen out of convenience - least squares is a frequent choice.

On the other hand the whole problem can be viewed as a situation where one is uncertain about the best value for the parameters, and models this situation by not just considering a fixed value as the solution, but contemplating a whole range of possible values, something which can be modeled by a random variable (RV). This is

true especially when prior knowledge is to be taken into account. In that case one wants to attach different weights to the prior knowledge and to the new knowledge learned from the observation. The probabilistic procedures for this are based on $Bayes's$ theorem, see e.g. [167]. This can be explained in a simple manner as that one models the uncertainty about a certain event - a parameter having a certain value here - with a probabilistic model. One then observes another variable, which in some way is dependent on or correlated with the parameter in question. This observation then can be used to correct or update the probabilistic model of the uncertainty we have about the value of the parameter. To be more specific these parameters are need to carry out the macro-scale prediction computation by solving the set of evolution equation for the state $u(t) \in \mathcal{U}$ at time $t \in [0,T]$ in the week form in (5.54) and internal variable flow equations in (5.36), for any loading program, which we will symbolically denote with:

$$\frac{\partial u(t)}{\partial t} + A\left(p; u(t)\right) = f(p;t) \tag{5.59}$$

and where A is an operator modeling the physics of the system, and $f \in \mathcal{U}^*$ (the dual space) is some external influence (action / excitation / loading). The model A and the action f depend on some parameters $p \in \mathcal{P}$. Some of these parameters may actually be 'controls', i.e. something one can influence and hence it is known exactly. By $q \in \mathcal{Q}$ we shall denote that component of the parameters p which we cannot control and where we are uncertain about their best value. In the following we shall only track the dependence on the uncertain part q trying to obtain their probability distribution and thus better define their values. It is important to say that this random variable are defined by corresponding transformation of the parameters p (often restricted to the positive cone to the vector space by bijective differentiable mapping T_q such that $q = T_q(p)$.

The observation of the system are the best prediction we could obtain by either micro-scale model computation or some experimental measurements $\hat{y} \in \mathcal{Y}$, where Y is the space of all possible measurements, typically some $\mathbb{R}^k$, assuming that the measurements consists of k real numbers each time it is observed. In addition to the mathematical model 5.59 describing the state evolution $t \to u(q;t)$, which also depends on the parameters p resp. q, one has to make the corresponding model for the observations or measurements, and their dependence on p resp. q. So the mathematical model for the observation is defined as quantity of interest as function of the state of the system

$$(q,t,\epsilon) \to Y(u(q;t),q,\epsilon) \in \mathcal{Y} \tag{5.60}$$

and the parameters q we would like to determine. The variable ϵ is meant to model possible errors, due to the observation or measurement procedure or due to the model 5.59 being less than perfect, i.e. model error. So $Y(u(q;t),q,\epsilon)$ is the mathematical model to predict what the observation at time t would be, given a certain value for the state $u(t)$ at time t, the parameters q, and the error ϵ.

It seems natural that we would be interested in choosing the parameter q such as to make the difference $\hat{y} - Y(u(q;t),q,\epsilon)$ as small as possible. The task of predicting

the state $u(q;t)$ for given q and t from 5.59, and subsequently a prediction or forecast for the observation $y = Y(u(q;t), q, \epsilon$ is called the forward problem. We shall assume that this is a well-posed problem in the sense of Hadamard for all possible values of $q \in \mathcal{Q}$.

To glean information about q from observing $\hat{y}$, one has to in some way invert the mapping in 5.60 $q \to Y(q) = \hat{y}$, where we have neglected the other variables for the sake of concise notation. This is called the *inverse* problem, and as the mapping $q \to Y(q)$ is usually not invertible, the inverse problem is ill-posed [165–167]. To approach ill-posed problems computationally directly is typically ill-advised as it is numerically unstable and hence would produce unreliable results. This means that one has to add some additional information to the situation for the inverse problem to become reliable and numerically stable.

The *regularization* approach, e.g. [165, 166], is proposed to make $q \in \mathcal{Q}$ in some way regular - hence the name - by desiring that the parameter be in some more *regular* subset $q \in \mathcal{Q}_0 \subset \mathcal{Q}$, and typically penalizing deviations from $\mathcal{Q}_0$. The kind of regularization proposed here concerns, widening the problem of finding the best q to a larger class of problems, where the knowledge about q is described probabilistically. More precisely, this means that one wants to update the probability distribution describing the knowledge about q to include the new information gained from observing $\hat{y}$. These updates rest on *Bayes's theorem* - e.g. [167] and are thus called *Bayesian updates*. There are intimate connections between the two approaches, with the main view being that the probabilistic approach gives some explanations resp. background information for otherwise seemingly ad-hoc decisions which have to be taken in the regularization approach.

The description of the general Bayesian updating procedure [168–171, 180] gives as follows. Proceeding from computed results by mathematical model in (5.59) and the measurement or observation operator defined in (5.60), for simplicity we envisage observations $y = Y(u(q;t), q, \epsilon)$ at discrete times $0 < t_1 < \cdots < t_n, \cdots \in [0, T]$, i.e

$$y_n := Y(u(q;t_n), q, \epsilon), \quad n = 1, \ldots; \tag{5.61}$$

which are different realization of quantity of interest provided by computations or the model of the measurement. From these observation one would like to obtain at each instant t_n both a new — and hopefully better — estimate for q and for the state $u(q;t_n)$. In the Bayesian framework (e.g. [167]) this is done by modeling the uncertainty about the value of q probabilistically, by assuming

$$q : \Omega \to \mathcal{Q} \quad \text{as a RV on a probability space}\,(\Omega, \mathfrak{U}, \mathbb{P}) \tag{5.62}$$

where Ω is the set of all possible realisations of q and the error ϵ in (5.60), and $\mathfrak{A}$ is the σ-algebra of measurable sets $\mathcal{E} \subset \Omega$ which may be assigned a probability $\mathbb{P}(\mathcal{E})$ via the *prior* probability measure $\mathbb{P}$ which represents our initial or prior probabilistic knowledge about q, as well as about the error ϵ in (5.60).

By introducing this random variable into the defining model equations (5.59), turns the state $u(q;t)$ into RV

$$u : \Omega \times [0,T] \to \mathcal{U}; \quad (\omega,t) \mapsto u(q(\omega);t), \tag{5.63}$$

as well as the predicted or forecast measurement Y in (5.60)

$$Y : \Omega \times [0,T] \to \mathcal{U}; \quad (\omega,t) \mapsto Y(u(q(\omega),t), q(\omega), \epsilon(\omega)). \tag{5.64}$$

The model evolution equation (5.59) has now become a *stochastic* or differential equation, which we will solve by Galerkin procedure by computing expected values, which concerns the integrals over domain Ω At fixed time $t = t_n$ in (5.64) the predicted observation y_n in (5.61) also becomes a RVs. What is actually measured or observed (e.g. computed by micro-scale model) at time t_n may be viewed as a realization $\omega_n \in \Omega$ of this random variable

$$\hat{y}_n = y_n(\omega_n) = Y(u(q(\omega_n),t_n), q(\omega_n), \epsilon(\omega_n)) = Y(u_n, q, \epsilon_n) \in \mathcal{Y}. \tag{5.65}$$

So the observation or measurement is a sequence of K samples of Y in (5.64), $\hat{\boldsymbol{y}} = (\hat{y}_1, \ldots, \hat{y}_n, \ldots, \hat{y}_N) \in \mathcal{Y}^N$. With such a sequence of observations, there are different ways how the update can be done. The simplest is to assume that after each observation we perform an update of the knowledge about q, which is one extreme where updating would proceeds in a purely sequential manner:

1. start with the *prior* $q_0(\omega)$ as *forecast* $q_f(\omega) = q_0(\omega)$, and set $k = 0$;
2. **loop** over $n := n+1$;
3. *forecast* or predict the observation at t_k as a RV $y_f(\omega) = y_n(\omega)$ from (5.64);
4. observe or measure $\hat{y}_n$ at time t_n as described in (5.65);
5. from $y_n(\omega)$ and $\hat{y}_n$ update the *forecast* $q_f(\omega) = q_{n-1}(\omega)$ to the *assimilated* $q_a(\omega)$, and set $q_n(\omega) = q_a(\omega)$;
6. **endloop**

At the extreme other end one could updating all in one step after the results of all realization are gettered:

1. from the prior or *forecast* $q_f(\omega) = q_0(\omega)$ predict or forecast the observations $\boldsymbol{y}_f(\omega) = (y_1(\omega), \ldots, y_N(\omega))$ at times $t_1, \ldots, t_N$;
2. observe or measure all the values $\hat{\boldsymbol{y}} = (\hat{y}_1, \ldots, \hat{y}_N)$ at times $t_1, \ldots, t_N$;
3. from $\hat{\boldsymbol{y}}$ and $\boldsymbol{y}_f(\omega)$ update the *forecast* $q_f(\omega)$ to the *assimilated* $q_a(\omega)$.

The steps 1–3 in this last algorithm are formally analogous to the steps 3–5 of the preceding sequential algorithm, just the forecast and observation vector are larger in the last all-in-one update procedure. Obviously it is also possible to mix the purely

sequential and the all-in-one procedures by updating in batches several times. The best strategy depend on a particular problem at hands. If we want to identify the probability distribution of parameters in $p = (K, G, \sigma_y, \beta, tan(\phi), tan(\psi), \sigma_u, G_{f,t}, G_{f,c})$, not only we split the choice of the quantity of interest Y into corresponding sequence of separating parameters governing elastic, hardening and softening response [133], but we also split the time sequence of realizations to privilege certain type of response. If the updating is used to control the particular loading program and the response of the system (5.59), would most probably choose the purely sequential procedure.

Hence we will focus on just one step, knowing the *forecast* RV $q_f(\omega)$ predicting or forecasting the observation RV $\mathbf{y}_f(\omega)$ — which may be just $\boldsymbol{y}_f(\omega) = y_n(\omega)$, or $\boldsymbol{y}_f(\omega) = (y_1(\omega), \ldots, y_N(\omega))$ — and observing the corresponding measurement $\hat{\mathbf{y}}$ we perform the update of the forecast $q_f(\omega)$ to the assimilated $q_a(\omega)$, i.e. the information or knowledge of the observation $\hat{\boldsymbol{y}}$ has been *assimilated* into the system. Two methods of Bayesian updates will be proposed: the first is Markov-Chain Monte Carlo (MCMC) that is updating the the probability measure having the same function $q(\omega)$, and the second is referred to as Gauss-Markov-Kalman filter that keeps the same measure but updates the function $q(\omega)$.

5.4.1 MCMC Bayesian updating of the measure

Bayes's theorem is considered as the consistent way to update a probabilistic description when new data in the form of the observation $\hat{\boldsymbol{y}}$ is available. Assume that $\mathcal{I}_q \subset \mathcal{Q}$ is some subset where the probabilistic model, in form of the *prior* RV q_f, gives a *prior* probability of $\mathbb{P}(\mathcal{I}_q)$. Then Bayes's theorem (e.g.[167]) states:

$$\mathbb{P}(\mathcal{I}_q|\mathcal{M}_y) = \frac{\mathbb{P}(\mathcal{M}|\mathcal{I}_q)}{\mathbb{P}(\mathcal{M}_y)}\mathbb{P}(I_q), \quad \text{if } \mathbb{P}(\mathcal{M}_y) > 0; \tag{5.66}$$

where $\mathcal{M}_y$ is the information provided by the measurement. It shows that the prior probability $\mathbb{P}(\mathcal{I}_q)$ is multiplied by the so-called Bayes-factor $\mathbb{P}(\mathcal{M}_y|\mathcal{I}_q)/\mathbb{P}(\mathcal{M}_y)$ to give the *posterior* conditional probability $\mathbb{P}(\mathcal{I}_q|\mathcal{M}_y)$, the probability of $\mathcal{I}_q$ *conditioned* on the observation $\mathcal{M}_y$. The numerator $\mathbb{P}(\mathcal{M}_y|\mathcal{I}_q)$ in the Bayes-factor is called the *likelihood* — the conditional probability of observing $\mathcal{M}_y$ under the condition that $\mathcal{I}_q$ is true — and the denominator $\mathbb{P}(\mathcal{M}_y)$, which is the total probability of observing $\mathcal{M}_y$ not knowing anything about q_f, is called the *evidence*.

It is worthwhile to observe from (5.66) that no matter what the observation and the resulting Bayes-factor, $\mathbb{P}(\mathcal{I}_q) = 0$ will always imply $\mathbb{P}(\mathcal{I}_q|\mathcal{M}_y) = 0$. Similarly, by using Bayes's theorem (5.66) on the set $\mathcal{Q} \setminus \mathcal{I}_q$ with $\mathbb{P}(\mathcal{Q} \setminus \mathcal{I}_q) = 1 - \mathbb{P}(\mathcal{I}_q)$, one sees that $\mathbb{P}(\mathcal{I}_q) = 1$ will always imply $\mathbb{P}(\mathcal{I}_q|\mathcal{M}_y) = 1$. Hence strong convictions in this sense in the prior probabilistic model are completely insensitive to any evidence. This should be avoided in the probabilistic model, unless there is a physical or logical impossibility involved. It has been called *Cromwell's* rule in Bayesian inference after Oliver Cromwell who famously wrote "...think it possible that you may be mistaken".

As one may glean from (5.66), Bayes's theorem only tells us how to change the *distribution* of the RV $q : \Omega \to \mathcal{Q}$. This is a probability measure on subsets of $\mathcal{Q}$ which

comes from the probability measure $\mathbb{P}$ in (5.62), such that in (5.66) for example for $\mathcal{I}_q \subseteq \mathcal{Q}$ one measures the probability of $q^{-1}(\mathcal{I}_q) \subseteq \Omega$. This measure, the distribution of q, is also known as the *push-forward*, as it is carried from Ω to $\mathcal{Q}$, and could be more precisely be denoted by $q_*\mathbb{P}$ or $\mathbb{P}_q$, but it is common for the sake of brevity to denote all probabilities just by the symbol $\mathbb{P}$, as it is clear from the context what is meant:

$$\mathbb{P}(\mathcal{I}_q) := q_*\mathbb{P}(\mathcal{I}_q) := \mathbb{P}_q(\mathcal{I}_q) = \mathbb{P}(q^{-1}(\mathcal{I}_q)) = \mathbb{P}(\{\omega \in \Omega \mid q(\omega) \in \mathcal{I}_q\}), \tag{5.67}$$

where the first three expressions denote the distribution resp. the push-forward measure of q, and the last two expressions are the original measure on subsets of Ω from (5.62). Analogous statements can be made for the other probabilities appearing in (5.66).

Now (5.66) describes how the distribution of the RV q should change when new evidence in the form of $\mathcal{M}_y$ is observed. From (5.67) one may see that this can be achieved in different ways. One possibility is to leave the map $q : \Omega \to \mathcal{Q}$ in (5.62) unchanged and change the measure $\mathbb{P}$ according to (5.66). A procedure which builds on this idea is the Markov-chain Monte Carlo (MCMC) method, which will be described subsequently.

Updating of the Probability Density: the main difficulty in using the statement of (5.66) as computational tool is that it requires that $\mathbb{P}(\mathcal{M}_y) > 0$. When the observation $\hat{\boldsymbol{y}}$ is one of a non-discrete or continuous RV, it is typical that the set $\mathcal{M}_y$ has vanishing probability measure, i.e. $\mathbb{P}(\mathcal{M}_y) = 0$, as for a continuous RV $\boldsymbol{y}_f(\omega)$ the observation is either $\mathcal{M}_y = \{y(\omega_n) = \hat{\boldsymbol{y}} = \hat{y}_n \in \mathcal{Y}\}$, or $\mathcal{M}_y = \{(y(\omega_1), \ldots, y(\omega_N) = \hat{\boldsymbol{y}} = (\hat{y}_1, \ldots, \hat{y}_N) \in \mathcal{Y}^N\}$. In any case it is usually a set of vanishing probability measure, and hence in (5.66) the Bayes-factor $\mathbb{P}(\mathcal{M}_y|\mathcal{I}_q)/\mathbb{P}(\mathcal{M}_y)$ then becomes the undefined expression 0/0, and ammn we will need some limiting argument [172, 173]. This has in the history of probability theory led to controversy on how to do the passage to the limit, cf. the *Borel-Kolmogorov paradox.*

One case where such a passage to the limit is possible is the case when all measures involved in (5.66) have probability density functions (pdf), with respect to the same background measure. In case $\mathcal{Q}$ and $\mathcal{Y}$ are finite dimensional vector spaces, this background measure is often the Lebesgue measure. A main requirement is that there is a joint pdf $\pi_{(Q,Y)}(q, \boldsymbol{y})$ of the RVs q and $\boldsymbol{y}$ [173]. In such case it is possible to state for the *conditional density* $\pi_{(Q|Y)}(q|\boldsymbol{y})$:

$$\pi_{(Q|Y)}(q|\boldsymbol{y}) = \frac{\pi_{(Q,Y)}(q, \boldsymbol{y})}{\pi_Y(\boldsymbol{y})} = \frac{\pi_{(Y|Q)}(\boldsymbol{y}|q)}{\pi_Y(\boldsymbol{y})}\pi_Q(q), \tag{5.68}$$

where

$$\pi_Y(\boldsymbol{y}) = \int_{\mathcal{Q}} \pi_{(Q,Y)}(q, \boldsymbol{y})dq = \int_{\mathcal{Q}} \pi_{(Y|Q)}(\boldsymbol{y}|q)\pi_Q(q)dq \tag{5.69}$$

is the pdf of the RV $\boldsymbol{y}$, the *evidence*, and $\pi_Q(q)$ is the *prior* pdf of q, and $\pi_{(Y|Q)}(\boldsymbol{y}|q)$ is the *likelihood* of $y = Y(q, \epsilon)$ given q. These terms are in direct correspondence with those in (5.66). The second part of the equation in both (5.68) and (5.69) comes

from factoring the joint density into the likelihood and the prior: $\pi_{(Q,Y)}(q,\boldsymbol{y}) = \pi_{(Y|Q)}(\boldsymbol{y}|q)\pi_Q(q)$, which is how the joint pdf is typically available.

After observing $\hat{\boldsymbol{y}}$, the *posterior* pdf of q is then given by $\pi_{(Q|Y)}(q|\hat{\boldsymbol{y}})$. Observe from (5.68) that Cromwell's rule is visible here again: if $\mathcal{I}_q \subset \mathcal{Q}$ is assigned a vanishing prior pdf, i.e. $\pi_Q(q) = 0$ for $q \in \mathcal{I}_q$, then no matter what the evidence in the Bayes-factor $\pi_{(Q,Y)}(q,\boldsymbol{y})/\pi_Y(\boldsymbol{y})$ for pdfs, the posterior $\pi_{(Q|Y)}(q|\boldsymbol{y})$ will also always be identically zero.

Let us point out that to evaluate (5.59), one may assume that the prior $\pi_Q(q)$ is given. However, to evaluate the conditional pdf or likelihood $\pi_{(Y|Q)}(\boldsymbol{y}|q)$, for each given q one has to solve for the model response and evaluate the forecast measurement in (5.60). This computational expense is amplified when the evidence $\pi_Y(\boldsymbol{y})$ in (5.69) has to be evaluated, as it is a often high-dimensional integral over $\mathcal{Q}$ requiring typically many evaluations of the likelihood.

Most computational approaches to determine the pdfs are based on variants of the Markov-chain Monte Carlo (MCMC) method [174–176, 168], where at least the evidence $\pi_Y(\boldsymbol{y})$ does not have to be evaluated, as these algorithms can evaluate the Bayes-factor directly as a ratio of densities. A simple version of a MCMC algorithm, also known as the Metropolis-Hastings algorithm [177], looks as follows [168]: The main idea is to construct a Markov-chain that has a stationary distribution of states, which will be the posterior distribution one is seeking. For this, the range of possible q's has to be quantized into X bins of equal background measure, i.e. in case of a Lebesgue background measure of equal $\mathcal{Q}$-volume, with representatives $\{q_\xi\}_{\xi=1}^X$. These representatives of the bins q_ξ are the states of the Markov-chain, which will be denoted by $\{\varsigma_k\}_{k=1,\ldots}$ in the order visited at step $k = 1,\ldots$ of the Markov-chain. Assuming that $\hat{\boldsymbol{y}}$ has been observed or measured, the Markov-chain steps are the following:

1. draw ξ randomly from $\{1,\ldots,X\}$;
2. starting in state q_ξ, set $\varsigma_1 := q_\xi$ and $k := 0$;
3. compute $\rho_\xi := \pi_{(Y|Q)}(\hat{\boldsymbol{y}}|q_\xi)\pi_Q(q_\xi)$; the product of likelihood and prior,
4. **loop** over $k := k+1$;
5. pick any state q_ζ with $\zeta \neq \xi$ randomly with probability $1/(X-1)$, this is the *proposal*;
6. if not already computed in a previous step, compute $\rho_\zeta := \pi_{(Y|Q)}(\hat{\boldsymbol{y}}|q_\zeta)\pi_Q(q_\zeta)$;
7. let $\alpha = \min\{1, \rho_\zeta/\rho_\xi\}$, this is the *acceptance probability*;
8. accept q_ζ with probability α, i.e. pick a sample of a uniformly distributed RV $U \in [0,1]$; and
9. **if** $U \leq \alpha$ **then**
10. set $\varsigma_{k+1} = q_\zeta$;

11. **else**
12. set $\varsigma_{k+1} = q_\xi$;
13. **endif**
14. **endloop**

One can then show [177, 174–176] that after the so-called *burn-in*, i.e. a number of steps which the Markov-chain needs to reach the stationary distribution, the relative frequency with which the states q_ξ are visited is equal to the *posterior* pdf $\pi_{(Q|Y)}(q_\xi|\hat{\boldsymbol{y}})$. One may observe that if the number ρ_ζ in line 6 of the algorithm, the product of likelihood and prior for the proposal state q_ζ is larger than for the current state q_ξ, i.e. $\rho_\zeta \geq \rho_\xi$, one has $\alpha = 1$ in line 7, and the new state is accepted in any case. As the ρ_ξ are proportional to the posterior conditional pdf $\pi_{(Q|Y)}(q_\xi|\hat{\boldsymbol{y}})$ at the representatives q_ξ, it is clear the the algorithm is a probabilistic search for the maximum of the posterior. It moves away from a state to lower posterior values in line 10 of the algorithm according to the posterior ratios. Obviously, one error involved in the algorithm is the quantization into bins and choosing the representatives q_ξ. Due to the required burn-in, one is not sure that the sequence of visited states ς_k is *stationary*, as the equilibrium distribution is only the asymptotic distribution. Estimating that the burn-in period is over has to be tested by looking at the stationarity of the sequence.

The main advantages of the method are certainly the simplicity of the formulation and the possibility to directly estimate the posterior conditional pdf $\pi_{(Q|Y)}(q_\xi|\hat{\boldsymbol{y}})$. We should warn though, that although the formulation is so simple, to use the method efficiently and correctly may not be.

The main drawbacks of the methods is potentially expensive step of often having to evaluate the likelihood $\pi_{(Y|Q)}(\hat{\boldsymbol{y}}|q_\zeta)$ in line 6 , and we shall return to this point later. Additionally, the algorithm is a Monte Carlo (MC) method, or more precisely a MC method within a MC-method, meaning that it converges only slowly with the number of samples, so that there will always be a sampling error. In addition, the successive Markov-chain samples are obviously not independent but highly *correlated*. This makes estimating any statistic other than the mean (e.g. the variance) difficult. Also usual statistical formulas for the accuracy of the estimates assume *independent* samples and are not directly applicable. And finally, if the likelihood function and prior pdf differ very much, the acceptance probabilities α in line 7 may be very low, $\alpha < 1$, meaning that practically the chain has gets stuck in some state and does not move on.

5.4.2 The Bayesian upadetes with linear Gauss-Markov-Kálmán filter

Another possibility, which was implicitly already alluded to in the description of the "forecast-observe-assimilate" algorithms above, is to leave the base measure $\mathbb{P}$ on Ω unchanged, and to change the RV from the forecast $q_f = q$ to the updated or assimilated q_a, such that $q_{a,*}\mathbb{P}(\mathcal{I}_q) = \mathbb{P}_{q_a}(\mathcal{I}_q) = \mathbb{P}(\mathcal{I}_q|\mathcal{M}_y)$, so that (5.66) is satisfied.

Such algorithms are often called *filters*, as the observation or measurement $\hat{\boldsymbol{y}}$ is filtered to update the forecast q_f to q_a. This is often advantageous if one needs a RV to do further forecast according to (5.60), as then the assimilated q_a becomes the new forecast.

The main idea here is to provide a convenient many of constructed probability measure, here in terms of conditional expectation, which is already already addressed by Kolmogorov himself. Here we use systematic use of expectation The expected value of a RV X defined on the probability space $(\Omega, \mathfrak{A}, \mathbb{P})$ in (5.62) is given by

$$\mathbb{E}(X) := \int_\Omega X(\omega)\, \mathbb{P}(d\omega), \tag{5.70}$$

and given a conditional probability measure such as the one in (5.66), the conditional expectation of the RV X is defined as

$$\mathbb{E}(X|\mathcal{M}_y) := \int_\Omega X(\omega)\, \mathbb{P}(dq|\mathcal{M}_y). \tag{5.71}$$

In the traditional setting, the probability measure and the conditional probability measure define the expectation and conditional expectation. However, Kolmogorov turned this around [172, 173] and defined conditional probabilities via the conditional expectation. Given the conditional expectation $\mathbb{E}(\cdot|\mathcal{M}_y)$ as an operator, the conditional probability is easily recovered through $\mathbb{P}(\mathcal{I}_q|\mathcal{M}_y) = \mathbb{E}(\mathbf{1}_{\mathcal{I}_q}|\mathcal{M}_y)$, where $\mathbf{1}_{\mathcal{I}_q}$ is the characteristic or indicator function of the subset $\mathcal{I}_q$, i.e. one has $\mathbf{1}_{\mathcal{I}_q}(q)$ equal to one iff $q \in \mathcal{I}_q$, and zero otherwise.

The question remains how to define the operator $\mathbb{E}(X|\mathcal{M}_y)$ for a RV X. The easiest point of departure for conditional expectation is to define it not just for one piece of measurement $\mathcal{M}_y$, but for sub-σ-algebras $\mathfrak{S} \subseteq \mathfrak{A}$. The connection with an event $\mathcal{M}_y$ is to take $\mathfrak{S} = \sigma(\boldsymbol{y}_f)$, the σ-algebra generated by $\boldsymbol{y}_f(\omega)$. This is the smallest sub-σ-algebra which contains all the sets $\boldsymbol{y}_f^{-1}(\mathcal{A}) \subseteq \Omega$ for measurable subsets $\mathcal{A} \subseteq \mathcal{Y}^N$.

The conditional expectation can then be defined for all RV $X \in L_1(\Omega, \mathfrak{A})$ as that RV measurable w.r.t $\mathfrak{S}$, i.e. in $L_1(\Omega, \mathfrak{S})$, which satisfies

$$\forall \mathcal{S} \in \mathfrak{S}: \quad \int_{\mathcal{S}} X\, \mathbb{P}(d\omega) = \int_{\mathcal{S}} \mathbb{E}(X|\mathfrak{S})\, \mathbb{P}(d\omega). \tag{5.72}$$

Using the indicator function $\mathbf{1}_{\mathcal{S}}$ and rearranging, (5.72) may written as an orthogonality condition

$$\forall \mathcal{A} \in \mathfrak{S}: \quad \int_\Omega \mathbf{1}_{\mathcal{A}} \left(X - \mathbb{E}(X|\mathfrak{S})\right)\, \mathbb{P}(d\omega) = 0. \tag{5.73}$$

Noting that span of the indicators $\mathbf{1}_{\mathcal{A}} \in L_\infty(\Omega, \mathfrak{S})$ is actually dense in $L_\infty(\Omega, \mathfrak{S})$, $\mathbf{1}_{\mathcal{A}}$ in (5.73) may be replaced by an arbitrary bounded RV $\chi \in L_\infty(\Omega, \mathfrak{S})$, enforcing the condition that $X - \mathbb{E}(X|\mathfrak{S})$ is *orthogonal* to $L_\infty(\Omega, \mathfrak{S})$:

$$\forall \chi \in L_\infty(\Omega, \mathfrak{S}): \quad \int_\Omega \chi \left(X - \mathbb{E}(X|\mathfrak{S})\right)\, \mathbb{P}(d\omega) = 0. \tag{5.74}$$

This may be regarded as a *Galerkin*-orthogonality, immediately suggesting computational procedures based on (5.73) resp. (5.74). Hence, for RVs X with finite variance, elements of the *Euclidean* or *Hilbert* space $X \in \mathcal{S} := L_2(\Omega, \mathfrak{A})$, the conditional expectation is defined by

$$\forall \chi \in \mathcal{S}_\infty : \quad \langle \chi | X - \mathbb{E}(X|\mathfrak{S}) \rangle := \int_\Omega \chi \left(X - \mathbb{E}(X|\mathfrak{S}) \right) \mathbb{P}(d\omega) = 0, \tag{5.75}$$

where $\mathcal{S}_\infty := L_2(\Omega, \mathfrak{S})$ is the L_2 subspace generated by the measurement sub-σ-algebra $\mathfrak{S}$. It is now clear that (5.75) are the conditions for minimizing the Euclidean L_2-distance from X to $\mathcal{S}_\infty$, i.e. defining an *orthogonal* projection P_∞ onto the closed subspace $\mathcal{S}_\infty \subset \mathcal{S}$:

$$\mathbb{E}(X|\mathfrak{S}) := P_\infty(X) = \arg \min_{\tilde{X} \in \mathcal{S}_\infty} \|X - \tilde{X}\|^2_{\mathcal{S}_\infty}. \tag{5.76}$$

If we take now the $\mathcal{Q}$-valued RV q instead of the real-valued RV X, one has to define the space $\mathcal{Q} := \mathcal{Q} \otimes \mathcal{S}$ of $\mathcal{Q}$-valued RVs of finite variance, and set $\mathcal{Q}_\infty := \mathcal{Q} \otimes \mathcal{S}_\infty$ to get as in (5.76) the orthogonal projection, again denoted by P_∞, onto the closed subspace $\mathcal{Q}_\infty \subset \mathcal{Q}$:

$$\mathbb{E}(q|\mathfrak{S}) := P_\infty(q) := \arg \min_{\tilde{q} \in \mathcal{Q}_\infty} \|q - \tilde{q}\|^2_{\mathcal{Q}}. \tag{5.77}$$

The distance squared $\|q - \tilde{q}\|^2_{\mathcal{Q}}$ in (5.77) may be regarded as a Bayesian *loss-function*. Requiring the derivative of the loss function in (5.77) to vanish again produces the Galerkin orthogonality conditions, but now in $\mathcal{Q}$:

$$\forall \tilde{q} \in \mathcal{Q}_\infty : \quad \langle \langle q - \mathbb{E}(q|\mathfrak{S}) | \tilde{q} \rangle \rangle_{\mathcal{Q}} = 0, \tag{5.78}$$

which actually implies the normally stronger condition that the covariance vanishes [169]:

$$\forall \tilde{q} \in \mathcal{Q}_\infty : \quad \mathbb{E}(\tilde{q} \otimes (q - \mathbb{E}(q|\mathfrak{S}))) = 0. \tag{5.79}$$

Furthermore, note that the $Doob - Dynkin$-lemma [172] assures us that if a RV like $\mathbb{E}(q|\mathfrak{S})$ is measurable w.r.t. $\mathfrak{S} = \sigma(\boldsymbol{y}_f)$, then $\mathbb{E}(q|\mathfrak{S}) = \phi_q(\boldsymbol{y}_f)$ for some measurable $\phi_q \in L_0(\mathcal{Y}^N; \mathcal{Q})$, where $L_0(\mathcal{Y}^N; \mathcal{Q})$ denotes the measurable maps from $\mathcal{Y}^N$ to $\mathcal{Q}$. More precisely one should write $\mathbb{E}(q|\mathfrak{S}) = \phi_q((\boldsymbol{y}_f(q))) = \phi_q \circ \boldsymbol{y}_f \circ q$. In this light the task of finding the conditional expectation may be seen as rephrasing (5.77) as: find $\phi_q \in L_0(\mathcal{Y}^N; \mathcal{Q})$ such that

$$\phi_q = \arg \min_{\varphi \in L_0(\mathcal{Y}; \mathcal{Q})} \|q - \varphi \circ \boldsymbol{y}_f \circ q\|^2_{\mathcal{Q}}. \tag{5.80}$$

One may conclude that ϕ_q is in some mean-square sense an inverse of $\boldsymbol{y}_f$.

Orthogonal decomposition and conditional expectation filter: as $\mathcal{Q}_\infty$ is a closed subspace of $\mathcal{Q}$ with projection $P_\infty : \mathcal{Q} \to \mathcal{Q}_\infty$, one has the orthogonal decomposition of $\mathcal{Q} = \mathcal{Q}_\infty \oplus \mathcal{Q}_\infty^\perp$, i.e.

$$q = P_\infty(q) + (I - P_\infty)(q) = \mathbb{E}(q|\mathfrak{S}) + (q - \mathbb{E}(q|\mathfrak{S})) = \phi_q(\boldsymbol{y}_f(q)) + (q - \phi_q(\boldsymbol{y}_f(q))). \tag{5.81}$$

This decomposition may be used to build a first version of a filter to produce an assimilated RV q_a, which at least has the conditional expectation correct. Observe that from (5.81), applying the projection P_∞ which, being a projection, satisfies $P_\infty(P_\infty(q)) = P_\infty(q)$, one obtains

$$\mathbb{E}(q|\mathfrak{S}) = P_\infty(q) = P_\infty(P_\infty(q)) + P_\infty((I - P_\infty)(q)) = P_\infty(q) = \phi_q(\boldsymbol{y}_f(q)). \quad (5.82)$$

As the new information from the observation $\hat{y}$ comes from the measurement map $\boldsymbol{y}_f$ and is all in the subspace $\mathcal{Q}_\infty$, following (5.81) one may define

$$q_a := \phi_q(\hat{y}) + (q_f - \phi_q(\boldsymbol{y}_f(q_f))), \quad (5.83)$$

where the component in $\mathcal{Q}_\infty$ has been changed to the constant $\phi_q(\hat{y})$ and the orthogonal component $q_f - \phi_q(\boldsymbol{y}_f(q_f))$ has been left as is. From (5.82) we can see that

$$\mathbb{E}(q_a|\mathfrak{S})(\hat{y}) = \phi_q(\hat{y}) = \mathbb{E}(q|\mathfrak{S})(\hat{y}).$$

We call q_a in (5.83) the *analysis*, *assimilated*, or *posterior* RV, incorporating the new information.

One should emphasize that it is the vector space setting of $\mathcal{Q}$ and $\mathcal{Y}$ which has made this formulation possible [169], also allowing for easy numerical computation. In case the parameters $q \in \mathcal{Q}$ are not without constraints, or not in a vector space, then they should be mapped to such quantities. For example, if q is elasticity tensor, then it has to be symmetric and positive definite. The symmetric tensors are of course a subspace, but the sub-manifold of positive definite ones is not a subspace, but an open cone. However, the symmetric positive definite tensors can be given the structure of a Riemanian manifold, and then distance is measured via geodesics. A simple case of this are positive scalars either used for bulk modulus or shear modulus; through the logarithm they are transformed into a vector space without constraints.

The linear Bayesian Gauss-Markov-Kálmán update: The minimisation in (5.80) is performed over all measurable $\varphi \in L_0(\mathcal{Y}^N; \mathcal{Q})$, a space which is typically very large and not easily accessible. But the vector space setting allows a simplification or approximation. One replaces in (5.80) the space $L_0(\mathcal{Y}^N; \mathcal{Q})$ by the subspace of *affine* mappings $\mathcal{A}(\mathcal{Y}^N; \mathcal{Q})$, mappings which are certainly measurable and of the form $\varphi(y) = Hy + b \in \mathcal{A}(\mathcal{Y}^N; \mathcal{Q}) \subset L_0(\mathcal{Y}^N; \mathcal{Q})$, where $b \in \mathcal{Q}$ is a constant and H is a linear continuous map $H \in \mathcal{L}(\mathcal{Y}^N; \mathcal{Q})$. Find $K \in \mathcal{L}(\mathcal{Y}^N; \mathcal{Q})$ and $c \in \mathcal{Q}$ such that

$$(K, c) = \arg\ \min_{H \in \mathcal{L}(\mathcal{Y}^N; \mathcal{Q}), b \in \mathcal{Q}} \|q - (H(\boldsymbol{y}_f \circ q) + b)\|_{\mathcal{Q}}^2 \quad (5.84)$$

As one sees immediately from (5.83), in the filter equation for q_a the constant $c \in \mathcal{Q}$ cancels, so that one only needs the *Kálmán-gain* $K \in \mathcal{L}(\mathcal{Y}^N; \mathcal{Q})$, see [178, 179]:

$$K := C_{q_f, \boldsymbol{y}_f} C_{\boldsymbol{y}_f}^{-1}, \quad (5.85)$$

$$C_{\boldsymbol{y}_f} := \mathbb{E}(\tilde{\boldsymbol{y}}_f(q_f) \otimes \tilde{\boldsymbol{y}}_f(q_f)), \quad (5.86)$$

$$C_{q_f, \boldsymbol{y}_f} := \mathbb{E}(\tilde{q_f} \otimes \tilde{\boldsymbol{y}}_f(q_f)), \quad (5.87)$$

where for any RV like q for the sake of brevity we set $\bar{q} := \mathbb{E}(q)$ such that $\tilde{q} := q - \bar{q}$ is the zero-mean part. From (5.84) we obtain the so-called *Gauss-Markov-Kálmán* (GMK) filter as an approximation of (5.83)

$$q_a := K(\hat{\boldsymbol{y}}) + (q_f - K(\boldsymbol{y}_f(q_f))) = q_f + K(\hat{\boldsymbol{y}}) - K(\boldsymbol{y}_f(q_f)) = q_f + K(\hat{\boldsymbol{y}} - \boldsymbol{y}_f(q_f)). \tag{5.88}$$

The name of this filter [169–171, 180] is due to the fact that it is a generalized version of the Gauss-Markov theorem [179], and gives a generalization of the well-known Kálmán filter [178]. In case $C_{\boldsymbol{y}_f}$ is not invertible or close to singularity, its inverse in 5.85 should be replaced by the Moore-Penrose pseudo-inverse. This update is in some ways very similar to the 'Bayes linear' approach, see [181]. If the mean is taken in 5.88, one obtains the familiar Kálmán filter formula [178, 179] for the update of the mean. But one may show [182] that (5.88) also contains the Kálmán update for the covariance. As in (5.84) the minimization is over a smaller space $\mathcal{A}(\mathcal{Y}^N; \mathcal{Q}) \subset L_0(\mathcal{Y}^N; \mathcal{Q})$, we are not using all the information available. Hence the value of the functional being minimized will remain larger, but the computation is simpler.

Discrete approximation: In the instances where we want to employ the theory detailed in the previous sections, the spaces $\mathcal{U}$ and $\mathcal{Q}$ are usually infinite dimensional, as is the space $\mathcal{S} = L_2(\Omega)$. For an actual computation they have to be discretized or approximated by finite dimensional spaces. The discretization if probability space is somewhat different from the finite element discretization, in the sense that the whole domain is discretized. In our examples we will chose finite element discretization and corresponding subspace. Hence let $\mathcal{Q}_M := \text{span}\{\varrho_m : m = 1, \ldots, M\} \subset \mathcal{Q}$ be an M-dimensional subspace with basis $\{\varrho_m\}_{m=1}^M$. An element of $\mathcal{Q}_M$ will be represented by the vector of RVs $\boldsymbol{q} = \left[q^1, ..., q^M\right]^T \in \mathcal{S}^M$ such that $\sum_{m=1}^M q^m \varrho_m \in \mathcal{Q}_M = \mathcal{Q}_M \otimes \mathcal{S}$. The space of possible measurements $\mathcal{Y}$ can usually be assumed to be finite dimensional, whose elements similarly are represented by a vector of coefficients $\boldsymbol{y} \in \mathbb{R}^R$. Observe that then $\hat{\boldsymbol{y}} \in \mathbb{R}^{R \cdot N}$ and $\boldsymbol{y}_f \in \mathbb{R}^{R \cdot N} \otimes \mathcal{S}$.

With this discretization, the MCMC-method can be carried out after the obvious modifications. For the conditional expectation and the GMK-filter things are also straight forward, as is shown next. On $\mathbb{R}^M$, representing $\mathcal{Q}_M$, the minimisation in (5.84) is translated to: find $\boldsymbol{K} \in \mathbb{R}^{M \times (R \cdot N)}$ and $c \in \mathbb{R}^M$ such that

$$(\boldsymbol{K}, \boldsymbol{c}) = \arg\ \min_{\boldsymbol{H} \in \mathbb{R}^{M \times (R \cdot N)}, \boldsymbol{b} \in \mathbb{R}^M} \|\boldsymbol{q} - (\boldsymbol{H}(\boldsymbol{y}_f(\boldsymbol{q})) + \boldsymbol{b})\|_{\boldsymbol{Q}}^2, \tag{5.89}$$

where the norm $\|\boldsymbol{q}\|_{\boldsymbol{Q}}$ results from the inner product $\langle\langle \boldsymbol{q}_1 | \boldsymbol{q}_2 \rangle\rangle_{\boldsymbol{Q}} := \mathbb{E}(\boldsymbol{q}_1^T \boldsymbol{Q} \boldsymbol{q}_2)$ with $\boldsymbol{Q}_{mn} = \langle\langle \varrho_m | \varrho_n \rangle\rangle_{\mathcal{Q}}$, the Gram matrix of the basis. Then the update corresponding to (5.88), more precisely its spatial semi-discretization, is

$$\boldsymbol{q}_a := \boldsymbol{q}_f + \boldsymbol{K}(\hat{\boldsymbol{y}} - \boldsymbol{y}_f(\boldsymbol{q}_f)), \quad \text{with} \tag{5.90}$$

$$\boldsymbol{K} = \boldsymbol{C}_{\boldsymbol{q}_f,\boldsymbol{y}_f}\boldsymbol{C}_{\boldsymbol{y}_f}^{-1}, \tag{5.91}$$

$$\boldsymbol{C}_{\boldsymbol{y}_f} = \mathbb{E}(\tilde{\boldsymbol{y}}_f(\boldsymbol{q}_f)\otimes\tilde{\boldsymbol{y}}_f(\boldsymbol{q}_f)), \tag{5.92}$$

$$\boldsymbol{C}_{\boldsymbol{q}_f,\boldsymbol{y}_f} = \mathbb{E}(\tilde{\boldsymbol{q}}_f\ \tilde{\boldsymbol{y}}_f^T) = \mathbb{E}(\tilde{\boldsymbol{q}}_f\otimes\tilde{\boldsymbol{y}}_f), \tag{5.93}$$

as before in (5.85) to (5.87). Let us note that, in contrast to the usual Kálmán-filter, here the quantities $\boldsymbol{q}_a, \boldsymbol{q}_f$, and $\boldsymbol{y}_f$ in (5.90) are RVs. With these specifications, a sampling or particle filter version of (5.90) can be carried out, this is the *Ensemble Kálmán filter* (EnKF), see [168**? ?**]. Here we shall follow a different tack.

Spectral or polynomial chaos projection: In preceding sections it was already indicated how computations could be carried out, by discretizing the RVs involved through sampling. Sampling the model (5.59) and the measurement operator (5.60) or even the spatially discretized RVs $\boldsymbol{y}_f$ which appear in all the algorithms may be computationally quite expensive. Therefore it is quite natural to try and find simpler representations for this, something what is known often as proxy- or surrogate models. Mathematically we can see this with the variables $q_f \in \mathcal{Q}\otimes\mathcal{S} = \mathcal{Q}$, $u \in \mathcal{U}\otimes\mathcal{S} = \mathcal{U}$, and $y_f \in \mathcal{Y}\otimes\mathcal{S} = \mathcal{Y}$. In the preceding section these were already discretised in the first factor of the tensor product to $\boldsymbol{q}_f \in \mathcal{Q}_M\otimes\mathcal{S}$ and $\boldsymbol{y}_f \in \mathbb{R}^{R\cdot N}\otimes\mathcal{S}$. As $\mathcal{Y}$ was assumed finite dimensional ($\mathcal{Y}\equiv\mathbb{R}^R$), no further discretisation was needed here in the first factor; and $\boldsymbol{y}_f$ a RV with values in $\mathbb{R}^{R\cdot N}$ comes from N measurement of R quantities at a time. Along with the discretization of $\mathcal{Q}_M \subset \mathcal{Q}$ typically one also has to discretize the model (5.59) in space by $\mathcal{U}_L \subset \mathcal{U}$, something what is standard (e.g. finite elements), and will not be further discussed.

But the second factor in those tensor products, the space of real-valued RVs $\mathcal{S}$, is typically an infinite dimensional space and has to be discretized as well for real computations. In a numerical sense the sampling used earlier is of course also a discretization. But here we want to introduce another one by explicitly choosing a subspace $\mathcal{S}_B \subset \mathcal{S}$. As for $\mathcal{Q}_M$ one picks a finite set $\{\Psi_\alpha\}_\alpha$ of B independent vectors in $\mathcal{S}$ which span the B-dimensional subspace $\mathcal{S}_B$, $\mathrm{span}\{\Psi_b\}_{b=1}^B = \mathcal{S}_B$. As $\mathcal{S} = L_2(\Omega)$, these independent vectors are in fact RVs with finite variance. Here we will use *Wiener's polynomial chaos* expansion (PCE) as basis. This is well-known by now, and has also descriptions in text-books [185] and monographs [186, 187]. Other possibilities [188] are the generalized PCE, or even other systems of RVs which are dense [189] in $\mathcal{S}$.

The approximation $\boldsymbol{q}_f$ for example may be achieved by either collocation/ interpolation at a suitable number of points $\omega_b \in \Omega$, or by projecting $\boldsymbol{q}_f \in \mathcal{Q}_M\otimes\mathcal{S}$ orthogonally to $\mathcal{Q}_M\otimes\mathcal{S}_B$; in fact, as we are in a Hilbert space, a least squares approximation or regression. Concretely, this means we minimize

$$\min\{\ \|\boldsymbol{q}_f - \sum_{b=1,m=1}^{B,M} q_{f,b}^m\Psi_b\varrho_m\|_{\mathcal{Q}}^2 \quad | \quad q_{f,b}^m \in \mathbb{R}, m=1,\dots,M, b=1,\dots,B\}. \tag{5.94}$$

This defines an orthogonal projection $P_B : \mathcal{S} \to \mathcal{S}_B$. We set $\boldsymbol{P}_B = I\otimes P_B$, and by setting $\boldsymbol{q}_{f,b} = \left[q_{f,b}^1,\dots,q_{f,b}^M\right]^T$, we see that the approximation $\boldsymbol{P}_B\boldsymbol{q}_f$ to $\boldsymbol{q}_f$ can be

written as $\boldsymbol{P}_B\boldsymbol{q}_f = \sum_b \boldsymbol{q}_{f,b}\Psi_b$. A similar projection is applied to the RVs $\boldsymbol{y}_f$ and $\boldsymbol{q}_a$ in (5.90).

Now [190, 191, 168–171, 180] project both sides of (5.90) with $\boldsymbol{P}_B$, to obtain

$$\boldsymbol{P}_B\boldsymbol{q}_a = \sum_{b=1}^{B} \boldsymbol{q}_{a,b}\Psi_b = \boldsymbol{P}_B\boldsymbol{q}_f + \boldsymbol{P}_B\boldsymbol{K}(\hat{\boldsymbol{y}} - \boldsymbol{y}_f(\boldsymbol{q}_f)) = \boldsymbol{P}_B\boldsymbol{q}_f + \boldsymbol{K}(\hat{\boldsymbol{y}} - \boldsymbol{P}_B\boldsymbol{y}_f(\boldsymbol{q}_f)) \tag{5.95}$$

$$= \sum_{b=1}^{B} \boldsymbol{q}_{f,b}\Psi_b + \boldsymbol{K}(\hat{\boldsymbol{y}} - \sum_{b=1}^{B} \boldsymbol{y}_{f,b}\Psi_b), \tag{5.96}$$

as obviously the projection $\boldsymbol{P}_B$ commutes with the Kálmán-gain operator $\boldsymbol{K}$. Now assume without loss of generality that the function / RV $\Psi_1 = 1$ is actually constant, whereas the Ψ_b for $b > 1$ satisfy $\mathbb{E}(\Psi_b) = 0$. Then the $b = 1$ term in (5.95) is for the mean, the rest ($b > 1$) has mean zero. We shall also assume in extension of these relations that the Ψ_b are orthonormal, i.e. $\mathbb{E}(\Psi_{b_1}\Psi_{b_2}) = \delta_{b_1,b_2}$. One obtains the stochastic discretization of (5.90):

$$\boldsymbol{q}_{a,1} = \boldsymbol{q}_{f,1} + \boldsymbol{K}(\hat{\boldsymbol{y}} - \boldsymbol{y}_{f,1}), \quad \text{and} \tag{5.97}$$

$$\boldsymbol{q}_{a,b} = \boldsymbol{q}_{f,b} - \boldsymbol{K}\boldsymbol{y}_{f,b} \quad \text{for } b > 1. \tag{5.98}$$

Denoting the canonical basis vectors in $\mathbb{R}^B$ as $\boldsymbol{e}_b$, one may set

$$q_a = \sum_{b=1}^{B} \boldsymbol{q}_{a,b} \otimes \boldsymbol{e}_b, \quad q_f = \sum_{b=1}^{B} \boldsymbol{q}_{f,b} \otimes \boldsymbol{e}_b, \quad y_f = \sum_{b=1}^{B} \boldsymbol{y}_{f,b} \otimes \boldsymbol{e}_b, \quad \hat{y} = \hat{\boldsymbol{y}} \otimes \boldsymbol{e}_1, \quad K = \boldsymbol{K} \otimes \boldsymbol{I}. \tag{5.99}$$

With this, the relations (5.97) and (5.98), the stochastic discretization of (5.90) may concisely be written as

$$q_a := q_f + K(\hat{y} - y_f). \tag{5.100}$$

The filter in (5.97) is the classical Kálmán-filter for the mean, the relations in (5.99) are a non-Gaussian extension of the Kálmán-filter, where it can be shown that it really extends the Kálmán-filter. This filter, and its concise form (5.100) is called the *spectral projection* Kálmán-filter (SPKF) or *polynomial chaos* Kálmán-filter (PCKF), where the former (SPKF) seems preferable. In contrast to the EnKF, this filter is formulated in an orthogonal basis, and hence does not suffer from the breakdown of the EnKF analyzed in [192].

It remains to show how to compute $\boldsymbol{K}$ in (5.91) from the covariances in (5.92) and (5.93), see also [168–171, 180]. Given the expansion of the RVs $\boldsymbol{q}_a, \boldsymbol{q}_f$, and $\boldsymbol{y}_f$, this is actually quite simple as any moment can be computed directly from the expansion. One has $\mathbb{E}(\boldsymbol{P}_B\boldsymbol{q}_f) = \overline{\boldsymbol{P}_B\boldsymbol{q}_f} = \boldsymbol{q}_{f,1}$ and $\widetilde{\boldsymbol{P}_B\boldsymbol{q}_f} = \sum_{b>1} \boldsymbol{q}_{f,b}\Psi_b$. The covariance $\boldsymbol{C}_{\boldsymbol{y}_f}$ of $\boldsymbol{y}_f$ in (5.92) will be approximated by the covariance of $\boldsymbol{P}_B\boldsymbol{y}_f$, similarly for $\boldsymbol{C}_{\boldsymbol{y}_f,\boldsymbol{q}_f}$ in

(5.93). Hence:

$$\boldsymbol{C}_{\boldsymbol{y}_f} \approx \mathbb{E}((\boldsymbol{P}_B \boldsymbol{y}_f) \otimes (\boldsymbol{P}_B \boldsymbol{y}_f)) = \sum_{b>1} \boldsymbol{y}_{f,b} \otimes \boldsymbol{y}_{f,b}; \tag{5.101}$$

$$\boldsymbol{C}_{\boldsymbol{q}_f,\boldsymbol{y}_f} \approx \mathbb{E}((\boldsymbol{P}_B \boldsymbol{q}_f) \otimes (\boldsymbol{P}_B \boldsymbol{y}_f)) = \sum_{b>1} \boldsymbol{q}_{f,b} \otimes \boldsymbol{y}_{f,b}. \tag{5.102}$$

Now all the terms needed for the update 5.100 have been explicitly stated and are readily computable.

5.5 Numerical simulations

In this section, we discuss the identification of the presented model parameters, by Markov chain Monte Carlo (MCMC) method and by Polynomial Chaos based Kalman filter for Linear Bayesian update (PceKF). Another important point for our discussion is related to the proper choice of the cost function or the measurements which are relevant to the appropriate parameters that we try to identify. In this way we can determine which numerical or experimental test favors the role of a certain parameter of interest and achieve a higher efficiency of the corresponding identification procedure. Any such cost function can be constructed not only from experimental measurements. Finally, based on our previous practice experience in deterministic setting (e.g. see [133]) we propose to split identification to elastic, hardening and softening parameters in order to reduce computational costs.

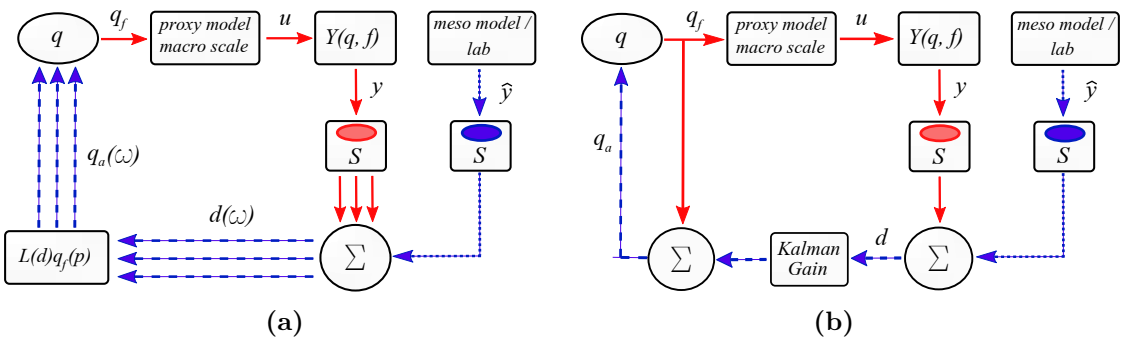

Figure 5.6: The algorithmic scheme of an inverse problem solved by (a) proxy MCMC filtering; (b) Square Root Polynomial Chaos based Linear Bayesian Update

Simplified representation and flow-chart for two proposed methods (PceKF and MCMC) for each set of parameters to be identified separately by taking into account different tests and measurements are shown in Figure 5.6. It is important to note that in the case of MCMC method the posterior is described by changing the distribution of the underlying RVs, while in case of PceKF the posterior is obtained by changing the RV. The main advantage of the MCMC algorithm (Figure 5.6a) is in being a model independent method. However, the main drawback is its slow convergence and very demanding procedure because one has to compute the system response for each new sample. One way to speed up the assimilation process is to introduce a proxy model on macro scale for the forecasted measurement, which is used in this work. The

computation starts with samples that are used as input in the deterministic proxy model on macro-scale. Once the response is computed, the measurement operator Y is applied and the value of the observable quantity y is diagnosed by a sensor. The predicted measurements are then compared to the meso-scale/experimental measurements, which further results in the distance measure d entering the likelihood function. The process is repeated all over again for the next sample which results with a posterior sample.

The issue of high computational cost in MCMC can be improved by using Bayesian linear methods. Recalling that the RV $q_a(\omega)$ can be numerically represented by either sampling $q_a(\omega_i)$ or as functional approximation such as polynomial chaos expansion. Here one may distinguish at least two numerical approaches to the given problem: the ensemble Kalman filter and the polynomial chaos based update [168]. In ensemble Kalman filter numerical estimates of q_a is performed in Monte Carlo fashion while in PceKF the random variables are functionally approximated. The algorithm which is used in this work is presented in Figure 5.6b and whole update process can be represented by only one loop.

5.5.1 Identification of elastic parameters

Given that the concrete is statistically isotropic material (see [24]) the elastic response of specimen defining the linear part of global response on a stress-strain diagram is described by only two parameters, bulk and shear moduli (K and G). In order to identify the shear modulus, which controls the resistance to the change of shape, we can use simple shear test (Figure 5.7a). For identification of bulk modulus, which controls the material resistance to the volume change, we can preferably use hydrostatic compression test (Figure 5.7b).

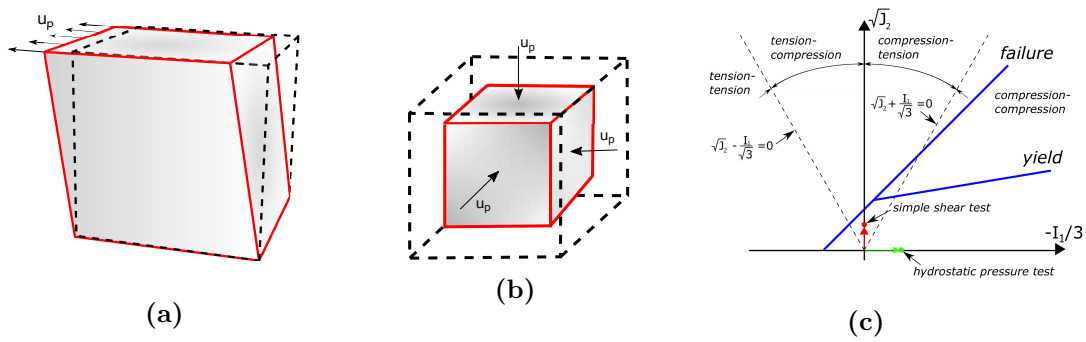

Figure 5.7: Numerical tests : (a) simple shear test; (b) hydrostatic pressure test; (c) loading path

Our prior knowledge for both elastic parameters, on which posterior distribution depends, is based on knowledge about Young's modulus and Poisson's ratio which are well-known in engineering practice. Namely, the mean value for Young's modulus and Poisson's ratio are chose as 30 GPa and 0.16, respectively.

In Figure 5.8 we display the shape of the prior, the likelihood function, and the posterior probability density function (pdf) obtained by MCMC method. The true

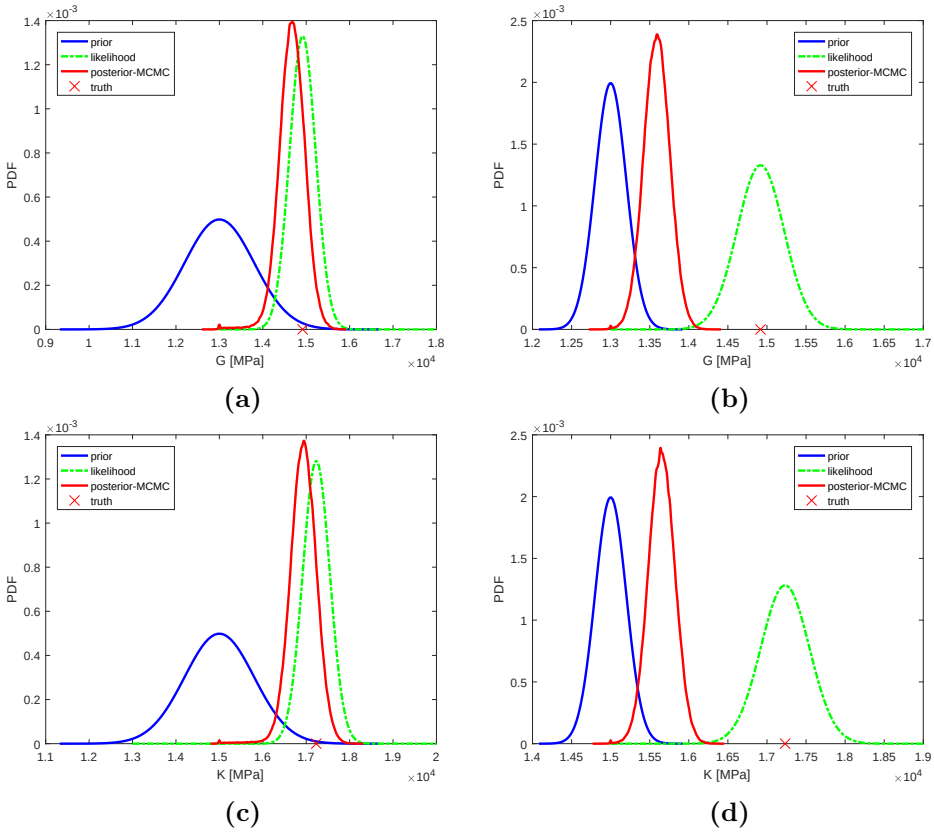

Figure 5.8: Comparison of prior and posterior pdf and the likelihood function for shear modulus - Simple shear test (upper row) and bulk modulus - hydrostatic compression test (lower row) with standard deviation for the prior σ_p=500 MPa (left) and σ_p=200 MPa (right) - energy measurements

value, obtained by deterministic identification in [133] for shear modulus is 14.918 GPa and for bulk modulus 17.232 GPa. These are obtained from simple shear test and hydrostatic compression test, respectively. We see that the mean and mode of the posterior have moved in the direction of the truth which are both taken as single point estimates, when compared to the prior (Figure 5.8a and Figure 5.8c). In Figure 5.8b and Figure 5.8d the posterior moved to the prior due to smaller standard deviation of the prior compared to the likelihood, which can be observed in case when our prior knowledge is more relevant than measurement. Dependence of the choice of measurements is presented in Figure 5.9, when we can note that either measuring the force (suitable for real experiment) or measuring the elastic energy (suitable for numerical tests) the resulting posterior distribution remains here the same, regardless of the chosen method, MCMC or PceKF.

The samples used for computation in MCMC method are drawn from proposal distribution with some probability r thus forming the corresponding sampling sequence. As presented in Figure 5.10 this sequence converges in distribution to our target posterior distribution, regardless of the starting point.

In Figure 5.11 we show that each new information from experiment is updating our knowledge about bulk modulus, resulting with sharper posterior distribution

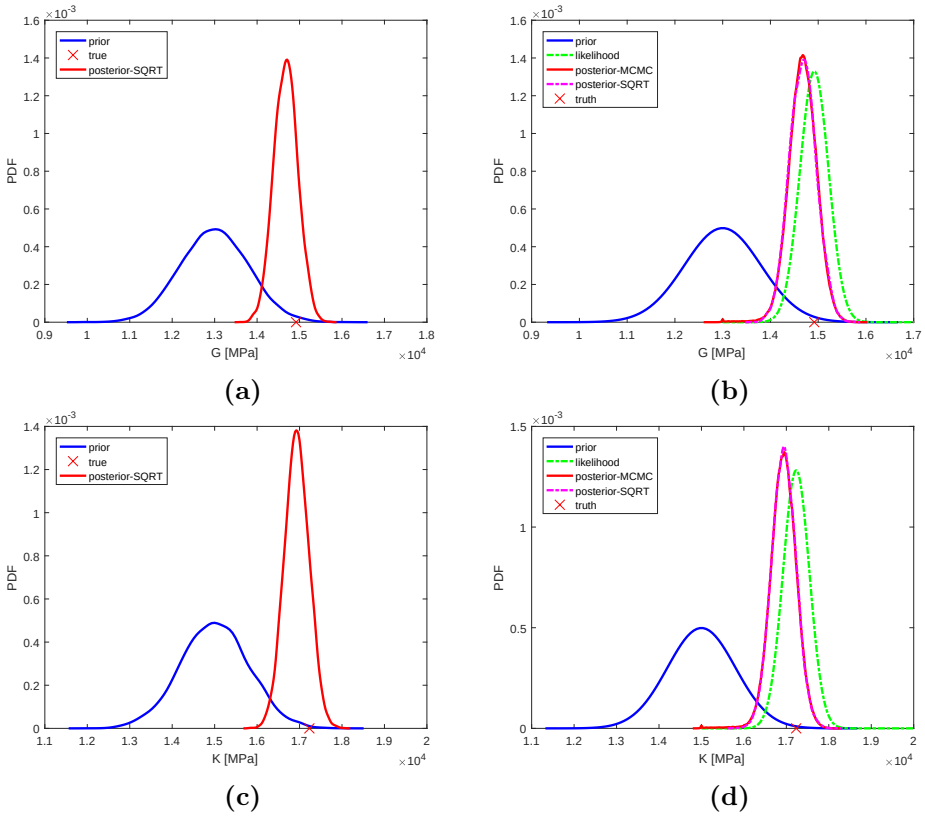

Figure 5.9: Prior and posterior pdf for shear modulus - simple shear test and Bulk modulus - hydrostatic compression test, obtained by SQRT Kalman filter (left - force measurements) and comparison with MCMC (right - energy measurements)

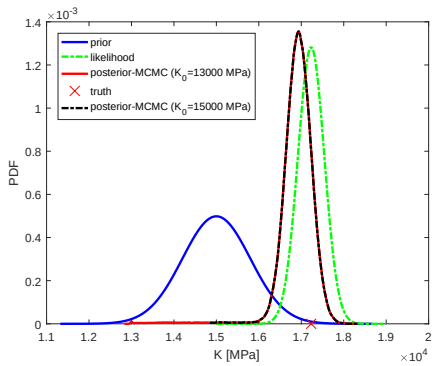

Figure 5.10: Comparison of prior and posterior pdf and the likelihood function for bulk modulus-hydrostatic compression test for different initial point of MC

(e.g. the standard deviation is decreasing). Posterior distribution after first update is used as prior for the next one. The measurement used in updating are taken from three elastic loading steps in case of simple shear test and hydrostatic compression test. Moreover, we can find that the same updated distribution are obtained with PceKF method (see Figure 5.12).

An interesting illustration is presented in Figure 5.13 with an inadequate choice of the test used for the parameters identification of interest. We note in particular

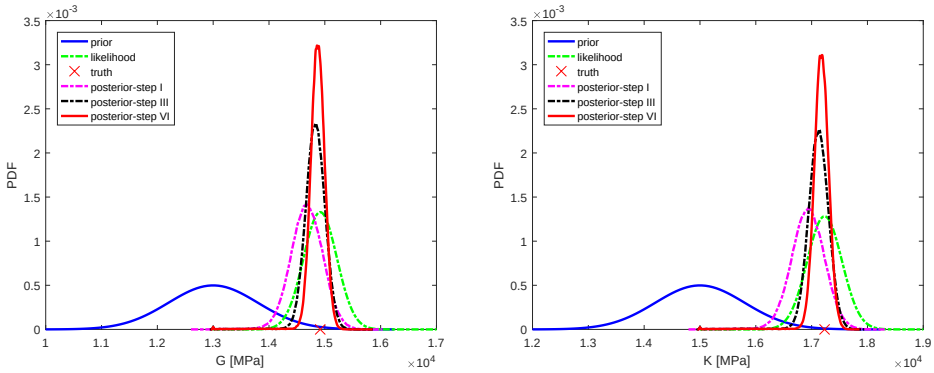

(a) (b)

Figure 5.11: MCMC update of elastic material parameters $\{K, G\}$ using elastic step of load: (a) simple shear test; (b) hydrostatic compresion test

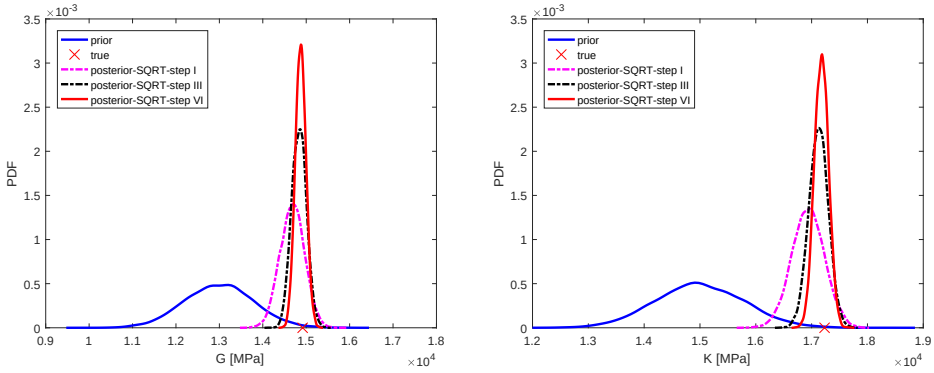

(a) (b)

Figure 5.12: The square root update of elastic material parameters $\{K, G\}$ using elastic step of load: (a) simple shear test; (b) hydrostatic compresion test

that information obtained in a simple shear test does not change likelihood function and posterior distribution which remains the same as the prior. The same conclusion pertains to deterministic identification revealing that simple shear test is not relevant for identification of bulk modulus, and on other side shear modulus cannot be identified from hydrostatic compression test.

The previous results are also supported by the plots of posterior 95% confidence intervals shown in Figure 5.14. With every new successive measurement, the probability region narrows down such that the interval becomes almost deterministic after few performed measurements. We note that even though the truth is assumed to be deterministic, the posterior 95% confidence interval does not disappear due to the measurement and model errors.

Figure 5.15 reveals macroscopic response in elastic stage for a specimen under uniaxial compression with the mean values of identified parameters. We can note that the difference between computed response and experimental one is small enough even for only one measurement taken into account. This difference is even smaller if we perform identification with several measurements in elastic stage.

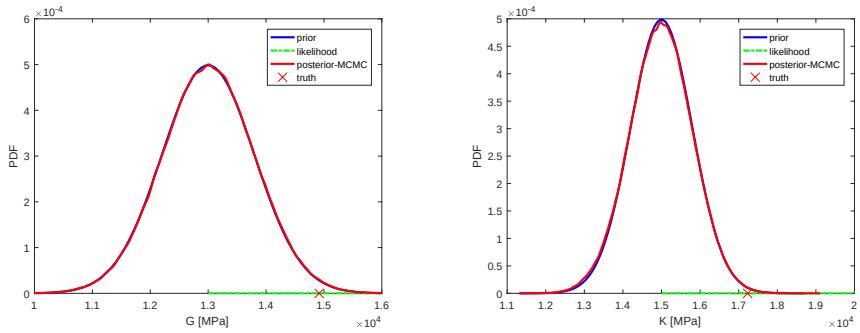

(a) **(b)**

Figure 5.13: Comparison of prior and posterior pdf and the likelihood function for shear modulus-hydrostatic compression test and for bulk modulus-simple shear test

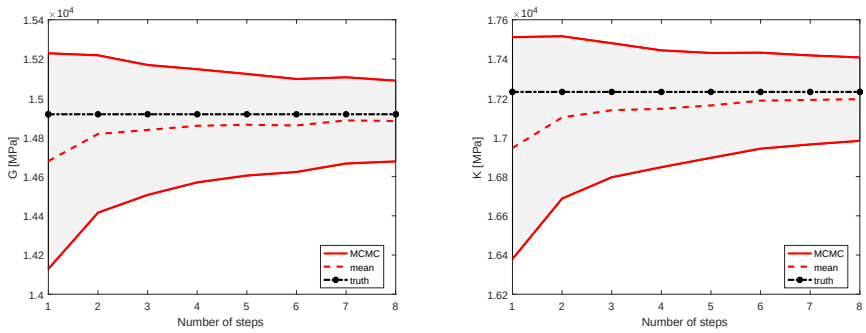

(a) **(b)**

Figure 5.14: Comparison of posterior PDF for different measurement points describing elastic material parameter: (a) shear modulus (G) - simple shear test; (b) bulk modulus (K) - hydrostatic compresion test

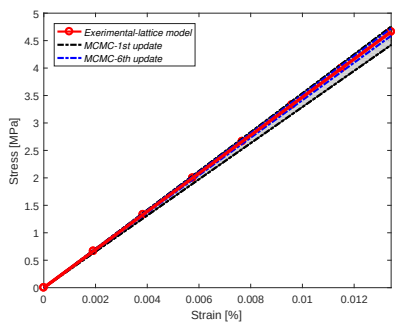

Figure 5.15: Macroscopic response in elastic range with computed parameters

Although this kind of calibration procedure is robust and accurate, the experiment dealing with a simple shear test and especially hydrostatic pressure test are rather difficult to perform in a fully reproducible way. For that reason, we turn to studying the possibility of parameter estimates by using the standard uniaxial compression test. In particular, the loading path in meridian plane clearly reveals that elastic parameters (K,G) can be also recovered by using measurements obtained in uniaxial tension or compression test (Figure 5.16b). In this case, the measurement of force

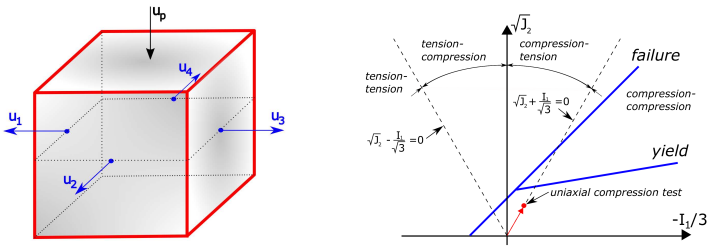

(a) (b)

Figure 5.16: (a) Displacements measured to evaluate the expansion $\Delta l = 0.25 \cdot (u_1 + u_2 + u_3 + u_4)$ of the specimen; (b) loading path

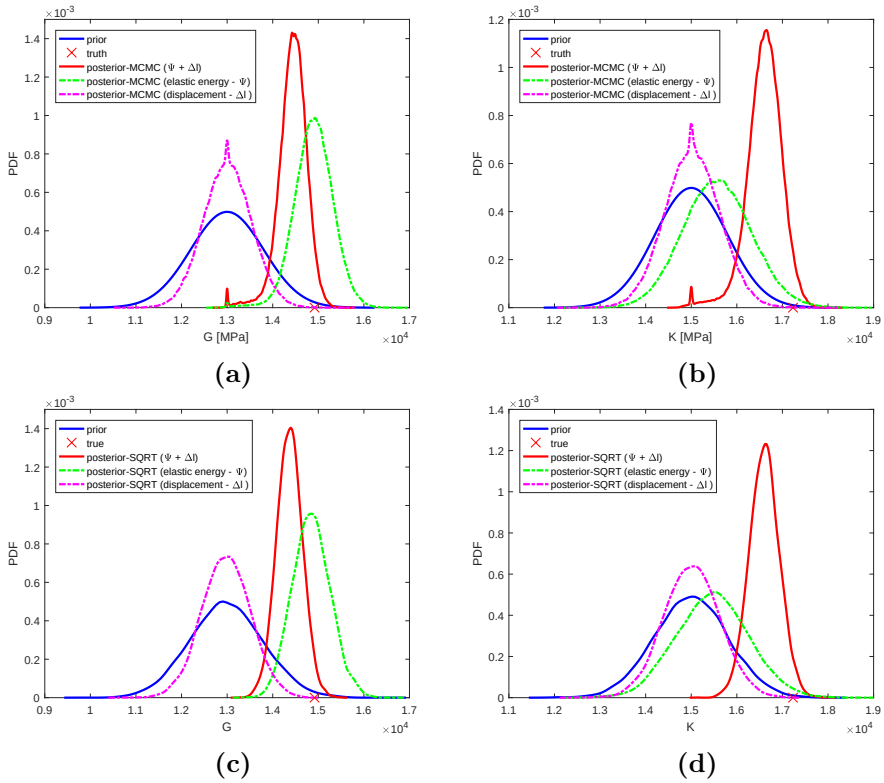

Figure 5.17: Comparison of prior and posterior pdf function for: (a) shear modulus; (b) bulk modulus performed on uniaxial compression test obtained by MCMC (upper row) and by SQRT Kalman filter (lower row)

or energy are not sufficient to perform identification, unless these measurements also include information about the specimen expansion. Figure 5.17 shows the updated parameters from these measurements revealing that uniaxial compression test improves better our knowledge about the shear modulus than about the bulk modulus regardless of the chosen method.

The dependence of the PCE on the polynomial order is investigated in Figure 5.18 where the accuracy of the sum of force approximation on the uniaxial compression test is plotted for different polynomial orders. By comparing the approximated solution against the reference value obtained by forward model, one concludes that

only the third order approximation can be safely used. In this case response in both direction (direction of K and G) match with forward model response. Otherwise, for lower values of the polynomial order the mean value is estimated correctly (the crossing point) but not the higher order moments (the lines do not match).

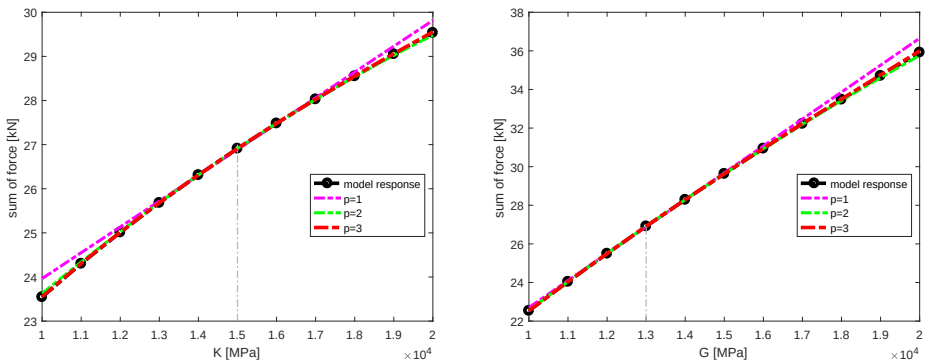

(a) **(b)**

Figure 5.18: Polynomial chaos approximation of the model response for uniaxial compression test: (a) bulk modulus; (b) shear modulus

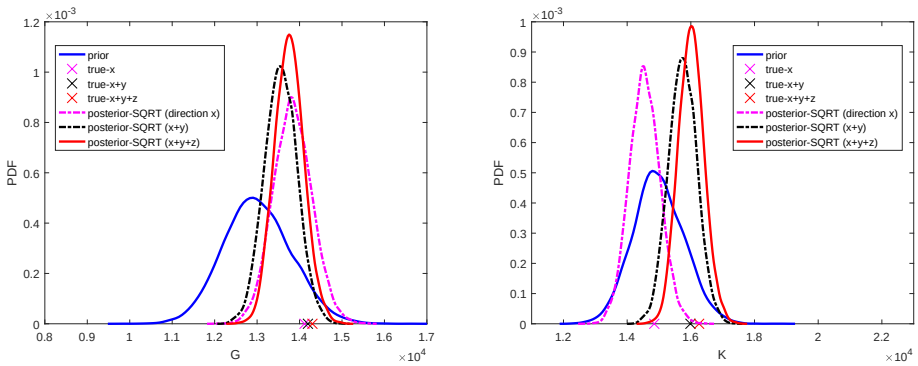

(a) **(b)**

Figure 5.19: Comparison of prior and posterior pdf function obtained by SQRT Kalman filter for: (a) shear modulus; (b) bulk modulus performed on uniaxial tension test for three loading direction

As mentioned before, the concrete can be considered statistically isotropic material, since the response for loading in any of three directions differs only a little. Here, we provide identification of both elastic parameters in sequential manner by using one measurement from uniaxial tension test with loading in three directions. We can note in Figure 5.19 that updating is similar to the one performed on one test with multiple measurements proving that response in three direction is almost the same. All these measurements are taken from uniaxial tension test obtained by meso-scale model with 50% of volume fraction of aggregates.

5.5.2 Identification of hardening parameters

Once we have identified the elastic parameters from the appropriate tests, we can continue towards the estimate of the hardening parameters. Namely, the parameters that we are trying to recover are now $p = (\sigma_y, \beta, tan(\phi), tan(\psi), \sigma_{\text{inf}})$ denoting the yield stress, the hardening parameter, the angle of internal friction, the angle of internal dilatancy and the ultimate limit stress for saturation type of hardening, respectively. Note, that hardening on macro-scale model follows after elastic response in compression test, whereas in tension test the elastic response is directly followed by softening part. The stress in hardening increases until it reaches σ_∞, which can be directly computed as $\sigma_\infty = \sigma_{max,ref} + \sigma_y$, where $\sigma_{max,ref}$ is the limit stress at stress-strain diagram obtained with numerical or experimental tests. With a such simplification there are four material parameters to be identified. Performing deterministic identification we can note that identifying these four parameters simultaneously, the cost function remains quite demanding to optimize. From definition of yield function and of plastic potential function we can note that these four parameters are split into two groups. First, the yield stress and the angle of internal friction $(\sigma_y, tan(\phi))$, which are sufficient to define yield function, and then the hardening parameter and the angle of internal dilatancy $(\beta, tan(\psi))$, which are sufficient to define plastic potential function. In addition to this simplification and to keep this optimization step efficient, the simulations is restricted to a limited loading range.

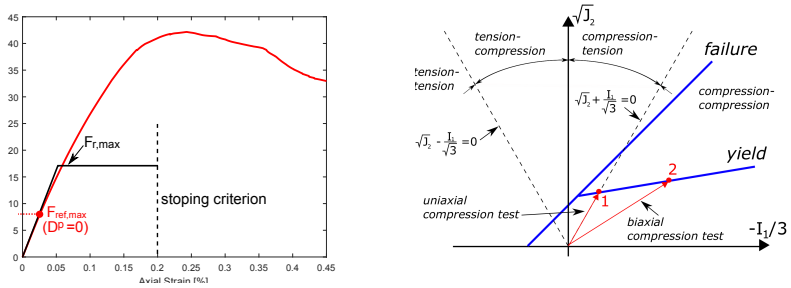

(a) (b)

Figure 5.20: (a) force measured on meso-scale model (red) and 3D solid model (black) with simplified model for identification of yield function; (b) loading path

Thus for the purpose of the first step in identification of σ_y and $tan(\phi)$ can be performed by setting the macro-scale model to ideal-plastic model (Figure 5.20a). The measurement of free potential energy ψ and dissipation D^p are taken here from uniaxial and biaxial compression tests performed on a plate specimen with dimension 150 x 30 x 150 cm (Figure 5.20b).

Figure 5.21 shows that we update our knowledge only if measurements from both biaxial and uniaxial test are taken into account, proving that the yield function can be recovered with minimum two measurements (red points in Figure 5.20b). If only measurements from uniaxial or biaxial compression tests are include into identification procedure, it results with a wide range of parameters that can provide the results, which is again in agreement with deterministic identification (Figure 5.22).

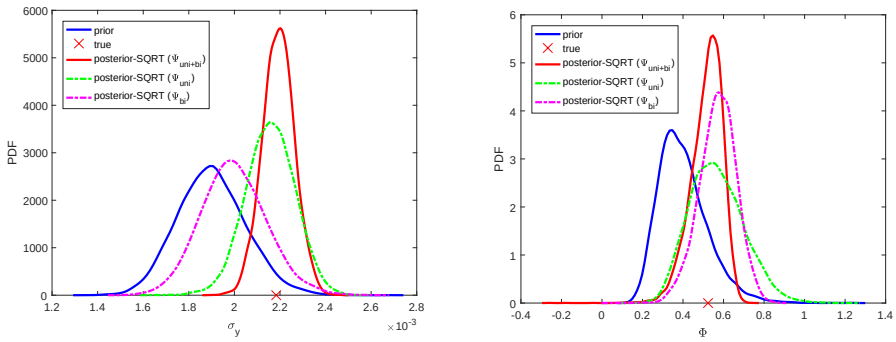

(a) **(b)**

Figure 5.21: Updates for plastic parameters $\{\sigma_y,\ tg_\Phi\}$ obtained by SQRT Kalman filter

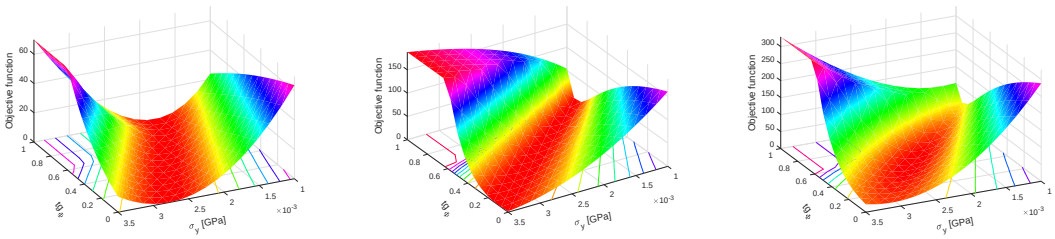

(a) **(b)** **(c)**

Figure 5.22: Objective function with measurements taken from: (a) uniaxial test; (b) biaxial test; (c) uniaxial and biaxial test combined

The second stage of identification of hardening parameters involves the angle of dilatancy $tan(\psi)$ and the hardening parameter β for saturation type of hardening. There are two requirements for the choice of measurements in this stage. First, measurements should be chosen between yield strain - ϵ_y and strain which corresponds to the limit stress. Second, the number of measurements should ensure convex objective function. If the first requirement is fulfilled the corresponding objective function depends only on values of the hardening parameter and the dilatancy angle, because bulk and shear modulus, as well as the yield stress and the angle of internal friction, are kept fixed with the optimal values determined during the previous stage.

To identify these two parameters we propose to include four measurements not only of force or dissipation but also of volumetric strain (Figure 5.23)

The choice of the cost function or measurements is explored in Figure 5.24. From Figures 5.24a-5.24b we can note that measuring only plastic dissipation is not sufficient to recover updated distribution for both parameters. Namely, our prior knowledge about angle of internal dilatancy remains unchanged due to lack of information. If we include in updating process information about volumetric strain in particular computational time then updated distribution is moving towards true value for each new measurements for hardening parameter β, while for the angle of internal dilatancy $\tan(\psi)$ only third and fourth measurements provides adequate information about this parameter.

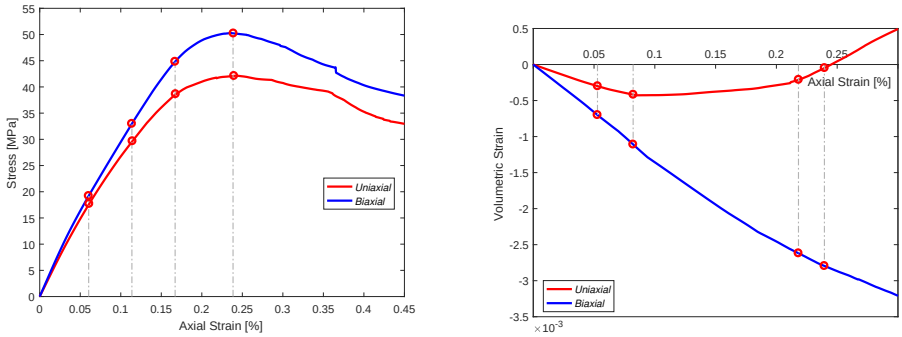

(a) (b)

Figure 5.23: Measurements for objective function for hardening parameters $(\beta, \tan(\psi))$ (a) stress-strain curve; (b) volumetric strain-axial strain

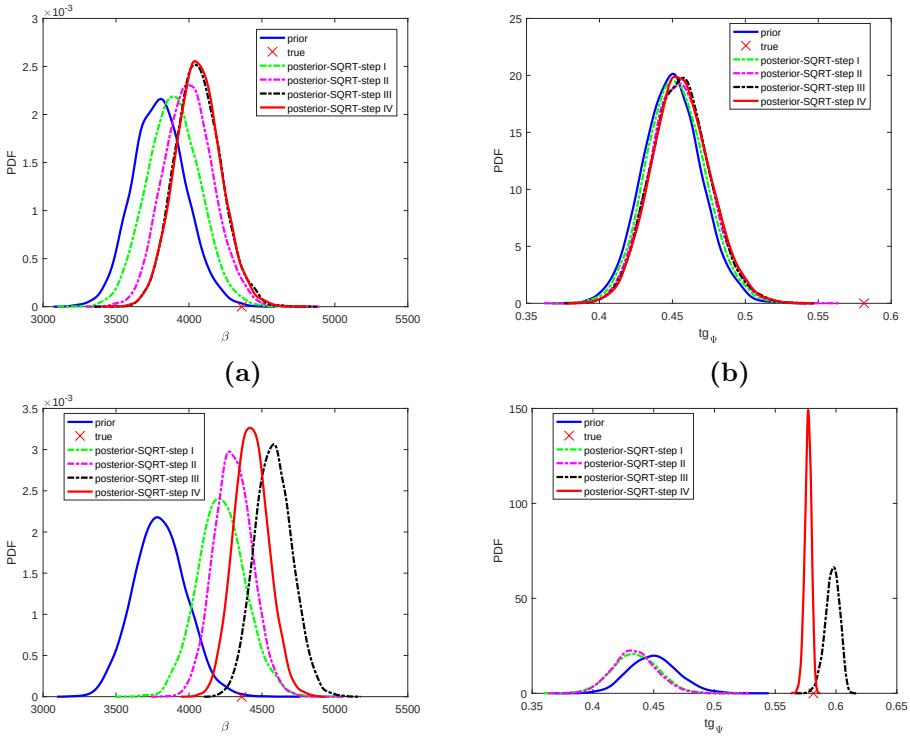

(a) (b)

(c) (d)

Figure 5.24: Updates for plastic parameters $\{\beta,\ tg_\Psi\}$ obtained by SQRT Kalman filter with four measurement (plastic dissipation - D^p) shown in (a)-(b) and (plastic dissipation - D^p + volumetric strain) shown in (c)-(d), taken from uniaxial compression test

The cost function obtained with deterministic identification is presented in Figure 5.25. We can note that optimal parameters are in wide range in direction of β opposite to the narrow range for the angle of internal dilatancy $\tan(\psi)$. These findings are in agreement with results obtained with stochastic identification where deviation about mean value is much higher for hardening parameter than for the angle of internal dilatancy.

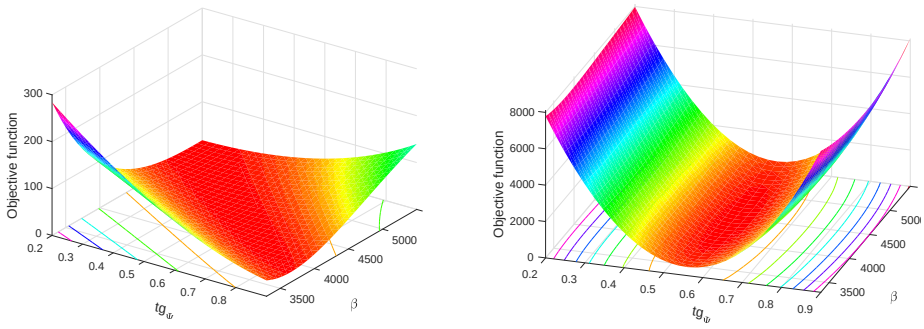

(a) **(b)**

Figure 5.25: Objective function J_9 with measurements taken from uniaxial compression test (a) plastic dissipation (D^p); (b) plastic dissipation (D^p) + volumetric strain

5.5.3 Identification of softening parameters

The last stage of identification involves the limit stress σ_u, the fracture energy in tension $G_{f,t}$ and the fracture energy in compression $G_{f,c}$. Variable σ_u represents a limit of hardening response phase of material, in compression and elasticity limit in tension. Either is followed by the appearance of macroscopic crack typically placed in the direction of principal elastic strain, but with different number or fracture energy release for tension versus compression case. There are two possibilities to determine the corresponding limit stress. The first is based on comparison of displacement corresponding to this event on meso-scale model or in experimental results with a macro-scale model. The second is based on comparison of maximum stress on reference curve with a maximum stress on macro model. Determination of displacement at which limit stress is reached is rather difficult task, and thus we turn to the second possibility. In order to recover both softening parameters $(\sigma_u, G_{f,t})$ in tension and $(\sigma_u, G_{f,c})$ compression, we take measurements of the limit stress on meso-scale model as well as measurements of total energy in two arbitrary steps in softening part of global response. In the case of experimental data we could also use measurements of volumetric strain, which can be stated in deterministic manner as local measurements, while the limit stress belongs to the global measurements.

In Figure 5.26 we present updated distributions for softening parameters and we can note that first measurement (step I) do not change the posterior distribution of fracture energy due to inadequate choice of measurements. Namely, the first measurement represent the limit stress on meso-scale model, and thus the information about fracture energy is not completed. In the subsequent steps the total energy becomes more relevant for fracture energy and it moves the distribution towards the truth value. Again, we can find that distribution of the limit stress is sharper compared to the distribution of fracture energy, which is in agreement with results obtained with deterministic identification (Figure 5.27).

The presented comments on uniaxial tension test can be stated also for uniaxial compression test (Figure 5.28). Here, we can note that limit stress is changed a little due to nonlinear fracture criterion, which can be observed on meso-scale model. This kind of behavior fits very well with the experimental results for concrete. Thus,

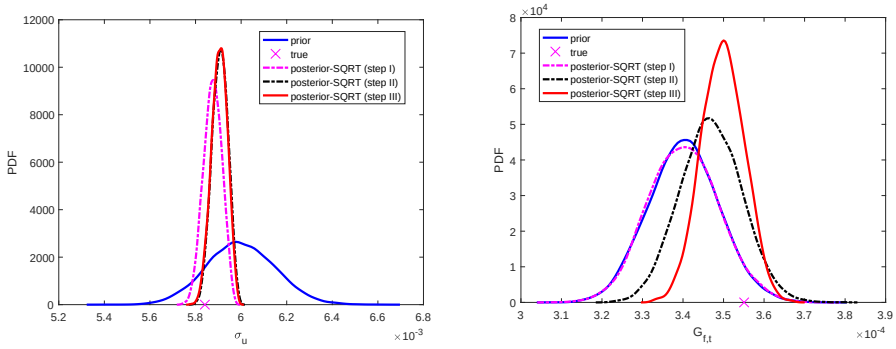

(a) (b)

Figure 5.26: Updates for softening parameters σ_u,and $G_{f,t}$ obtained by SQRT Kalman filter with three measurements taken from uniaxial tension test

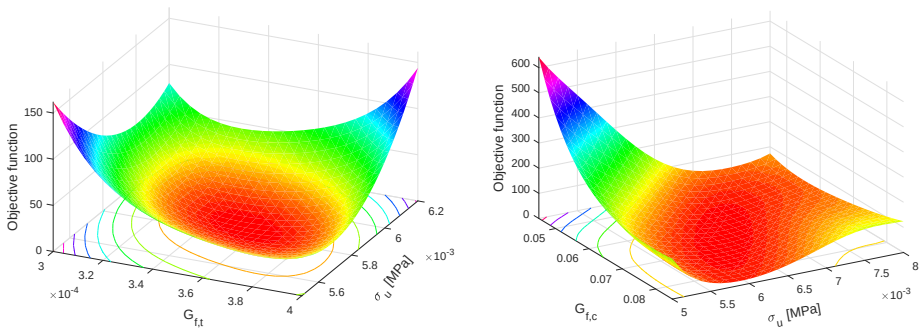

(a) (b)

Figure 5.27: Objective function for: (a) uniaxial tension test; (b) uniaxial compression test

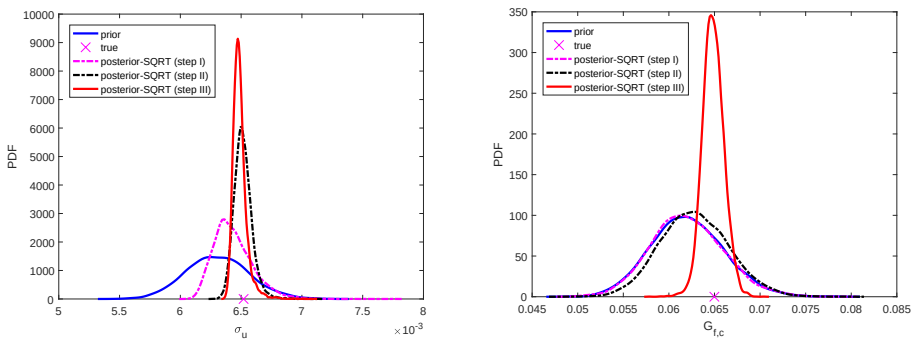

(a) (b)

Figure 5.28: Updates for softening parameters σ_u,and $G_{f,t}$ obtained by SQRT Kalman filter with three measurements taken from uniaxial compression test

with such an approach to identification we can determine which model is good for particular test or which parameters we should use on macro scale in order to describe behavior typical of concrete-like materials.

In Figure 5.29 we plot global response with parameters corresponding to 2.5% fractil value, marked as lower limit curve and with parameters which correspond to

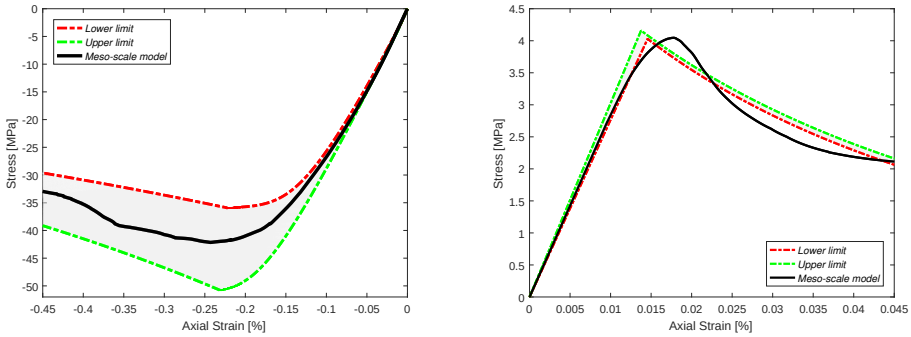

(a) (b)

Figure 5.29: Global response compute with 95% confidence interval of posterior distribution for: (a) uniaxial compression test; (b) uniaxial tension test

97.5% fractil value of posterior distribution marked as upper limit curve. We can note that elasticity parameters remains almost deterministic, while limit stress in compression varies much more than limit stress in tension. Fracture energy with each new measurement moves to the true value both in tension and in compression.

5.5.4 Simultaneous identification of all macro-scale model parameters and use of standard experiments

In this last example we want to illustrate two important points concerning possible difficulty for solving such identification problems: first using only standard experimental results, and second an alternative strategy to the one advocated herein that would attempt to identify all model parameters simultaneously. As for the former, we show that the standard uniaxial compression test for concrete is often insufficient to allow for robust identification of all model parameters, at least not in a unique manner. For illustration, we performed identification on the specimen presented in Figure 5.30 where the only measurements are those for force-displacement diagram, which is the usual type of results obtained by real experiments. We show that in such a case even elastic parameters can not be fully identified. Namely, the updated probability distribution of the shear modulus indeed moves towards the true value, but all updates for the bulk modulus stay only close to the prior. As for other two parameters we identified, the distribution of the yield stress remains unchanged compared to the prior, while distribution of the angle of internal friction moves towards the true value, but only after third plastic step. This clearly illustrates the need for more elaborate measurements in the standard tests, or using the computational results obtained by the presented meso-scale model for providing a very robust identification.

If the model does not offer the clear split between the groups parameters controlling different response phases (e.g. micro-plane model of concrete [193]), we have to use an alternative approach in which identification of all macro-scale model parameters and their probability distributions are computed simultaneously. First difficulty with such an approach is its excessive cost. Namely, the simultaneous

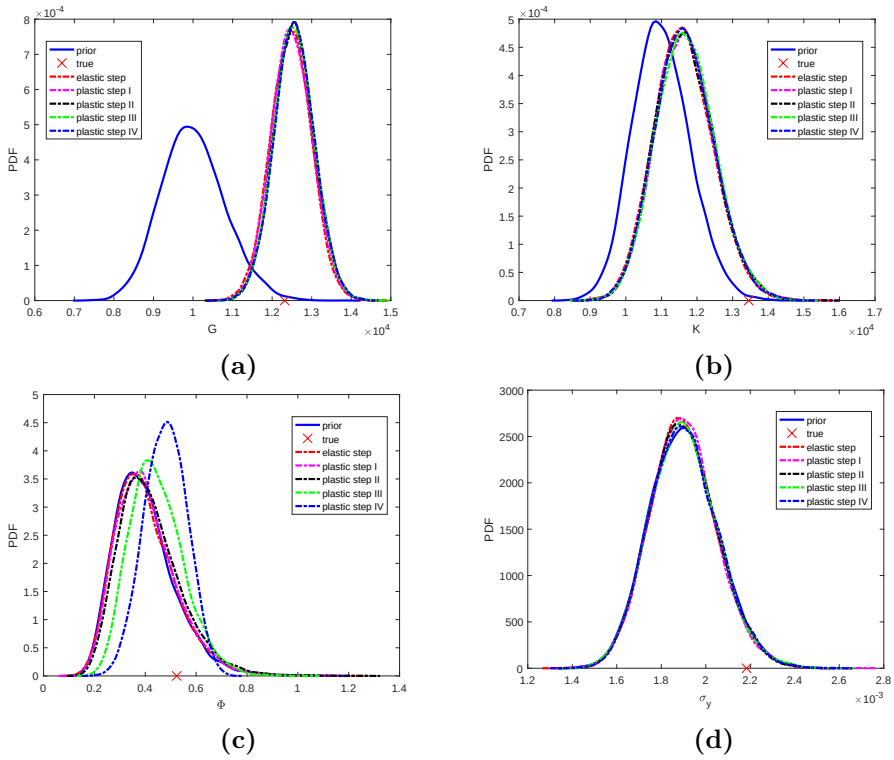

Figure 5.30: Updates for elastic and hardening parameters performed simultaneously on uniaxial compression test with measurements of force-displacement diagram

identification of all parameters requires computation of a proxy model for eight parameters in 4^8 integration points for third order polynomial. Such an identification would be very expensive computationally, resulting with days of computations.

For the sake of illustration, we here perform the identification by using a proxy model with four parameters, which still requires a considerable computations with 4^6 or 4^4 integration points. More precisely, we perform computations for three different groups of parameters where elastic parameters are simultaneously identified with either the yield stress and the angle of internal friction in the first group, or with the hardening parameter and the angle of internal dilatancy in the second group, or yet with the limit stress and the fracture energy in compression in the third group.

The usual measurements of force-displacement diagram would not be sufficient to carry out any such identification procedure. Thus, we need to complement these measurement with the computational results, or 'measurements'. In particular, in the elastic stage we take one measurement of elastic energy, in hardening we take four measurements of plastic dissipations along with volumetric strain, while in the softening stage we take measurements of the limit stress as well as measurements of total energy in two arbitrary steps. All these 'measurements' are made in fact by using the meso-scale model computations. The results for corresponding updates of elastic and plastic parameters' distributions are presented in Figure 5.31.

We can note in Figure 5.31a and Figure 5.31b that prior knowledge about elastic parameters is moved to the true value after elastic step while subsequent measurements taken in the hardening stage would no longer move their distribution

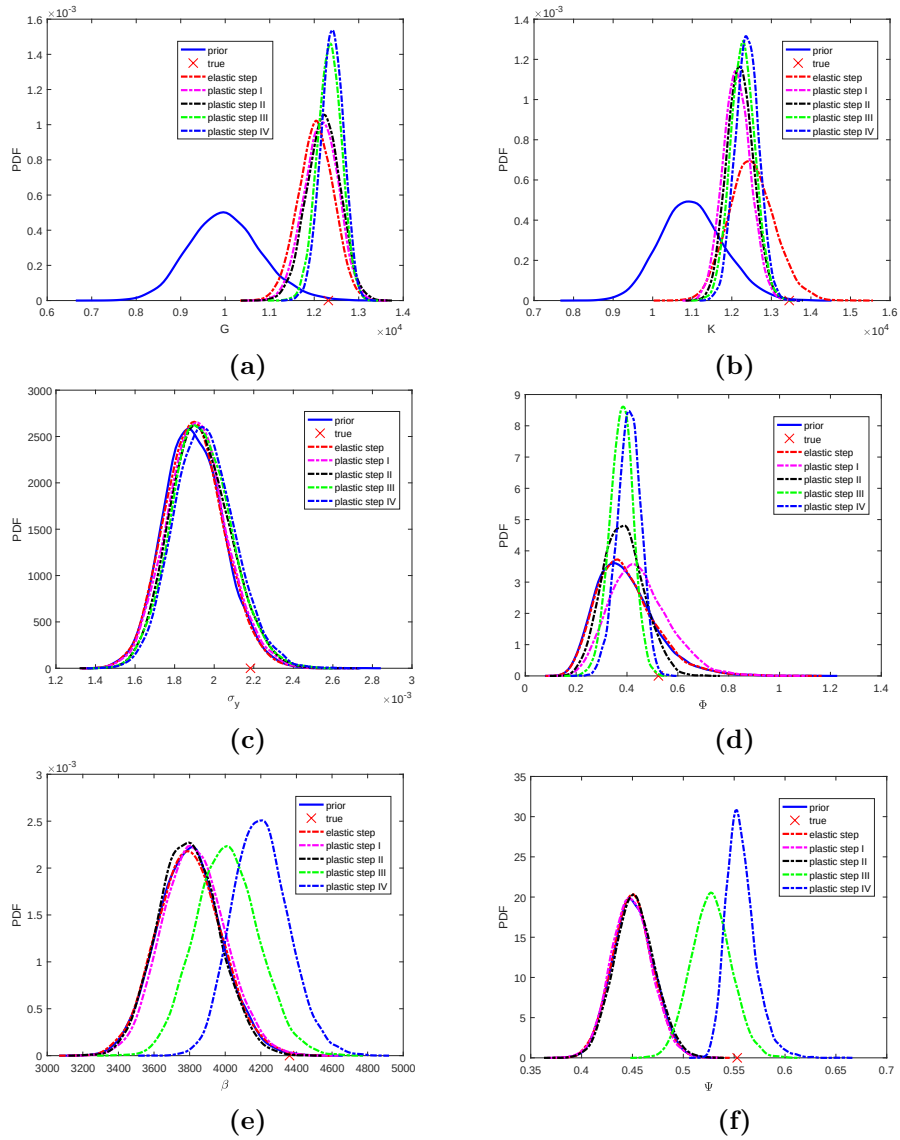

Figure 5.31: Updates for elastic and plastic parameters performed simultaneously on uniaxial compression test

towards the true value. This indicates that the elastic parameters can be identified by only using the measurements made in elastic response stage. Moreover, we can see from Figure 5.31 that elastic measurements do not change prior knowledge about plastic parameters. Namely, the identification of the yield stress and angle of internal friction can not be performed only with uniaxial compression test measurements (Figure 5.31c and Figure 5.31d). The measurements that are taken at a later stage of hardening provide much more information about angle of internal dilatancy and hardening parameter than any measurement made at the early stage. Similarly, from Figure 5.32 we can see that the elastic measurements do not affect prior knowledge about softening parameters (e.g. see Figure 5.32.a-b).

The final parameter identification attempt is here carried out with a group of six parameters that consists of two hardening parameters in compression, the

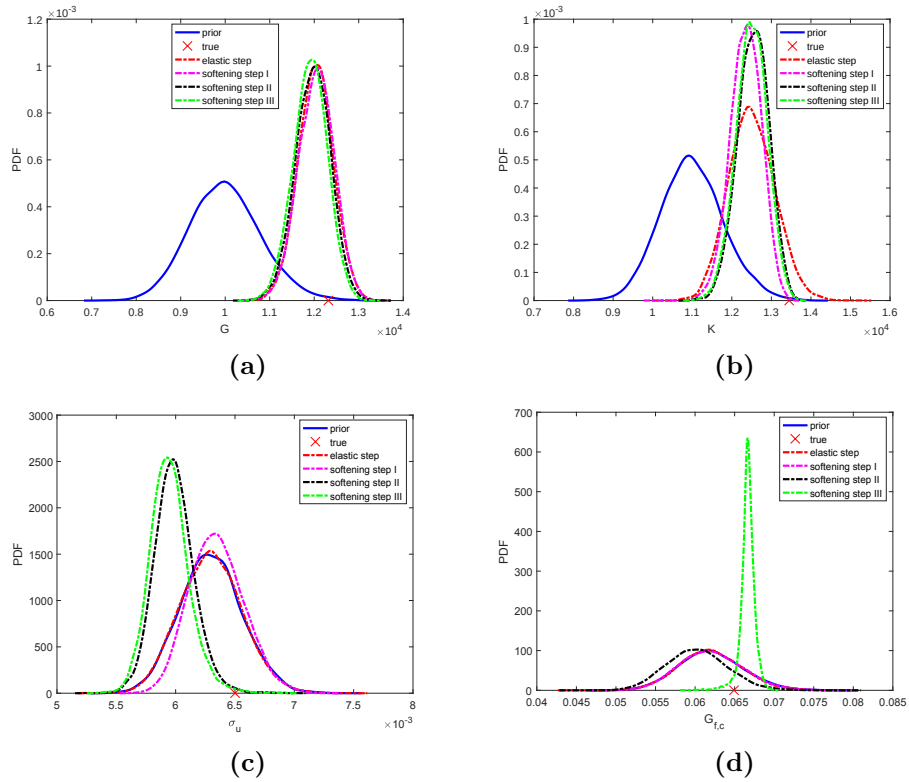

Figure 5.32: Updates for elastic and softening parameters performed simultaneously on uniaxial compression test

hardening parameter and the angle of internal dilatancy in shear, and two softening parameters. Again we find that the measurements made in softening stage do not provide any additional information either about elastic parameters nor about hardening parameters. In Figure 5.33.a-b, as well as Figure 5.33.c and Figure 5.33.d, we can find that measurements in hardening stage are irrelevant for softening parameters. In such a case, a reduced computational cost of splitting the parameters identification produces the same results as with the simultaneous computations of all parameters. This fully confirms the interest of the identification procedure split which we used in the previous examples.

5.6 Final comments on the presented stochastic plasticity identification

In this chapter we propose the reduced macro-scale model for concrete with multi-surface plasticity criteria for fracture process zone with parameters defined as random variables, along with the embedded-discontinuity finite element localized failure criteria with parameters also defined as random variables. At macro-scale we build multi-surface model which can better reproduce the behavior of massive structures by taking into account different types of dissipative mechanisms: a bulk dissipation characterized by the development of micro-cracks (by using Drucker-Prager citerion

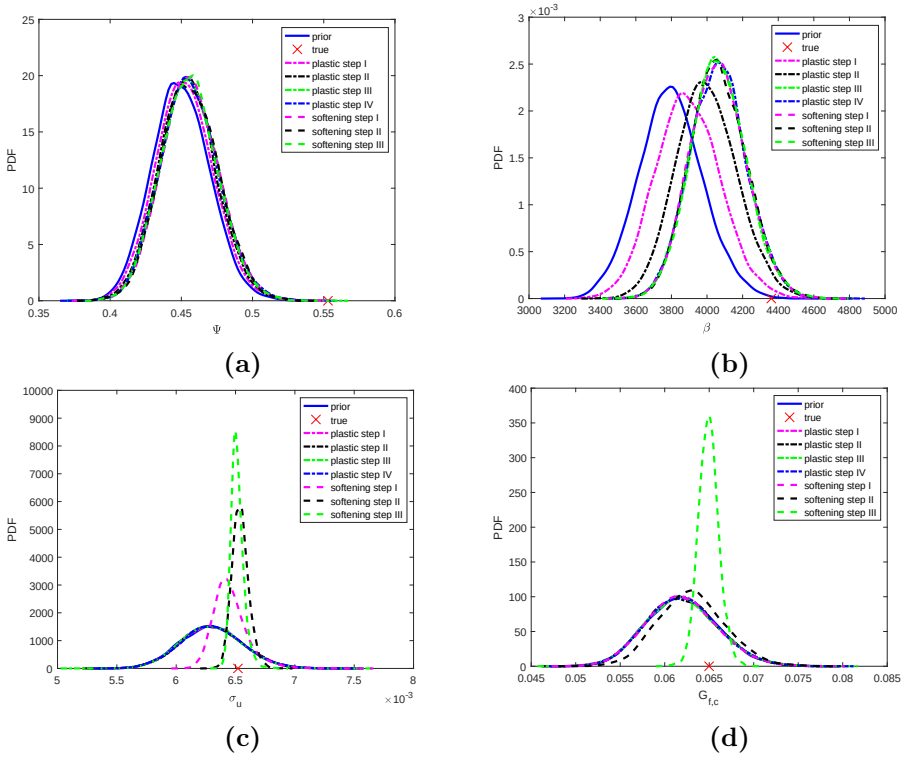

Figure 5.33: Updates for hardening and softening parameters performed simultaneously on uniaxial compression test

with non-associative flow rule) and a surface dissipation in localization zones in terms of the macro-cracks (with St. Venant plasticity criterion). The main advantage of such multi-surface plasticity model is in its ability to represent the complete set of global failure modes for concrete in tension, compression or shear. Another advantage of the proposed model is in its ability to represent three different stages of deformations in compression, with linear elastic, followed by hardening and finally by localized softening, whereas in tension it is sufficient to take elastic stage followed by unstable softening response. We note that all such elaborate features have to be combined in a single macro-scale model in order to provide the corresponding match with fine scale models of concrete.

In order to quantify the loss of information in bridging the scales from meso to macro, we account for the crucial role of uncertainties at both scales. Namely, the model parameters at meso-scale are here considered as random field. Moreover, the macro-scale model is also the one of stochastic plasticity. We used Bayesian inference to compensate for model reduction providing the probability distribution of macro-scale model parameters, which can provide better predictive properties to such model for any choice of plasticity criteria (and not only those used herein). We have shown that information used in such an identification approach should be obtained by using not only experimental test results but also the simulation results obtained with meso-scale model for concrete. The most significant finding concerns the use of energy or dissipated energy (or dissipation) to successfully update the macro-scale model parameters probability distributions. In order to provide

an additional information about parameters uncertainty it would be desirable to further combine all these computational results with more detailed experimental measurements (e.g digital image correlation or tomography), but this is not very convenient due to very large size of concrete specimen used in testing.

The reduced macro-scale model for concrete will have the local (point-wise) multi-surface plasticity criteria for fracture process zone with parameters defined as random fields, along with the embedded-discontinuity finite element localized failure criteria with parameters also defined as random fields. We consider two sources of uncertainty in development of this scale bridging: i) uncertainties in the choice of meso-scale fracture parameters and ii) uncertainties in the microstructure of meso-scale model. This results with a fairly limited number of sources of uncertainty that can be expressed in terms of random fields, and further transferred by KLE into uncorrelated Gaussian random variables, which renders the stochastic Galerkin approach feasible in terms of computational cost required for constructing probability distributions in terms of Bayesian updates.

Two different methods for Bayesian inference have been tested and compared in the proposed approach that allows incorporating new information generated in a particular loading program. The first method Markov Chain Monte Carlo (MCMC) is identified as updating the measure, whereas the second method Polynomial Chaos Kalman Filter(PceKF) is updating the measurable function. We carried out various numerical tests and show that the identification approach split into three stages leads to not only substantial computational savings, but also provides more reliable results. We confirm that posterior distribution of elastic parameters is the same for both methods, as well as for different choice of the cost function or measurements (either free energy or force). We propose identification procedure for tests which are not difficult to impose in a laboratory environment, like uniaxial compression test. We observe that such kind of test favors shear modulus due to restrained lateral displacements corresponding to higher friction between the load plates and the specimen. Hardening parameters which characterize the behavior of concrete in compression are identified in two steps. First, the parameters which defines the yield function, and latter the parameters which define plastic potential function. We show that local measurements of volumetric strain provides essential information about angle of internal dilatancy. The measurements of ultimate stress on reference curve along with total energy is sufficient to obtain the posterior distribution of softening parameters. We also find that limit stress and fracture energy varies more in compression than in tension.

6

Conclusions and future perspectives

In this chapter we present an overview of the proposed approach as well as comments on the obtained results. The scientific contributions of this work and perspectives for future work are given.

This thesis aimed to provide solution for inverse problem by direct coupled nonlinear mechanics-probability problem in heterogeneous materials. It is based on combination of two different approaches: the generalized ED-FEM that has the role to provide the corresponding failure mechanisms and fracture model; and stochastic upscaling where any coarse scale can retain the unresolved physics of the smaller scale in terms of the corresponding probability distribution properties to match quantity-of-interest.

Meso-scale model for concrete relies on spatial beam models, as a class of discrete lattice models. Such a model can represent the multi-phase structure of concrete, namely cement paste and aggregates, considered as lattice elements representing cohesive links between the Voronoi cells. The beam element is represented by 3D Timoshenko beam, embedded with strong discontinuities in local coordinate system directions, capable to simulate the localized failure in modes I, II and III. Due to this enhancement complete mesh independency of crack propagation is ensured. Aggregate size is taken in agreement with well-known aggregates grading curves in concrete mixture (EMPA and Fuller). Spreading aggregates in domain of interest with Poisson distribution provides realistic values of phase volume fraction. Gaussian distribution is used to represent heterogenities of each phase which takes into account the Interface Transition Zone (ITZ) through the weakening of concrete. The results of numerical simulation with proposed model indicate that resistance to tension and compresion is influenced by volume fraction of aggregates while two different failure mechanisms are observed. It was shown that model is capable to provide a reliable results in biaxial loading which fits very well with experimental results made for concrete.

The presented macro-scale model is developed as multisurface plasticity model for concrete that takes into account both the contribution of a strain hardening with non-associative flow rule as well as a strain softening model components for full set of different 3D failure modes. The plasticity model is represented with Drucker-Prager yield criterion, with similar plastic potential function governing hardening behavior while strain softening behavior is represented with St. Venant criterion. The reason why we take non-associative flow rule is based on experimental observations where it is noted that during hardening concrete-like materials shows nonlinear volume change. For representing the failure, a displacement jump is embedded in the solid element to describe the postpeak behavior providing complete mesh independency of the discrete approximation constructed by the finite element methods. Although none of the above ingredients are novel in the field of computational solid mechanics when considered separately we have extended them and combined them into the proposed concrete model and provide more realistic representation of the limit state of massive structures. Numerical examples validate the model against experimental results for different deformation modes, reproducing also crack patterns on reinforced concrete beams under bending.

The presented identification procedure for macro-scale model is perfomed in sequential way. Due to the fact that all ingredients of macro-scale model have physical interpretation we made calibration of material parameters relevant to particular stage. Objective functions are constructed so that both measurement of

force and displacement either energy and dissipation is appropriate. We observe that for experimental setting major difficulty concerns for properly recognition of the structural response stages.

Model reduction from meso-scale model to macro-scale model is considered as a part of a scale-coarsening strategy. Namely, all scales are considered as uncertain and probability computation is performed. First, an off-line probability computation in terms of pre-processing by Bayesian updates of many realizations for particular composite material microstructure to define meso-scale parameters as random fields. Second, an on-line probability computation to carry on with uncertainty propagation starting from such meso-scale to structural scale. Each unknown parameter of reduced model is modeled as a random variable when we are modeling homogeneous material while for heterogeneous material, these material parameters are described as random fields. We choose p-method mesh refinement over probability domain and h-method over spatial domain to make appropriate discretizations. Latter, by using Stochastic Galerkin method we construct the forward model outputs in terms of Wiener polynomial chaos expansion (PCE). Such model approximation provides outputs more quickly the the full forward model. The probabilistic procedure of identification with two different methods based on *Bayes's* theorem that allows incorporating new observation generated in a particular loading program are presented. These methods, MCMC and PceKF, have been tested and compared and we observed that updating the measure (MCMC) or updating the measurable function (PceKF) results with the same distribution. It also seems that second method (PceKF) is the fastest than first method (MCMC). Moreover, with proposed approach we can recover any probability distribution of structure failure modes for advanced safety evaluation, contrary to pre-defined distributions which is currently used.

The scientific contributions of this work are related to the following: two novel models with full set of 3D failure modes for heterogeneous materials on meso-scale and macro-scale are developed; development of an inverse problem for concrete-like materials based on sequential computation not only for global response but for hardening stage as well; development of novel multi-scale two-way coupling approach for modeling of fracture with the probabilistic description.

The proposed approach can be extended to take into account nonlinear constitutive law on macro-scale model. Also, the application for reinforcement concrete could be considered with extension about bonding phenomena integrated into the model. Deterministic identification procedure could be extended by taking into account experimental measurements not just of force and displacement but also the measurements on surface with digital image correlation (DIC) methods. Regarding the probabilistic identification future work could be extended with the uncertainty which comes from spatial distribution of aggregates. Also, it could be considered the solution to a multiphysics problem on micro-scale to improve a posteriori distribution on meso-scale. We can also consider the application of proposed approach to the other types of materials and structures, such as soils, or rocks, or masonry structures.

References

[1] Ollivier JP, Maso JC, Bourdette B. Interfacial transition zone in concrete. Adv Cem Based Mater 1995;2:30-8. doi 10.1016/1065-7355(95)90037-3.

[2] Wriggers P, Moftah SO. Mesoscale models for concrete: Homogenisation and damage behaviour. Finite Elem Anal Des 2006;42:623-36. doi:10.1016/J.FINEL.2005.11.008.

[3] Bentz, D.P., CEMHYD3D: A three-dimensional cement hydration and microstructure development modeling package. version 3.0., (2005)

[4] Roelfstra, P., Sadouki, H., Wittmann, F., Le beton numerique, M&S, 18:327-335, 1985.

[5] Schlangen E., Garboczi E.J. New method for simulating fracture using an elastically uniform random geometry lattice, Int J Engng Sci 34 (1996) 1131-1144

[6] Schlangen E., Van Mier J.G.M. Experimental and numerical analysis of micromechanisms of fracture of cement-based composites, Cem Conc Compos 14 (1992) 105-118

[7] Schlangen E., Van Mier J.G.M. Simple lattice model for numerical simulation of fracture of concrete materials and structures,Mater Struct 25 (1992) 534-542

[8] Cusatis G, Bazant ZP, Cedolin L. Confinement-shear lattice CSL model for fracture propagation in concrete. Comput Methods Appl Mech Eng 2006;195:7154-71, doi:10.1016/J.CMA.2005.04.019

[9] Lilliu G., van Mier J.G.M. 3D lattice type fracture model for concrete, Eng Fract Mech 70 (2003) 927-941

[10] Berton S., Bolander J.E. Crack band model of fracture in irregular lattices, Comput Methods Appl Mech Eng 195 (2006), 7172-7181

[11] Vonk, R., Softening of concrete loaded in compression, PhD thesis, Tech. Univ. Eindhoven, The Netherlands, 1992

[12] Stankowski, T., Numerical simulation of progressive failure in particle composites, PhD thesis, University of Colorado, Boulder, USA, 1990

[13] Cusatis G, Bazant ZP, Cedolin L. Confinement-Shear Lattice Model for Concrete Damage in Tension and Compression: II. Computation and Validation. J Eng Mech 2003;129:1449-58. doi:10.1061/(ASCE)0733-9399(2003)129:12(1449).

[14] Landis EN, Bolander JE. Explicit representation of physical processes in concrete fracture. J Phys D Appl Phys 2009;42:214002. doi:10.1088/0022-3727/42/21/214002.

[15] Cusatis G, Pelessone D, Mencarelli A. Lattice Discrete Particle Model (LDPM) for failure behavior of concrete. I: Theory, Cem Conc Compos 33 (2011) 881-890

[16] Bazant ZP, Tabbara MR, Kazemi MT, PijaudierâĂŘCabot G. Random Particle Model for Fracture of Aggregate or Fiber Composites. J Eng Mech 1990;116:1686-705. doi:10.1061/(ASCE)0733-9399(1990)116:8(1686).

[17] Kawai T. New discrete models and their application to seismic response analysis of structures, Nucl Eng Des 1978;48:207-29. doi:10.1016/0029-5493(78)90217-0.

[18] Escoda J, Jeulin D, Willot F, Toulemonde C. Three-dimensional morphological modelling of concrete using multiscale Poisson polyhedra. J Microsc 2015;258:31-48. doi:10.1111/jmi.12213.

[19] Lisjak A, Grasselli G. A review of discrete modeling techniques for fracturing processes in discontinuous rock masses. J Rock Mech Geotech Eng 2014;6:301-14. doi:10.1016/J.JRMGE.2013.12.007.

[20] Nagai K, Sato Y, Ueda T. Mesoscopic Simulation of Failure of Mortar and Concrete by 3D RBSM. J Adv Concr Technol 2005;3:385-402. doi:10.3151/jact.3.385.

[21] Bolander JE, Saito S. Fracture analyses using spring networks with random geometry. Eng Fract Mech 1998;61:569-91. doi:10.1016/S0013-7944(98)00069-1.

[22] Nagai K, Sato Y, Ueda T, Kakuta Y. Numerical simulation of fracture process of plain concrete by rigid body spring method. 2002.

[23] Nikolic M., Karavelic E., Ibrahimbegovic A., Miscevic P. Lattice Element Models and Their Peculiarities, Archives of Computational Methods in Engineering (2017) doi:10.1007/s11831-017-9210-y

[24] Karavelic E., M. Nikolic, Ibrahimbegovic A., Kurtovic A., Concrete meso-scale model with full set of 3D failure modes with random distribution of aggregate and cement phase. Part I: Formulation and numerical implementation, Comp. Methods Appl. Mech. Eng., early view, (2018)

[25] Rots J.G., Invernizzi S. Regularized sequentially linear saw-tooth softening model, Int J Numer Anal Meth Geomech 28 (2004) 821-856

[26] Simo J.C., Oliver J., Armero F. An analysis of strong discontinuities induced by strain-softening in rate-independent inelastic solids, Comput Mech 12 (1993) 277-296

[27] Ortiz M., Leroy Y., Needleman A. A finite element method for localization failure analysis, Comput Methods Appl Mech Engrg 61 (1987) 189-214

[28] Ibrahimbegovic A., Brancherie D. Combined hardening and softening constitutive model of plasticity: precursor to shear slip line failure, Comput Mech 31 (2003) 88-100

[29] Ibrahimbegovic A., Melnyk S. Embedded discontinuity finite element method for modeling of localized failure in heterogeneous materials with structured mesh: an alternative to extended finite element method, Comput Mech 40 (2007) 149-155

[30] Zubelewicz A, Bazant ZP. Interface Element Modeling of Fracture in Aggregate Composites. J Eng Mech 1987;113:1619-30. doi:10.1061 (ASCE)0733-9399(1987)113:11(1619).

[31] Benkemoun N., Hautefeuille M., Colliat J.B., Ibrahimbegovic A. Failure of heterogeneous materials: 3D meso-scale FE models with embedded discontinuities. Internat J Numer Methods Eng 82 (2010) 1671-1688

[32] Benkemoun N, Ibrahimbegovic A, Colliat JB. Anisotropic constitutive model of plasticity capable of accounting for details of meso-structure of two-phase composite material. Comput Struct, 90-91 (2012) 153-162

[33] Liu JX, Deng SC, Zhang J, Liang NG. Lattice type of fracture model for concrete. Theor Appl Fract Mech 2007;48:269-84. doi:10.1016/J.TAFMEC.2007.08.008.

[34] Man H-K, van Mier JGM. Damage distribution and size effect in numerical concrete from lattice analyses. Cem Concr Compos 2011;33:867-80. doi:10.1016/J.CEMCONCOMP.2011.01.008.

[35] Wang X, Jivkov AP. Combined Numerical-Statistical Analyses of Damage and Failure of 2D and 3D Mesoscale Heterogeneous Concrete. Math Probl Eng 2015;2015:1-12. doi:10.1155/2015/702563.

[36] Comby-Peyrot I, Bernard F, Bouchard P-O, Bay F, Garcia-Diaz E. Development and validation of a 3D computational tool to describe concrete behaviour at mesoscale. Application to the alkali-silica reaction. Comput Mater Sci 2009;46:1163-77. doi:10.1016/J.COMMATSCI.2009.06.002.

[37] De Schutter G, Taerwe L. Random particle model for concrete based on Delaunay triangulation. Mater Struct 1993;26:67-73. doi:10.1007/BF02472853.

[38] Bernard, F., Kamali, S., Prince, W., 3D multi-scale modelling of mechanical behaviour of sound and leached mortar, CCR, 38:449-458, 2008.

[39] Caballero, A., Lopez, C. M., Carol, I., 3D meso-structural analysis of concrete specimens under uniaxial tension, Comp. Meth. Appl. Mech. Eng., 195:7182-195, 2006.

[40] Wang XF, Yang ZJ, Yates JR, Jivkov AP, Zhang C. Monte Carlo simulations of mesoscale fracture modelling of concrete with random aggregates and pores. Constr Build Mater 2015;75:35-45. doi:10.1016/J.CONBUILDMAT.2014.09.069.

[41] Ren W, Yang Z, Sharma R, Zhang C, Withers PJ. Two-dimensional X-ray CT image based meso-scale fracture modelling of concrete. Eng Fract Mech 2015;133:24-39.

[42] Computing A. HyperMesh Reference Manual-: Version 2.1. Altair Computing, Incorporated; 1997.

[43] Geuzaine C., Remacle J.F. Gmsh: a three-dimensional finite element mesh generator with built-in pre- and post-processing facilities. Internat J Numer Methods Eng 11 (2009) 1309-1331

[44] Si H. TetGen, a Delaunay-based quality tetrahedral mesh generator. ACM Trans Math Softw 2015;41:11.

[45] Vervuurt A, Van Vliet MR., van Mier JGM, Schlangen E. SIMULATIONS OF TENSILE FRACTURE IN CONCRETE. In: Wittmann FH, editor. Proc. Fram., AEDIFICATIO Publishers; 1995.

[46] Du C-B, Sun L-G. Numerical Simulation of Aggregate Shapes of Two-Dimensional Concrete and Its Application. J Aerosp Eng 2007;20:172-8. doi:10.1061/(ASCE)0893-1321(2007)20:3(172).

[47] Voronoi G. Nouvelles applications des parametres continus a la theorie des formesquadratiques. Deuxieme memoire. Recherches sur les paralleelloedres primitifs. J Fur Die Reine Und Angew Math 1908;134:198-287.

[48] Delaunay B. Sur la sphere vide. A la memoire de Georges Voronoi. Bull l'Academie Des Sci l'URSS 1934:793-800.

[49] Fuller WB, Thompson SE. The Laws of proportioning Concrete. Trans Am Soc Civ Eng 1907;LIX:67-143.

[50] Gal E, Ganz A, Hadad L, Kryvoruk R. Development of a Concrete Unit Cell. Int J Multiscale Comput Eng 2008;6:499-510. doi:10.1615/IntJMultCompEng.v6.i5.80.

[51] Shahbeyk S, Hosseini M, Yaghoobi M. Mesoscale finite element prediction of concrete failure. Comput Mater Sci 2011;50:1973-90. doi:10.1016/J.COMMATSCI.2011.01.044.

[52] Unger JF, Eckardt S, Konke C. A mesoscale model for concrete to simulate mechanical failure. Comput Concr 2011;8:401-23. doi:10.12989/cac.2011.8.4.401.

[53] Kim S-M, Abu Al-Rub RK. Meso-scale computational modeling of the plastic-damage response of cementitious composites. Cem Concr Res 2011;41:339-58. doi:10.1016/J.CEMCONRES.2010.12.002.

[54] Contrafatto L, Cuomo M, Greco L. Meso-scale simulation of concrete multiaxial behaviour. Eur J Environ Civ Eng 2017;21:896-911. doi:10.1080/19648189.2016.1182085.

[55] Shanaka K. Ductility design of very-high strength concrete columns (100 MPa-150 MPa). 2016.

[56] Ngo T, Lee H, Vimonsatit V, Kristombu Baduge K, Mendis P. Properties of Matrix, Aggregate and Interfacial Transition Zone in Very High Strength Concrete (> 100 MPa) Using Nanoindentation Techniques. Int. Fed. Struct. Concr. 5th Int. fib Congr., 2018.

[57] Yilmaz O, Molinari J-F. A mesoscale fracture model for concrete. Cem Concr Res 2017;97:84-94. doi:10.1016/J.CEMCONRES.2017.03.014.

[58] Inglis, C.E., (1913), Stresses in a plate due to the presence of cracks and sharp corners,Transactions of the Royal Institute of Naval Architectes, 60,219-241)

[59] Griffith, A. A. (1921), The phenomena of rupture and flow in solids (PDF), Philosophical Transactions of the Royal Society of London, A, 221 (582-593): 163-198,

[60] Ngo, D., Scordelis, A., Finite element analysis of reinforced concrete beams, Journal of theACI, 64(14):152-163, 1967.

[61] Hillerborg, A., Modeer, M., Petersson, P., Needleman, A., Analysis of crack formation and crack growth in concrete by means of fracture mechanics and finite elements, CCR, 6:773-782, 1976.

[62] Rashid, Y. R., Analysis of prestressed concrete pressure vessels, Nuclear Engng. Design, 7:334-344, 1968.

[63] Bazant, Z. P., Oh, L., Crack band theory for fracture in concrete, M&S, 16:155-177, 1983

[64] Needleman, A., A continuum model for void nucleation by inclusion debonding. Journal of Applied Mechanics, 54(3):525-531, 1987

[65] Hillerborg, A., Numerical methods to simulate softening and fracture of concrete. Fract Mech of Concr, Struct Appl and Numer Calc 10.1007/978-94-009-6152-4-3, 1985.

[66] Cervenka, V. Inelastic finite element analysis of reinforced concrete panels under in-plane loads,PhD Thesis, University of Colorado, USA 1970 .

[67] Rots, J.G.,G. Nauta, P , Kuster, G.M.A., Blaauwendraad, Johan, Smeared Crack Approach and Fracture Localization in Concrete. HERON, 30 (1), 1985. 30,1985.

[68] Cosserat, E., and Cosserat, F., Theorie des corps deformables, Herman et Fils, Paris, 1909

[69] Bazant Z, Pijaudier-Cabot G., Nonlocal continuum damage, localization instability and convergence, ASME Journal of Applied Mechanics 1988;55:287-93

[70] Armero F, Garikipati K., Recent advances in the analysis and numerical simulation of strain localization in inelastic solids In: Owen E, Onõate DRJ, Hinton E (eds), Proceedings of Computational Plasticity IV, pp. 547-561 Barcelona, CIMNE,1995.

[71] Mosler J., Meschke G., Analysis of mode I failure in brittle materials using the strong discontinuity approach with higher order elements, in: 2nd European Conference on Computational Mechanics, Cracow, 2001

[72] Nikolic M., Ibrahimbegovic A. Rock mechanics model capable of representing initial heterogeneities and full set of 3D failure mechanisms, Comput Methods Appl Mech Eng 290 (2015) 209-227

[73] Ibrahimbegovic A. Nonlinear Solid Mechanics: Theoretical Formulations and Finite Element Solution Methods, Springer, London, 2009.

[74] Ibrahimbegovic A., Wilson E. A modified method of incompatible modes, Commun Appl Numer Method 7 (1991) 187-194

[75] Nikolic M., Ibrahimbegovic A. Miscevic P. Discrete element model for the analysis of fluid-saturated fractured poro-plastic medium based on sharp crack representation with embedded strong discontinuities, Comput Methods Appl Mech Eng 298 (2016) 407-427

[76] Nikolic M., Ibrahimbegovic A., Miscevic P. Brittle and ductile failure of rocks: Embedded discontinuity approach for representing mode I and mode II failure mechanisms, Internat J Numer Methods Eng 102 (2015) 1507-1526

[77] Grassl P., Jirasek M. Meso-scale approach to modelling the fracture process zone of concrete subjected to uniaxial tension, Int J Solids Struct 47 (2010) 957-968

[78] Grassl P., Gregoire D., Solano L.R., Pijaudier-Cabot G. Meso-scale modelling of the size effect on the fracture process zone of concrete, Int J Solids Struct 49 (2012) 1818-1827

[79] Vassaux M., Oliver-Leblond C., Richard B., Ragueneau F. Beam-particle approach to model cracking and energy dissipation in concrete: Identification strategy and validation, Cem Conc Compos 70 (2016) 1-14

[80] Schlangen E., Garboczi E.J. Fracture simulations of concrete using lattice models: computational aspects, Engineering fracture mechanics 57 (1997) 319-332

[81] Neville A.M., Brooks J.J. Concrete Technology 2nd Edition, Prentice Hall, (2010)

[82] Lubliner J. Plasticity theory, Mac-Millan, (1990).

[83] Lemaitre J., Chaboche J-L. Mecanique des Materiaux Solides, Dunod, (2004).

[84] Ibrahimbegovic A., Delaplace A. Microscale and mesoscale discrete models for dynamic fracture of structures built of brittle materials, Comput Struct 81 (2003) 1255-1265

[85] Taylor R.L, FEAP Finite element Analysis Program. University of California, Berkeley, http://www.ce.berkeley.edu.rlt

[86] Moosavi M., Bawden W.F., Shear strength of Portland cement grout, Cem Conc Compos 25 (2003) 729-735

[87] Yoshitake I., Uno T., Scanlon A., Simplified Test of Cracking Strength of Concrete Element Subjected to Pure Shear, J Mater Civ Eng 23 (2011) 999-1006

[88] Mindess S., Young J.F., Darwin D. Concrete 2nd Edition, Prentice Hall, (2003)

[89] Ibrahimbegovic A., Markovic D., Gatuingt F. Constitutive model of coupled damage-plasticity and its finite element implementation. Revue Europeenne des Elements Finis, 12 (2003) 381-405

[90] Colliat JB, Ibrahimbegovic A, Davenne L. Saint-Venant multi-surface plasticity model in strain space and in stress resultants, Eng Computation, 22 (2005) 536-557

[91] Sang-Keun L.,Young-Chul S., Sang-Hoon H. Biaxial behavior of plain concrete of nuclear containment building, Nucl Eng Design 227 (2004) 143-153

[92] Kupfer H., Hilsdorf H.K. Behavior of concrete under biaxial stress, ACI J Proc 66 (1969) 656-666

[93] Carpinteri A., Ingraffea AR.,Fracture mechanics of concrete, Martinus Nijhoff editor, The Netherlands, 1984

[94] Dolarevic S., Ibrahimbegovic A. A modified three-surface elasto-plastic cap model and its numerical implementation, Comput Struct 85 (2007) 419-430

[95] Dugdale D., Yielding of steel sheets containing slits, J. Mech. Phys. Solids 8 (1960) 100-108.

[96] Barenblatt G., The mathematical theory of equilibrium cracks in brittle fracture, Adv. Appl. Mech. 7 (1962) 55-129.

[97] Jirasek M., Zimmermann Th., Analysis of rotating crack model, J. Eng. Mech. ASCE 124 (1998) 842-851.

[98] Jirasek M., Zimmermann Th., Rotating crack model with transition to scalar damage, J. Eng. Mech. ASCE 124 (1998) 277-284.

[99] Bittencourt T.N., Wawrzynek P.A., Ingraffea A.R., Sousa J.L.,Quasi-automatic simulation of crack propagation for 2D LEFM problems, Engineering Fracture Mechanics 55 (2), 321-334.

[100] Borst Rüde, Sluys LJ., Mühlhaus HB., Pamin J., Fundamental issues in fnite element analyses of localization and deformation,Engineering Computations 1993,10:99-121.

[101] Pijaudier-Cabot G, Bazant Z., Nonlocal damage theory, ASCE Journal of Engineering Mechanics 1987;113(10):1512-33.

[102] Grassl P., Jirasek M. , Damage-plastic model for concrete failure, International journal of solids and structures 43 (22-23), 7166-7196, 2006.

[103] Oliver J., Continuum modelling of strong discontinuities in solid mechanics using damage models, Comput. Mech. 17 (1-2) (1995) 49-61.

[104] Feist C.,Hofstetter G., An embedded strong discontinuity model for cracking of plain concrete, Computer Methods in Applied Mechanics and Engineering 195 (52), 7115-7138

[105] Mosler J., Meschke G., 3D modeling of strong discontinuities in elastoplastic solids: fixed and rotating localization formulations, Internat. J. Numer. Methods Engrg. 57 (11) (2003) 1553-1576.

[106] Jirasek M., Zimmermann T.,Embedded crack model: Basic formulation. Int. J. Numer. Meth. Eng. 50: 1269-1290,2001.

[107] Stanic A., Solution methods for failure analysis of massive structural elements., Ph.D. thesis, University of Technology in Compiègne, France, 2017

[108] Do, X.N., Ibrahimbegovic, A., and Brancherie, D. (2017). Dynamics framework for 2D anisotropic continuum-discrete damage model for progressive localized failure of massive structures. Computers and Structures, 183:14-26

[109] Boyard S., C. Lebris, T. Lelievre, Y. Madey, Reduced basis techniques for stochastic problems, Arch. Comput. Methods Eng., 17, 435-454, (2010)

[110] Belytschko, T., Fish, J., Engelmann, B.E., 1988. A Finite element with embedded localization zones. Computer Methods in Applied Mechanics and Engineering 70, 59-89.

[111] Sluys, L.J., Berends, A.H., 1998. Discontinuous failure analysis for mode-I and mode-II localization problems. International Journal of Solids and Structures 35 (31-32), 4257-4274.

[112] Kratzig, W. B., Polling, R. (2004), An elasto-plastic damage model for reinforced concrete with minimum number of material parameters. Computers and Structures, 82(15-16), 1201-1215.

[113] Chen, A.C., Chen, W.F., Constitutive relations for concrete. Journal of Engineering Mechanics Division, ASCE 101, 465-481, 1975.

[114] Willam, K. J. and Warnke, E. P., Constitutive models for the triaxial behavior of concrete. Proceedings of the International Assoc. for Bridge and Structural Engineering , vol 19, pp. 1- 30,1975.

[115] Ulm, F-J., Coussy, O., Bazant, Z., The "Chunnel" Fire. I: Chemoplastic softening in rapidly heated concrete. ASCE Journal of Engineering Mechanics, vol. 125, no. 3, pp. 272-282, 1999.

[116] Linder, C., Armero, F. 2007. Finite elements with embedded strong discontinuities for the modeling of failure in solids. International Journal for Numerical Methods in Engineering 72: 1391-1433.

[117] Petersson, P. E. 1981. Crack growth and development of fracture zones in plain concrete and similar materials. Report No. TVBM-1006, Division of Building Materials, University of Lund, Lund, Sweden, 1981.

[118] Christensen, J. and K. Willam, Finite element analysis of concrete in shear, Proc. Symp. on the Interaction of Non-nuclear Munitions with Structures, U.S. Air Force Academy, Colorado, 101-106,1983

[119] Roscoe, K. H., An apparatus for the application of simple shear to soil samples, Proc. 3rd Int. Conf. Soil Mech., Zurich, Vol. 1, 129-170,1953.

[120] Vermeer P. A.,de Borst R., Non-associated plasticity for soils, concrete and rock,Heron, 1984.

[121] Carpinteri A., Ingraffea AR.,Fracture mechanics of concrete, Martinus Nijhoff editor, The Netherlands, 1984

[122] ETH Zurich, IBK, RC Tie Beam - Prediction Competition; 2013. http://www.ibk.ethz.ch/ma/competition.

[123] Bui N.N., Ngo M.,Nikolic M., Brancherie D., Ibrahimbegovic A., Enriched Timoshenko beam finite element for modeling bending and shear failure of reinforced concrete frames, Comput Struct, 143 (2014) 9-18.

[124] Lagarias J. C., J. A. Reeds, M. H. Wright, and P. E. Wright, Convergence Properties of the Nelder-Mead Simplex Method in Low Dimensions, SIAM Journal of Optimization, Vol. 9, Number 1, 1998, pp. 112-147

[125] Iacono C. , L.J. Sluys, and J.G.M. van Mier. Estimation of model parameters in nonlocal damage theories by inverse analysis techniques. Computer Methods in Applied Mechanics and Engineering, 195(52):7211-7222, 2006.

[126] Mahnken R. , E. Stein. Parameter identification for viscoplastic models based on analytical derivatives of a least-squares functional and stability investigations.International Journal of Plasticity, 12(4):451-479, 1996

[127] Mahnken R. . Identification of Material Parameters for Constitutive Equations. Encyclopedia of Computational Mechanics Part 2. Solids and Structures, John Wiley & Sons, Ltd., 2004, Chapter 19

[128] Maier G. , M. Bocciarelli and G. Bolzon and R. Fedele. Inverse analyses in fracture mechanics. International Journal of Fracture, 138:47-73, 2006.

[129] Furukawa R. , G. Yagawa. Inelastic Constitutive Parameter Identification Using an Evolutionary Algorithm with Continuous Individuals. International Journal for Numerical Methods in Engineering 40:1071-1090, 1997.

[130] Ibrahimbegovic A. , C. Knopf-Lenoir, A. Kuřerová, and P. Villon. Optimal design and optimal control of elastic structures undergoing finite rotations. International Journal for Numerical Methods in Engineering, 61(14):2428-2460, 2004

[131] Lepš M. . Single and Multi-Objective Optimization in Civil Engineering. Evolutionary Algorithms and Intelligent Tools in Engineering Optimization, Southampton: WIT Press, 2005, 320-341.

[132] Pyrz M. , F. Zairi. Identification of viscoplastic parameters of phenomenological constitutive equations for polymers by deterministic and evolutionary approach. Modelling Simul. Mater. Sci. Eng. 15:85-103, 2007.

[133] Kučerová A., D. Brancherie, A. Ibrahimbegovic, J. Zeman, Z. Bittnar, Novel anisotropic continuum-discrete damage model capable of representing localized failure of massive structures. Part II: identification from tests under heterogeneous stress field, International Journal of Engineering Computations, 26, 128-144 (2009)

[134] Waszczyszyn Z. , L. Ziemiański. Neurocomputing in the analysis of selected inverse problems of mechanics of structures and materials. Computer Assisted Mechanics and Engineering Sciences, 13(1):125-159, 2006.

[135] Pichler B. , R. Lackner, and H.A. Mang. Back analysis of model parameters in geotechnical engineering by means of soft computing. International Journal for Numerical Methods in Engineering, 57(14):1943-1978, 2003.

[136] Stefanou G., M. Georgiudakis, M. Papadrakakis, Sequentially linear analysis of structures with stochastic material properties, in M. Papadrakakis, G. Stefanou (eds.) 'Multiscale Modeling and Uncertainty Quantification of Materials and Structures', Springer, pp. 19-39, (2014)

[137] Hofstetter G., H.A. Mang, Computational Mechanics of Reinforced Concrete Structures, Vieweg, (1995) ISBN-10: 3528063904

[138] Meschke G., Pichler B., Rots J.G., (eds.), Computational modeling of concrete structures, CRC Press, pp. 1-1034, (2018), ISBN 9781138741171

[139] Belytschko T., J.-H. Song, Coarse-graining of multiscale crack propagation, Int. J. Numer. Meth. Engng., 81, 537-563, (2010)

[140] Chinesta F., P. Ladeveze, A. Ammar, E. Cueto, A. Nouy, Proper Generalized Decomposition in Extreme Simulations, IACM Expressions, 26, 1-6, (2009)

[141] Nouy A., A priori model reduction through Proper Generalized Decomposition for solving, Comp. Meth. Appl. Mech. Eng., 199, 1603-1623, (2010)

[142] Eigel M., C. Gittelson, Ch. Schwab, E. Zander, Adaptive stochastic Galerkin FE, Comput. Methods Appl. Mech. Eng., 270, 247-269, (2014)

[143] Ladeveze P., D. Neron, Model Order Reduction for nonlinear problems involving complex time-varying loadings, Proceedings ECCM-ECFD, 6th European Conf. Comp. Solid Mech. 7th European Conf. Comp. Fluid Dynamics, 11-15 June, (2018)

[144] Larsson F., F. Fritzen, On goal-oriented error estimation for model order reduction in computational homogenization of hyperelastic microstructures, Proceedings ECCM-ECFD, 6th European Conf. Comp. Solid Mech. 7th European Conf. Comp. Fluid Dynamics, 11-15 June,(2018)

[145] Reese S., S. Kastian, D. Moser, L. Grasedyck, Proper orthogonal decomposition (POD) combined with hierarchical tensor approximation (HTA) in the context of uncertain parameters, Proceedings ECCM-ECFD, 6th European Conf. Comp. Solid Mech. 7th European Conf. Comp. Fluid Dynamics, 11-15 June, (2018)

[146] Shinozuka, M., M. Feng, J. Lee, T. Naganuma. Statistical Analysis of Fragility Curves, J. Eng. Mech., 126, 1224-1231, (2000)

[147] Ladeveze P., G. Puel, T. Romeuf, Lack of knowledge in structural model validation, Comput. Methods Appl. Mech. Eng., vol. 197, pp. 4697-4710, (2006)

[148] Lamon J., Ceramics reliability: Statistical analysis of multiaxial failure using Weibull approach and the multiaxial elemental strength model, Compos. Sci. Tech., 69, 1607-1614, (2009)

[149] Bazant Z.P., Probability distribution of energetic-statistical size effect in quasit-brittle failure, Proba. Eng. Mech., 19, 307-319, (2004)

[150] Shell M.S., The relative entropy is fundamental to multiscale and inverse thermodynamic problems, J. Chem. Phys. 129 (14),114108, (2008)

[151] Ibrahimbegovic A., H.G. Matthies, Probabilistic Multiscale Analysis of Inelastic Localized Failure in Solid Mechanics, Computer Assisted Methods in Engineering and Science, 19, 277-304, (2012)

[152] Grigoriu, N. Zabaras, Probability and materials: from nano-to macro-scale: a summary. Probabilistic Engineering Mechanics, 193-199, (2006)

[153] Matthies H., Uncertainty quantification with stochastic finite elements, in (E. Stein et al.), Encyclopedia Comp. Mechanics, Wiley ch44, 1-70, (2007)

[154] Karavelic E., Ibrahimbegovic A., Dolarevic S., Multi-surface plasticity model for concrete with 3D hardening/softening failure modes for tension, compression and shear, Computers and Structures, 221, 74-90, (2019)

[155] Marzouk Y.M., H.N. Najm, L.A. Rahn, Stochastic spectral methods for efficient Bayesian solution of inverse problems, Journal of Computational Physics, 224, 560-586, (2007)

[156] Parlett B.N., The Symmetric Eigenvalue Problem. Prentice Hall, (1980)

[157] Ibrahimbegovic A., H.C. Chen, E.L. Wilson, R.L. Taylor, Ritz Method for Dynamic Analysis of Linear Systems with Non-Proportional Damping, Int. J. Earthquake Engng. Structural Dynamics, 19, 877-889, (1990)

[158] Zienkiewicz O.C. and R.L. Taylor, The Finite Element Method, Elsevier, (2005)

[159] Sanchez-Palencia E., Non homogeneous media and vibration theory. Lecture notes in physics. Berlin: Springer, (1980)

[160] Lions J.-L., Asymptotic calculus of variations, Academic Press, (1980)

[161] Lions J.-L., Y. Maday, G. Turinici, A "parareal" in time discretization of PDE's, C.R. lAcademie des Sci. - Ser. I Math. 332 (7) (2001)

[162] Simo J.C., J. Oliver, F. Armero, An analysis of strong discontinuities induced by strain-softening in rate-independent inelastic solids. Computational Mechanics, 12, 277-296, (1993)

[163] Jirasek M., T. Zimmerman, Embedded crack model. Part II: Combination with smeared cracks, Int. J. Numer. Meth. Engng., 50, 1291-1305, (2001)

[164] Ibrahimbegovic A., Markovic D., 'Strong coupling methods in multi-phase and multi-scale modeling of inelastic behavior of heterogeneous structures', Computer Methods in Applied Mechanics and Engineering, 192, 3089-3107, (2003a)

[165] Engl H. W. , C. W. Groetsch, Inverse and Ill-Posed Problems, Academic Press, New York, NY, 1987.

[166] Engl H. W. , M. Hanke, A. Neubauer, Regularization of inverse problems, Kluwer, Dordrecht, 2000.

[167] Tarantola A., Inverse Problem Theory and Methods for Model Parameter Estimation, SIAM, Philadelphia, PA, 2005.

[168] Rosic B. V. , A. Kucerova, J. Sykora, O. Pajonk, A. Litvinenko, H. G. Matthies, Parameter identification in a probabilistic setting, Engineering Structures 50 (2013) 179-196. doi:10.1016/j.engstruct.2012.12.029.

[169] Matthies H. G. , E. Zander, B. V. Rosic, A. Litvinenko, O. Pajonk, Inverse problems in a Bayesian setting, in: A. Ibrahimbegovic (Ed.), Computational Methods for Solids and Fluids - Multiscale Analysis, Probability Aspects, and Model Reduction, Vol. 41 of Computational Methods in Applied Sciences, Springer, Berlin, 2016, pp. 245-286. doi:10.1007/978-3-319-27996-1.

[170] Rosic B. , J. Sykora, O. Pajonk, A. Kucerova, H. G. Matthies, Comparison of numerical approaches to Bayesian updating, in: A. Ibrahimbegovic (Ed.), Computational Methods for Solids and Fluids - Multiscale Analysis, Probability Aspects, and Model Reduction, Vol. 41 of Computational Methods in Applied Sciences, Springer, Berlin, 2016, pp. 427-461. doi:10.1007/978-3-319-27996-1.

[171] Matthies H. G. , E. Zander, B. V. Rosic, A. Litvinenko, Parameter estimation via conditional expectation: a Bayesian inversion, Advanced Modeling and Simulation in Engineering Sciences 3 (2016) 24. doi:10.1186/s40323-016-0075-7.

[172] Bobrowski A. , Functional Analysis for Probability and Stochastic Processes, Cambridge University Press, Cambridge, 2005.

[173] Rao M. M. , Conditional Measures and Applications, CRC Press, Boca Raton, FL, 2005.

[174] Gilks W. R. , S. Richardson, D. Spiegelhalter, Markov Chain Monte Carlo in Practice, Chapman & Hall, Boca Raton, FL, 1995.

[175] Madras N. , Lectures on Monte Carlo Methods, American Mathematical Society, Providence, RI, 2002.

[176] Gamerman D. , H. F. Lopes, Markov Chain Monte Carlo: Stochastic Simulation for Bayesian Inference, Chapman & Hall, Boca Raton, FL,2006.

[177] Metropolis N. , A. W. Rosenbluth, M. N. Rosenbluth, A. H. Teller, E. Teller, Equation of state calculations by fast computing machines,Journal of Chemical Physics 21 (1953) 1087-1092. doi:10.1063/1.1699114.

[178] Kalman R. E. , A new approach to linear filtering and prediction problems, Transactions of the ASME-J. of Basic Engineering (Series D) 82 (1960) 35-45.

[179] Luenberger D. G. , Optimization by Vector Space Methods, John Wiley & Sons, Chichester, 1969.

[180] Matthies H. G. , A. Litvinenko, B. V. Rosic, E. Zander, Bayesian parameter estimation via filtering and functional approximations, arXiv: 1611.09293 [math.NA] (2016). URL http://arxiv.org/abs/1611.09293

[181] Goldstein M. , D. Wooff, Bayes linear statistics, Wiley Series in Probability and Statistics, John Wiley & Sons, Chichester, 2007.

[182] Pajonk O. , B. V. Rosic, A. Litvinenko, H. G. Matthies, A deterministic filter for non-Gaussian Bayesian estimation - applications to dynamical system estimation with noisy measurements, Physica D 241 (2012) 775-788. doi:10.1016/j.physd.2012.01.001.

[183] Evensen G. , The ensemble Kalman filter for combined state and parameter estimation, IEEE Control Systems Magazine 29 (2009) 82-104.

[184] Evensen G., Data Assimilation, The Ensemble Kalman Filter., Springer, Berlin, 2007.

[185] Xiu D. , Numerical methods for stochastic computations: a spectral method approach, Princeton University Press, Princeton, NJ, 2010.

[186] Le Maitre O. P., O. M. Knio, Spectral methods for uncertainty quantification, Scientific Computation, Springer, Berlin, 2010.

[187] Smith R. C. , Uncertainty Quantification: Theory, Implementation, and Applications,, Vol. 12 of Computational Science & Engineering,SIAM, Philadelphia, PA, 2014.

[188] Xiu D. , G. E. Karniadakis, The Wiener-Askey polynomial chaos for stochastic differential equations, SIAM Journal of Scientific Computing 24 (2002) 619-644.

[189] Janson S. , Gaussian Hilbert spaces, Cambridge University Press, Cambridge, 1997.

[190] Rosic B. V. , A. Litvinenko, O. Pajonk, H. G. Matthies, Sampling-free linear Bayesian update of polynomial chaos representations, Journal of Computational Physics 231 (2012) 5761-5787. doi:10.1016/j.jcp.2012.04.044.

[191] Pajonk O. , B. V. Rosic, H. G. Matthies, Sampling-free linear Bayesian updating of model state and parameters using a square root approach, Computers and Geosciences 55 (2013) 70-83. doi:10.1016/j.cageo.2012.05.017.

[192] Schillings C. , A. M. Stuart, Analysis of the ensemble Kalman filter for inverse problems, SIAM Journal on Numerical Analysis 53 (3) (2017)1264-1290. doi:10.1137/16M105959X.

[193] Kučerová A., M. Leps, Soft computing-based calibration of microplane M4 model parameters: Methodology and validation, Advances in Engineering Software 72, pp. 226-235, (2014)

A

Tables

Realization$j$	Direction$i$	Tension strength σ_{ti}^{j}(MPa)	Compressive strength σ_{ci}^{j}(MPa)
1	1(X)	2.744	-24.767
	3(Z)	2.636	-23.266
2	1(X)	2.681	-25.477
	3(Z)	2.696	-26.197
3	1(X)	2.515	-24.520
	3(Z)	2.703	-25.456
4	1(X)	2.588	-25.739
	3(Z)	2.742	-26.580
5	1(X)	2.509	-23.033
	3(Z)	2.554	-23.017
6	1(X)	2.507	-23.946
	3(Z)	2.641	-23.560

Table A.1: Uniaxial strength with 50% of aggregates

Combined regions	u_1(mm),u_3(mm)	σ_1^1/σ_c^1	σ_3^1/σ_c^1	σ_1^2/σ_c^2	σ_3^2/σ_c^2	σ_1^3/σ_c^3	σ_3^3/σ_c^3
Tension-tension	0.0000,0.0200	0.000	0.112	0.000	0.103	0.000	0.106
	0.0173,0.0100	0.113	0.091	0.113	0.083	0.112	0.086
	0.0100,0.0173	0.097	0.120	0.100	0.108	0.099	0.113
	0.0200,0.0000	0.104	0.000	0.105	0.000	0.103	0.000
	0.0056,0.0192	0.065	0.119	0.057	0.108	0.057	0.113
	0.0192,0.0056	0.112	0.057	0.113	0.054	0.111	0.078
	0.0200,0.0200	0.111	0.117	0.109	0.105	0.110	0.108
Compression-compression	0.0000,-0.2000	0.000	-1.000	0.000	-1.000	0.000	-1.000
	-0.1732,-0.1000	-1.220	-0.969	-1.273	-1.028	-1.272	-1.077
	-0.1000,-0.1732	-1.040	-1.251	-1.126	-1.197	-1.074	-1.216
	-0.2000,0.0000	-1.000	0.000	-1.000	0.000	-1.000	0.000
	-0.0872,-0.1800	-0.976	-1.248	-1.052	-1.190	-1.026	-1.214
	-0.1800,-0.0872	-1.224	-0.862	-1.280	-0.966	-1.260	-1.017
	-0.2000,-0.2000	-1.181	-1.186	-1.211	-1.162	-1.211	-1.190
	-0.1990,-0.0200	-1.192	-0.445	-1.210	-0.508	-1.200	-0.466
	-0.0200,-0.1990	-0.421	-1.152	-0.432	-1.163	-0.524	-1.118
	-0.1950,-0.0444	-1.224	-0.589	-1.253	-0.669	-1.231	-0.685
	-0.0444,-0.1950	-0.647	-1.208	-0.654	-1.181	-0.729	-1.172
	-0.2000,-0.0020	-1.156	-0.346	-1.167	-0.414	-1.168	-0.330
	-0.0020,-0.2000	-0.315	-1.126	-0.309	-1.147	-0.378	-1.085
Tension-compression	0.1732,-0.1000	0.107	-0.639	0.106	-0.583	0.103	-0.634
	0.1936,-0.0500	0.106	-0.512	0.115	-0.318	0.111	-0.424
	0.0224,-0.0380	0.071	-0.810	0.071	-0.802	0.069	-0.826
	0.0173,-0.0200	0.082	-0.707	0.089	-0.686	0.085	-0.728
Compression-tension	0.1732,-0.1000	-0.604	0.130	-0.606	0.101	-0.615	0.106
	0.1936,-0.0100	-0.507	0.124	-0.306	0.107	-0.321	0.114
	0.0224,-0.0380	-0.801	0.083	-0.809	0.074	-0.817	0.076
	0.0173,-0.0200	-0.686	0.100	-0.680	0.087	-0.686	0.090

Table A.2: Ratios of ultimate strength with respect to σ_c along X and Z directions under different couples of imposed displacements for realization 1,2 and 3

Combined regions	u_1(mm),u_3(mm)	σ_1^4/σ_c^4	σ_3^4/σ_c^4	σ_1^5/σ_c^5	σ_3^5/σ_c^5	σ_1^6/σ_c^6	σ_3^6/σ_c^6
Tension-tension	0.0000,0.0200	0.000	0.103	0.000	0.111	0.000	0.112
	0.0173,0.0100	0.113	0.087	0.119	0.095	0.117	0.096
	0.0100,0.0173	0.097	0.107	0.100	0.114	0.104	0.110
	0.0200,0.0000	0.101	0.000	0.109	0.000	0.105	0.000
	0.0056,0.0192	0.058	0.107	0.094	0.114	0.056	0.113
	0.0192,0.0056	0.114	0.056	0.117	0.086	0.115	0.059
	0.0200,0.0200	0.107	0.106	0.115	0.111	0.114	0.108
Compression-compression	0.0000,-0.2000	0.000	-1.000	0.000	-1.000	0.000	-1.000
	-0.1732,-0.1000	-1.316	-1.030	-1.319	-1.152	-1.330	-1.142
	-0.1000,-0.1732	-1.124	-1.251	-1.192	-1.295	-1.175	-1.292
	-0.2000,0.0000	-1.000	0.000	-1.000	0.000	-1.000	0.000
	-0.0872,-0.1800	-1.087	-1.248	-1.161	-1.292	-1.125	-1.300
	-0.1800,-0.0872	-1.310	-0.981	-1.319	-1.075	-1.324	-1.101
	-0.2000,-0.2000	-1.240	-1.206	-1.279	-1.272	-1.320	-1.244
	-0.1990,-0.0200	-1.200	-0.510	-1.270	-0.452	-1.283	-0.514
	-0.0200,-0.1990	-0.421	-1.185	-0.467	-1.205	-0.520	-1.194
	-0.1950,-0.0444	-1.264	-0.742	-1.305	-0.685	-1.304	-0.779
	-0.0444,-0.1950	-0.719	-1.221	-0.709	-1.237	-0.791	-1.231
	-0.2000,-0.0020	-1.183	-0.355	-1.244	-0.357	-1.250	-0.367
	-0.0020,-0.2000	-0.311	-1.159	-0.328	-1.182	-0.354	-1.180
Tension-compression	0.1732,-0.1000	0.103	-0.604	0.111	-0.669	0.105	-0.630
	0.1936,-0.0500	0.112	-0.359	0.119	-0.431	0.113	-0.385
	0.0224,-0.0380	0.069	-0.834	0.076	-0.850	0.071	-0.850
	0.0173,-0.0200	0.084	-0.735	0.093	-0.749	0.088	-0.749
Compression-tension	0.1732,-0.1000	-0.572	0.104	-0.634	0.113	-0.615	0.113
	0.1936,-0.0100	-0.322	0.110	-0.352	0.125	-0.379	0.119
	0.0224,-0.0380	-0.785	0.075	-0.817	0.082	-0.825	0.078
	0.0173,-0.0200	-0.666	0.088	-0.721	0.096	-0.714	0.092

Table A.3: Ratios of ultimate strength with respect to σ_c along X and Z directions under different couples of imposed displacements for realization 4,5 and 6